Determination of Source Finiteness and Depth of Large Earthquakes

Thesis by
Jiajun Zhang

In Partial Fulfillment of the Requirements
for the Degree of
Doctor of Philosophy

California Institute of Technology
Pasadena, California

1988

(submitted September 18, 1987)

Acknowledgements

I greatly appreciate the help, advice, and company of the students, faculty and staff at Caltech throughout my stay at the Seismological Laboratory.

I am extremely grateful to Professors Hiroo Kanamori, Bradford Hager, and Donald Helmberger for their support, help, and invaluable advice during my graduate study in the Lab.

My thesis adviser, Hiroo Kanamori, has been extremely patient with me and provided continuing instruction, encouragement, and enthusiasm for my work.

Thanks to my colleague students and friends, particularly Keith Echelmeyer, Hsui-Lin Liu, Patricia Scott, Marianne Walck, Thorne Lay, Mario Vassiliou, Henry Nataf, Steve Grand, Holly Eissler, Vicki LeFevre, Ronan Le Bras, Luciana Astiz, Robert Svendsen, John Vidale, Richard Stead, and John Louie.

Abstract

In this thesis, a method to retrieve the source finiteness, depth of faulting, and the mechanisms of large earthquakes from long-period surface waves is developed and applied to several recent large events.

In Chapter 1, source finiteness parameters of eleven large earthquakes were determined from long-period Rayleigh waves recorded at IDA and GDSN stations. The basic data set is the seismic spectra of periods from 150 to 300 sec. Two simple models of source finiteness are studied. The first model is a point source with finite duration. In the determination of the duration or source-process times, we used Furumoto's phase method and a linear inversion method, in which we simultaneously inverted the spectra and determined the source-process time that minimizes the error in the inversion. These two methods yielded consistent results. The second model is the finite fault model. Source finiteness of large shallow earthquakes with rupture on a fault plane with a large aspect ratio was modeled with the source-finiteness function introduced by Ben-Menahem. The spectra were inverted to find the extent and direction of the rupture of the earthquake that minimize the error in the inversion. This method is applied to the 1977 Sumbawa, Indonesia, 1979 Colombia-Ecuador, 1983 Akita-Oki, Japan, 1985 Valparaiso, Chile, and 1985 Michoacan, Mexico earthquakes. The method yielded results consistent with the rupture extent inferred from the aftershock area of these earthquakes.

In Chapter 2, the depths and source mechanisms of nine large shallow earthquakes were determined. We inverted the data set of complex source spectra for a moment tensor (linear) or a double couple (nonlinear). By solving

a least-squares problem, we obtained the centroid depth or the extent of the distributed source for each earthquake. The depths and source mechanisms of large shallow earthquakes determined from long-period Rayleigh waves depend on the models of source finiteness, wave propagation, and the excitation. We tested various models of the source finiteness, Q, the group velocity, and the excitation in the determination of earthquake depths.

The depth estimates obtained using the Q model of Dziewonski and Steim (1982) and the excitation functions computed for the average ocean model of Regan and Anderson (1984) are considered most reasonable. Dziewonski and Steim's Q model represents a good global average of Q determined over a period range of the Rayleigh waves used in this study. Since most of the earthquakes studied here occurred in subduction zones Regan and Anderson's average ocean model is considered most appropriate.

Our depth estimates are in general consistent with the Harvard CMT solutions. The centroid depths and their 90 % confidence intervals (numbers in the parentheses) determined by the Student's t test are: Colombia-Ecuador earthquake (12 December 1979), d = 11 km, (9, 24) km; Santa Cruz Is. earthquake (17 July 1980), d = 36 km, (18, 46) km; Samoa earthquake (1 September 1981), d = 15 km, (9, 26) km; Playa Azul, Mexico earthquake (25 October 1981), d = 41 km, (28, 49) km; El Salvador earthquake (19 June 1982), d = 49 km, (41, 55) km; New Ireland earthquake (18 March 1983), d = 75 km, (72, 79) km; Chagos Bank earthquake (30 November 1983), d = 31 km, (16, 41) km; Valparaiso, Chile earthquake (3 March 1985), d = 44 km, (15, 54) km; Michoacan, Mexico earthquake (19 September 1985), d = 24 km, (12, 34) km.

In Chapter 3, the vertical extent of faulting of the 1983 Akita-Oki, and 1977 Sumbawa, Indonesia earthquakes are determined from fundamental and overtone Rayleigh waves. Using fundamental Rayleigh waves, the depths are determined from the moment tensor inversion and fault inversion. The observed overtone Rayleigh waves are compared to the synthetic overtone seismograms to estimate the depth of faulting of these earthquakes. The depths obtained from overtone Rayleigh waves are consistent with the depths determined from fundamental Rayleigh waves for the two earthquakes. Appendix B gives the observed seismograms of fundamental and overtone Rayleigh waves for eleven large earthquakes.

Table of Contents

Acknowledgements ii
Abstract iii

Introduction 1

Chapter 1: Source Finiteness of Large Earthquakes Measured from Long-Period Rayleigh Waves

1.1. Introduction 6
1.2. Model of Seismic Source 8
1.3. Source Process Time 13
1.4. Data 14
1.5. Source Process Time Measured from Phase 16
1.5.1. Method 16
1.5.2. Results 17
1.6. Source Process Time Measured by a Linear Inversion Method 20
1.6.1. Method 20
1.6.2. Results 23
1.7. Inversion for the Rupture Model of Large Earthquakes 38
1.7.1. Results 40
1.7.2. 1983 Akita-Oki, Japan Earthquake 43
1.7.3. 1979 Colombia-Ecuador Earthquake 52
1.7.4. 1985 Valparaiso, Chile Earthquake 57
1.7.5. 1985 Michoacan, Mexico Earthquake 62
1.7.6. 1977 Sumbawa, Indonesia Earthquake 67
1.8. Conclusions 73
1.9. References 77

Chapter 2: Depth of Large Earthquakes Determined from Long-Period Rayleigh Waves

2.1. Introduction 84
2.2. Method 87
2.2.1. Moment Tensor Inversion 87
2.2.2. Fault Inversion 88
2.3. Earth Model 90
2.3.1. Phase Velocity and Q 90
2.3.2. Excitation 92
2.4. Source Finiteness 94
2.5. Data 98
2.6. Depth Determination 98
2.6.1. 1979 Colombia-Ecuador Earthquake 99
2.6.2. 1980 Santa Cruz Is. Earthquake 108
2.6.3. 1981 Samoa Earthquake 116
2.6.4. 1981 Playa Azul, Mexico Earthquake 122
2.6.5. 1982 El Salvador Earthquake 126
2.6.6. 1982 New Ireland Earthquake 130
2.6.7. 1983 Chagos Bank Earthquake 134
2.6.8. 1985 Valparaiso, Chile Earthquake 137
2.6.9. 1985 Michoacan, Mexico Earthquake 141
2.7. Resolution of Depth 143
2.8. Discussion 146
2.9. Conclusions 147
2.10. References 149

Chapter 3: Depths of the 1977 Sumbawa and 1983 Akita-Oki Earthquakes Determined from Long-Period Rayleigh Waves

3.1. Introduction 157
3.2. Inversion of Fundamental-Mode Rayleigh Waves 160
3.2.1. Correction for Source Finiteness 161
3.2.2. Correction for Propagation 165
3.2.3. Inversion Results 165
3.3. Overtone Amplitude 174
3.4. Discussion 179

3.5. Conclusions 182
3.6. References 184

Appendix A: Inversion of Long-Period Rayleigh and Love Waves

A.1. Moment Tensor Inversion of Love Waves 190
A.2. Double Couple Inversion of Love Waves 192
A.3. Moment Tensor and Double Couple Inversion
of both Rayleigh and Love Waves 193

Appendix B: Seismograms of the Vertical Component of Rayleigh Waves 196

Introduction

This thesis concerns the determination of the length, rupture velocity, and vertical extent of faulting of large earthquakes.

One of the most important source parameters is the vertical extent of faulting of large earthquakes. Most large and great earthquakes such as the 1960 Chilean earthquake and the 1964 Alaskan earthquake occur at subduction-zone thrust boundaries. Another class of earthquakes consists of large normal-fault earthquakes which occur near the trench axis. The notable examples are the 1933 Sanriku, Japan earthquake and the 1977 Sumbawa, Indonesia earthquake.

The vertical extent of faulting of large thrust events provides key information on the nature of interplate coupling at subduction zones. Many recent studies suggest that interplate interaction is a key element that determines tectonic features at plate boundaries. Also, estimation of seismic slip rate at subduction plate boundaries is essential for assessment of long-term seismic potential. In order to accurately estimate seismic slip rate from seismic moment, we need to have accurate estimates of the fault length and width. Direct determination of the vertical extent of faulting provides this key information on the fault width.

The study of the state of the stress in the subducting plate is important for a better understanding of the dynamics of subduction and of distribution of earthquake generating stress near subduction plate boundaries.

Normal-fault earthquakes near the trench axis are usually considered to be due to bending of an oceanic plate as it begins to subduct at the trench.

Another possibility is that these events are caused by extensional stress due to the negative buoyancy of the subducting slab, as well as by the bending stress, and break through almost the entire thickness of the lithosphere. Accurate determination of the vertical extent of faulting of these earthquakes is the key to resolution of this problem.

The vertical extent of faulting of large earthquakes is usually inferred from the extent of the aftershock activity. This method, however, is indirect and vague. The lack of aftershocks at a large depth does not necessarily mean that no seismic slip occurs there during faulting of the earthquake. The vertical extent of faulting could be estimated from geodetic data, but for earthquakes along subduction zones, geodetic coverage is seldom complete enough to determine the depth of faulting.

Modeling of seismic body waves often provides a good estimate of the hypocentral depth. For very large earthquakes, however, body waves are often off-scale or, even if they are on-scale, too complex to model. Furthermore, the hypocentral depth does not necessarily represent the overall vertical extent of faulting. It thus appears that the use of long-period seismic waves is the only means to directly determine the depth extent of faulting.

In this thesis, I present the results of detailed investigations into the use of long-period Rayleigh waves for the determination of the vertical extent of faulting of large earthquakes. The normal mode theory and the finite-source model are the basis of the present study. The basic data I used in this thesis are the seismograms of long-period Rayleigh waves recorded at the IDA (International Deployment of Accelerographs) and GDSN (Global Digital Seismograph Network) stations.

In order to estimate the vertical extent of faulting of large earthquakes, the seismic "Doppler effect" on the seismic waves must be accurately evaluated. Chapter 1 concerns the measurement of the source finiteness of large earthquakes, which produces the seismic Doppler effect.

I first investigated the effect of the earth's lateral heterogeneity on the spectra of surface waves. Recent progress in the studies of the lateral heterogeneity of the earth made possible a direct use of surface wave data in the determination of the source finiteness of large earthquakes. The propagation phase delay is calculated along the great circle path of each wave train using the phase velocity of laterally heterogeneous earth models.

I used two simple models of the source finiteness. The first is a point source with finite duration. The second is the finite-fault model, of which the parameters are the fault length, rupture velocity, and rise time.

I then adapted an inversion procedure to invert the observed spectra of Rayleigh waves. The source-finiteness effect can be measured without knowledge of the source mechanism, the depth of the source, and the excitation functions.

I determined the source-finiteness parameters of eleven large shallow earthquakes. My results are consistent with the rupture extent inferred from the aftershock area of these earthquakes.

In Chapter 2, the depths and source mechanisms of nine large shallow earthquakes were determined. The accuracy of the depth determination depends critically on how accurately we can correct the observed spectra for the source-finiteness effect and propagation effects on both phase and amplitude. Also the choice of the excitation functions is important.

I used the results obtained in Chapter 1 to correct for the source finiteness. The propagation effects on the phase can be estimated with good accuracy using recently developed laterally heterogeneous earth models at periods longer than 150 sec. The propagation effects on the amplitude can be estimated using global average Q models. The difference in the depth estimate determined for different Q models is small. However, the difference is systematic for different models, and is significant for shallow events. The effect of different earth models used for the computation of excitation functions is small.

In Chapter 3, the vertical extent of faulting of the 1983 Akita-Oki, and 1977 Sumbawa, Indonesia earthquakes are determined from fundamental and overtone Rayleigh waves. The Akita-Oki earthquake has been studied thoroughly by many investigators using seismic, geodetic and tsunami data, and the vertical extent of faulting is determined well. These studies suggest that the vertical extent of the faulting of the earthquake is approximately 30 km or less. This earthquake provides a test of the reliability of the depth estimate of large shallow earthquakes using the method presented in Chapter 2.

Inversion of fundamental-mode Rayleigh waves yields a centroid depth of 18km and 48km for the Akita-Oki and the Sumbawa earthquakes respectively. The result for the Akita-Oki earthquake is consistent with the estimate made from the aftershock, geodetic and tsunami data obtained by other investigators.

I compared the amplitude of overtone Rayleigh waves to fundamental-mode Rayleigh waves to obtain an independent estimate of the centroid depth. The results are consistent with those from fundamental modes. Combining

the results from the fundamental-mode and overtone Rayleigh waves I conclude that the centroid depth of the 1977 Sumbawa earthquake ranges from 30 to 40 km. If the fault plane extends to the surface, the above estimate indicates a vertical extent of faulting of 60 to 80km. If the fault plane extends to a depth of 10km, the vertical extent is 50 to 70km. The faulting of the Sumbawa earthquake extends over a significantly larger depth range than the Akita-Oki earthquake, and involved a substantial part of the oceanic plate.

As the quality of seismic data and the resolution of laterally heterogeneous earth models improve in the future, I hope that the method developed in this thesis will provide a useful tool for the determination of the depth extent of faulting of large earthquakes.

Chapter 1

Source Finiteness of Large Earthquakes Measured from Long-Period Rayleigh Waves

1.1 Introduction

The radiation of seismic waves from large earthquakes lasts many tens or hundreds of seconds. Because of the large spatial extent and long duration of large earthquakes, the energy is released in long-period waves (100 sec or greater). Investigations of long-period characteristics of the source process of large earthquakes are important for a better understanding of the mechanism of stress release in earthquakes.

Various methods for the study of rupture propagation have been developed since the great Chilean earthquake of May 22, 1960 which provided the first evidence for rupture propagation (Benioff et al., 1961, Press et al., 1961, Ben-Menahem, 1961). However, it is difficult to estimate the rupture area of earthquakes with confidence. The extent of faulting of an earthquake is often inferred from the aftershock area as well as the pattern of surface faulting, crustal deformation, intensities, and tsunamis. Although these data are extremely valuable, there is no direct proof that the aftershock area and the deformation pattern represent the extent of seismic faulting. In some cases, no surface breakage is observed, and no data of the crustal deformation are available. Very often the time variation of the aftershock pattern and the

uncertainty of the aftershock locations, which are usually determined from observations at teleseismic distances, make the estimations of the rupture extent difficult.

Several investigators (e.g. Ruff and Kanamori, 1983, Kikuchi and Kanamori, 1982, 1986, Hartzell and Heaton, 1985) developed methods to study the rupture process of large earthquakes using long-period body waves. Because the period of the waves used in these studies is relatively short, the details of fault rupture or source complexity of large earthquakes can been studied. The source time functions resolved at each station indicate complexity of the rupture process. However, for very large earthquakes, most of the seismograms are off-scale and the observed waveforms are very complex. The determination of the far-field time function is very difficult, particularly for the total duration of the rupture. Recently Ekstrom and Dziewonski (1986) inverted the broad band displacement of P-waveforms for the moment rate distribution in time and space of the 1985 Michoacan, Mexico earthquake, and obtained the rupture direction, velocity, and other important details of the moment release.

In this paper, we determined the source finiteness of large shallow earthquakes from long-period Rayleigh waves recorded at IDA (International Deployment of Accelerographs: Agnew et al. 1976) and GDSN (Global Digital Seismograph Network: Engdahl et al. 1982) stations. The basic data are Rayleigh-wave spectra of periods from 150 to 300 sec. First we approximate the source finiteness by a single parameter, the source-process time, and then by a more detailed line-source model with a few parameters. In the determination of source-process times, we use Furumoto's method (Furumoto, 1979,

Furumoto and Nakanishi, 1983) and a linear inversion method in which we invert the spectra at different periods simultaneously to determine the source-process time. The linear inversion method is similar to the method used by Romanowicz and Monfret (1986).

For several earthquakes, we employed the source-finiteness function introduced by Ben-Menahem (1961) and inverted the spectra to determine the extent and direction of the rupture of the earthquake which minimize the error in the inversion.

1.2 Model of Seismic Source

We first describe the seismic source model used in this paper. We use the notation of Kanamori and Given (1981). We take the spherical coordinate system (r, θ, ϕ) and the Cartesian coordinate system (x, y, z) used by Kanamori and Given (1981). The source spectrum of the vertical component Rayleigh waves excited by a step-function point source is a linear function of a frequency-independent moment tensor $(M_{xx}, M_{yy}, M_{zz}, M_{xy}, M_{yz}, M_{xz})$. We write the source spectrum as

$$\hat{V}(\omega, h, \phi) = \alpha(\omega, h, \phi) + i\ \beta(\omega, h, \phi) . \tag{1}$$

For a deviatoric moment tensor, the real (α) and imaginary (β) parts of the spectrum are

$$\alpha = -P_R^{(1)}(\omega, h) M_{xy} \sin 2\phi + \frac{1}{2} P_R^{(1)}(\omega, h)(M_{yy} - M_{xx}) \cos 2\phi$$

$$- \frac{1}{2} S_R^{(1)}(\omega, h)(M_{yy} + M_{xx}) , \tag{2a}$$

$$\beta = Q_R^{(1)}(\omega, h)M_{yz}\sin\phi + Q_R^{(1)}(\omega, h)M_{xz}\cos\phi , \qquad (2b)$$

where ω is the angular frequency, $P_R^{(1)}$, $S_R^{(1)}$, and $Q_R^{(1)}$ are the excitation functions given by Kanamori and Stewart (1976), which depend on the elastic properties in the source region and the source depth, h.

The source spectrum $\hat{V}(\omega, h, \phi)$ can be calculated from the spectrum of the surface wave seismogram $\hat{U}_r(\vec{r},\omega)$ recorded at point $P(r, \theta, \phi)$ by

$$\hat{V}(\omega, h, \phi) = (\sin\theta)^{\frac{1}{2}}\hat{U}_r(\vec{r},\omega)\exp(\frac{\omega a\theta'}{2QU})\exp(\frac{i\omega a\theta'}{c})$$

$$\exp(-\frac{1}{4}\pi i)\exp(-\frac{1}{2}m\pi i)/\hat{I}(\omega),$$

where $\hat{I}(\omega)$ is the instrument response; Q the quality factor, U the group velocity, c the phase velocity, a the radius of the Earth, θ' the propagation distance, and m the number of the polar or antipodal passages. For a moment-tensor or a double-couple source, $\hat{V}(\omega, h, \phi) = \hat{V}^*(\omega, h, \phi+\pi)$, where $*$ denotes complex conjugate (Furumoto, 1979, Furumoto and Nakanishi, 1983).

For large earthquakes, the size of the physical source region and the duration of the motion at the source are comparable to the wavelength and period of the seismic waves, and the source has to be treated as a finite source (Ben-Menahem, 1961).

The effect of the source finiteness on surface-wave radiation can be modelled by a traveling disturbance model (Ben-Menahem, 1961). In this model we write the Fourier spectra of the seismogram at point $P(r, \theta, \phi)$ as

$$\hat{U}(\vec{r},\omega) = \hat{C}(\vec{r},\omega) \cdot \hat{A}(\omega) \cdot \hat{F}(\omega,\Theta) \cdot \hat{R}(\omega) \cdot \hat{I}(\omega), \qquad (3)$$

where $\hat{A}$ is the effect of attenuation, $\hat{F}$ the rupture propagation, $\hat{C}$ the displacement spectrum due to a step-function point source in an elastic earth, and $\hat{R}$ represents the dislocation time function of the point source. $\hat{C}(\vec{r},\omega)$ can be expressed as

$$\hat{C}(\vec{r},\omega) = \frac{1}{(\sin\theta)^{1/2}}\exp(i\phi_i)\exp(\frac{-i\omega a\theta'}{c})\exp(\frac{1}{2}m\pi i)\ .\ \hat{V}(\omega, h, \phi)\ , \quad (4)$$

where ϕ_i is the initial phase, $\hat{V}(\omega, h, \phi)$ is the source spectrum of a point source with step time function. If the source time function is $f(t)$, then $\hat{R}(\omega) = i\ \omega\ \hat{f}(\omega)$. In particular, if $f(t)$ is a linear ramp function with rise time τ, $\hat{R}(\omega)$ is expressed as

$$\hat{R}(\omega) = \frac{\sin(\omega\tau/2)}{(\omega\tau/2)}\exp(-i\omega\tau/2)\ . \quad (5)$$

$\hat{F}$ is the source-finiteness function introduced by Ben-Menahem (1961); for a bilateral faulting

$$\hat{F}(\omega,\Theta) = \frac{L_1}{L}\ e^{-iX_1}\ \frac{\sin X_1}{X_1} + \frac{L_2}{L}e^{-iX_2}\ \frac{\sin X_2}{X_2}\ , \quad (6)$$

where

$$X_1 = \frac{\omega L_1}{2V_1}(1 - \frac{V_1}{c}\cos\Theta)\ ,$$

and

$$X_2 = \frac{\omega L_2}{2V_2}(1 + \frac{V_2}{c}\cos\Theta)\ .$$

Here the total length of the fault $L = L_1 + L_2$ is divided into two segments

of length L_1 and L_2 rupturing in opposite directions (Figure 1). V_1 and V_2 are the rupture velocities on the two segments of the fault, c the phase velocity, and Θ the azimuth of the station measured from the direction of rupture along L_1. If ϕ_f is the strike of fault segment L_1, and ϕ_s is the azimuth of the station, then $\Theta = \phi_s - \phi_f$.

The source rise time and rupture propagation cause a phase delay; for a unilateral fault with rupture velocity V and length L, the phase delay can be written as $\exp\{-i\ (\ X_L + phase\ [\hat{R}\ (\omega)]\ )\ \}$, where $X_L = \frac{\omega L}{2V}(1 - \frac{V}{c}\cos\Theta)$. The source-process time observed at azimuth Θ can be written as

$$t_s = 2\ X_L\ /\ \omega + 2\ phase\ [\hat{R}\ (\omega)]\ /\ \omega.$$

If the source dislocation time function is a ramp function with rise time τ, then the source-process time is given as

$$t_s = \frac{L}{V}\ (1 - \frac{V}{c}\ \cos\Theta) + \tau\ . \tag{7}$$

The azimuthal average of (7) gives the overall source-process time,

$$t_s = \frac{L}{V} + \tau\ . \tag{8}$$

For a bilateral faulting, the overall source-process time can be obtained in the same way, with L in (8) replaced by the length of the larger segment.

The overall source finiteness effect is given by

$$\hat{R}\ (\omega)\ \hat{F}\ (\omega) = \frac{\sin(\omega\ t_f\ /2)}{(\omega\ t_f\ /2)}\ \frac{\sin(\omega\ \tau/2)}{(\omega\ \tau/2)}\exp(-i\,\omega\ t_s\ /2)\ , \tag{9}$$

where $t_f = L\ /\ V$ is the rupture duration or the rupture time.

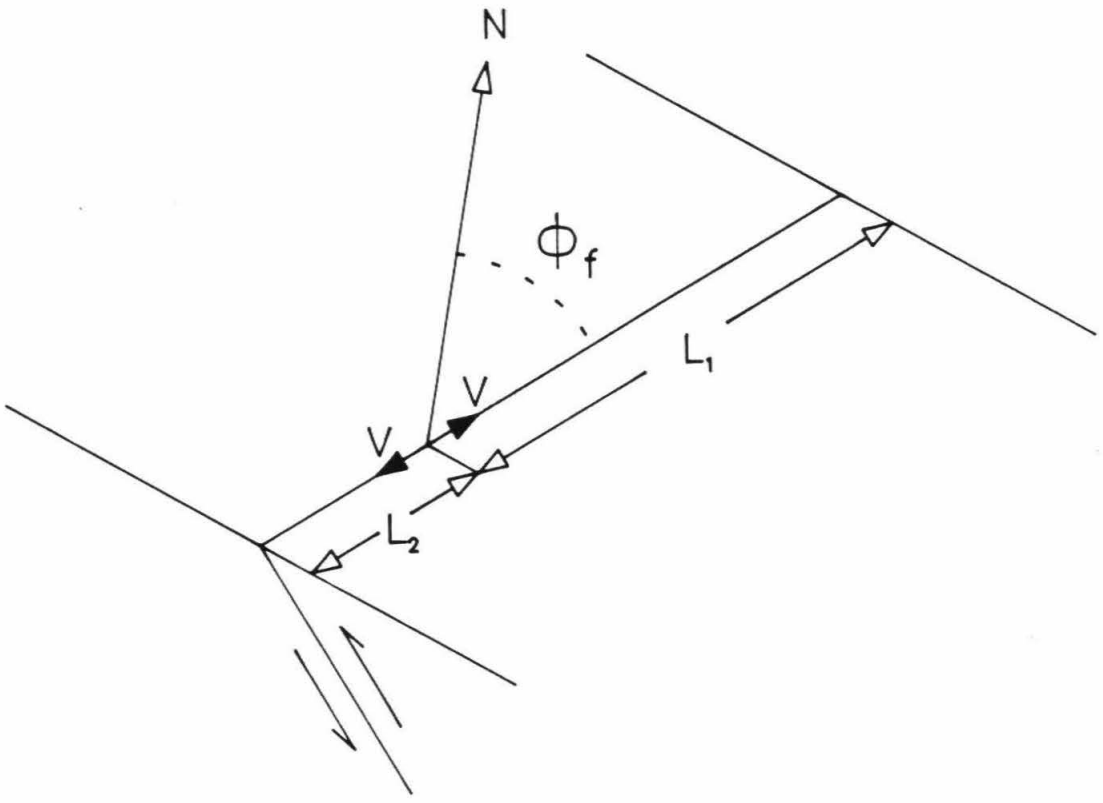

Figure 1.1 Geometry of a source with bilateral rupture propagation. The fault is divided into two segments of lengths L_1 and L_2 that rupture in opposite directions with the rupture velocity V. The azimuth of the rupture ϕ_f is measured from the north to the L_1 direction.

1.3 Source Process Time

First we investigate the source finiteness using the overall source-process time. Implicit in this analysis is the assumption that the source is spatially represented by a centroid and the time history of faulting is represented by a source time function with a finite source-process time.

Furumoto (1979) introduced source-process times to explain observed phase shift from that expected from a step function point source. Kanamori and Given (1981) used the source-process time to approximate the effect of the source finiteness and finite rise time on the observed phase of surface waves in a study of source-parameters of large earthquakes.

In the Centroid-Moment Tensor method developed by Dziewonski, Chou, and Woodhouse (1981), the duration of the source and other source parameters are obtained simultaneously in a inversion scheme (Dziewonski and Woodhouse 1983). The source time or duration was also studied by the method of total-moment spectra (Silver and Jordan, 1983), and by the moment-tensor recovery method (Riedesel and Jordan, 1986). All of these methods assume a centroid in space with a finite duration in time, and the definition of the source time varies for different methods. The source times obtained by these methods are an overall source duration which includes both the temporal and spatial finiteness of the earthquake process.

There are large discrepancies between the estimates of the earthquake source times obtained by different investigators. For example, the source time of the August 19, 1977 Sumbawa, Indonesia earthquake obtained by different studies ranges from a few sec to 70 sec (Silver and Jordan 1983, Furumoto and

Nakanishi 1983, Silver et al. 1986). For the December 12, 1979 Colombia-Ecuador earthquake, a factor of two difference exists in the source times obtained in different studies (Silver and Jordan 1983, Giardini et al. 1985). A similar discrepancy is found for the July 17, 1980 Santa Cruz Island earthquake (Nakanishi and Kanamori 1982, Giardini et al. 1985). The cause of these large discrepancies in the source times obtained by different methods has not been resolved yet.

1.4 Data

Table 1 lists the hypocentral parameters of the earthquakes studied here determined by the National Earthquake Information Center (NEIC) except for the depths, which are taken from the Harvard Centroid-Moment Tensor solutions (Dziewonski et al., 1983, 1985, 1986, Giardini et al., 1985).

We used digital seismograms recorded at IDA and GDSN stations. The GDSN seismograms were low-pass filtered with a cut-off period of 30 sec and decimated to a sample per 10 sec. We used the data over a period range from 150 to 300 sec. Since the vertical component of Rayleigh waves is affected by ground noise and higher-mode contaminations to a lesser degree than radial component, we used only vertical components. The stations close to the source or its antipode were not used.

We windowed, tapered, and Fourier-transformed each wave train to obtain the displacement spectrum $\hat{U}(\vec{r},\omega)$. In order to correct for the phase shift due to the propagation, we used the average phase velocity for each

Table 1.1 : Epicentral Data for Events Used in This Study

Event	Location	Date	UTC h:m:s	Latitude	Longitude	M_s	Depth,km (CMT)
1	Sumbawa, Indonesia	Aug. 19, 1977	06:08:55.2	11.085°S	118.464°E	7.9	23.3
2	Colombia-Ecuador	Dec. 12, 1979	07:59:03.3	1.598°N	79.358°W	7.7	19.7
3	Santa Cruz Is.	July 17, 1980	19:42:23.2	12.525°S	165.916°E	7.9	34.0
4	Samoa	Sept. 1, 1981	09:29:31.5	14.960°S	173.085°W	7.7	20.0
5	El Salvador	June 19, 1982	06:21:58.0	13.313°N	89.339°W	7.0	51.9
6	Tonga	Dec. 19, 1982	17:43:54.9	24.133°S	175.854°W	7.7	29.2
7	New Ireland	March 18, 1983	09:05:50.0	4.884°S	153.581°E	7.6	69.9
8	Akita-Oki, Japan	May 26, 1983	02:59:59.6	40.462°N	139.102°E	7.7	12.6
9	Chagos Bank	Nov. 30, 1983	17:46:0.6	6.852°S	72.110°E	7.7	10.0
10	Valparaiso, Chile	Mar. 3, 1985	22:47:07.3	33.135°S	71.871°W	7.8	40.7
11	Michoacan, Mexico	Sept. 19, 1985	13:17:47.3	18.190°N	102.533°W	8.1	21.3

propagation path computed for the laterally heterogeneous earth model (M84C) obtained by Woodhouse and Dziewonski (1984). We computed the spectra at the periods of 150, 175, 200, 225, 256, 275, and 300 sec.

1.5 Source Process Time Measured from Phase

We first used Furumoto's (Furumoto, 1979, Furumoto and Nakanishi, 1983). method to determine the source-process times. In this method, the source-process time is obtained from wave trains recorded at a single station. The advantage of this method is that we need to know only the average phase velocity along the entire great-circle path, which can be directly determined from the data. We do not need detailed information on the lateral heterogeneity. Furumoto (1979) used hand-digitized seismograms recorded at WWSSN stations to determine the source times. Nakanishi and Kanamori (1982) used digital seismograms recorded at IDA stations to measure the source times. In order to use this method, three surface wave trains at a station are necessary. Because of this requirement, usually only a few stations can be used.

1.5.1 Method

In this method the source-process time is calculated from the observed surface-wave phases. From the phase spectra of vertical component of

Rayleigh waves the source-process time t_s is calculated from

$$\phi_{2n} + \phi_{2m+1} + (n+m)(\phi_{2n} - \phi_{2n+2}) + 2\phi_{inst} = -\omega t_s , \qquad (10)$$

where ϕ_{inst} is the phase delay due to the seismograph, and ϕ_{2n} , ϕ_{2n+2}, and ϕ_{2m+1} are the phases R_{2n} , R_{2n+2} , and R_{2m+1} respectively (Nakanishi and Kanamori, 1982).

This method, which determines the source time at a single station, eliminates the uncertainty in the initial phase at the source. In (10), because R_{2n} and R_{2n+2} have the same initial phase, and R_{2n} has the initial phase which differs from that of R_{2m+1} only by sign, the initial phase terms are canceled. The terms ϕ_{2n} - ϕ_{2n+2} and ϕ_{2n} + ϕ_{2m+1} are determined only by the propagation phase delays along the great circle path. Thus, the results are independent of the mechanism of the source.

1.5.2 Results

Because of the large size of the earthquakes studied, most R_1 seismograms are off-scale. The later phases such as R_5 and R_6 are usually contaminated by other phases and noise. Therefore we used only R_2, R_3, and R_4 phases for the calculation.

The source times measured from different stations scatter considerably, especially at the period of 150 sec; the source times measured for the same station but at different periods also show quite a large scatter. Figure 2 shows the average and standard deviation of measured source-process times from

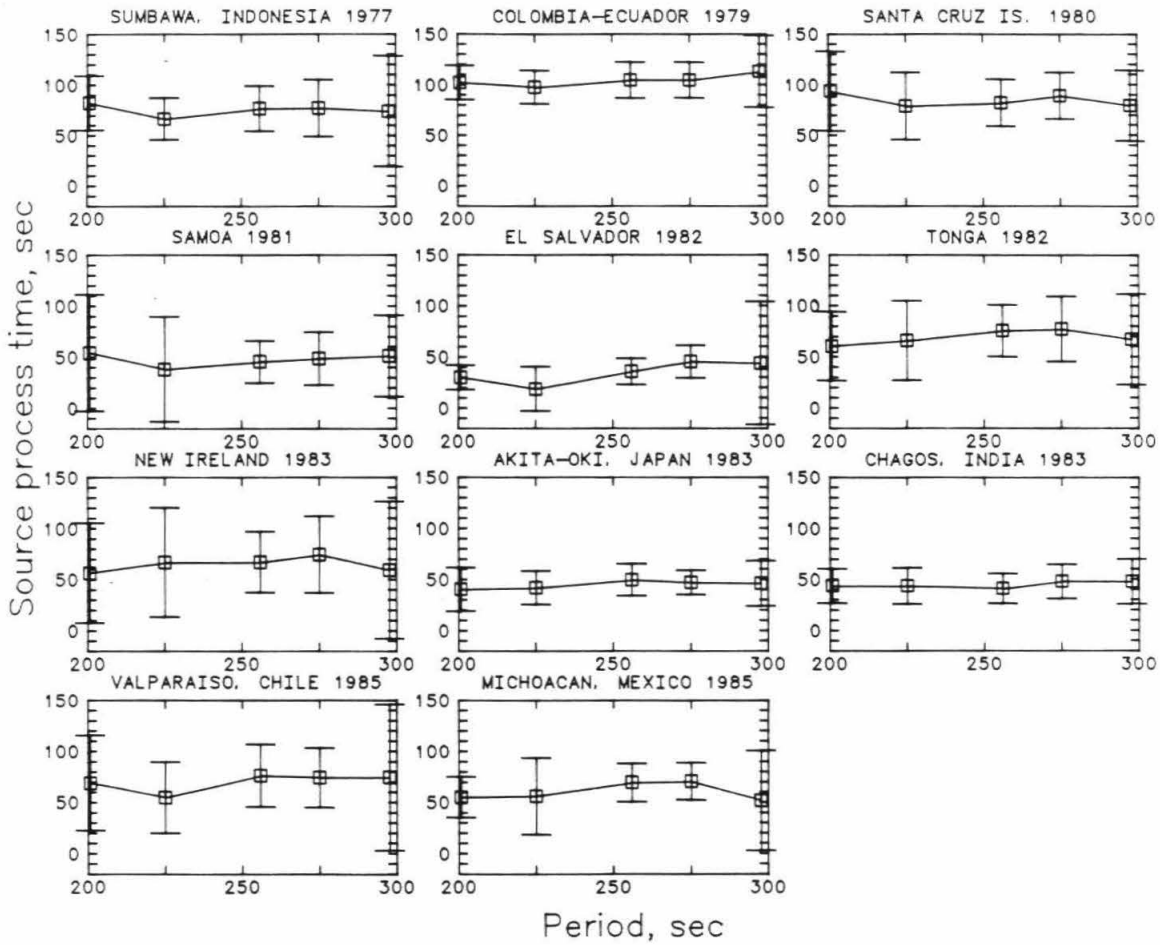

Figure 1.2 The average and the standard deviation of source-process times as function of period measured from Rayleigh-wave phases R_2, R_3, and R_4 recorded at IDA and GDSN stations for 11 large earthquakes by Furumoto's phase method.

Table 1.2 : Source-Process Times for Events Used in This Study

Event	Location	M_o $\times 10^{27}$dyne.cm (CMT)	τ (sec)			No. of Observations		Type of fault	Remark
			(CMT)	(I)	(II)	(I)	(II)		
1	Sumbawa, Indonesia	36	60	77 ± 25	79	7	20	N	(1),(2),(3)
2	Colombia-Ecuador	17	45	104 ± 18	118	12	33	T	(4)
3	Santa Cruz Is.	4.8	35	86 ± 23	88	22	46	T	(5)
4	Samoa	1.9	40	47 ± 23	45	16	48	N	
5	El Salvador	1.1	26	40 ± 14	35	11	56	N	
6	Tonga	2.0	43	76 ± 29	62	22	53	T	
7	New Ireland	4.6	30	71 ± 33	58	16	45	T	
8	Akita-Oki, Japan	4.6	40	48 ± 14	46	9	26	T	(6)
9	Chagos Bank	4.1	34	45 ± 16	63	17	55	N	
10	Valparaiso, Chile	10	69	75 ± 30	69	19	41	T	(7)
11	Michoacan, Mexico	11	77	70 ± 18	77	29	56	T	(8)

(I), Furumoto and Nakanishi's phase analysis method; (II), linear inversion method this paper; N, Normal fault; T, thrust fault; (1), 2 sec (Silver and Jordan 1983); (2), 43 sec (Silver et al. 1986); (3), 67 sec (Furumoto and Nakanishi 1983); (4), 112 sec (Silver and Jordan 1983); (5), 83 sec (Nakanishi and Kanamori 1982); (6), 64 sec (Satake 1985); (7), 87 sec (Riedesel and Jordan 1986); (8), 85 sec (Riedesel et al. 1986);

various stations at periods from 200 to 300 sec for each earthquake. Because the scatter is relatively small at 256 and 275 sec periods, we used only the data at these two periods. We took the average of the measurements at the period of 256 and 275 sec as our estimate of the source-process time. Table 2 lists these estimates under column (I). The standard deviation and the number of the station-source pairs used in the final calculation are also listed. In general the standard deviation of the measurements for each earthquake is about 30 % of the average. The source-process times of some of the earthquakes analyzed in this study were also estimated by Furumoto and Nakanishi (1983) and Nakanishi and Kanamori (1982). Although our data sets of these events are different from theirs, our estimates are consistent with their results.

The source-process time of the Sumbawa, Indonesia, earthquake (event 1) was also measured by Furumoto and Nakanishi (1983) using the data of WWSSN stations. Our estimate is 10 sec longer than their estimate (67 sec). Since the standard deviation is 25 sec in our measurements, the difference between these results is insignificant.

1.6 Source Process Time Measured by a Linear Inversion Method

1.6.1 Method

The second method we used to obtain the source-process time is a linear inversion method. It calculates the error in the least squares (LS) inversion

solution described by Kanamori and Given (1981) for a given source-process time. The error is a function of the source-process time used. The time which gives the minimum error is taken as the estimate of the true source-process time. Romanowicz and Monfret (1986) proposed a similar method to measure source-process times. Our method differs from theirs in that we use both the amplitude and phase data and determine the source-process time at a single period. In the following, we describe the method first.

If the Rayleigh wave seismograms are obtained from three or more stations with azimuths $\phi_1 \cdots \phi_N$ from the source, the system of equations (2) can be solved by the method of least squares. Romanowicz and Guillemant (1984) proposed a two-step inversion procedure to solve the system. The first step inversion solves the following system

$$B\ D = V \tag{11}$$

where

$$B = \begin{bmatrix} -\sin 2\phi_1 & \frac{1}{2}\cos 2\phi_1 & -\frac{1}{2} & 0 & 0 \\ 0 & 0 & 0 & \sin\phi_1 & \cos\phi_1 \\ -\sin 2\phi_2 & \frac{1}{2}\cos 2\phi_2 & -\frac{1}{2} & 0 & 0 \\ 0 & 0 & 0 & \sin\phi_2 & \cos\phi_2 \\ . & . & . & . & . \\ . & . & . & . & . \\ . & . & . & . & . \\ -\sin 2\phi_N & \frac{1}{2}\cos 2\phi_N & -\frac{1}{2} & 0 & 0 \\ 0 & 0 & 0 & \sin\phi_N & \cos\phi_N \end{bmatrix},$$

and

$$D = \Big[P_R^{(1)}(\omega, h)M_{xy}, P_R^{(1)}(\omega, h)(M_{yy} - M_{xx}), S_R^{(1)}(\omega, h)(M_{yy} + M_{xx}),$$

$$Q_R^{(1)}(\omega, h)M_{yz}, Q_R^{(1)}(\omega, h)M_{xz}\Big]^T ,$$

and

$$V = \Big[\alpha(\omega, h, \phi_1), \beta(\omega, h, \phi_1), \cdots, \alpha(\omega, h, \phi_N), \beta(\omega, h, \phi_N)\Big]^T ,$$

where B is an $2N \times 5$ real matrix and V is a real vector with dimension 2N. The minimum sum of squares of the LS problem is $\rho_{LS}^2 = \|(I - B(B^T B)^{-1}B^T)V\|_2^2$, which is independent of excitation functions.

The source-process time is the sum of the two characteristic times of the seismic source, the rise time and the rupture time. Since the spatio-temporal variation of the rupture on a fault plane is very complex, the rise time cannot be defined in a straightforward way. However, for a wide range of earthquakes, there seems to be an approximately linear relation between the observed rupture time t_f and the overall rise time τ, which is $\tau \sim 0.1\ t_f$ (Kanamori and Anderson, 1975). In determining the source-process time using the linear inversion method, we adopted this relation. This allowed us to determine the source-process time t_s in a single variable search by the linear inversion scheme.

We first computed the displacement spectra $\hat{U}_r(\vec{r},\omega)$ for individual Rayleigh wave trains. Then for a trial source-process time t_s, we calculated the source finiteness correction $\hat{R}(\omega)$ using (9), with $t_f = t_s/1.1$, and $\tau = t_s/11$. We then corrected $\hat{U}_r(\vec{r},\omega)$ for the source finiteness to obtain the source spectra $\hat{V}(\omega)$. We inverted the spectra by solving (11) and obtained an error which measured the misfit between the data and the model. The error is a

function of the source-process time used for the corrections. The source-process time which yields a minimum of the function is our estimate. In the applications of the method, we used the data at periods of 150, 175, 200, 225, 256, 275, and 300 sec.

1.6.2 Results

Since this method does not require a particular phase combination of surface waves at each station, such as a trio of phases needed for Furumoto's method, we could use many R_2 phases. Another advantage of this method over Furumoto's method is that it uses both amplitude and phase data of observed spectra.

Table 3 lists the surface wave phases used in the inversion. Phases with large noise were not included. Most of the phases used are R_2 or R_3. The data set used in the inversion is much larger than that used in Furumoto's method.

This method requires the correction for the phase delay due to the propagation before the inversion. The recent progress in the study of the lateral heterogeneity of the earth made possible a direct use of the phase information in the measurement of the source-process times (Okal, 1977, Dziewonski and Steim, 1982, Woodhouse and Dziewonski, 1984, Nakanishi and Anderson, 1983, 1984, Tanimoto, 1985, Tanimoto and Kanamori, 1986). In order to correct for the phase delay, we calculated phase velocities along individual paths using a laterally heterogeneous earth model (M84c) obtained by Woodhouse and

Table 1.3 : Phase Data for Each Event

Event	Phases
1	CMO($R_{4,5}$), RAR($R_{3,4}$), HAL(R_6) , CTAO, CHTO, SNZO, TATO, MAJO, KAAO($R_{2,3,4}$), ANMO($R_{3,4}$)
2	BDF, CMO, ESK, HAL, TWO($R_{3,4}$), RAR($R_{2,3,4}$) , ANMO, ANTO, BCAO, NWAO, GRFO, SNZO, KAAO, MAJO, ZOBO, KONO
3	CMO, ESK, GAR, GUA, HAL, RAR, SEY, TWO, NNA($R_{3,4}$) , ANMO, ANTO, BOCO, CHTO, GUMO, BCAO, NWAO , GRFO, TATO, SNZO, CTAO, KAAO, MAJO, KONO
4	CMO, ERM, ESK, GUA, HAL, KIP, KMY, NNA, PFO, SPA, TWO, BDF(R_3), SEY($R_{3,4}$) , ANMO, GUMO, GRFO, TATO, CTAO, KAAO, MAJO, KONO, SCP, TAU, NWAO($R_{3,4}$), LON(R_3)
5	BDF, CMO, ERM, GUA, KIP, KMY, NNA, PFO, SJG, SSB, SUR, TWO , ANMO, SNZO, TATO, NWAO, GUMO, GRFO, GACO, BOCO, CTAO, MAJO, KONO, BDF, KEV, LON, SCP, TOL
6	SJG, GUA, NNA, HAL, BJT, TWO, PFO, ERM, ESK(R_3), SUR(R_3), CMO, KMY , ANMO, ANTO, BCAO(R_3), NWAO, GRFO, TATO, SNZO, GACO, GUMO, CTAO, MAJO(R_3), KONO, SCP, COL, KEV, BDF, JAS(R_3)
7	CMO, ERM, TWO, KMY, PFO, BJT, ESK, BDF(R_3), NNA(R_3), ALE(R_3) , ANMO, ANTO, NWAO(R_2), GRFO, TATO, SNZO, GACO, CTAO, MAJO, KONO, COL, LON, KEV, AFI, TAU(R_2)
8	RAR, KMY, ESK, ALE, PFO, TWO, SJG, ANTO, GRFO, NWAO, SNZO, CTAO, KONO

9	ALE(R_2), BDF, CMO, ESK, GUA, HAL, PFO(R_3), RAR, TWO, ANMO, BOCO, GUMO, BCAO, NWAO, GRFO, TATO, SNZO, GACO, CTAO, MAJO, KONO, SCP, LON(R_2), HON, KEV, GDH, SLR, BDF, TAU
10	ESK($R_{3,4}$), CMO($R_{3,4}$), ALE($R_{3,4}$), PFO, KIP(R_3), HAL, GUA($R_{3,4}$), SUR($R_{3,4}$), ANMO, BCAO, NWAO, GRFO, GACO, CTAO, SCP, LON, AFI, SLR, BDF, TOL, TAU
11	PFO($R_{3,4}$), KIP, HAL(R_2), GUA(R_2), SJG, ESK(R_2), SUR($R_{3,4}$), TWO($R_{3,4}$), ALE(R_3), BDF, ERM(R_3), RAR($R_{3,4}$), NNA, ANMO, ANTO, CHTO, BCAO, NWAO, GRFO, TATO, GACO, CTAO, KONO(R_3), SCP(R_2), COL, HON, KEV, AFI, GDH, BDF, TOL, TAU(R_3)

Dziewonski (1984).

Figure 3 shows, for each earthquake studied, the error curve of the inversion for source-process times in the range of 0 to 140 sec. For each trial value of the source-process time t_s , we obtained an error, the root-mean-square (rms) in the inversion at a period, which is $\rho_{LS}/\sqrt{2N}$. For each earthquake, the curves for the periods of 200, 225, 256, 275, and 300 sec are of similar shape, with a single minimum. Figure 3 shows that for most earthquakes studied here, the minimum decreases and the corresponding source-process time increases as the period increases from 200 to 275 sec.

The December 12, 1979 Colombia-Ecuador earthquake (event 2) has the longest source-process time, measured from both the linear inversion method and the phase method, of all the earthquakes studied here. The estimates at 256 and 275 are fairly close, with the value at 275 sec slightly larger. The estimate at the period of 300 sec is about 10 sec smaller than that at 275 sec. Kanamori and Given (1981) obtained the rupture velocity 2 km/sec and rupture length 230 km for the earthquake. This implies that the duration of the source process is about 110 sec which is consistent with our results.

For the Santa Cruz Island earthquake (event 3), the estimates at the periods from 150 and 300 sec with every 25 sec increment, are 60, 71, 76, 73, 85, 91, and 83 sec respectively.

For the Mexico earthquake (event 11), the estimates were between 68 and 80 sec for all the data sets used, with the maximum of 80 sec at 275 sec period.

The source-process time obtained from the inversion method depends on the phase velocity model used. The dependence can be seen from Figure 4,

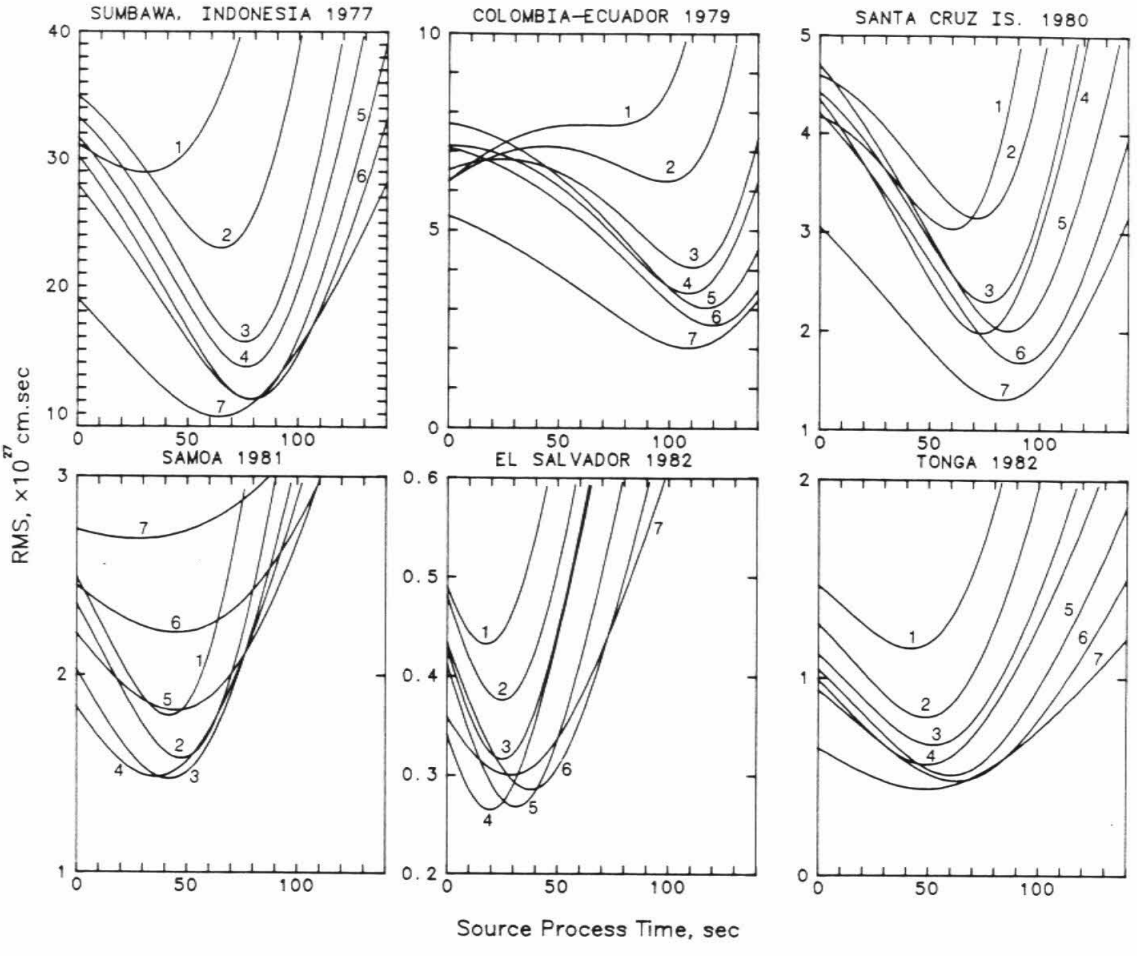

Figure 1.3 The *rms* error plotted versus trial source-process time for the inversion at the periods of (1) 150, (2) 175, (3) 200, (4) 225, (5) 256, (6) 275, and (7) 300 sec respectively. The time corresponding to the minimum error on each curve is taken as the source-process time measured at that period.

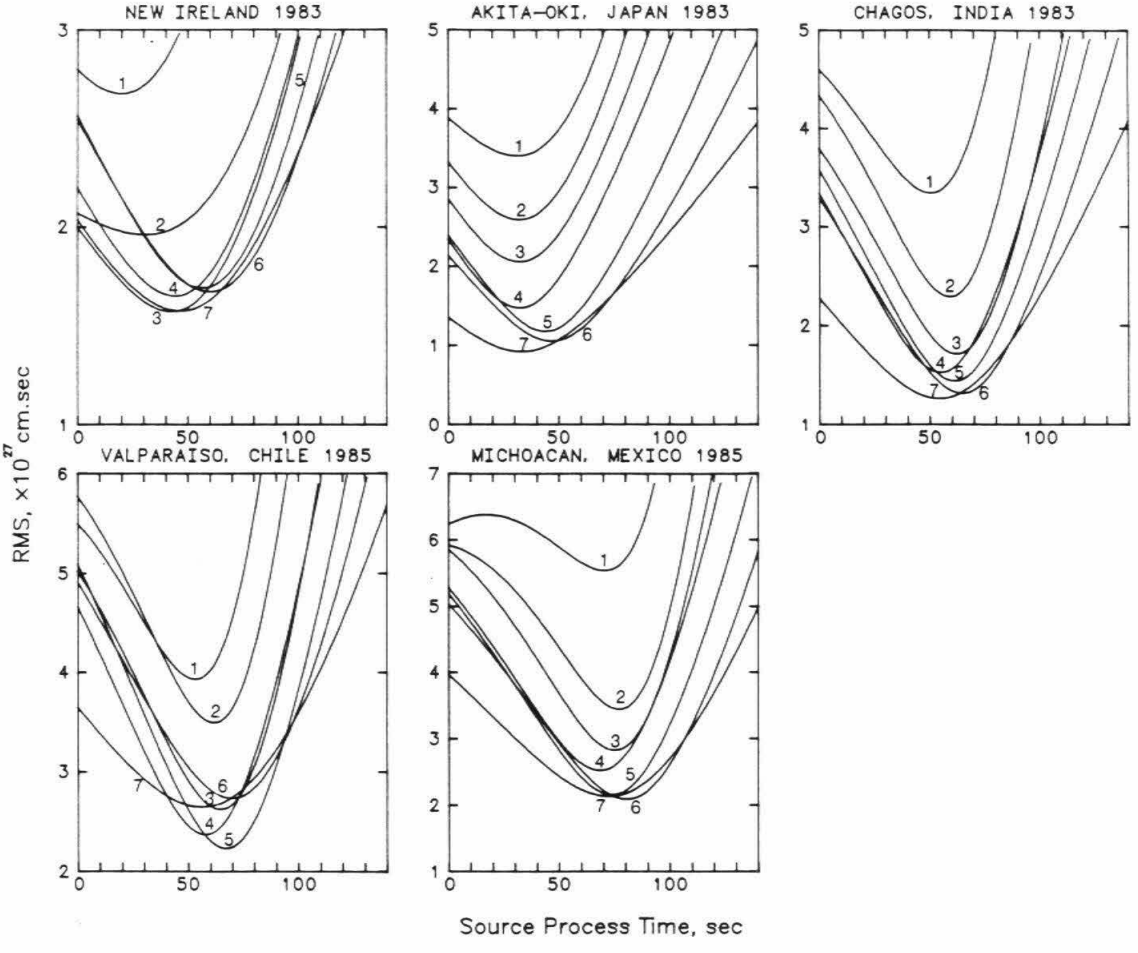

Figure 1.3 (continued)

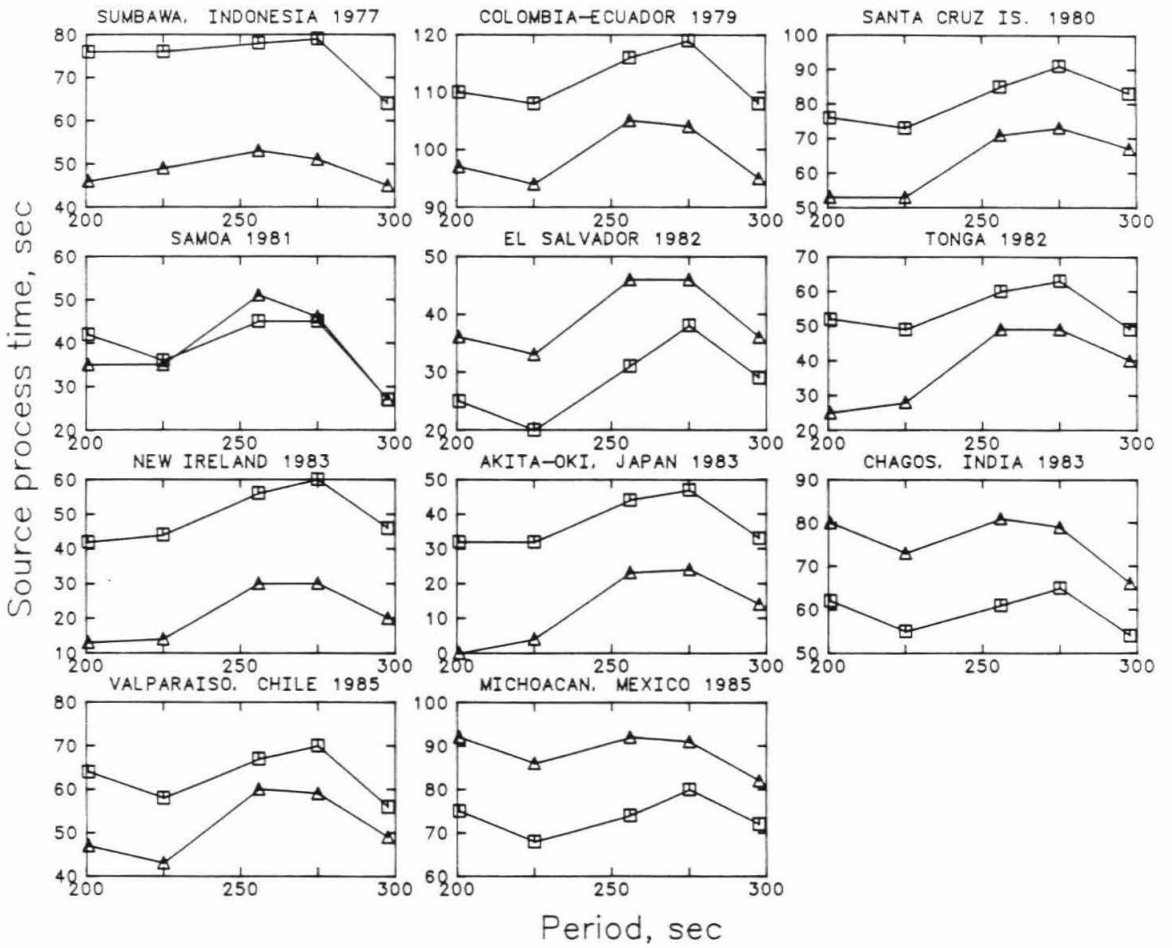

Figure 1.4 Source-process time of 11 large earthquakes determined at the periods of 200, 225, 256, 275, and 300 sec from the inversion method. Source-process time versus period curves are given for two phase velocity models; phase velocity is calculated (1) from the average observed normal-mode periods compiled by Gilbert and Dziewonski (1975) (triangles), (2) from a laterally heterogeneous earth model (M84C) obtained by Woodhouse and Dziewonski (1984) (squares).

which shows the source-process times of 11 earthquakes obtained at the periods from 200 sec to 300 sec, for the model M84C and for a homogeneous model(HOM) of phase velocities. The homogeneous model was obtained from the average observed normal-mode periods compiled by Gilbert and Dziewonski (1975). Kanamori and Given (1981) used these phase velocities in a study for the earthquake-source parameters. For the earthquakes studied in this paper, the average difference between the estimates of the source-process times for the model M84C and for the model HOM is around 10 sec. For the Sumbawa and the Akita-Oki earthquakes, the model M84c gives estimates 20 sec or more greater than the model HOM. For the Colombia-Ecuador earthquake, the estimates from the model M84C are about 10 sec larger than those from the homogeneous model. On the contrary, the model HOM gives estimates 10 sec or more greater than the model M84C for the El Salvador, the Chagos, and the Mexico earthquakes.

Since the phase velocity due to propagation and the source-process time trade off directly (see equation (4)), it is not surprising that the estimate of the source-process time depends on the phase velocity of the model. In order to illustrate this, we calculated, for each earthquake, the mean and the standard deviation of phase velocities of M84C for all the paths used, and compared the mean with the phase velocity of HOM. Table 4 lists the phase velocities at the period of 256 sec for M84C and HOM and the source-process times obtained for each earthquake by the moment tensor inversion at the period of 256 sec. Although the difference between the mean phase velocity of M84C and the velocity of HOM in the period range considered is less than one percent, it correlates with the difference of the source-process times obtained with

Table 1.4 : Source-Process Times Measured at 256 sec Period for Two Models, t_{M84C} and t_{HOM}.

Event	Location	V_{M84C} (km/sec)	$\sigma_{M84C,\times 10^{-3}}$ (km/sec)	$\frac{V_{M84C}-V_{HOM}}{V_{HOM}}$ (%)	t_{M84C} (sec)	t_{HOM} (sec)	$t_{M84C}-t_{HOM}$ (sec)	$t' - t_{HOM}$ (sec)
1	Sumbawa, Indonesia	4.9668	4.3	.092	80	54	26	5
2	Colombia-Ecuador	4.9633	4.0	.023	116	105	11	7
3	Santa Cruz Is.	4.9670	2.8	.097	85	71	14	-1
4	Samoa	4.9629	4.6	.015	45	51	-6	-8
5	El Salvador	4.9629	7.6	.015	32	46	-14	-17
6	Tonga	4.9626	5.5	.007	60	49	11	10
7	New Ireland	4.9682	4.1	.121	56	30	26	9
8	Akita-Oki, Japan	4.9695	4.5	.148	44	23	21	-1
9	Chagos Bank	4.9594	8.6	-.056	61	81	-20	-11
10	Valparaiso, Chile	4.9627	3.9	.011	67	60	7	5
11	Michoacan, Mexico	4.9606	7.8	-.032	74	92	-18	-13

V_{M84C} and σ are the mean and standard deviation of the path-average phase velocities for M84C. The phase velocity $V_{HOM} = 4.9622$ km/sec. t' is the source-process time obtained when the phase velocities of M84C are modified so that the average is equal to the phase velocity of HOM. (i.e. the phase velocities of M84C are multiplied by V_{HOM}/V_{M84C}.)

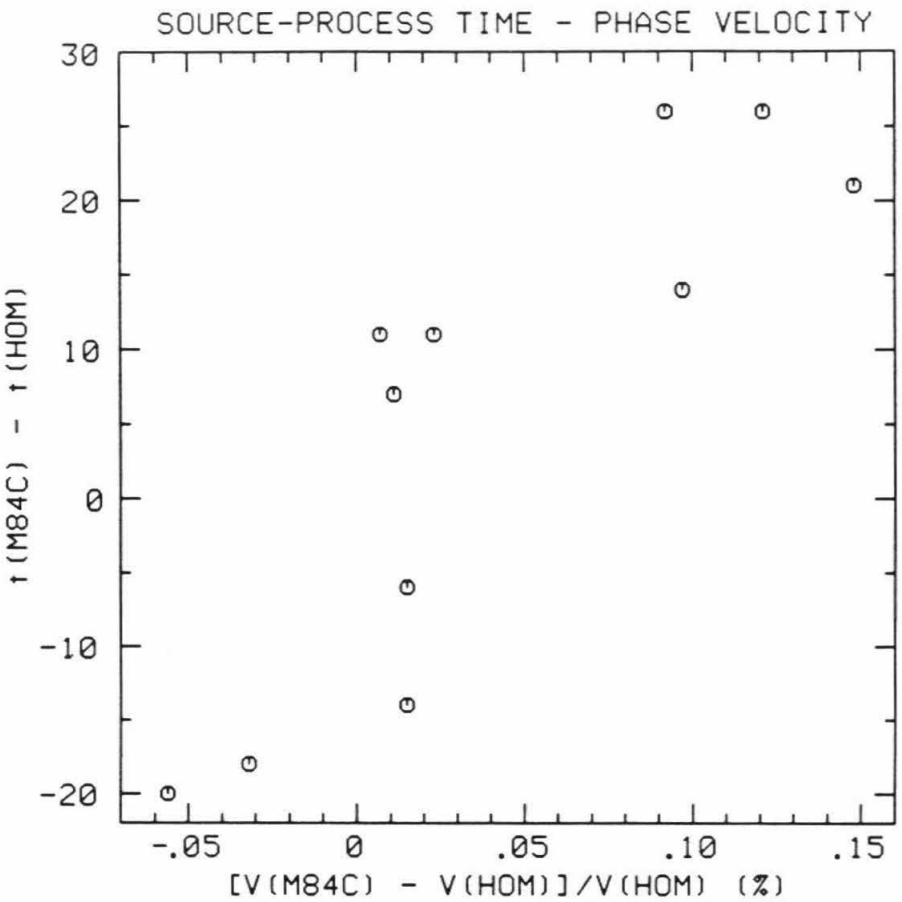

Figure 1.5 The difference between source-process times versus the difference between phase velocities for the period of 256 sec. $t(M84C)$ and $t(HOM)$ are the source-process times determined by the moment tensor inversion at the period of 256 sec with M84C and HOM respectively. V(M84C) is the path-average phase velocity of M84C, and V(HOM) is the phase velocity of HOM.

these models (Figure 5).

For the Akita-Oki earthquake, the average phase velocity of M84C is about 0.15 percent faster than the phase velocity of HOM. When the phase velocities for M84C on each path are modified so that the average of the phase velocities equals to the phase velocity of HOM, the source-process time obtained is about the same as that with HOM (Table 4). For the Sumbawa earthquake, although the mean and standard deviation of the phase velocities of M84C are about the same as that for other events, the difference of the source-process times for the two models is larger than that for other events (Figure 4). The average phase velocity of M84C is about 0.1 percent faster than that of HOM. However, the phase difference accumulate more for this event than other events because R_4 and R_5 are used for this event while shorter path phases R_2 and R_3 are used for other events. The reduction of the average phase velocity accounts for about 80 per cent difference of the source-process times shown in Figure 4, which is about 26 sec. However, for the El Salvador earthquake, although the average phase velocity of M84C is slightly faster than that of HOM, the source-process times obtained with M84C is about 10 sec shorter than that with HOM.

On the other hand, for the Mexico earthquake, the average phase velocity of M84C is slightly slower than that of HOM; and only about 25 per cent of the difference of the source-process times can be explained by the difference of the average phase velocity. The Chagos Arch earthquake has the slowest average phase velocity of M84C for all the earthquakes studied here. The difference of the average phase velocity can account for about 50 per cent of the difference of the source-process times obtained with the two models.

Table 4 shows that for some earthquakes the difference between the average phase velocities in the reference models cannot account for the difference between the estimates of the source-process time with different models. Since the propagation phase delay also depends on the length of individual path, the difference in the average phase velocity alone cannot explain all the differences in the source-process time. Waves with long paths have larger phase anomalies than waves with short paths. Hence, for a particular earthquake, the source-process time determined using long-path waves usually has strong model dependence than that using short-path waves. In any event, a use of good phase velocity model is critically important for the accurate determination of the source-process time.

Because the estimates obtained at 256 and 275 sec are considered more reliable than at other periods, we took the average of the two estimates at these periods obtained with the model M84C as our final estimate of the source-process time. These estimates are listed under column II in Table 2. The number of the observed spectra used in the inversion for each earthquake is also listed.

Table 2 shows that, for the earthquakes studied, the estimates for the source-process time obtained from Furumoto's method and the linear inversion method in general agree well. In particular, for the Santa Cruz Island earthquake (event 3) these estimates agree fairly well. Using Furumoto's method, Nakanishi and Kanamori (1982) obtained 83 sec source-process time from the data of IDA stations. From the data of IDA and GDSN stations, we obtained 86 sec using Furumoto's method, and 88 sec using the linear inversion method.

We used an empirical relation between the rupture time and the rise time. However, the ratio may vary for different earthquakes. We tested the effect of the ratio τ/t_f on the estimate of the source-process time. The results show that the estimates of the source-process time are stable for a wide range of the ratio; for example, for any assumed ratio, they differ less than 5 per cent for the Colombia, the Santa Cruz, and the Mexico earthquakes, for both the model M84C and HOM.

Furumoto and Nakanishi (1983) found that the seismic moment is proportional to the cube of the source time. This relation is consistent with the empirical relation between the seismic moment and the fault length if the average rupture velocity is constant for all the earthquakes. Figure 6 shows the relation between the source-process times determined in this study from Furumoto's method and the linear inversion method and the seismic moments of the Centroid-Moment Tensor solutions for these earthquakes. For the earthquakes with a seismic moment 10^{28} dyne.cm or greater, the source-process times obtained from the two methods are almost the same. The solid line in the figure represents the linear relation between $\log M_0$ and $\log\tau$ obtained by Furumoto and Nakanishi (1983) for unilateral low-angle thrust earthquakes. The Sumbawa, Indonesia earthquake is a normal-fault event with a relatively short source-process time. Among the thrust earthquakes in this study, the Tonga, Santa Cruz Island, and Colombia-Ecuador earthquakes have much longer source process than expected from the general trend.

The details of the source time function were not considered in this study. Because the period of the waves used is relatively long compared to the source-process times of the earthquakes, the results are not sensitive to the

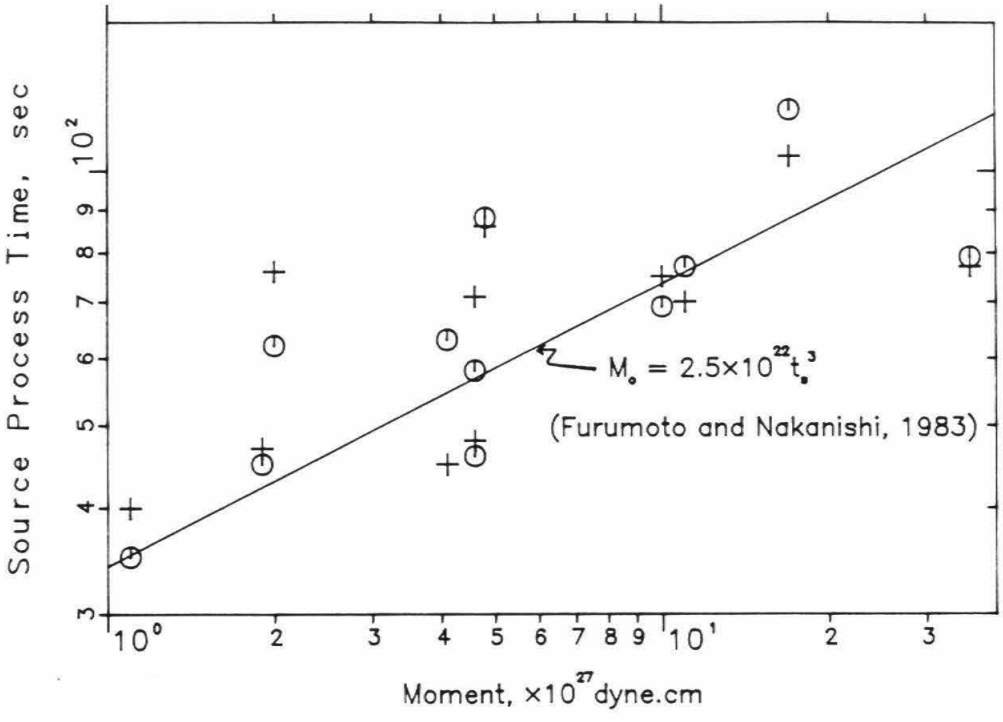

Figure 1.6 Relation between the seismic moment M_0 and the source-process time of 11 large earthquakes. The solid line is an empirical relation for low-angle thrust-fault earthquakes obtained by Furumoto and Nakanishi (1983). The M_0 of the centroid-moment tensor solution determined by Dziewonski and his co-workers is used. The circles and crosses indicate the source-process times determined in this study from the linear inversion method and Furumoto's method, respectively.

details of the rupture process. In order to resolve the details of the source process short-period waves must be used.

The source times of these earthquakes were determined also by many other investigators. Dziewonski and Woodhouse (1983) calculate the duration of the large earthquakes by inverting the body waves and mantle waves for a centroid moment tensor. The half durations of the Centroid-Moment Tensor (CMT) solutions of these earthquakes were multiplied by 2 and listed in the Table 2. The durations from the CMT solutions of the Sumbawa, Valparaiso, and Michoacan earthquakes agree well with the source-process time obtained in this study. However, for the Colombia-Ecuador earthquake, the source-process time obtained in this study is about 2 to 3 times larger than the duration estimated from the CMT solution. Since the two methods use different type of data and technique, the difference between the results may indicate that the source process of this earthquake is complex.

The source times of some of the earthquakes studied in this paper have also been determined by the methods of total-moment spectra of Silver and Jordan (1983) and the moment-tensor recovery method of Riedesel and Jordan (1986). Our results are generally consistent with theirs. However, for the Sumbawa, Indonesia earthquake there is a significant difference between the results obtained by different methods. This earthquake has the largest moment among the events studied. The cause of this large discrepancy between these studies is not known.

1.7 Inversion for the Rupture Model of Large Earthquakes

In this section, we investigate the rupture pattern of some large earthquakes using the finite moving source model of Ben-Menahem (1961). In this model, the surface wave spectrum is represented by a product of the point-source spectrum and the finiteness spectrum. For an earthquake that has a much larger horizontal extent than depth extent, this horizontal moving-source model is an adequate approximation. Many large shallow subduction zone earthquakes fall into this category.

The method proposed by Ben-Menahem has been used to study the source finiteness of many large earthquakes (Ben-Menahem and Toksö z, 1962, 1963a, 1963b). For earthquakes with a relatively short rupture length, for example, the May 26, 1983 Akita-Oki, Japan earthquake with a rupture length about 100 km long, the directivity effects are not sufficiently large. Kanamori (1970a, 1970b) used the method of synthetic seismograms of a moving-dislocation model to match the observed asymmetry of the surface wave radiation pattern from as many stations as possible in various azimuths.

We used an inversion method to determine the rupture model of large earthquakes. We first describe the method briefly. First, we calculate the source-finiteness effect $\hat{R}(\omega)$ and $\hat{F}(\omega)$ for a given source finiteness model. We then invert the spectra $\hat{V}(\omega)$ corrected for the source finiteness by solving (11) and compute the error. We then estimate the rupture dimension and azimuth for a given rupture velocity by minimizing the error.

The data sets used in this section are the same as those used in the previous section. In correcting for the source-finiteness effects given by (5) and (6),

we assume that the point source with a ramp time function propagates in the opposite directions from the epicenter with the same rupture velocity. The rise time is assumed to be proportional to the rupture time ($\tau = \gamma\, t_f$). For a given source-finiteness model (the rupture velocity V, rupture azimuth ϕ_f, and rupture lengths L_1 and L_2), the error ρ_{LS} in the LS problem is computed. For fixed ϕ_f and V, the error is a function of the rupture lengths L_1 and L_2. We contour the errors on the (L_1, L_2) plane to determine the values of L_1 and L_2 which minimize the error. We also calculate the errors as a function of the rupture azimuth for given rupture lengths, and obtained the minimum error $\min_{\Theta, L_1, L_2} \rho_{LS}(\Theta, L_1, L_2)$. The azimuth which minimizes ρ_{LS} gives the estimate of the rupture azimuth.

We performed the LS inversion for the periods of 150, 175, 200, 225, 256, 275, and 300 sec separately. The estimates of the rupture lengths and azimuths obtained at different periods are usually different.

The observability of the source finiteness (the rupture length, rupture azimuth etc) depends on not only the signal to noise ratio of the seismograms but also the magnitude of the source-finiteness effect. Both of them are functions of the period. Hence, we assess the observability in the following way. We first compute the average amplitude spectrum by

$$\overline{V}(\omega) = \sum_i | \hat{V}(\omega, h, \phi_i) | / N ,$$

where N is the number of phases used. The effect of the finiteness is given by $\hat{R}(\omega)\, \hat{F}(\omega, \phi_i)$. Since $\hat{R}\hat{F}$ is equal to 1 for a point source, $| \hat{R}(\omega)\, \hat{F}(\omega, \phi_i) - 1 |$ gives the magnitude of the spectral variation due to the source finiteness. Hence, we use

$$\bar{S}(\omega) = \sum_i | \hat{R}(\omega) \hat{F}(\omega,\phi_i) - 1 | / N$$

as a measure of the average source-finiteness effect.

The misfit between the observed and the synthetic seismograms computed for the best-fit model,

$$\epsilon(\omega) = \min_{\Theta,L_1,L_2} \rho_{LS}(\Theta, L_1, L_2) / \sqrt{2N} ,$$

is a measure of the noise. Using these measures, we define $\eta(\omega)$ by

$$\eta(\omega) = \bar{V}(\omega) \bar{S}(\omega) / \epsilon(\omega) , \qquad (12)$$

which can be used as a measure of the observability of the source-finiteness.

1.7.1 Results

We applied this method to four large earthquakes, the May 26, 1983 Akita-Oki, Japan earthquake, December 12, 1979 Colombia-Ecuador earthquake, March 3, 1985 Valparaiso, Chile earthquake, and September 19, 1985 Michoacan, Mexico earthquake. We also studied the August 19, 1977 Sumbawa, Indonesia earthquake, which had the largest moment release since the great 1965 Rat Is. earthquake.

Figure 1.7 Contours for the rms error obtained in the inversion at the periods of (a) 256, and (b) 275 sec for the 1983 Akita-Oki, Japan earthquake. Number shown on each contour is the rms error. L_1 is assumed toward the north and L_2 to the south. The rupture velocity and the ratio γ of the rise time τ to the rupture time t_f is assumed to be 2.5 km/sec and 0.1 respectively. The dash line indicates the contour with a variance significantly larger than the minimum in 90 per cent confidence in the F test.

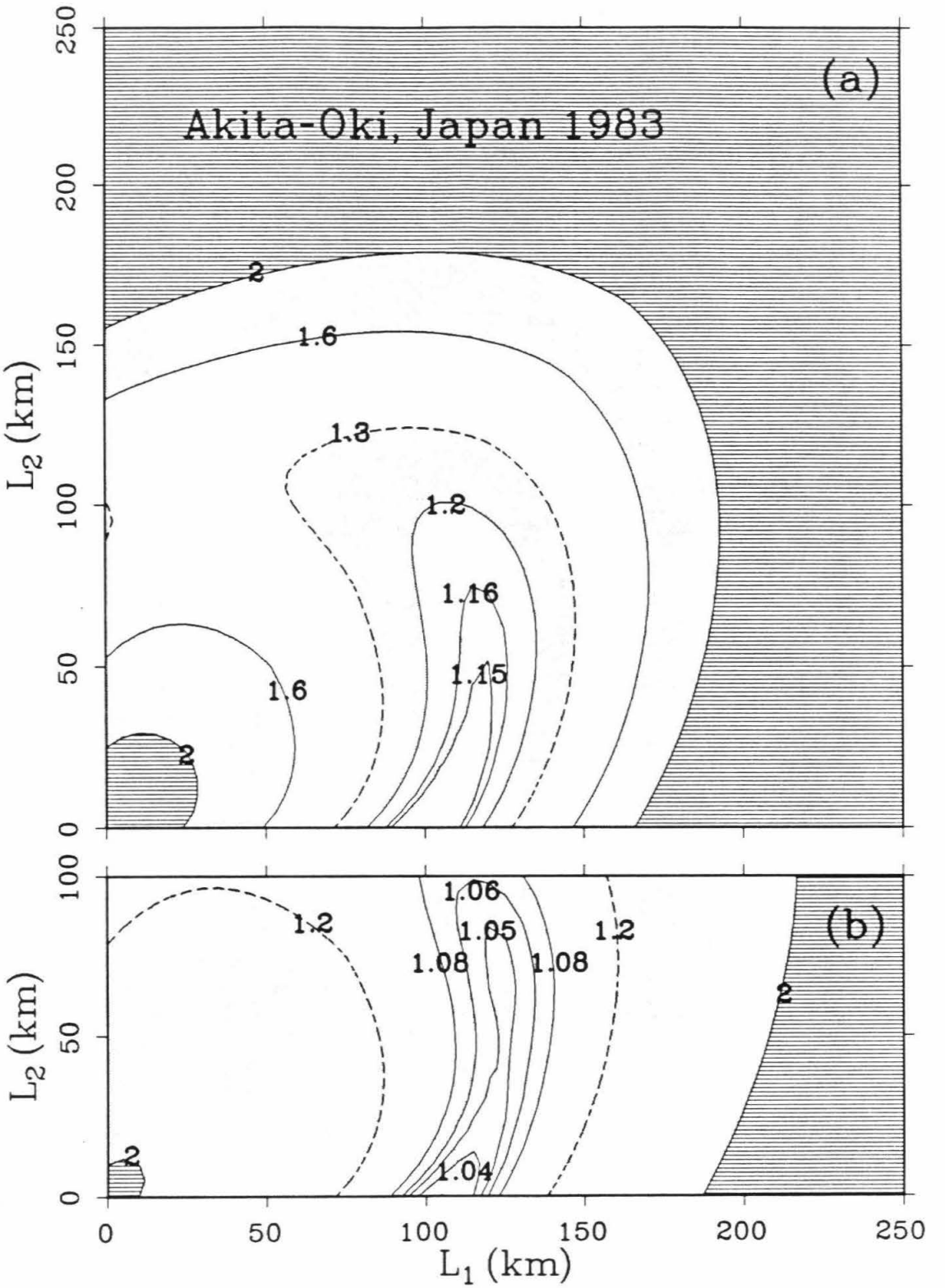
(a)
Akita-Oki, Japan 1983
2
1.6
1.3
1.2
1.16
1.15
1.6
2
(b)
1.06
1.2
1.05
1.2
1.08
1.08
2
2
1.04
L_2 (km)
L_1 (km)
0
50
100
150
200
250

1.7.2 1983 Akita-Oki, Japan Earthquake

The aftershock distribution of the Akita-Oki earthquake determined by a microearthquake network (Tohoku Univ. and Hirosaki Univ., 1984) indicates a north-south strike of the fault plane. Satake (1985) estimated the fault length to be 120 km based on the aftershock distribution during the 5 days immediately after the main shock. The main shock was located near the southern end of the aftershock area.

We used twenty-six Rayleigh-wave phases (mostly R_2 and R_3) recorded at IDA, SRO, and ASRO stations. In principle we could determine the rupture length and the rupture azimuth simultaneously. However, in this study, we first fix the rupture azimuth and determine the rupture length by minimizing the error. Then using this rupture length, we vary the azimuth to determine the value which minimizes the error. We repeat this procedure, but the estimate of the rupture length remains the same for the revised value of the azimuth, because the revision is usually very small. For this earthquake we assumed that the rupture was to the north with a rupture velocity of 2.5 km/sec. The rupture velocity is usually about 2 - 3 km/sec for many large earthquakes.

In determining the rupture length the trial values of the length L_1 and L_2 range from 0 to 250 km. The *rms* errors of the inversion for the period of 256 sec are shown in Figure 7a by contours. There is a minimum on the contour map, at $L_1 = 100$ km and $L_2 = 0$, which indicates unilateral rupture to the north. The error of the inversion near the minimum depends on L_1 rather than L_2. We computed the 90 % confidence interval for L_1, ΔL_1, by

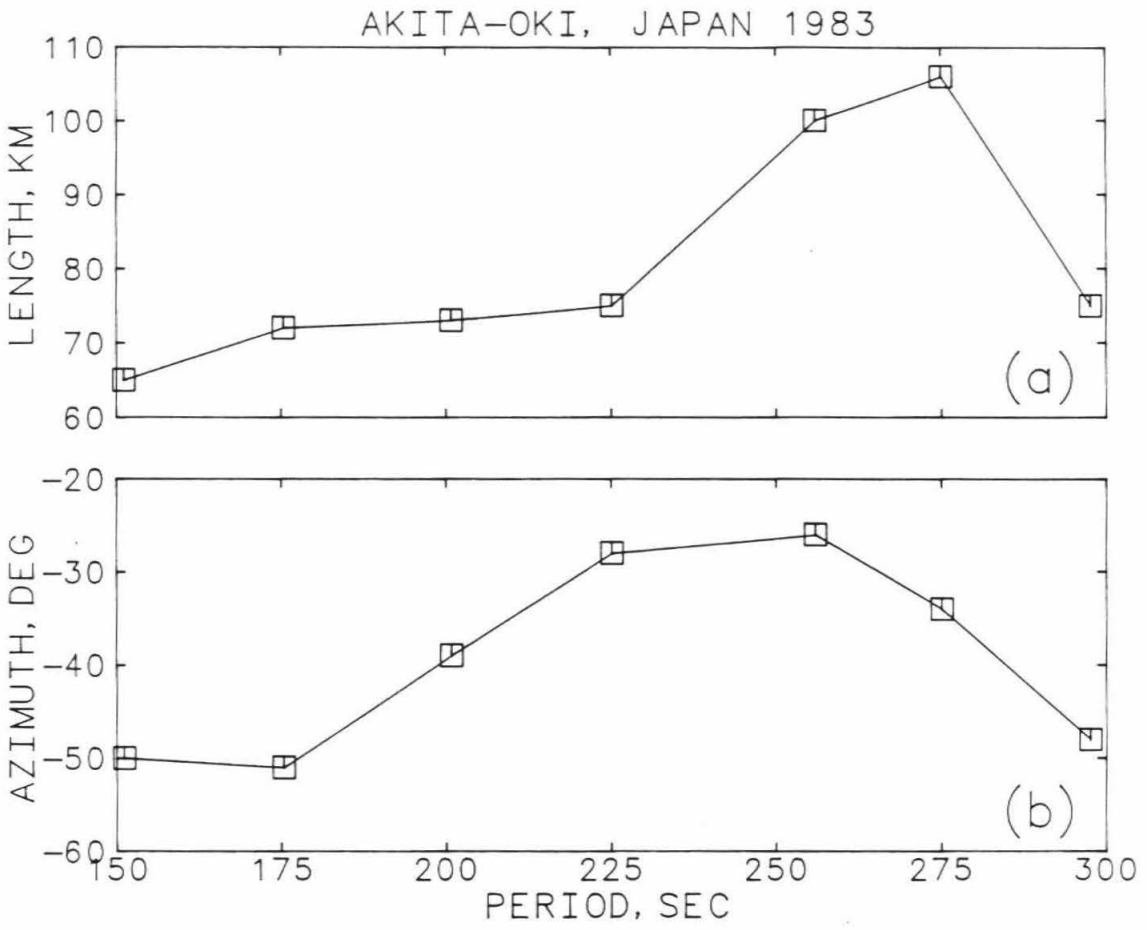

Figure 1.8 The rupture length (a) and azimuth (b) determined at periods from 150 to 300 sec for the Akita-Oki, Japan earthquake.

comparing the variances computed for L_1 which gives the minimum error and for $L_1 + \Delta L_1$. The confidence interval ΔL_1 was then determined by applying the F test to the variance ratio. The 90 per cent confidence interval for L_1 is estimated to be 29 km. In this paper, the estimate and the confidence interval are written as $L_1 = 100 \pm 29$ km. The rupture length L_2 cannot be determined with confidence.

The contour maps for other periods are similar in shape and have also a minimum corresponding to unilateral rupture to the north. The minimum on contour maps increases as the period decreases. Figure 7b shows the contours for the period of 275 sec. The error is smaller at this period than at 256 sec. The minimum is at $L_1 = 106$ km with a 90 per cent confidence limit of 32 km. The rupture lengths estimated at the period of 256 and 275 sec are consistent with the extent of the aftershock area.

Figure 8a shows the estimates of the rupture length obtained from the inversion at periods from 150 to 300 sec. The estimates of the rupture length for different periods show a large scatter.

Figure 9a shows the curves of the average amplitude spectrum $\overline{V}(\omega)$, magnitude of the spectral variation due to the source finiteness $\overline{S}(\omega)$, and the measure of the observability of the source-finiteness effect $\eta(\omega)$ in the period range from 150 to 300 sec. In the figure the maxima of $\overline{V}(\omega)$ and $\eta(\omega)$ are normalized to 1 in the period range. We calculated the source-finiteness effect using a northward unilateral rupture with a length of 120 km and a velocity of 2.5 km/sec. The average source finiteness effect $\overline{S}(\omega)$ of this rupture model at 150 sec is about a factor of 2 larger than that at 300 sec; it is approximately linear, monotonically decreasing with the period. The rupture causes an

Figure 1.9 Akita-Oki, Japan earthquake. (a) $\overline{V}(\omega)$ (crosses), $\overline{S}(\omega)$ (triangles), and $\eta(\omega)$ (squares) at various periods. (b) The rupture length versus the ratio γ for the rupture velocities of 2, 2.5, and 3 km/sec. The inversion is at the period of 256 sec. The rupture is assumed to be unilateral toward the north. (c) The *rms* error versus azimuth for the inversion at the period of 256 sec. The rupture is assumed to be unilateral with a fault length of 100 km. γ is assumed to be 0.1. (d) The rupture azimuth versus the ratio γ for the rupture velocities of 2, 2.5, and 3 km/sec. The inversion is at the period of 256 sec. The rupture is assumed to be unilateral with a length of 100 km.

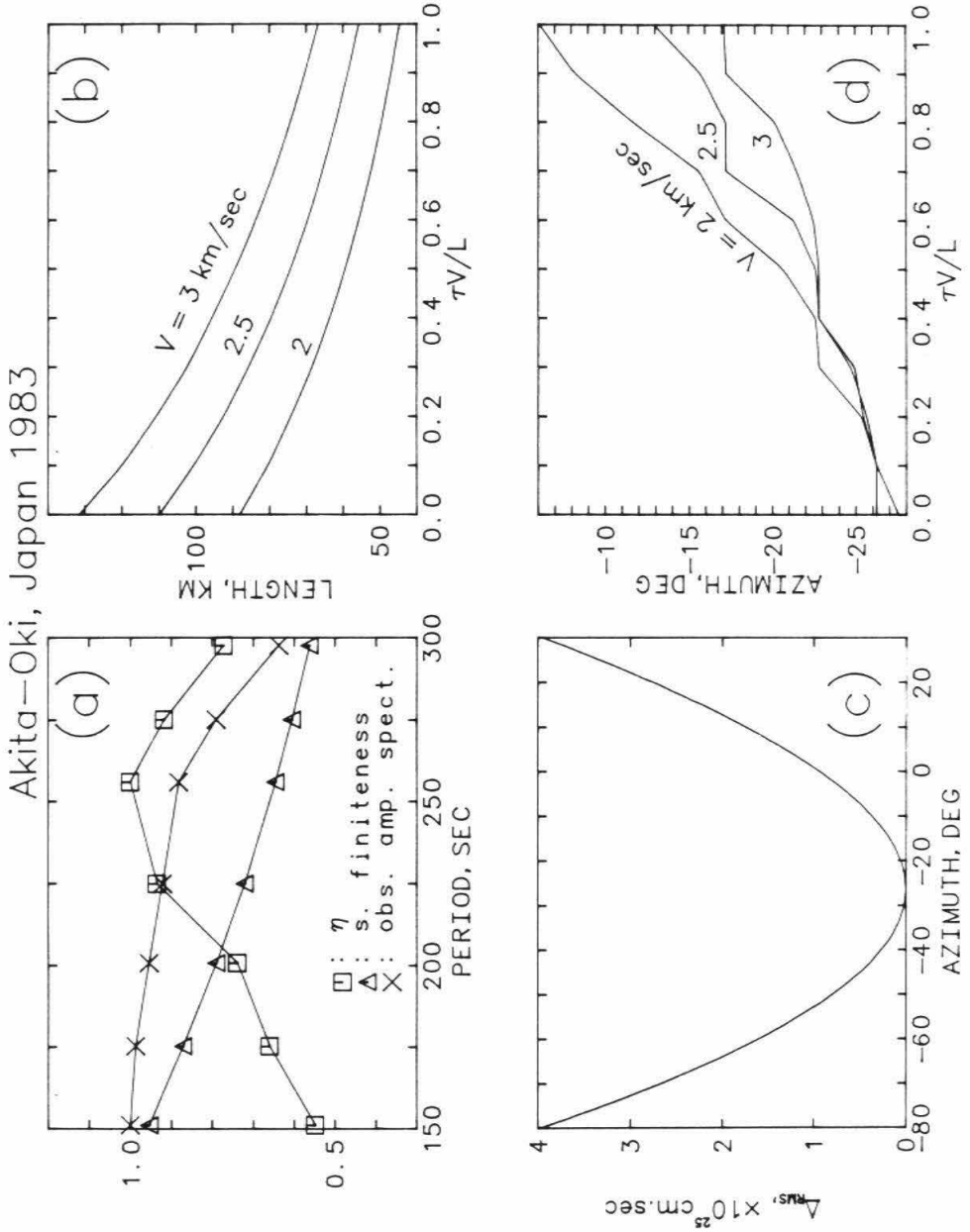
Akita-Oki, Japan 1983
(a)
(b)
(c)
(d)
□: η
△: s. finiteness
×: obs. amp. spect.
PERIOD, SEC
LENGTH, KM
V = 3 km/sec
2.5
2
τV/L
AZIMUTH, DEG
V = 2 km/sec
2.5
3
AZIMUTH, DEG

azimuthal variation of the amplitude spectra of about 34 percent at 150 sec, and 8 percent at 300 sec. The magnitude of the azimuthal variation is also a monotonically decreasing function of the period. Figure 9a shows that the average observed amplitude is larger at short periods than at long periods. However, because the noise level at short periods is much higher than at long periods, the overall observability of the source-finiteness at short periods becomes smaller than at long periods. Note that $\eta(\omega)$ in Figure 9a is largest at 256 sec.

Figure 8a shows that the estimates of the rupture length at periods 256 and 275 sec are much larger than those at other periods. The fault length resolved at other periods decreases as $\eta(\omega)$ becomes smaller.

We then determined the rupture azimuth, for the rupture length shown in Figure 8a. For the period of 256 sec, we obtained $N26^{o}\ W$ (Figure 9c) for the rupture length of 100 km. The azimuths were obtained in the same way for other periods and are shown in Figure 8b.

Because the data are considered more reliable around 256 sec than at other periods, and the observability of the source-finiteness around 256 sec is relatively large as shown in Figure 9a, we took the results for the rupture length and azimuth obtained at 256 sec as our estimates.

The estimated azimuth, $N26^{o}\ W$, is the overall trend of the aftershock area. Shimazaki and Mori (1983) and Ishikawa et al. (1984) found from the body-wave data that this earthquake is a multiple event with the first small event followed by two large events. The aftershock distribution indicates that the aftershock area can be divided into two parts; the northern part with a strike of NNW, and the southern part with a strike of NNE (Satake, 1985).

The two major events of the multiple-shock are located at these parts of the aftershock zone (Shimazaki and Mori, 1983, Ishikawa et al., 1984). Satake(1985) found that a fault model which consists of two segments, each 60 km long, to $N20^o\ W$ at the north and $N20^o\ E$ at the south of the center of the fault explains the waveforms of the tide gage records better than the model with the fault extending 120 km long toward the north.

In the determination of the rupture length and azimuth, the rupture velocity V and the ratio γ of rise time τ to rupture time t_f was assumed to be 2.5 km/sec and 0.1 respectively. Although these values are considered reasonable, they may vary for different events. To see the effect of varying the rupture velocity and γ on the estimate of the rupture length and azimuth, we tried inversions of the data at 256 sec for various rupture velocities and γ. We varied the rupture velocity between 2 and 3 km/sec, and γ between 0 and 1, a much wider range than that observed, which is usually between 0.025 to 0.25 (Kanamori and Anderson, 1975).

Figure 9b shows the results for the rupture length. In general, as the ratio and rupture velocity increase, the estimate of the rupture length decreases. Figure 9b shows that the rupture length estimated for a rupture velocity between 2 and 3 km/sec and $\gamma = 0.1$ is consistent with the length of the aftershock area. Figure 9d shows the results for the rupture azimuth. For a given γ, the azimuths estimated for different rupture velocities were within about 10^o.

Figure 1.10 Contours for the rms error obtained in the inversion at the period of 256 sec for three large earthquakes. The rupture velocity and the ratio γ is assumed to be 2.5 km/sec and 0.1 respectively. (a) For the 1979 Colombia-Ecuador earthquake. L_1 is assumed toward $N20^o\,E$ and L_2 toward $S20^o\,W$. (b) For the 1985 Valparaiso, Chile earthquake. L_1 is assumed toward the south and L_2 toward the north. (c) For the 1985 Michoacan, Mexico earthquake. L_1 is assumed toward $S50^o\,E$ and L_2 toward $N50^o\,W$.

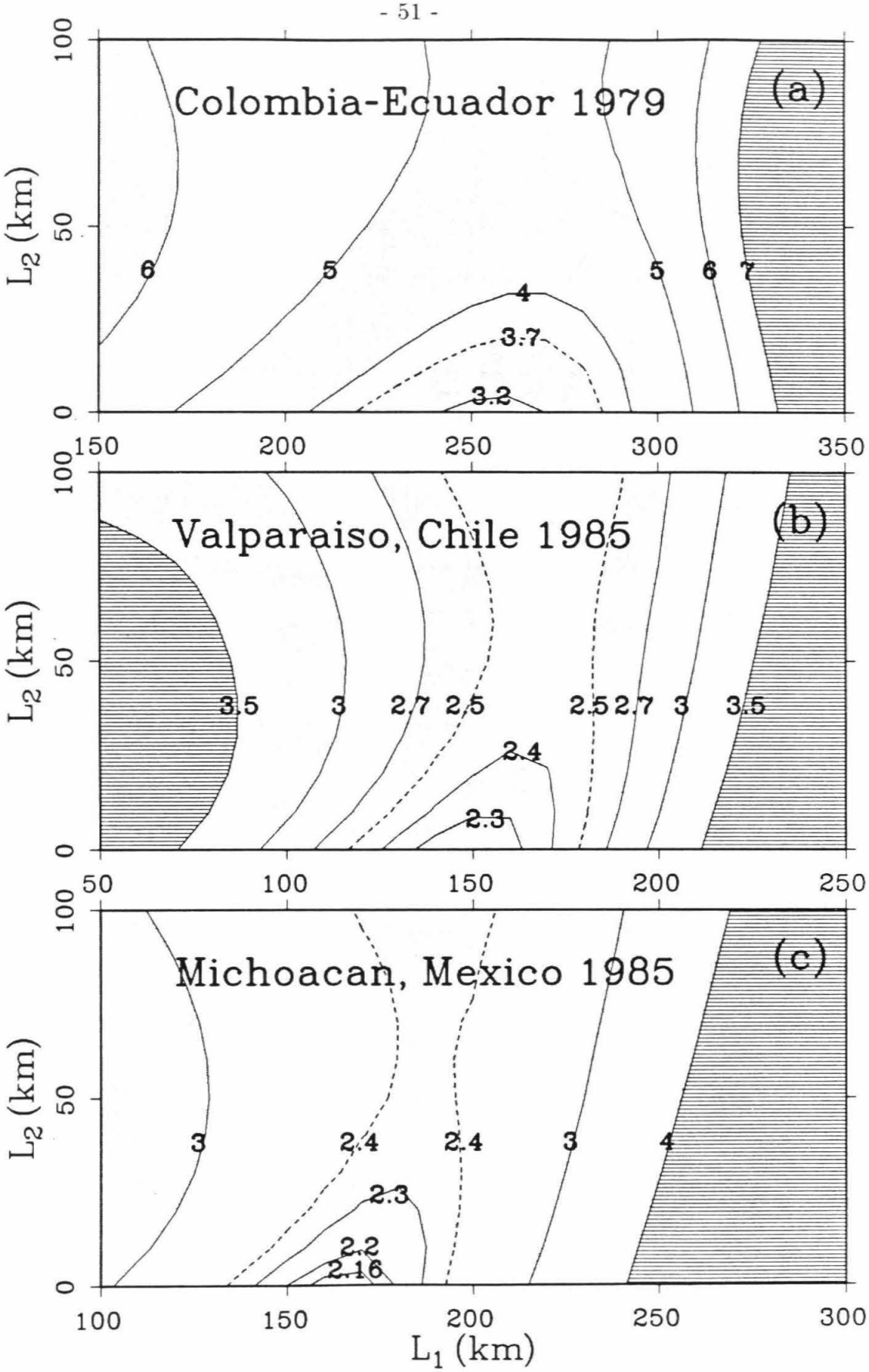
Colombia-Ecuador 1979
(a)
6
5
4
3.7
3.2
5
6
7
Valparaiso, Chile 1985
(b)
3.5
3
2.7
2.5
2.4
2.3
2.5
2.7
3
3.5
Michoacan, Mexico 1985
(c)
3
2.4
2.3
2.2
2.16
2.4
3
4
L_2 (km)
L_1 (km)
0
50
100
150
200
250
300
350

1.7.3 1979 Colombia-Ecuador Earthquake

The December 12, 1979 Colombia-Ecuador earthquake occurred at the plate-boundary between the subducting Nazca plate and the overriding South America plate that produced the great ($M_s = 8.7$) earthquake of 31 January 1906. The aftershock area of the 1979 event is presumably along a part of the segment that had previously ruptured during the great 1906 earthquake (Kanamori and McNally, 1982, Mendoza and Dewey, 1984).

The aftershocks of the 1979 Colombia-Ecuador earthquake were relocated by Mendoza and Dewey (1984). The 1-day aftershock pattern suggested that the earthquake ruptured unilaterally to the northeast with a fault length of at least 270 km. No significant expansion of the aftershock area within the 3 months following the earthquake was observed.

We used 33 Rayleigh wave phases (R_2 and R_3). In determining the rupture length we assumed a rupture velocity of 2.5 km/sec in the direction $N20^o E$, which is parallel to the aftershock area. Figure 10a shows the error of the inversion at the period of 256 sec. The rupture model of the earthquake is well resolved. Figure 10a indicates that the rupture is almost unilateral, with $L_1 = 256 \pm 25$ km, and $L_2 < 20$ km. The shape of the contours in Figure 10a is different than that for the Akita-Oki earthquake (Figure 7), for which only L_1 is well constrained by the inversion.

The inversions at other periods indicate also unilateral faulting. The estimated rupture lengths are shown in Figure 11a for each period. The lengths estimated from the inversions at 256 and 275 sec are 256 and 257 km respectively, and are larger than those estimated from other periods.

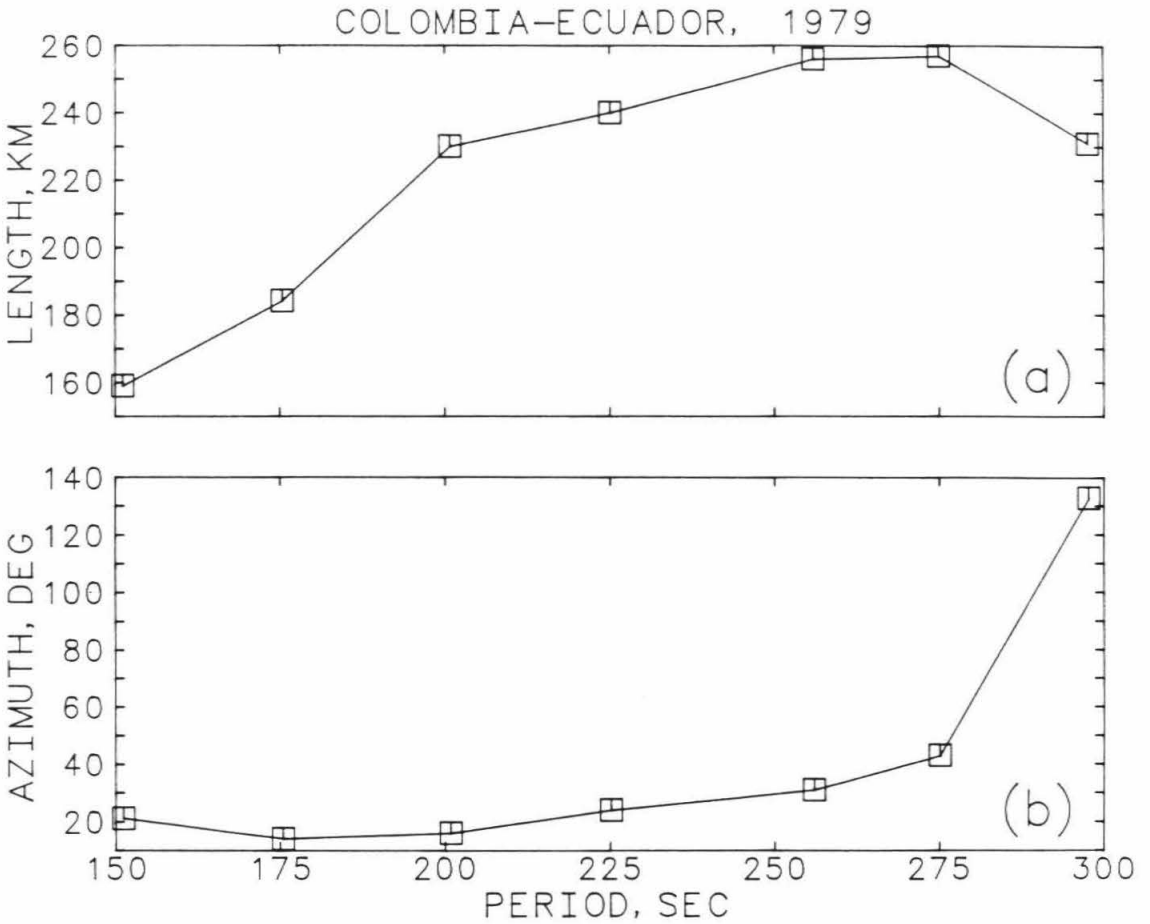

Figure 1.11 The rupture length (a) and azimuth (b) determined at periods from 150 to 300 sec for the Colombia-Ecuador earthquake.

Figure 12a shows $\overline{V}(\omega)$, $\overline{S}(\omega)$, and $\eta(\omega)$ in the period range from 150 to 300 sec. The source finiteness model used to calculate $\overline{S}$ is an unilateral rupture toward $N20^{o}E$ with a rupture length of 250 km and a rupture velocity of 2.5 km/sec. Because of the large length of the rupture, it produces much larger effects on the source spectrum than that for the Akita-Oki earthquake. The source finiteness produces an azimuthal variation of the spectral amplitude of about 87 percent at 150 sec, and about 30 percent at 300 sec. For the Colombia-Ecuador earthquake, the ratio between the size of the magnitudes of the source finiteness $\overline{S}$ at 150 sec and 300 sec, and between the azimuthal variations at these two periods is smaller than for the Akita-Oki earthquake.

Figure 12c shows the error as a function of the azimuth from -20^{o} to 90^{o} for the inversion at the period of 256 sec using a rupture length of 250 km. The error has a minimum at 31^{o}. The estimated rupture azimuths for different periods are shown in Figure 11b. The estimates at different periods agree well except at the period of 300 sec. Since $\eta(\omega)$ peaks at 256 sec, as shown in Figure 12a, we took 256 km and $N31^{o}E$ as our estimate of the rupture length and rupture azimuth of the Colombia-Ecuador earthquake. These estimates are consistent with the aftershock pattern of the earthquake.

Figure 12b shows the estimate of the rupture length obtained by inversions of the data at 256 sec for various rupture velocities and ratio γ. The figure shows that the rupture length estimated for a rupture velocity between 2 and 3 km/sec and $\gamma = 0.1$ is consistent with the length of the aftershock area. Figure 12d shows the results for the rupture azimuth obtained from inversions of the data at 256 sec for various rupture velocities and γ. For a given γ, the azimuths estimated for different rupture velocities are within

Figure 1.12 Colombia-Ecuador earthquake. (a) $\overline{V}(\omega)$ (crosses), $\overline{S}(\omega)$ (triangles), $\eta(\omega)$ (squares) at various periods. (b) Rupture length versus the ratio γ for the rupture velocities of 2, 2.5, and 3 km/sec. The inversion is at the period of 256 sec. The rupture is assumed to be unilateral toward the $N20^{o}E$. (c) The rms error versus azimuth for the inversion at the period of 256 sec. The rupture is assumed to be unilateral with a fault length of 256 km. γ is assumed to be 0.1. (d) The rupture azimuth versus the ratio γ for the rupture velocities of 2, 2.5, and 3 km/sec. The inversion is at the period of 256 sec. The rupture is assumed to be unilateral with a length of 256 km.

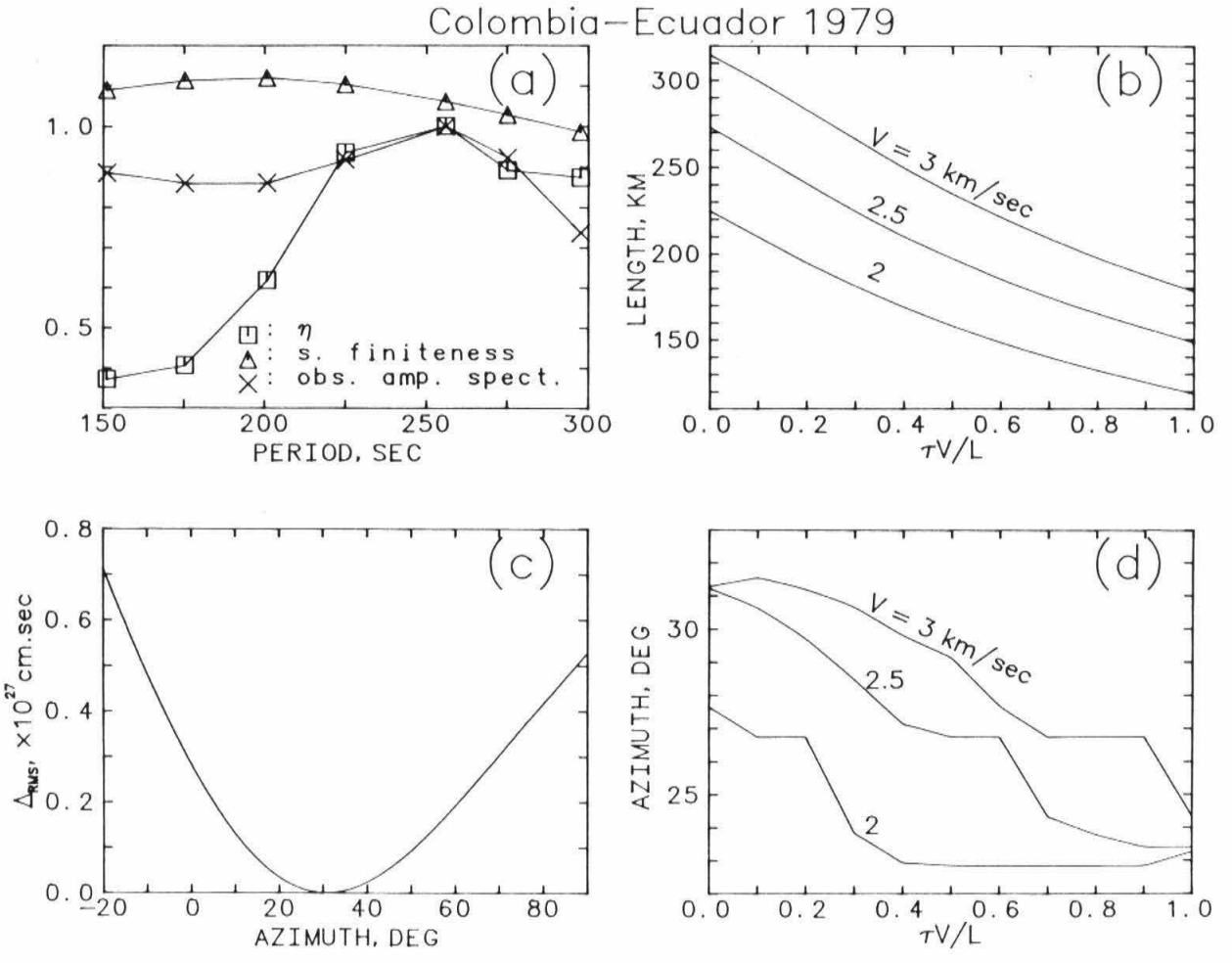
Colombia–Ecuador 1979
(a)
1.0
0.5
□ : η
△ : s. finiteness
× : obs. amp. spect.
150
200
250
300
PERIOD, SEC
(b)
300
250
200
150
LENGTH, KM
V = 3 km/sec
2.5
2
0.0
0.2
0.4
0.6
0.8
1.0
τV/L
(c)
0.8
0.6
0.4
0.2
0.0
Δ_{RMS}, $\times 10^{27}$ cm.sec
−20
0
20
40
60
80
AZIMUTH, DEG
(d)
30
25
AZIMUTH, DEG
V = 3 km/sec
2.5
2
0.0
0.2
0.4
0.6
0.8
1.0
τV/L

about 10^o .

Kanamori and Given (1981) used group delays of Rayleigh waves to determine the rupture parameters. The estimated rupture length is 230 km and rupture velocity is 2 km/sec. Beck and Ruff (1984) studied the P-wave source time functions and surface wave directivity of this earthquake. Their results show that most of the displacement of this earthquake occurred in an asperity to the NE of and close to the epicenter. Hartzell and Heaton (1985) obtained the source time function which is at least 120 sec long using the record of the Pasadena Benioff 1-90 seismometer. Our results are in general consistent with their results.

1.7.4 1985 Valparaiso, Chile Earthquake

The March 3, 1985 Valparaiso, Chile earthquake($M_s = 7.8$) occurred in an area which had been identified as a seismic gap by Kelleher (1972) on the basis of historical seismicity of Chile. The distribution of aftershocks of the earthquake located by USGS during the first three months after the main shock suggests that the rupture propagated to the south. The aftershock area did not show significant expansion. The aftershocks recorded by a portable array between 8 and 17 March defined an area of about 170 km in length with a strike toward the south (Comte et al., 1986). The aftershocks which occurred during one day after the main shock and were relocated by Dewey et al. (1985) fill in the same area, and the aftershock area extends 125 km southward of the epicenter and 75 km to the north.

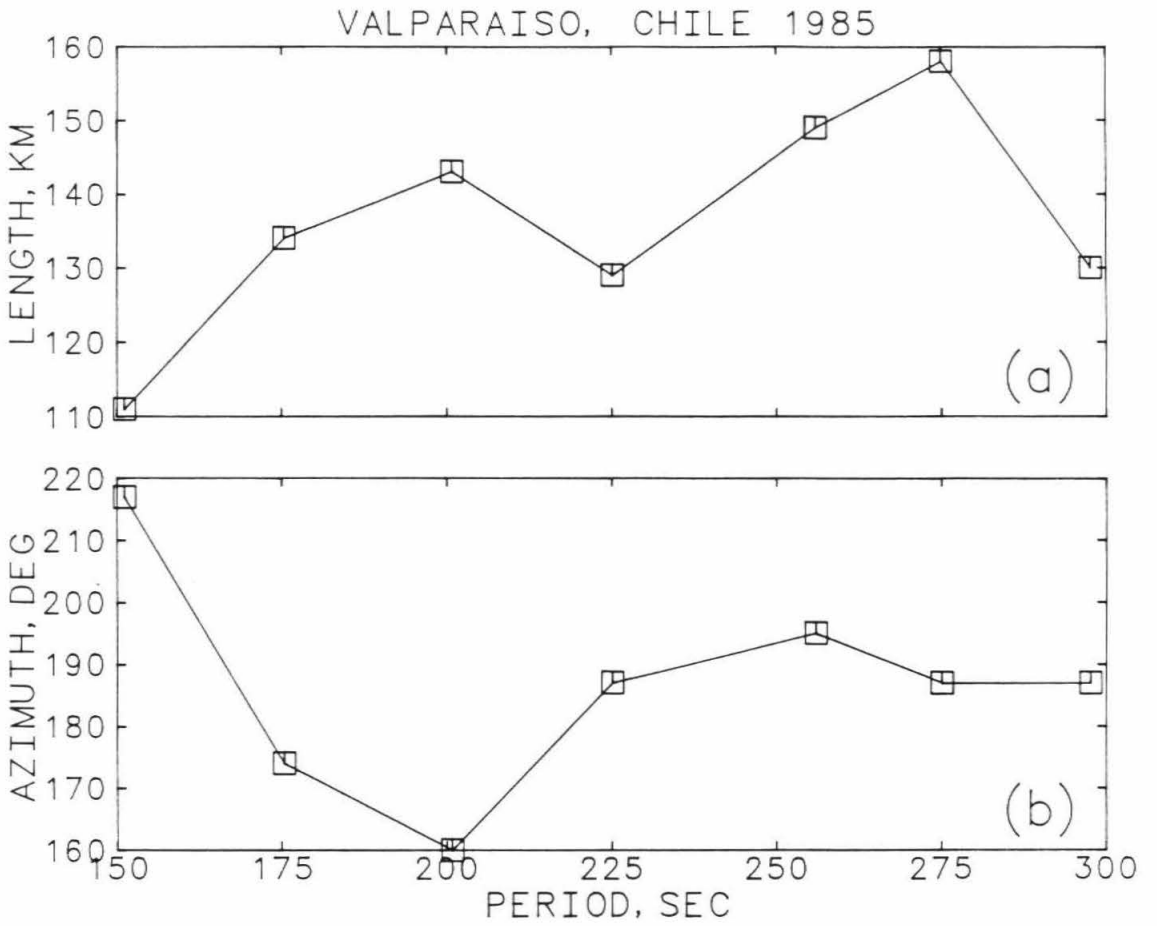

Figure 1.13 The rupture length (a) and azimuth (b) determined at periods from 150 to 300 sec for the Valparaiso, Chile earthquake.

We inverted 41 Rayleigh-wave phases (R_2 and R_3) recorded at IDA and GDSN stations for the source directivity. We first determined the rupture length assuming that the rupture propagated in the north-south direction with a velocity of 2.5 km/sec. Figure 10b is the contour map for the inversion at the period of 256 sec, which shows a minimum corresponding to unilateral faulting with $L_1 = 149\ km$ and a 90 percent confidence limit of 27 km. The rupture length L_2 is not constrained well. The inversion at other periods (Figure 13a) also shows that the rupture is unilateral to the south.

Figure 13c shows the error as a function of the trial azimuth for the inversion at 256 sec, which has the minimum at 195^o. The errors are for the unilateral rupture with the rupture length L_1 fixed at 149 km. Figure 13b shows the rupture azimuths estimated at various periods. The rupture azimuths estimated at periods of 256 and 275 sec are 195^o and 187^o respectively.

Figure 14a shows $\overline{V}(\omega)$, $\overline{S}(\omega)$, and $\eta(\omega)$ as functions of frequency. The average amplitude has the maximum value at 256 sec. We calculated the source finiteness effect using a model with a rupture length of 150 km and a rupture velocity of 2.5 km/sec toward the south. The function $\eta(\omega)$ has a peak at 256 sec and shows a smaller variation for different periods than for the Akita-Oki and Colombia-Ecuador earthquake. We estimate the rupture of the Chile earthquake to be 149 km long in $S\,15^o\,W$. These estimates are consistent with the aftershock distribution.

Figure 14b shows the estimate of the rupture length obtained from inversions of the data at 256 sec for various rupture velocities and γ. The rupture length estimated for a rupture velocity between 2 and 3 km/sec and $\gamma = 0.1$ is

Figure 1.14 Valparaiso, Chile earthquake. (a) $\overline{V}(\omega)$ (crosses), $\overline{S}(\omega)$ (triangles), and $\eta(\omega)$ (squares) at various periods. (b) Rupture length versus the ratio γ for the rupture velocities of 2, 2.5, and 3 km/sec. The inversion is at the period of 256 sec. The rupture is assumed to be unilateral toward the south. (c) The rms error versus azimuth for the inversion at the period of 256 sec. The rupture is assumed to be unilateral with a fault length of 149 km. γ is assumed to be 0.1. (d) The rupture azimuth versus the ratio γ for the rupture velocities of 2, 2.5, and 3 km/sec. The inversion is at the period of 256 sec. The rupture is assumed to be unilateral with a length of 149 km.

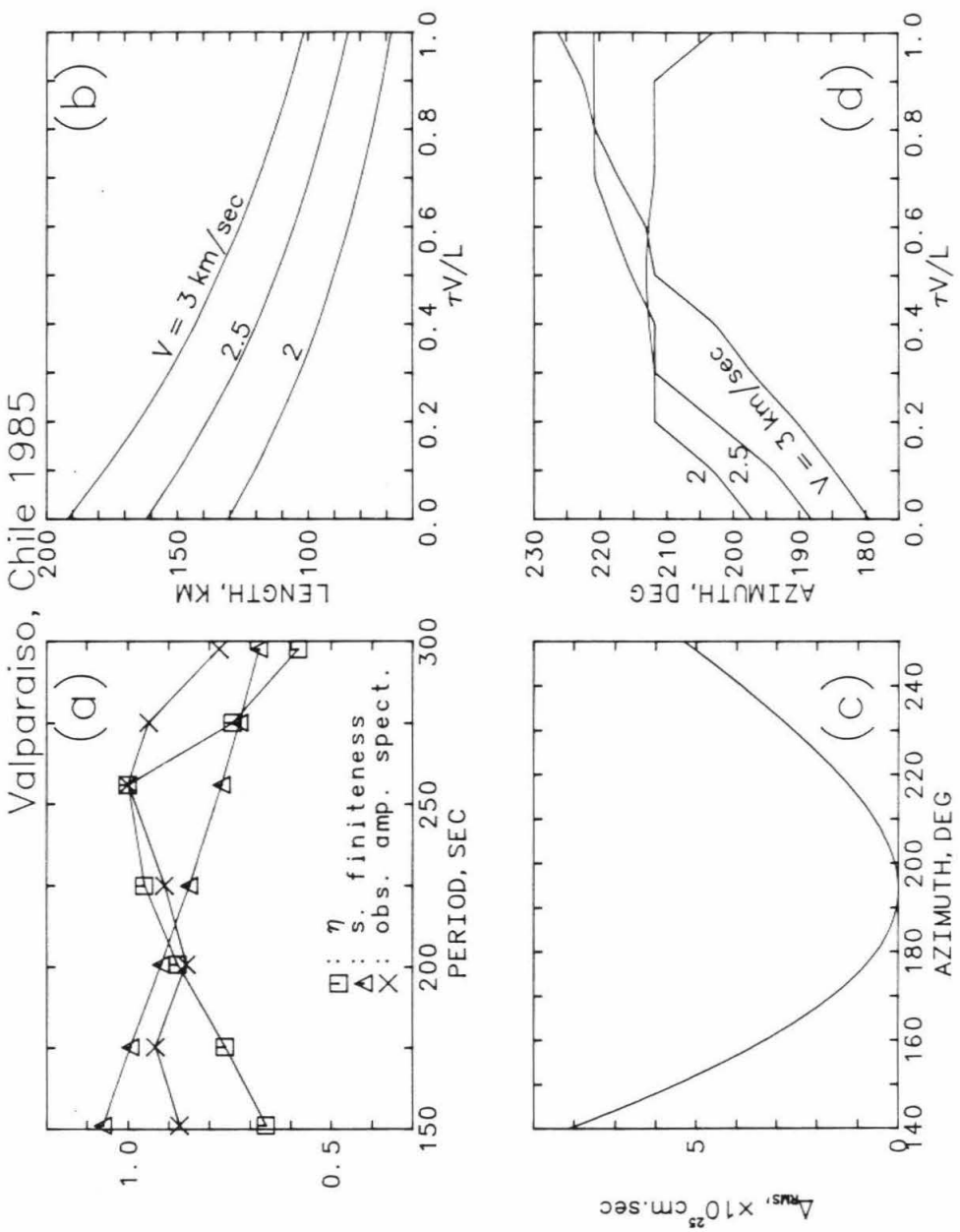
Valparaiso, Chile 1985
(a)
(b)
(c)
(d)
□: η
△: s. finiteness
×: obs. amp. spect.
PERIOD, SEC
LENGTH, KM
V = 3 km/sec
2.5
2
τV/L
AZIMUTH, DEG
AZIMUTH, DEG
Δ_RMS, x10^23 cm.sec

consistent with the length of the aftershock area. Figure 14d shows the rupture azimuth obtained from inversions of the data at 256 sec for various rupture velocities and γ. For a given γ, the azimuths estimated for different rupture velocities are within about 20^o .

Christensen and Ruff (1986) analyzed the source-time functions of body waves of this earthquake and found that the main rupture of this earthquake initiated near the epicenter and propagated to the south about 75 km with an average rupture velocity of 2 km/sec. If we assumed that the overall rupture velocity was 2 km/sec, then our estimate of the rupture length would be 130 km, which is the length of the aftershock zone south of the epicenter. The rupture to the north which is suggested by the aftershocks to the north of the epicenter cannot be resolved by our analysis.

1.7.5 1985 Michoacan, Mexico Earthquake

The September 19, 1985 Michoacan, Mexico earthquake($M_s = 8.1$) is a shallow, interplate event which broke a segment of the Middle America subduction zone. From the aftershocks recorded by a local strong motion array and a network of portable seismographs, the rupture area of the earthquake was estimated to be about 170 km long along its strike to the southeast (UNAM seismology group, 1986). The main shock was located near the northern end of the aftershock area.

We used 56 Rayleigh wave phases (R_2 and R_3) recorded at IDA and GDSN stations. We determined the rupture length assuming a rupture

velocity of 2.5 km/sec in the direction parallel to the strike of the aftershock zone, $N130^{o}E$. The inversion at all the periods indicated that the rupture was unilateral to $N130^{o}E$ direction. The error is minimized for a model with $L_1 = 165 \pm 30$ km (Figure 10c). Similar to the Chile earthquake, the rupture length in the opposite direction L_2 was not resolved well. Figure 15a shows the rupture lengths estimated at various periods.

The azimuth is estimated to be 123^{o} at the period of 256 sec (Figure 16c). Figure 15b shows the rupture azimuths estimated at various periods.

Figure 16a shows $\overline{V}(\omega)$, $\overline{S}(\omega)$, and $\eta(\omega)$ at various periods for the earthquake. We calculated the source finiteness effect using a model with a rupture length of 170 km, a rupture velocity of 2.5 km/sec in the azimuth of 130^{o}. The average observed amplitudes for the periods from 150 to 275 sec show a small scatter. The value of $\eta(\omega)$ at 256 sec is larger than that at other periods. We took 165 km and 123^{o} obtained from inversions at 256 sec as our estimate of the rupture length and azimuth respectively.

Figure 16b shows the rupture length estimated at the period of 256 sec for various rupture velocities and γ. The rupture length estimated for a rupture velocity between 2 and 3 km/sec and $\gamma = 0.1$ is consistent with the length of the aftershock area. Figure 16d shows the rupture azimuth estimated at the period of 256 sec for various rupture velocities and γ. The azimuths estimated for different rupture velocities are within about 10^{o} for a given γ.

Details of the rupture pattern of this earthquake have been studied by several investigators using body waves. Modeling of long-period P-waves suggests two subevents separated by about 27 sec in time (Eissler et al., 1986, UNAM seismology group, 1986, Houston and Kanamori, 1986), with the

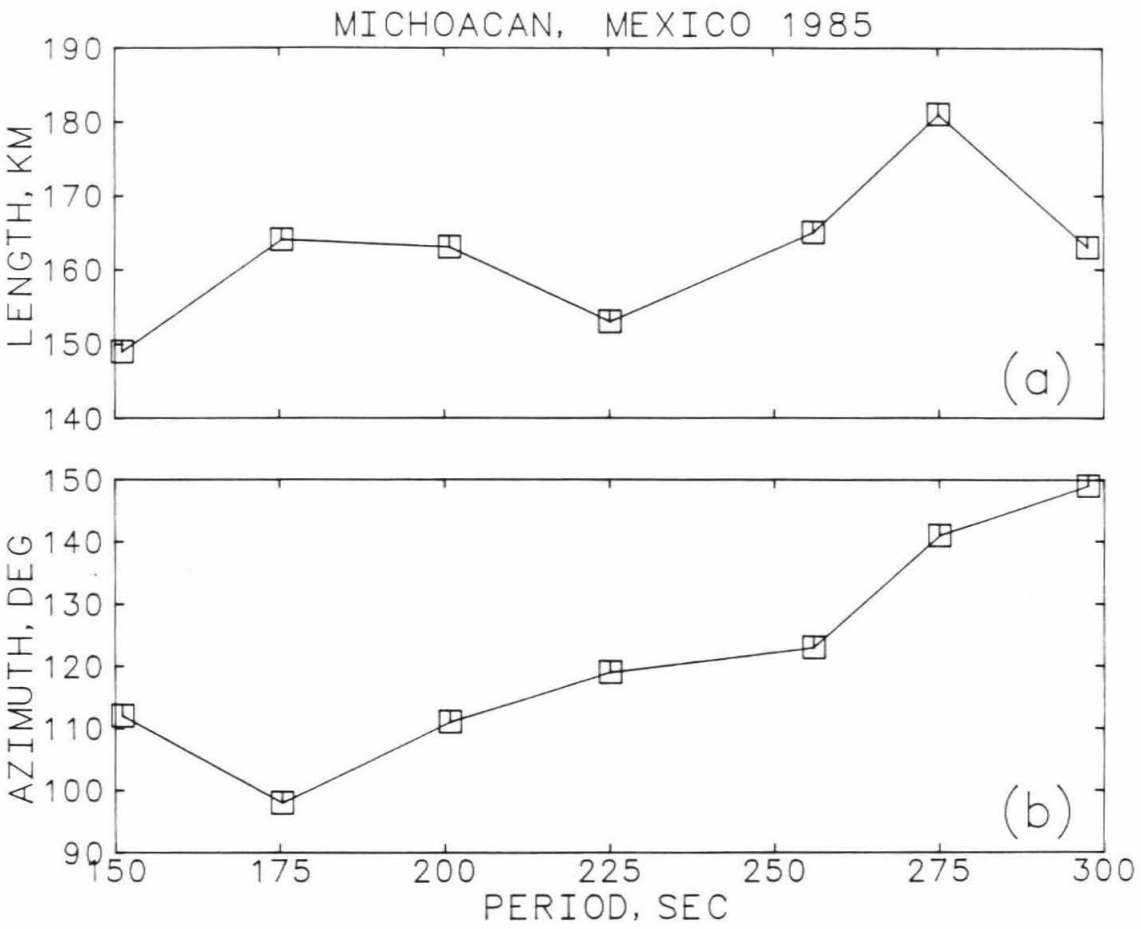

Figure 1.15 The rupture length (a) and azimuth (b) determined at periods from 150 to 300 sec for the Michoacan, Mexico earthquake.

Figure 1.16 Michoacan, Mexico earthquake. (a) $\overline{V}(\omega)$ (crosses), $\overline{S}(\omega)$ (triangles), and $\eta(\omega)$ (squares) at various periods. (b) Rupture length versus the ratio γ for the rupture velocities of 2, 2.5, and 3 km/sec. The inversion is at the period of 256 sec. The rupture is assumed to be unilateral toward the $S50^{o}E$. (c) The rms error versus azimuth for the inversion at the period of 256 sec. The rupture is assumed to be unilateral with a fault length of 165 km. γ is assumed to be 0.1. (d) The rupture azimuth versus the ratio γ for the rupture velocities of 2, 2.5, and 3 km/sec. The inversion is at the period of 256 sec. The rupture is assumed to be unilateral with a length of 165 km.

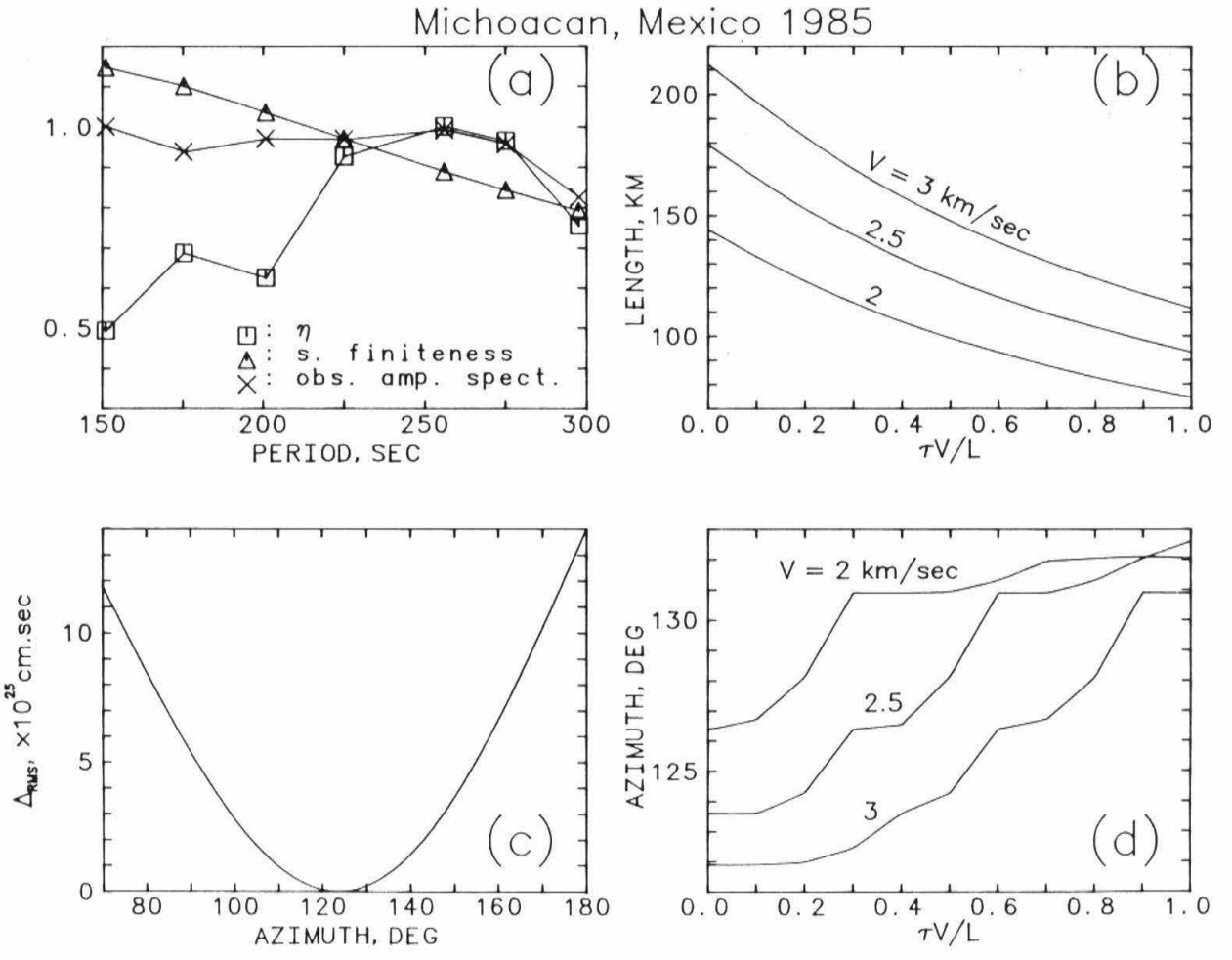
Michoacan, Mexico 1985
(a)
1.0
0.5
□: η
△: s. finiteness
×: obs. amp. spect.
150
200
250
300
PERIOD, SEC
(b)
200
150
100
LENGTH, KM
V = 3 km/sec
2.5
2
0.0
0.2
0.4
0.6
0.8
1.0
τV/L
(c)
10
5
0
Δ_RMS, ×10^25 cm.sec
80
100
120
140
160
180
AZIMUTH, DEG
(d)
V = 2 km/sec
2.5
3
130
125
AZIMUTH, DEG
0.0
0.2
0.4
0.6
0.8
1.0
τV/L

second event located to the southeast of the first event. The existence of the two subevents is also suggested by the near-field strong motions (Anderson, 1986). Ekstrom and Dziewonski (1986) inverted the deconvolved displacement P-wave pulses for the moment rate distribution in time and space. Their results show that the rupture, with a total length of 180 km and an apparent velocity of 2.7 km/sec toward the southeast, released the moment mainly in two subevents, the second of which was located approximately 70 km southeast of the first and occurred 28 sec later. Our results from long-period surface waves are in general consistent with theirs.

1.7.6 1977 Sumbawa, Indonesia Earthquake

The Sumbawa, Indonesia earthquake ($M_s = 7.9$) of August 19, 1977, which occurred near the eastern end of the Java trench, is the largest normal-fault earthquake since the Sanriku earthquake of 1933 (Stewart, 1978, Given and Kanamori, 1980). According to the International Seismological Centre (ISC) bulletin, the aftershocks that occurred during one day after the main shock are distributed in a zone elongated in the $N\,60^{o}\,E$ direction. Relocation studies of the aftershocks yielded a similar pattern of aftershock distribution (Fitch et al., 1981, Spence, 1986). The one-day aftershock area relocated by Fitch et al. (1981) extends about 200 km in the $N\,60^{o}\,E$ direction.

Unfortunately, because of the very large size of the event, most of the Rayleigh-wave phases with paths shorter than R_4 were off scale at the 5 IDA stations, and we had to use the phases with longer paths. A total of 22

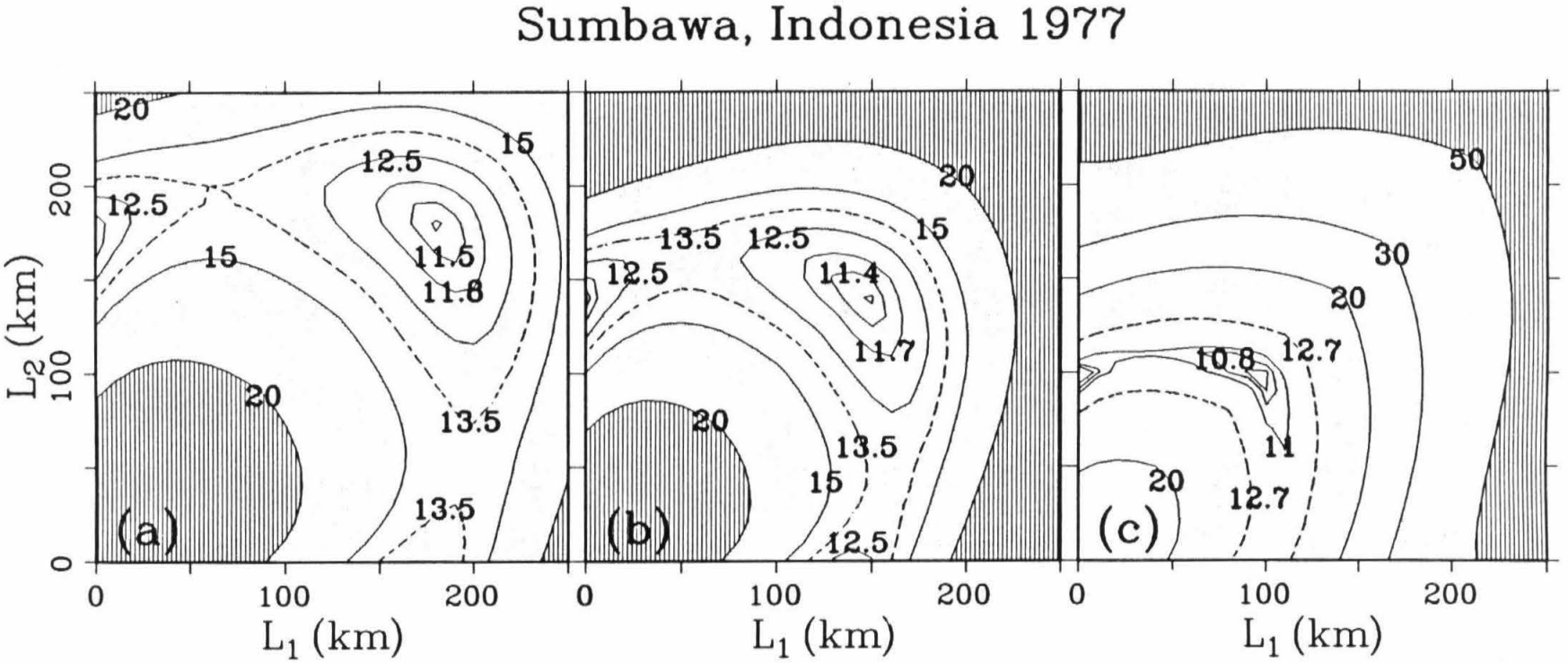

Figure 1.17 Contours for the *rms* error obtained in the inversion at the period of 256 sec for the Sumbawa, Indonesia earthquake. The azimuth of the rupture along L_1 is assumed to be N60°E and along L_2 to be S60°W. (a) The contours for a rupture velocity of 2.5 km/sec and the $\gamma = 0.1$. (b) The contours for a rupture velocity of 2 km/sec and the $\gamma = 0.1$. (c) The contours for a rupture velocity of 2 km/sec and the $\gamma = 0.6$.

Rayleigh-wave phases were used in the inversion. Because of the very long propagation path of the phases used, the quality of the data set is not as good as that of other earthquakes.

First, we assumed a rupture velocity V of 2.5 km/sec in the $N60^{o}E$ direction to determine the rupture length. The contour pattern of the inversion error obtained was significantly different from those obtained for other earthquakes studied in this paper. Figure 17a shows the contours for the inversion at the period of 256 sec. There are 3 local minima, which are associated with a bilateral rupture and two unilateral ruptures. The minimum corresponding to the bilateral rupture is much broader than those of the other two minima. The result from the inversion at other periods is similar to that in Figure 17a. The bilateral minimum indicates a rupture of 200 km on each side of the epicenter. The total rupture length is 400 km, which is about twice as long as the aftershock zone.

If the aftershock area represents the extent of the faulting, this estimate is a gross overestimate, which may be caused by the poor quality of the data. Another reason for this discrepancy with the aftershock area may arise from the nature of the actual rupture, which is significantly different from the rupture model we assumed in this method. If the rupture propagated down-dip or up-dip of the fault plane for considerable time compared with the whole rupture process, the results of our inversion might not be meaningful.

The estimated rupture length could be reduced if a larger rise time and a smaller rupture velocity were used in inversion. For the bilateral faulting, we determined the length using various rupture velocities and γ at 256 sec. Figure 17b shows the results for $V = 2$ km/sec and $\gamma = 0.1$. The best model is

Figure 1.18 Sumbawa, Indonesia earthquake. (a) $\overline{V}(\omega)$ (crosses), $\overline{S}(\omega)$ (triangles), and $\eta(\omega)$ (squares) at various periods. (b) Rupture length L versus the ratio γ for the rupture velocities of 2, 2.5, and 3 km/sec. The inversion is at the period of 256 sec. The rupture is assumed to be strictly bilateral ($L_1 = L_2 = L$) with L_1 toward $N60^o E$. (c) The rms error versus azimuth for the inversion at the period of 256 sec. The rupture is assumed to be bilateral with the half fault length L of 100 km. γ is assumed to be 0.1. (d) The rupture azimuth versus the ratio γ for the rupture velocities of 2, 2.5, and 3 km/sec. The inversion is at the period of 256 sec. The rupture is assumed to be strictly bilateral with a half length L of 100 km.

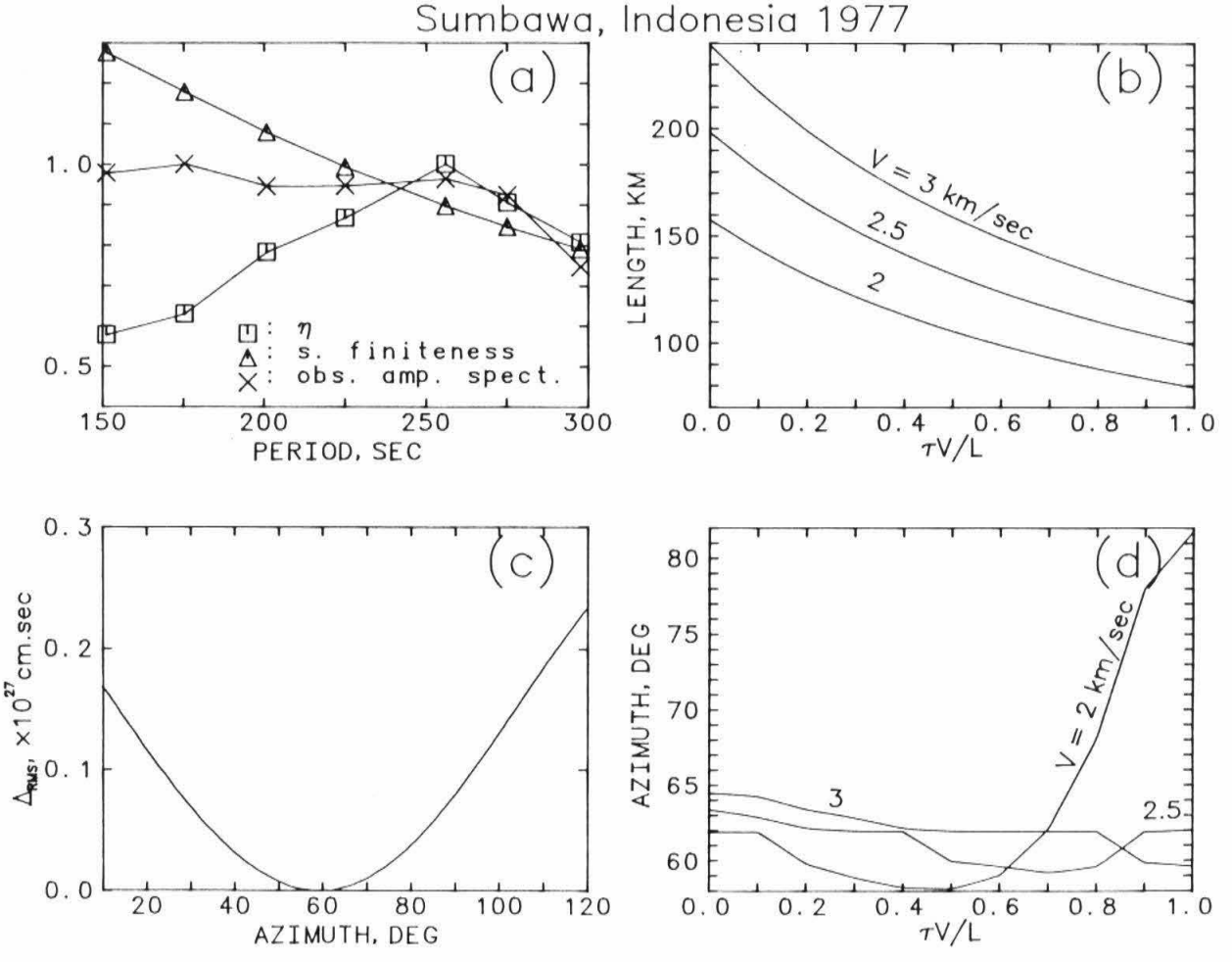
Sumbawa, Indonesia 1977
(a)
1.0
0.5
150
200
250
300
PERIOD, SEC
□ : η
△ : s. finiteness
× : obs. amp. spect.
(b)
200
150
100
LENGTH, KM
V = 3 km/sec
2.5
2
0.0
0.2
0.4
0.6
0.8
1.0
τV/L
(c)
0.3
0.2
0.1
0.0
Δmus, ×10^27 cm.sec
20
40
60
80
100
120
AZIMUTH, DEG
(d)
80
75
70
65
60
AZIMUTH, DEG
V = 2 km/sec
3
2.5
0.0
0.2
0.4
0.6
0.8
1.0
τV/L

a bilateral faulting with a rupture length of about 140 km on each side of the epicenter. An even smaller rupture length was obtained for $\gamma = 0.6$ and V = 2 km/sec (Figure 17c). The minimum of bilateral faulting is for a rupture length of 100 km on each side of the epicenter and a 30 sec rise time.

Figure 18a shows $\overline{V}(\omega)$, $\overline{S}(\omega)$, and $\eta(\omega)$. The model used to calculate the finiteness effect is a bilateral rupture of 100 km long on each side of the epicenter with a rupture velocity of 2 km/sec, and a 30 sec rise time. Figure 18a shows that $\eta(\omega)$ is the largest at the period of 256 sec, same as for other four earthquakes studied in this paper.

Figure 18b shows the rupture length as a function of γ for V = 2, 2.5, and 3 km/sec for the earthquake. It is similar to those for the other four earthquakes. If the one day aftershock area represents the rupture area of the earthquake, this figure indicates that the earthquake had a small rupture velocity and a large γ such as those used for Figure 17c. The large γ indicates that the rise time is about half of the rupture time which represents the duration of horizontally faulting.

This unusually long rise time may represent the duration of down-dip or up-dip rupture propagation of the earthquake. In our source-finiteness analysis, the rupture propagation is assumed to be horizontal. For a down-dip or up-dip rupture on a vertical fault plane, the variation of the spectrum due to the rupture is independent of azimuth, which can result in an apparent long rise time in our analysis. For displacements of far-field body waves and surface waves, the effect of rupture propagation in vertical direction can be described using an apparent rise time which is the rupture time in the vertical direction (Hirasawa and Stauder, 1965, Ben-Menahem and Singh, 1981).

Figure 18c shows the differential error as a function of the azimuth for the inversion at 256 sec. The error is obtained for bilateral rupture with a rupture length of 100 km on each side of the epicenter, $V = 2$ km/sec, and $\tau = 30$ sec. The estimate of the rupture azimuth is $N60^o E$, which agrees well with the azimuth of the aftershock area. The rupture azimuth determined at the periods from 150 to 300 sec is between $N60^o E$ and $N65^o E$. Figure 18d shows the estimated azimuth as function of γ for V = 2, 2.5, and 3 km/sec. For $\gamma \leq 0.7$ the rupture azimuths estimated for different V differ within about 5^o.

If the average rupture velocity is between 2 and 3 km/sec and the rupture length is comparable to that of the aftershock area (about 200 km), then the earthquake might have a considerably larger down-dip extent than that of other four earthquakes studied in this paper. Suppose that the rupture velocity on the down-dip or up-dip direction of the fault plane is 2 km/sec, the fault extent would be approximately 60 km in width for a 30 sec apparent rise time. Using the seismic moment obtained by Giardini et al. (1985), the seismic slip of the earthquake would be about 6 m. If the moment of Given and Kanamori (1980) is used, the slip would be about 9 m.

1.8 Conclusions

We determined the source-finiteness parameters of eleven large earthquakes from long-period (150 to 300 sec) Rayleigh waves recorded at IDA and GDSN stations. We investigated two simple models of source finiteness. The

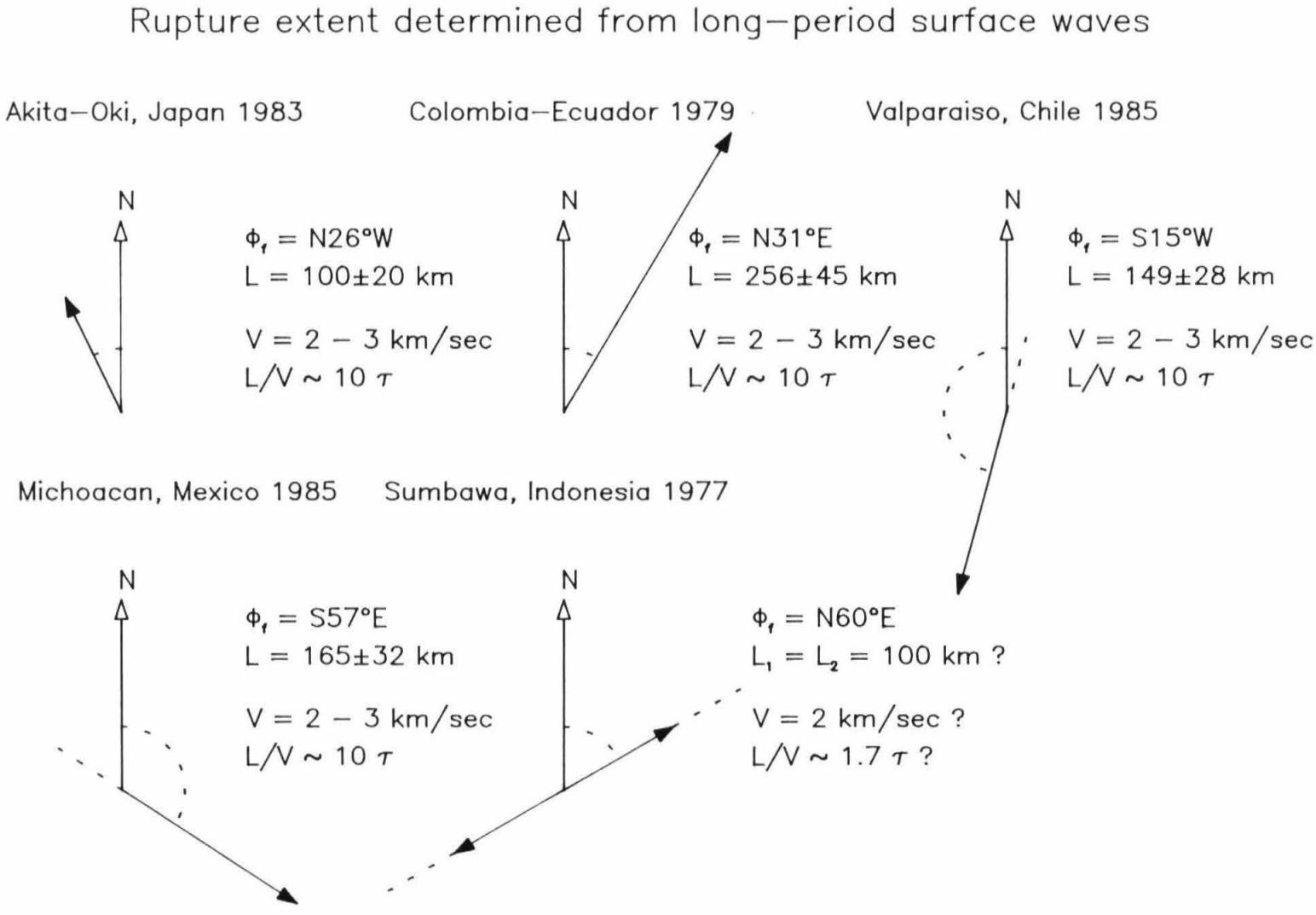

Figure 1.19 Summary of the rupture extent determined from long-period Rayleigh-waves for several large earthquakes.

parameter of the first model is the source-process time. We determined the source-process times of the earthquakes using Furumoto's method and a linear inversion method. The source-process times obtained from the inversion method with a laterally heterogeneous earth model M84C (Woodhouse and Dziewonski, 1984) in general agree well with those obtained by Furumoto's method.

The source-process times of the Sumbawa (Indonesia), Colombia-Ecuador, Valparaiso (Chile), and Michoacan (Mexico) were estimated to be 79, 118, 69, and 77 sec respectively using the linear inversion method with the model M84C.

The correction for the regional phase velocity difference yields significantly different source-process times by the inversion method. The source-process times obtained using the model M84C can differ as much as a factor of two from that using a homogeneous earth model.

In the second source finiteness model we used the directivity function of Ben-Menahem (1961). The parameters of the model are the rupture length, rupture azimuth, rupture velocity, and the ratio γ of the rise time to the rupture time. The method inverts the data set of complex spectra of observed surface-wave trains from as many stations as possible by solving a simple least-square problem. Because the error obtained in the inversion is independent of the excitation functions, the estimates are reliable even when the source depth and mechanism are not known a priori. The estimates of the source-finiteness from inversions using different data sets are stable.

Figure 19 summarizes the results for the source finiteness of 5 large earthquakes. Although surface-wave data provide good estimates of gross rupture

parameters, the details of the source process cannot be determined. The details can be resolved better by body-wave studies (e.g. Ruff and Kanamori, 1983, Beck and Ruff, 1984, Ekstrom and Dziewonski, 1986). However, if the moment release of a large earthquake is uniform on the fault plane, the extent of the entire rupture cannot be resolved by body waves alone. If a significant portion of the fault plane ruptured smoothly and generated only longer-period (larger than 100 sec) waves, the source dimension obtained from body waves could be much smaller than the extent of the actual rupture. For the Colombia-Ecuador earthquake the long-period surface waves indicate a longer source duration than body waves. The source duration estimated from body waves is approximately 60 sec which is about half the duration estimated from surface waves (Ruff and Kanamori, 1983, Beck and Ruff, 1984). Surface-wave results are more representative of the extent and duration of the entire rupture of large earthquakes.

For the Sumbawa earthquake, our results suggest that the geometry of the fault plane is different from that of the other earthquakes studied. The Sumbawa earthquake is the only event studied here that indicates bilateral faulting. The rupture models estimated for the Akita-Oki, Colombia-Ecuador, Valparaiso, and Michoacan earthquakes are all unilateral. However, the location of the main shock with respect to the aftershock area of these earthquakes suggests some bilateral component. Our method can not resolve the rupture length of the shorter segment of a bilateral rupture if it is much shorter than the longer segment. The methods described in this paper provide an objective estimate of the source finiteness of large shallow earthquakes.

1.9 References

Agnew, D., Berger, J., Buland, R., Farrell, W. and Gilbert, F., 1976. International deployment of accelerometers: a network for very long period seismology. *EOS Trans. AGU*, 57: 180-188.

Anderson, J.G., Bodin, P., Brune, J.N., Prince, J., Singh, S.K., Quaas, R. and Onate, M., 1986. Strong ground motion from the Michoacan, Mexico, earthquake. *Science*, 233: 1043-1049.

Beck, S.L. and Ruff, L.J., 1984. The rupture process of the great 1979 Colombia earthquake: evidence for the asperity model. *J. Geophys. Res.*, 89: 9281-9291.

Benioff, H., Press, F. and Smith, S.W., 1961. Excitation of the free oscillations of the Earth by earthquakes. *J. Geophys. Res.*, 66: 605-620.

Ben-Menahem, A., 1961. Radiation of seismic surface waves from finite moving sources. *Bull. Seism. Soc. Am.*, 51: 401-435.

Ben-Menahem, A. and Singh, S.J., 1981. Seismic Waves and Sources, Springer-Verlag, New York.

Ben-Menahem, A. and Toksö z, M.N., 1962. Source-mechanism from spectra of long-period seismic surface-waves. *J. Geophys. Res.*, 67: 1943-1955.

Ben-Menahem, A. and Toksö z, M.N., 1963a. The Alaska earthquake of July 10, 1958. *Bull. Seism. Soc. Am.*, 53: 905-919.

Ben-Menahem, A. and Toksö z, M.N., 1963b. Source-mechanism from spectra of long-period seismic surface-waves, 2. The Kamchatka earthquake of Nov. 4, 1952. *J. Geophys. Res.*, 68: 5207-5222.

Christenson, D.H. and Ruff, L.J., 1986. Rupture process of the March 3, 1985 Chilean earthquake. *Geophys. Res. Lett.*, 13: 721-724.

Comte, D., Eisenberg, A., Lorca, E., Pardo, M., Ponce, L., Saragoni, R., Singh, S.K. and Suarez, G., 1986. The 1985 Central Chile earthquake: A repeat of previous great earthquake in the region? *Science*, 233:449-453.

Dewey, J.W., Choy, G.L. and Nishenko, S.P., 1985. Asperities and paired thrust zones in the focal region of the Chilean earthquake of March 3, 1985 (abstract). *EOS Trans. AGU*, 66: 950.

Dziewonski, A.M. and Steim, J.M., 1982. Dispersion and attenuation of mantle waves through waveform inversion. *Geophys. J. R. astr. Soc.*, 70: 503-527.

Dziewonski, A.M. and Woodhouse, J.H., 1983. An experiment in systematic study of global seismicity: Centroid-moment tensor solutions for 201 moderate and large earthquakes of 1981. *J. Geophys. Res.*, 88: 3247-3271.

Dziewonski, A.M., Chou, T.-A. and Woodhouse, J.H., 1981. Determination of earthquake source parameters from waveform data for studies of global and regional seismicity. *J. Geophys. Res.*, 86: 2825-2852.

Dziewonski, A.M., Franzen, J.E. and Woodhouse, J.H., 1983. Centroid-moment tensor solutions for April-June, 1983. *Phys. Earth Planet. Inter.*, 33: 243-249.

Dziewonski, A.M., Franzen, J.E. and Woodhouse, J.H., 1985. Centroid-moment tensor solutions for January-March, 1985. *Phys. Earth Planet. Inter.*, 40: 249-258.

Dziewonski, A.M., Franzen, J.E. and Woodhouse, J.H., 1986. Centroid-moment tensor solutions for July-September, 1985. *Phys. Earth Planet. Inter.*, 42: 205-214.

Eissler, H., Astiz, L. and Kanamori, H., 1986. Tectonic setting and source parameters of the September 19, 1985 Michoacan, Mexico earthquake. *Geophys. Res. Lett.*, 13: 569-572.

Ekström, G. and Dziewonski, A.M., 1986. A very broad band analysis of the Michoacan, Mexico earthquake of September 19, 1985. *Geophys. Res. Lett.*, 13: 605-608.

Engdahl, E.R., Peterson, J. and Orsini, N.A., 1982. Global digital networks - currect status and future directions. *Bull. Seism. Soc. Am.*, 72: S242-S259.

Fitch, T.J., North, R.G. and Shields, M.W., 1982. Focal depths and moment tensor representations of shallow earthquakes associated with the great Sumba earthquake. *J. Geophys. Res.*, 86: 9357-9374.

Furumoto, M., 1979. Initial phase analysis of R waves from great earthquakes. *J. Geophys. Res.*, 84: 6867-6874.

Furumoto, M. and Nakanishi, I., 1983. Source times and scaling relations of large earthquakes. *J. Geophys. Res.*, 88: 2191-2198.

Giardini, D., Dziewonski, A.M. and Woodhouse, J.H., 1985. Centroid-moment tensor solutions for 113 large earthquakes in 1977-1980. *Phys. Earth Planet. Inter.*, 40: 259-272.

Gilbert, F. and Dziewonski, A.M., 1975. An application of normal mode theory to the retrieval of structure parameters and source mechanisms from seismic spectra. *Phil. Trans. R. Soc. Lond. A.*, 278: 187-269.

Given, J.W. and Kanamori, H., 1980. The depth extent of the 1977 Sumbawa, Indonesia earthquake. *EOS Trans. AGU*, 61: 1044.

Hartzell, S.H. and Heaton, T.H., 1985. Teleseismic time functions for large, shallow subduction zone earthquakes. *Bull. Seism. Soc. Am.*, 75: 965-1004.

Hirasawa, T. and Stauder, W., 1965. On the seismic body waves from a finite moving source. *Bull. Seism. Soc. Am.*,, 55: 237-262.

Houston, H. and Kanamori, H., 1986. Source characteristics of the 1985 Michoacan, Mexico earthquake at periods of 1 to 30 seconds. *Geophys. Res. Lett.*, 13: 597-600.

Ishikawa, Y., Takeo, M., Hamada, N., Katsumata, M., Satake, K., Abe, K., Kikuchi, M., Sudo, K., Takahashi, M., Kashiwabara, S. and Mikami, N., 1984. Source process of the 1983 Japan Sea earthquake. *Chikyu*, 6: 11-17(in Japanese).

Kanamori, H., 1970a. Synthesis of long-period surface waves and its application to earthquake source studies - Kurile Island earthquake of October 13, 1963. *J. Geophys. Res.*, 75: 5011-5027.

Kanamori, H., 1970b. The Alaska earthquake of 1964: Radiation of long-period surface waves and source mechanism. *J. Geophys. Res.*, 75: 5029-5040.

Kanamori, H. and Anderson, D.L., 1975. Theoretical basis of some empirical relations in seismology. *Bull. Seism. Soc. Am.*, 65: 1073-1095.

Kanamori, H. and Given, J.W., 1981. Use of long-period surface waves for rapid determination of earthquake-source parameters. *Phys. Earth Planet. Inter.*, 27: 8-31.

Kanamori, H. and McNally, K.C., 1982. Variable rupture mode of the subduction zone along the Ecuador-Colombia coast. *Bull. Seism. Soc. Am.*, 72: 1241-1253.

Kanamori, H. and Stewart, G.S., 1976. Mode of the strain release along the Gibbs fracture zone, Mid-Atlantic ridge. *Phys. Earth Planet. Inter.*, 11: 312-332.

Kelleher, J.A., 1972. Rupture zone of large South American earthquakes and some predictions. *J. Geophys. Res.*, 77: 2087-2103.

Kikuchi, M. and Kanamori, H., 1982. Inversion of complex body waves. *Bull. Seism. Soc. Am.*, 72, 491-506.

Kikuchi, M. and Kanamori, H., 1986. Inversion of complex body waves - II. *Phys. Earth and Planet. Int.*, 43, 205-222.

Mendoza, C. and Dewey, J.W., 1984. Seismicity associated with the great Colombia-Ecuador earthquakes of 1942, 1958, and 1979: Implications for barrier models of earthquake rupture. *Bull. Seism. Soc. Am.*, 74: 577-593.

Nakanishi, I. and Anderson, D.L., 1983. Measurements of mantle wave velocities and inversion for lateral heterogeneity and anisotropy - I. Analysis of great circle phase velocities. *J. Geophys. Res.*, 88: 10267-10283.

Nakanishi, I. and Anderson, D.L., 1984. Measurements of mantle wave velocities and inversion for lateral heterogeneity and anisotropy - II. Analysis by the single-station method. *Geophys. J. R. astr. Soc.*, 78: 573-617.

Nakanishi, I. and Kanamori, H., 1982. Effects of lateral heterogeneity and source process time on the linear moment tensor inversion of long-period Rayleigh waves. *Bull. Seism. Soc. Am.*, 72: 2063-2080.

Okal, E.A., 1977. The effect of intrinsic oceanic upper-mantle heterogeneity on regionalization of long-period Rayleigh-wave phase velocities. *Geophys. J. R. astr. Soc.*, 49: 357-370.

Press, F., Ben-Menahem, A. and Toksöz, M.N., 1961. Experimental determination of earthquake fault length and rupture velocity. *J. Geophys. Res.*, 66: 3471-3485.

Riedesel, M.A., Jordan, T.H., Sheehan, A.F. and Silver, P.G., 1986. Moment-tensor spectra of the 19 Sept 85 and 21 Sept 85 Michoacan, Mexico, earthquakes. *Geophys. Res. Lett.*, 13: 609-612.

Romanowicz, B.A. and Guillemant, P., 1984. An experiment in the retrieval of depth and source mechanism of large earthquakes using very long-period Rayleigh wave data. *Bull. Seism. Soc. Am.*, 74: 417-437.

Romanowicz, B.A. and Monfret, T., 1986. Source process times and depth of large earthquakes by moment tensor inversion of mantle wave data and the effect of lateral heterogeneity. *Ann. Geophy.*, 4: B, 3, 271-283.

Ruff, L. and Kanamori, H., 1983. The rupture process and asperity distribution of three great earthquakes from long-period diffracted P-waves. *Phys. Earth Planet. Inter.*, 31: 202-230.

Satake, K., 1985. The mechanism of the 1983 Japan Sea earthquake as inferred from long-period surface waves and tsunamis. *Phys. Earth Planet. Inter.*, 37: 249-260.

Shimazaki, K. and Mori, J., 1983. Focal mechanism of the May 26, 1983 Japan Sea earthquake. *Progr. Abstr. Seism. Soc. Jpn.*, 2: 15.

Silver, P.G. and Jordan, T.H., 1983. Total moment spectra of fourteen large earthquakes. *J. Geophys. Res.*, 88: 3273-3293.

Silver, P.G., Riedesel, M.A., Jordan, T.H. and Sheehan, A.F., 1986. Low frequency properties of the Sumbawa earthquake of 1977. *EOS Trans. AGU*, 67: 309.

Spence, W., 1986. The 1977 Sumba earthquake series: Evidence for slab pull force acting at a subduction zone. *J. Geophys. Res.*, 91: 7225-7239.

Stewart, G.S., 1978. Implications for plate tectonics of the August 19, 1977 Indonesia decoupling normal fault earthquake. *EOS Trans. AGU*, 59: 326.

Tohoku University and Hirosaki University, 1984. Foreshock and aftershock activities of the 1983 Central Japan Sea earthquake. *Rep. Coord. Comm. Earthq. Pred.*, 31: 22-33(in Japanese).

Tanimoto, T., 1985. The Backus-Gilbert approach to the three-dimensional structure in the upper mantle - I. Lateral variation of surface wave phase velocity with its error and resolution. *Geophys. J. R. astr. Soc.*, 82: 105-123.

Tanimoto, T. and Kanamori, H., 1986. Linear programming approach to moment tensor inversion of earthquake sources and some tests on the three-dimensional structure of the upper mantle. *Geophys. J. R. astr. Soc.*, 84: 413-430.

UNAM seismology group, 1986. The September 19, 1985 Michoacan earthquake: Aftershock distribution and history of rupture. *Geophys. Res. Lett.*, 13: 573-576.

Woodhouse, J.H. and Dziewonski, A.M., 1984. Mapping the upper mantle: Three-dimensional modeling of Earth structure by inversion of seismic waveforms. *J. Geophys. Res.*, 89: 5953-5986.

Chapter 2

Depth of Large Earthquakes Determined from Long-Period Rayleigh Waves

2.1 Introduction

Investigation of the depth extent of faulting of large earthquakes is important for a better understanding of the state of stress and the mechanical properties of fault zones. Large shallow thrust earthquakes usually occur on the interface between the subducting oceanic lithosphere and the overriding continental or island-arc lithosphere, and are due to the relative plate motion. The earthquakes which occurred seaward of, or beneath, the trench within the oceanic plate are mainly normal-fault events and are interpreted as the results of bending or arching of the oceanic plate or the slab pulling. The tearing of the lithosphere is also considered as the cause of some shallow earthquakes. The distribution and mechanism of earthquakes near mid-ocean-ridges may indicate that the thermal contraction resulted from cooling of the hot material moving away from the ridge is an important source of stress in young lithospheres (Wiens and Stein, 1983, 1984; Bergman and Solomon, 1984).

The depth and other source parameters of earthquakes have been traditionally determined from the arrivals of the earliest waves, which have a common origin at a point in the source region. Another approach to estimate these parameters is to use the waveforms or spectra of body waves, surface

waves, or free oscillations of the earth excited by the earthquake. For large earthquakes the results obtained from the second approach are not related to the motion of a point in source region at any moment, but are spatially and temporally averaged quantities about the source of the earthquake. In this approach, the centroid location and time are determined, which represent in some sense the best location and time of an equivalent point source (Backus and Mulcahy, 1976; Dziewonski et al., 1981; Dziewonski and Woodhouse, 1983).

Many studies have focused on the determination of source parameters, from long-period surface wave or free oscillation data (Aki, 1960a, b; Kanamori, 1970; Gilbert and Dziewonski, 1975; Dziewonski et al., 1981; Kanamori and Given, 1981; Silver and Jordan, 1983). For very large earthquakes, the centroid depth from long-period data may not coincide with that from shorter period, body-wave observations. Romanowicz and Guillemant (1984) proposed a method to retrieve the centroid depth and the moment tensor of large earthquakes using spectra of long-period Rayleigh waves. The determination of the centroid depth involves a nonlinear inverse problem.

There are several difficulties preventing accurate depth determination using long-period surface waves. First, large shallow earthquakes have large rupture extent and long duration. Their lateral rupture extent is often comparable to, or larger than, the vertical extent. The source process of large earthquakes is in general complex, because asperities in the fault zone cause complexities in the spatial and temporal variation of the dislocation along the fault plane. Second, the differences in the lithosphere structure between different regions may not be negligible in the excitation of these waves. Third,

the corrections for the propagation effects on the amplitudes and phases of waves are often very large.

Recent progress in the studies of source finiteness (Romanowicz and Monfret, 1986; Zhang and Kanamori, 1987) and the lateral heterogeneity of the earth (Nakanishi and Anderson, 1983, 1984; Woodhouse and Dziewonski, 1984; Tanimoto, 1985, 1986) made possible a direct use of surface wave data in the determination of the depth extent of large earthquakes. Various global average or laterally heterogeneous models for the phase velocity, the group velocity, Q, and surface wave excitation or free oscillation of the earth have been developed (e.g. Kanamori, 1970; Dziewonski and Anderson, 1981; Dziewonski and Steim, 1982; Anderson and Given, 1982; Nakanishi and Anderson, 1984; Regan and Anderson, 1984). An examination of the effects of the choice of different earth models on the determination of the depth and other source parameters is necessary.

In this paper, we made a detailed study in the depth determination of large shallow earthquakes using various models for the excitation and propagation of surface waves. We first describe the method to retrieve the depth and the mechanism of a moment tensor or double couple source, which is similar to the method of Romanowicz and Guillemant (1984). We determined the source depth and mechanism of nine earthquakes from long-period Rayleigh waves recorded at IDA (International Deployment of Accelerographs) and GDSN (Global Digital Seismograph Network) stations.

2.2 Method

2.2.1 Moment Tensor Inversion

We determine the depth and mechanism of the earthquake from long-period Rayleigh waves by the moment tensor inversion using the method of Romanowicz and Guillemant (1984), in which the system (2) is solved in two steps. In the first step, the system (11) is solved for $D(\omega)$ using the data vector $V(\omega)$ at several frequencies: $\omega_1, \omega_2, \cdots, \omega_K$.

In the second step, the moment tensor is determined from the vectors $D(\omega_i)$, $(i = 1, \ldots, K)$ for given excitation functions. The moment tensor can be obtained by solving the following system

$$\Gamma M = \Lambda , \tag{13}$$

where

$$\Gamma = \left[\Gamma_1 , \Gamma_2 , \cdots , \Gamma_K \right]^T ,$$

$$\Gamma_i = diag \left[P_R^{(1)}(\omega_i , h), P_R^{(1)}(\omega_i , h), S_R^{(1)}(\omega_i , h), \right.$$

$$\left. Q_R^{(1)}(\omega_i , h), Q_R^{(1)}(\omega_i , h) \right], \quad (i = 1, \ldots, K) ,$$

$$M = \left[M_{xy} , (M_{yy} - M_{xx}), (M_{yy} + M_{xx}), M_{yz} , M_{xz} \right]^T ,$$

and

$$\Lambda = \left[D^T(\omega_1), D^T(\omega_2), \ldots, D^T(\omega_K) \right]^T .$$

The minimum sum of squares of the least-squares (LS) problem in the second

step can be written as $\rho_{LS}^2 = \| (I - \Gamma (\Gamma^T \Gamma)^{-1}\Gamma^T)\Lambda \|_2^2$. For each trial source depth, we calculate the error, $\rho_{LS}/\sqrt{5K}$, the root-mean-square (*rms*) of the residuals of the inversion. Since the excitation function depends on the depth, the error is a function of the depth. We invert (13) for the moment tensor and find the depth that minimizes the error. However, if only one frequency is considered (K=1) the error vanishes for any given trial depth, since Γ becomes diagonal and (13) is solved exactly.

2.2.2 Fault Inversion

The method of Romanowicz and Guillemant (1984) can be extended to estimate the source parameters and depth of a double couple source. If the source is a double couple, (2) is replaced by

$$\alpha = P_R^{(1)}(\omega, h)\, M_o\ p_R + S_R^{(1)}(\omega, h)\, M_o\ s_R \ , \tag{14a}$$

$$\beta = Q_R^{(1)}(\omega, h)\, M_o\ q_R \ , \tag{14b}$$

where M_o is the scalar seismic moment, s_R , p_R , and q_R , are determined from the fault parameters, dip angle δ, slip angle λ, and strike ϕ_f defined by Ben-Menahem et al. (1965) (also see Kanamori and Stewart, 1976).

For Rayleigh waves, the system (11) is solved in the first step for $D(\omega)$ at various frequencies. Here the matrix B remains the same, while the vector $D(\omega)$ is replaced by

$$D = \Big[P_R^{(1)}(\omega, h)m_1,\ P_R^{(1)}(\omega, h)m_2,\ S_R^{(1)}(\omega, h)m_3,$$
$$Q_R^{(1)}(\omega, h)m_4,\ Q_R^{(1)}(\omega, h)m_5\Big]^T \ ,$$

where

$$m_1 = M_o\,(-\cos\lambda\,\sin\delta\,\cos 2\phi_f\; - \sin\lambda\,\sin\delta\,\cos\delta\,\sin 2\phi_f\;)\,,$$

$$m_2 = M_o\,(2\,\cos\lambda\,\sin\delta\,\sin 2\phi_f\; - 2\,\sin\lambda\,\sin\delta\,\cos\delta\,\cos 2\phi_f\;)\,,$$

$$m_3 = M_o\,(-2\,\sin\lambda\,\sin\delta\,\cos\delta)\,,$$

$$m_4 = M_o\,(-\cos\lambda\,\cos\delta\,\sin\phi_f\; + \sin\lambda\,\cos 2\delta\,\cos\phi_f\;)\,,$$

$$m_5 = M_o\,(\sin\lambda\,\cos 2\delta\,\sin\phi_f\; + \cos\lambda\,\cos\delta\,\cos\phi_f\;)\,.$$

Note m_i (i=1,...,5) can be written as $m_1 = M_{xy}$, $m_2 = M_{yy} - M_{xx}$, $m_3 = M_{yy} + M_{xx}$, $m_4 = M_{yz}$, and $m_5 = M_{xz}$, where M_{xx} , M_{yy} , M_{xy} , M_{xz} , and M_{yz} are components of the moment tensor corresponding to the double couple.

In the second step, a system in the form of (13) is solved for M_o , δ, λ, and ϕ_f using the vector Γ. Here Γ_i (i=1, ...,K) remain the same as in (13), while the vector M is replaced by $M = (m_1\,,\ m_2\,,\ m_3\,,\ m_4\,,\ m_5)$ where m_i's are the nonlinear functions of δ, λ, and ϕ_f , defined above.

For a given depth, we solve the nonlinear system for M_o , δ, λ, and ϕ_f and calculate the error, $\rho_{LS}\,/\sqrt{5K}$. We find the depth of the double couple source which minimizes the error.

The methods for the depth determination from Love waves and from both Rayleigh and Love waves are given in the Appendix.

2.3 Earth Model

The determination of the depth extent of earthquakes from surface waves requires an accurate description of excitation characteristics and propagation effects.

2.3.1 Phase Velocity and Q

Recently several laterally heterogeneous earth models of phase velocities have been proposed (Nakanishi and Anderson, 1983, 1984; Woodhouse and Dziewonski, 1984; Tanimoto, 1985, 1986). In this study, the phase shifts of surface waves due to propagation are corrected using the laterally heterogeneous earth model M84C. Romanowicz and Monfret (1986) used several models of phase velocity to correct for the observed phase delays due to propagation. Their results indicate that the choice of the phase velocity model is not critical to the estimates of the depth and source parameters.

The propagation effects on the amplitude are corrected with models of group velocity and Q. In the period range concerned, the global average of the group velocity of mantle Rayleigh waves is probably good to better than 1% (Mills and Hales, 1977, 1978; Mills, 1978; Fukao and Kobayashi, 1983; Dziewonski and Steim, 1982; Nakanishi and Anderson, 1984). In the following, we use three different models, which are the model of Kanamori (1970), PREM (Dziewonski and Anderson, 1980), and the model of Nakanishi and Anderson (1984).

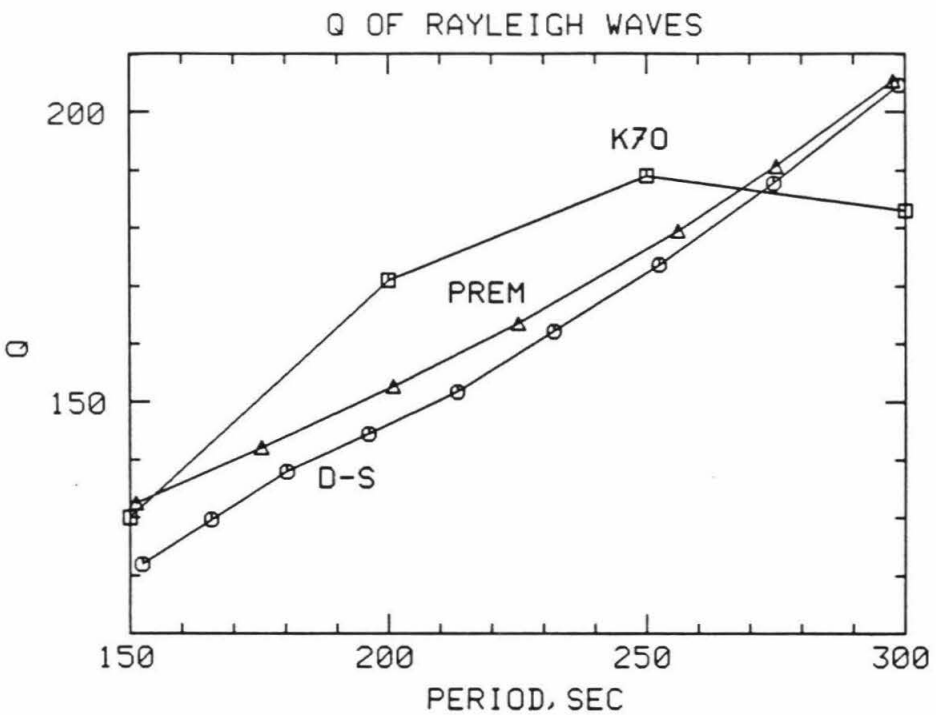

Figure 2.1 Comparison of three models of attenuation of Rayleigh waves, the model of Kanamori (1970) (squares), the PREM model (triangles), and the model of Dziewonski and Steim (1982) (circles).

In contrast with the similarities between the group velocity data given by different investigators, the published data on attenuation of surface waves or normal modes often differ by more than 5% in the period range from 150 to 300 sec. Figure 1 shows the Q values in the period range for three models, the model of Kanamori (1970), PREM, and the model of Dziewonski and Steim (1982). In the period range concerned, the last model is consistent with the data set compiled by Anderson and Given (1982) from Anderson and Hart (1978a, b), Chael and Anderson (1982), Nakanishi(1979), and Dziewonski and Steim (1982). We determined the depths of earthquakes using three models of the group velocity and Q. The first model is the model of Kanamori (1970) (here referred to as K70). The second model is PREM. The third model uses the Q given by of Dziewonski and Steim (1982), and group velocities of Nakanishi and Anderson (1984). Later we will refer to the last model as D-S. Since these models differ principally in Q rather than in the group velocity, we will call them Q models.

2.3.2 Excitation

As seen from (13), the wave excitation is directly related to the determination of source parameters. We investigated the effect of different choices of the earth model on the depth estimates. We used four spherically symmetric earth models:

(1). 5.08M (Press, 1970, Kanamori, 1970). This model is the simplest considered here, in which the lithosphere (LID) spans a depth range from 16 km, the depth of the Moho, to 71 km, the top of the low velocity zone (LVZ),

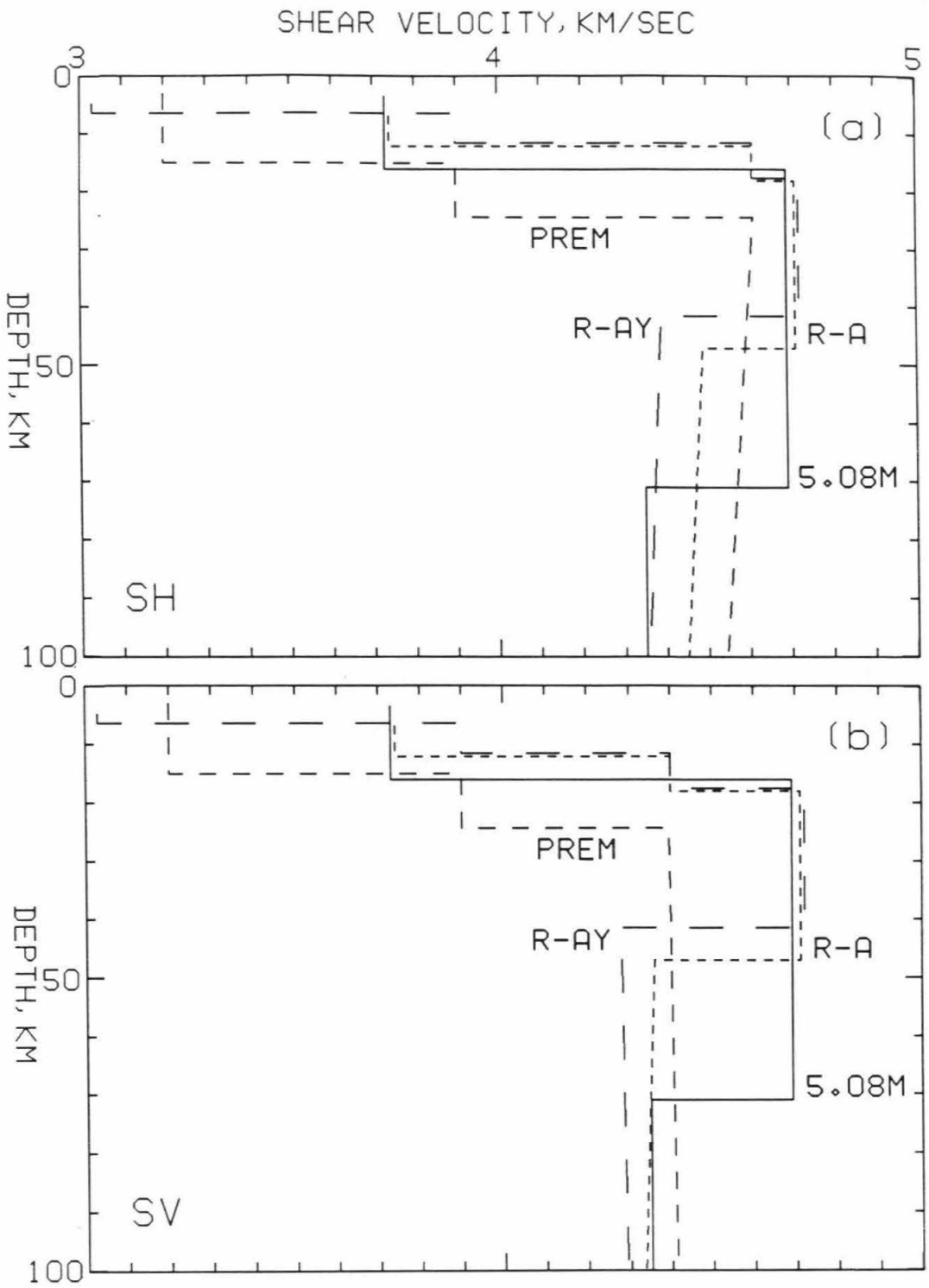

Figure 2.2 Shear velocities at a reference period of 1 sec in the uppermost 100 km for the models of 5.08M (Press, 1970, Kanamori, 1970), PREM (Dziewonski and Anderson, 1981), the average ocean (R-A) and 20 - 50 Ma ocean (R-AY) of Regan and Anderson (1984). Horizontal (a) and vertical (b) components of shear velocities are shown for layers of anisotropic structure.

where the shear-wave velocity drops by 7%.

(2). The PREM model (Dziewonski and Anderson, 1981).

(3). The average oceanic model A of Regan and Anderson (1984) (here referred to as R-A). This model has a LID from 12 km to 47 km, the top of the LVZ, where the velocity discontinuity is about 7%.

(4). The model for the ocean of 20-50 Ma in age of the ocean floor of Regan and Anderson (1984) (here referred to as R-AY). This model is close to R-A except that the LID is thinner and the velocity in the crust is higher.

Figures 2a and 2b show the shear velocity at a reference period of 1 sec in the upper 100 km for these earth models. PREM, R-A, and R-AY are anisotropic. In PREM there is no LID at the period of 1 sec, and the bottom of the LID is at 80 km depth at the period of 200 sec. In these anisotropic models, at a reference period of 200 sec, the velocity above the LVZ in each model remains about the same as that at 1 sec, while in the LVZ it drops by about 2% from the velocity at 1 sec. A very pronounced high-velocity LID is a prominent feature of 5.08M, R-A, and R-AY compared with PREM. For each earth model, we computed the source excitations and used them for the depth determination.

2.4 Source Finiteness

Because of the long duration and the large spatial extent of the earthquakes studied here, the source phase and amplitude spectra for the period range considered differ considerably from the spectra of a point source with a step time function. The magnitude of the source-finiteness effect on the

spectra of long-period surface waves and the observability of the source finiteness can be measured using the method of Zhang and Kanamori (1987). The observability of the source finiteness is measured by $\eta(\omega) = \overline{V}(\omega)\ \overline{S}(\omega)\ /\ \epsilon(\omega)$, where $\overline{V}(\omega)$ is the amplitude spectrum averaged over all stations, $\overline{S}(\omega)$ is the magnitude of the spectral variation due to the source finiteness, and $\epsilon(\omega)$ is a measure of the noise given by the error in the inversion. For the 1979 Colombia-Ecuador earthquake, $\overline{S}$ is greater than 1 for the period range of 150 to 300 sec, indicating that the deviation from the point-source spectra is significant.

Several simple models have been used to represent the source of large earthquakes. The first model is a point source with a step time function. The second model is a point source with a step time function with a delay time, which is determined from the phase spectra. The delay time may be considered as the half source duration. This model is used by Romanowicz and Monfret (1986). The phase spectra are corrected for the source-finiteness effects before the inversion. The third is a point source with finite source duration. The last is a finite fault or propagating source. For the last two models, both the amplitude and phase spectra are corrected before the inversion. Zhang and Kanamori (1987) used a finite-fault model to study the source directivity of large earthquakes. The model parameters are the rupture length, the rupture azimuth, the rupture velocity, and the rise time.

The source finiteness causes phase delay. Ben-Menahem (1961) introduced the directivity function and showed that radiation of waves is strongly diminished at the periods close to the rupture time. In general the source finiteness diminishes the amplitude of short period waves. Shallow

earthquakes have relatively more short-period energy than deep earthquakes for the fundamental surface waves in the period range concerned. Therefore, the inversion of the spectra which are not corrected for the phase delay or the amplitude effects due to the source finiteness tends to place the centroid at a depth greater than the true depth. In order to determine the depth of large earthquakes from long-period surface waves source-finiteness effects must be corrected using adequate models.

In this study, we used the finite-fault models of the earthquakes of the 1979 Colombia-Ecuador, the 1985 Valparaiso, Chile, and the 1985 Michoacan, Mexico determined by Zhang and Kanamori (1987). For other earthquakes studied here, we first computed $\eta(\omega)$ at various periods from 150 to 300 sec, which measures the observability of the source finiteness at a given period. Except for the 1981 Samoa earthquake, all other earthquakes have largest $\eta(\omega)$ at 256 sec. Therefore, we used the data set of 256 sec period to obtain the finite fault models of these earthquakes. In determining the source-finiteness models of these earthquakes we used the spectra with the amplitudes corrected for the propagation effects using a spherically symmetric model of Q and the group velocity K70.

For earthquakes of relatively small size, such as the 1982 El Salvador and 1981 Playa Azul, Mexico earthquake, the determination of the source directivity is difficult. The finite-fault models of these earthquakes cannot be determined well. However, for these relatively small earthquakes, the difference between the depth obtained using a point source model with finite duration and that using the finite-fault model is very small (less than 5 km). In the following, we estimate the depth of large earthquakes using the finite-fault

Table 2.1 : Epicentral Data for Events Used in This Study

Event	Location	Date	UTC h:m:s	Latitude	Longitude	M_s
1	Colombia-Ecuador	Dec. 12, 1979	07:59:03.3	1.598°N	79.358°W	7.7
2	Santa Cruz Is.	July 17, 1980	19:42:23.2	12.525°S	165.916°E	7.9
3	Samoa	Sept. 1, 1981	09:29:31.5	14.960°S	173.085°W	7.7
4	Playa Azul, Mexico	Oct. 25, 1981	03:22:15.5	18.048°N	102.084°W	7.3
5	El Salvador	June 19, 1982	06:21:58.0	13.313°N	89.339°W	7.0
6	New Ireland	March 18, 1983	09:05:50.0	4.884°S	153.581°E	7.6
7	Chagos Bank	Nov. 30, 1983	17:46:0.6	6.852°S	72.110°E	7.7
8	Valparaiso, Chile	Mar. 3, 1985	22:47:07.3	33.135°S	71.871°W	7.8
9	Michoacan, Mexico	Sept. 19, 1985	13:17:47.3	18.190°N	102.533°W	8.1

model, although the source directivity of some earthquakes cannot be determined with confidence.

2.5 Data

Table 1 lists the hypocentral parameters of nine large earthquakes studied here determined by the National Earthquake Information Center (NEIC). The basic data are spectra at periods from 150 to 300 sec computed from the vertical component Rayleigh waves (R_2 and R_3 phases). The periods used are 150, 175, 200, 225, 256, 275, and 300 sec. The propagation corrections in the phase are made with the laterally heterogeneous earth model (M84C) obtained by Woodhouse and Dziewonski (1984).

2.6 Depth Determination

We determined the source depth of the nine large earthquakes from the spectra of long-period Rayleigh waves using the methods described above. We inverted the spectra corrected for the source finiteness for a moment tensor or a double couple to determine the depth which minimizes the error in the inversion.

We used various Q models and excitation functions discussed above. For the purpose of illustrating the method, we used the simplest combination, K70 Q model and excitation functions computed for model 5.08M. This combination is denoted by (K70, 5.08M). In order to see the effect of Q model and excitation functions on the depth, we tried different combinations which are

denoted in a similar fashion.

2.6.1 1979 Colombia-Ecuador Earthquake

The December 12, 1979 earthquake occurred near the coast of Ecuador and caused an extensive damage in the Pasto-Tumaco-Buenaventura area and on Gergona island, Colombia. The earthquake was located about 80 km landward from the Colombia trench. It is a very large thrust event which occurred at the boundary between the subducting Nazca plate and the overriding South America plate. The earthquake caused large tsunamis three meters (peak-to-peak) high along the Colombia coast and extensive subsidence up to 1.6 m along a 200 km long segment along the coast (Herd et al., 1981). This indicates that the depth of the earthquake is shallow.

The aftershocks of the earthquake are distributed from the depth of a few km to about 35 km (Mendoza and Dewey, 1984). The hypocenter of the main shock was determined at the depth of 29 km by ISC (International Seismological Center), and 24 km by NEIC. Mendoza and Dewey (1984) pointed out that the depth phases in the complex P-wave trains of the earthquake cannot be identified with confidence, but the data from regional stations permitted the determination of the focal depth of 37.5 km with a precision of about 19 km by using only P-wave arrival-time data.

The Centroid-moment-tensor solution of the earthquake obtained by Giardini et al. (1985) has a depth of 20 km. Romanowicz and Guillemant (1984) estimated the centroid depth of the earthquake in the range from 0 to 30 km for the assumed source time $\tau = 60$ to 75 sec using long-period

Rayleigh waves. Silver and Jordan (1983) estimated the depth of the earthquake to be about 29 km.

We determined the delay time and source-process time of the earthquake to be 58 and 118 sec respectively from long-period Rayleigh waves. The source directivity of the earthquake is represented by an unilateral rupture of 256 km long with a rupture velocity of 2.5 km/sec to $N31^{o}E$ and the ratio of rise time to rupture time $\gamma = 0.1$ (Zhang and Kanamori, 1987). We inverted the spectra corrected for the source-finiteness at the periods of 150, 175, 200, 225, 256, 275, and 300 sec to determine $D(\omega)$ by solving (11). Then, for each trial depth, we inverted (13) for a moment tensor or a double couple. We determined the depth of the moment tensor or double couple which minimizes the error in the inversion.

In calculating the amplitude spectrum of $\hat{V}$ from the observed spectrum, values of group velocities and Q are required. The inversion of (13) is made with excitation functions computed for a given earth model. Since the Colombia-Ecuador earthquake is the largest among the earthquakes studied here, we determined its depth using various models of the source finiteness, the wave propagation, and the excitation. First, we examined the effects of the source-finiteness model on the depth determination using the combination (K70, 5.08M).

Figure 3 shows the *rms* error in the moment tensor inversion as a function of the assumed centroid depth for various source finiteness models for the Colombia-Ecuador earthquake. The minimum of each error curve gives the estimate of the centroid depth for each model. There are significant differences between the estimates of the depth for different source-finiteness

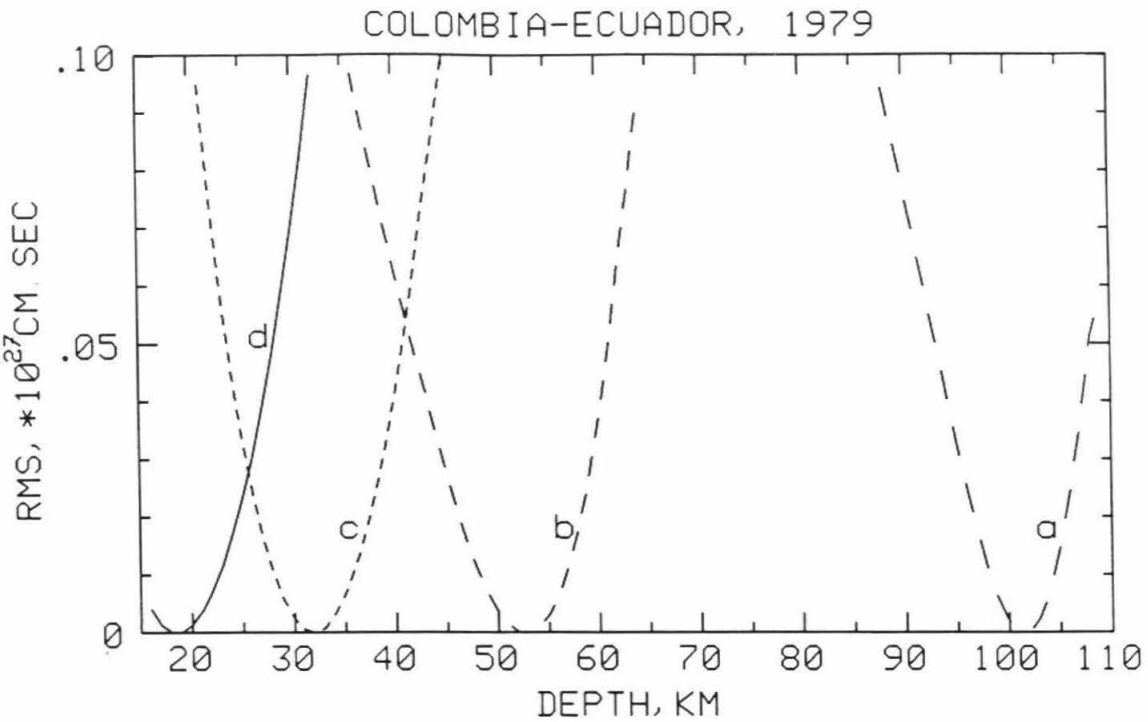

Figure 2.3 Colombia-Ecuador earthquake. Residual versus depth curves by the moment tensor inversion are given for four different source finiteness models: (a) step-function point source; (b) constant time delay, $\tau_d = 58$ sec; (c) point source with finite duration, $t_s = 118$ sec, $\tau = t_f / 10$; (d) finite-fault model, L = 256 km, v = 2.5 km/sec, $\phi_f = 31^o$, $\tau = 0.1 \times L/v$. The models K70 and 5.08M are used for attenuation and excitation respectively. Each curve is plotted relatively to its minimum.

models. The point source model has the largest depth, 102 km. The estimates of the depth for the models of the time delay and the point source with finite duration are 53 and 32 km respectively.

For other earthquakes, we also made comparison between the estimates of the depth for these different source-finiteness models. For all the earthquakes studied here the inversion places the centroid at the largest depth for the point source model, and places the centroid for the time delay model at a depth larger than that for the point source model with finite duration.

For the Colombia-Ecuador earthquake, the centroid depth was determined at 19 km for the finite-fault model (Figure 3), which is significantly shallower than that for the point source model of finite duration. For other earthquakes no systematic difference between the depths obtained for the two models was found.

Figures 4a and 4b show the *rms* versus centroid-depth curves for the finite-fault model from the moment tensor inversion and fault inversion respectively. The estimates of the depth obtained from the two methods are the same, 19 km. The estimate is consistent with the depth of the Centroid-Moment-Tensor solution obtained by Giardini et al. (1985).

Since the earthquake generated a large tsunami and an extensive subsidence on the coast of the Colombia, the rupture of the earthquake may have reached the surface. Using the excitation functions computed by Kanamori and Given (1981) for the distributed source with uniform dislocation extending from the surface to a certain depth, we inverted the data for the moment tensor and double couple to determine the depth extent of the faulting. The estimates of the depth extent is 30 km from the moment tensor inversion, and 33

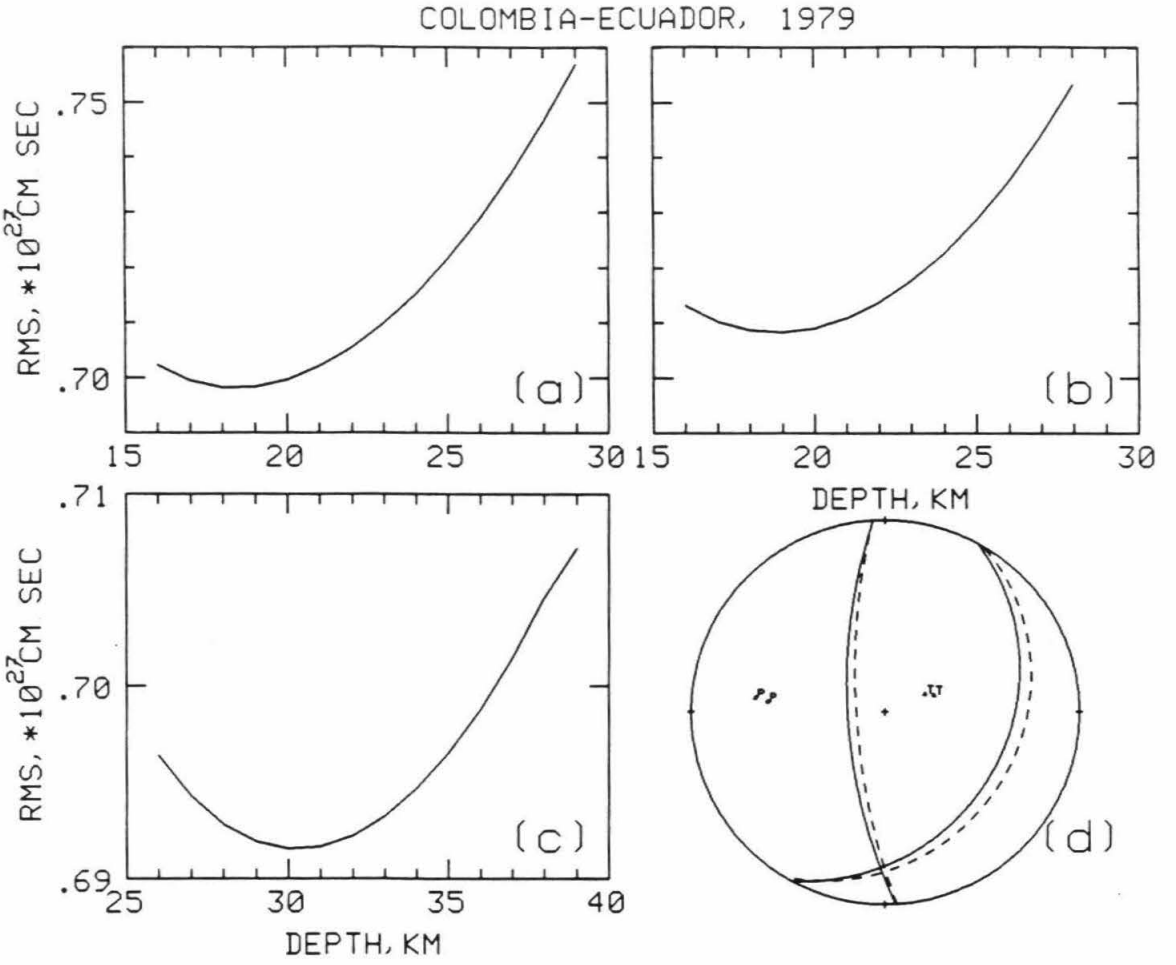

Figure 2.4 Colombia-Ecuador earthquake. Residual versus depth curves are given for the finite-fault model. (a) point source (centroid) by the moment tensor inversion; (b) point source (centroid) by the fault inversion; (c) distributed source by the moment tensor inversion; (d) the mechanism of the major-double couple listed in Table 2 (solid line) is compared to the model (4) of Kanamori and Given (1981) (dash line). The models K70 and 5.08M are used.

km from the fault inversion. Figure 4c shows the the *rms* versus depth-extent curve from the moment tensor inversion, which has a minimum at 30 km.

Table 2 lists the moment tensor solution for the centroid depth at 19 km, which is essentially a pure double couple. In Figure 4d, the major double couple of the moment tensor is compared with the solution of model (4) of Kanamori and Given (1981). Our results agree well with theirs. Table 3 lists the fault solution, which indicates thrust faulting toward the east with a small right lateral strike-slip component and a scalar moment $M_o = 14.1 \times 10^{27} dyne.cm$. The fault plane extended from the surface to about 33 km deep with the centroid at a depth of 19 km.

We now examine the effect of various models of the wave propagation and excitation on the depth estimate of the earthquake. Figure 5 shows the *rms* errors in the moment tensor inversion for several models of the group velocity, Q, and the excitation function for the depth range from 10 to 30 km with the source-finiteness effects corrected using the finite-fault model.

Figure 5a shows the results for different models of Q using the excitation functions computed for 5.08M. We used three models of Q, K70, PREM, and D-S. The estimate of the depth obtained using K70 is deeper than that using PREM and D-S.

Figure 5b shows the results for different models of excitation functions using D-S for Q. We used three models of excitation functions, 5.08M, PREM, and R-A. The PREM model gives a deeper depth than 5.08M and R-A.

Figure 5c shows the results for three combinations of models: (K70, 5.08M), (PREM, PREM), and (D-S, R-A). The depth obtained with the last model is 11 km.

Table 2.2 : Results by moment tensor inversion with (K70, 5.08M).

Event	Location	Depth (km)	M_{xy}	$M_{yy}-M_{xx}$	$M_{yy}+M_{xx}$	M_{yz}	M_{xz}	Major double couple							m_o/M_o
								M_o	δ_1	λ_1	ϕ_1	δ_2	λ_2	ϕ_2	(%)
1	Colombia-Ecuador	19	-2.5 ±0.2	-9.6 ±0.4	-10.3 ±0.2	10.4 ±2.7	-2.1 ±2.7	15.2	25.1	119.5	28.6	68.3	77.0	176.6	5
2	Santa Cruz Is.	41	1.6 ±0.2	-5.7 ±0.3	-6.1 ±0.2	2.8 ±0.3	0.3 ±0.3	6.9	34.0	76.6	337.8	57.0	98.9	173.8	1
3	Samoa	19	-0.76 ±0.1	-2.18 ±0.2	1.74 ±0.1	-0.02 ±0.6	2.33 ±0.6	3.2	70.5	258.2	93.5	22.7	300.1	205.7	10
4	Playa Azul, Mexico	43	0.18 ±0.01	0.50 ±0.02	-0.76 ±0.02	0.27 ±0.02	-0.42 ±0.02	0.92	28.4	78.0	282.0	62.2	96.4	115.5	9
5	El Salvador	52	-0.40 ±0.03	-1.15 ±0.05	1.14 ±0.03	0.46 ±0.03	-0.45 ±0.03	1.4	59.1	285.1	300.9	34.0	246.4	93.2	5
6	New Ireland	77	3.6 ±0.2	-3.9 ±0.5	-5.9 ±0.4	-0.6 ±0.1	1.8 ±0.1	7.2	40.3	110.1	162.2	52.6	73.7	316.6	12
7	Chagos Bank	36	-0.9 ±0.1	-6.0 ±0.2	6.0 ±0.1	-1.3 ±0.2	4.5 ±0.2	7.7	63.9	274.1	103.3	26.4	261.7	270.0	2
8	Valparaiso, Chile	48	-0.21 ±0.3	-7.3 ±0.6	-9.4 ±0.4	8.2 ±0.5	-0.5 ±0.5	12.6	23.7	95.4	4.2	66.4	87.6	178.3	8
9	Michoacan, Mexico	30	2.2 ±0.1	4.5 ±0.3	-7.1 ±0.2	-1.2 ±0.4	-5.1 ±0.4	9.2	30.8	119.1	306.2	63.4	73.9	93.2	13

Moment tensor is in units of 10^{27} dyne.cm; M_o and m_o are the scalar moments of the major double couple and minor double couple respectively; depth is for the centroid; δ_1 is the dip, λ_1 the rake, and ϕ_1 the strike in degree.

Table 2.3 : Results by fault inversion with (K70, 5.08M).

Event	Location	Depth(km)	M_o	δ	λ	ϕ
1	Colombia-Ecuador	19	14.1±1.6	25.4±3.9	107.7±6.3	23.3±3.7
2	Santa Cruz Is.	41	6.8±0.2	34.1±1.4	76.2±4.2	337.5±3.2
3	Samoa	17	3.4±0.7	74.2±3.8	252.8±4.3	83.3±3.0
4	Playa Azul, Mexico	42	0.87±0.02	27.6±0.9	79.6±3.7	282.8±2.8
5	El Salvador	51	1.4±0.03	59.7±0.8	285.9±1.6	301.8±1.5
6	New Ireland	78	7.1±0.3	40.1±0.7	106.1±2.1	159.6±2.9
7	Chagos Bank	36	7.6±0.2	63.9±0.8	274.5±3.3	103.7±2.3
8	Valparaiso, Chile	44	12.1±0.5	21.1±1.1	95.2±5.9	3.9±4.8
9	Michoacan, Mexico	30	8.3±0.4	29.3±2.0	107.6±5.6	301.3±3.7

M_o is the scalar moment($\times 10^{27}$ dyne.cm), δ the dip, λ the rake, and ϕ the strike.

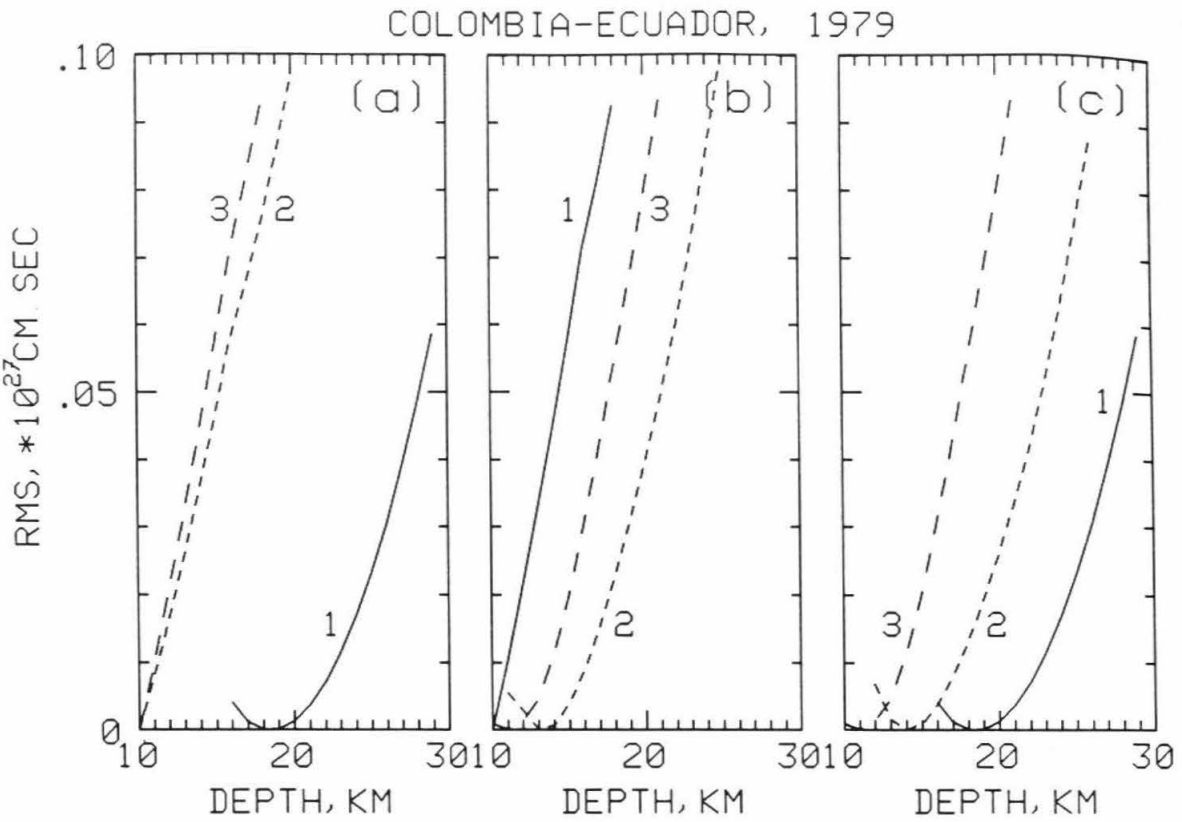

Figure 2.5 Colombia-Ecuador earthquake. Residual versus depth curves by the moment tensor inversion are given for the finite-fault model for verious models of Q, the group velocity, and the excitation. (a) the model 5.08M is used for the excitation and K70 (1), PREM (2), D-S (3) for Q and the group velocity. (b) the model D-S is used for Q and the group velocity and 5.08M (1), PREM (2), R-A (3) for the excitation. (c) the models D-S and R-A (1), PREM (2), and K70 and 5.08M (3) are used for attenuation and excitation. Each curve is plotted relatively to its minimum.

As we have illustrated above, the depth estimate depends on the choice of the source finiteness model, Q model, and excitation functions. For the 1979 Colombia-Ecuador earthquake, if we used the most reasonable source finiteness model, we obtained a range of 10 to 20 km for the estimate of the centroid depth. For a very shallow depth (e.g. less than 15 km), the inversion becomes unstable (Kanamori and Given, 1981). The results obtained above indicate that the centroid depth of the Colombia-Ecuador earthquake is shallower than 20 km. In Table 4, the result obtained for (D-S, R-A) with a fixed dip angle of 15^o is listed.

From the dip angle (25^o), the depth extent (33 km), and the rupture length (256 km), we calculated the width and the area of the fault: $W = 70km$, $A = 2 \times 10^4\ km^2$. Using the rigidity $\mu = 5 \times 10^{11} dyne/cm^2$, we have the average dislocation $\bar{D} = M_0/\mu A \sim 1.4m$, and the stress drop $\Delta\sigma = 8\mu\bar{D}/3\pi W \sim 8$ bars for a scalar moment $M_0 = 14 \times 10^{27} dyne.cm$.

2.6.2 1980 Santa Cruz Is. Earthquake

The July 17, 1980 Santa Cruz Is. earthquake occurred in the northern region of the New Hebrides island arc. The arc extends from latitude $11^o\ S$ to $21^o\ S$ and forms a part of the boundary between the Pacific and Australian plates. To the west of the Santa Cruz volcanic chain, the northern New Hebrides trench is well-developed with a strike of $N20^o\ W$. The earthquake is located to the east of, and very close to, the trench axis, where the oceanic trench starts to bend westward. The CMTS depth of the earthquake is 34 km. In this region the Australian plate moves $N75^o\ E$ with respect to the Pacific

Table 2.4 : Results by moment tensor inversion with (D-S, R-A).

Event	Location	Depth (km)	M_{xy}	$M_{yy}-M_{xx}$	$M_{yy}+M_{xx}$	M_{yz}	M_{xz}	Major double couple M_o	δ_1	λ_1	ϕ_1	δ_2	λ_2	ϕ_2	m_o/M_o (%)
1	Colombia-Ecuador	11	-	-	-	-	-	21.4	15.0	60.0	358.0	77.5	97.6	208.8	-
			-	-	-	-	-								
2	Santa Cruz Is.	36	1.5	-5.8	-5.5	3.3	0.2	6.8	31.6	73.1	336.0	59.9	100.1	175.6	6
			±0.2	±0.3	±0.2	±0.3	±0.3								
3	Samoa	15	-0.78	-2.26	1.61	-0.01	4.9	5.4	80.0	261.9	90.8	12.8	308.7	310.2	6
			±0.1	±0.2	±0.1	±1.3	±1.3								
4	Playa Azul, Mexico	41	0.18	0.52	-0.71	0.28	-0.44	0.89	27.4	75.7	280.0	63.5	97.3	116.0	5
			±0.01	±0.02	±0.02	±0.02	±0.02								
5	El Salvador	49	-0.41	-1.17	1.04	0.48	-0.47	1.4	60.7	286.9	302.6	33.4	242.6	90.8	7
			±0.03	±0.05	±0.03	±0.03	±0.03								
6	New Ireland	75	3.5	-4.0	-6.0	-0.6	1.7	7.2	40.4	109.2	162.4	52.3	74.3	317.8	11
			±0.2	±0.5	±0.4	±0.1	±0.1								
7	Chagos Bank	31	-1.0	-6.0	5.3	-1.6	5.5	8.3	68.1	274.6	104.4	22.4	258.7	272.3	5
			±0.1	±0.2	±0.1	±0.3	±0.3								
8	Valparaiso, Chile	44	-0.14	-7.5	-8.6	9.3	-0.5	12.8	21.0	95.2	3.6	69.1	88.0	178.1	5
			±0.3	±0.6	±0.4	±0.5	±0.5								
9	Michoacan, Mexico	24	2.2	4.5	-6.3	-1.8	-7.5	10.5	24.4	128.9	308.4	71.2	74.0	86.8	12
			±0.1	±0.3	±0.2	±0.4	±0.4								

Same as Table 2, except for the model of Q, the group velocity, and the excitation, which are from Dziewonski and Steim (1982), Nakanishi and Anderson (1984), and Regan and Anderson (1984), respectively.

plate (Le Pichon, 1968; Chase, 1971; Molnar and Sykes, 1971; Johnson and Molnar, 1972). The focal mechanisms of the large New Hebrides events that occurred through 1970 to the north of 16^{o} latitude show shallow thrust faulting with a consistent east-northeast slip vector (Johnson and Molnar 1972).

The July 17, 1980 ($M_s = 7.9$) earthquake occurred about 50 km away to the west of the epicenter of the July 8, 1980 ($M_s = 7.5$) earthquake. The aftershocks of the two earthquakes are not clearly distinguishable. From the NEIC PDE report, the aftershocks between July 8 and July 17 are distributed to the south of the epicenter of the July 8 earthquake; however, after the July 17 earthquake most of the aftershocks occurred to the north of the epicenter of the July 17 earthquake. The aftershocks after the July 17 earthquake are distributed in an area of about 120 km long, and the aftershock area did not expand significantly. The close location of the two large earthquakes and the abrupt change of the location of the seismic activity before and after the July 17 event suggest that both of the July 8 and July 17 events initiated from almost the same site, but the first event ruptured to the south and the second rupture to the north. We considered the aftershock area of the July 17 event to be about 120 km long to the north, which is consistent with the analysis of the 1980 earthquake sequence of Tajima et al. (1987).

We determined the rupture length and azimuth of the July 17 earthquake. The inversions of the spectra indicate that the rupture of the earthquake is unilateral to the north of the epicenter. Figures 6a and 6b show the rupture length and the rupture azimuth estimated for various ratio of the rise time, τ, to rupture time, t_f , ($\gamma = \tau / t_f$) and several rupture velocities V respectively. Using $V = 2$ km/s and $\gamma = 0.5$, the estimates of the rupture

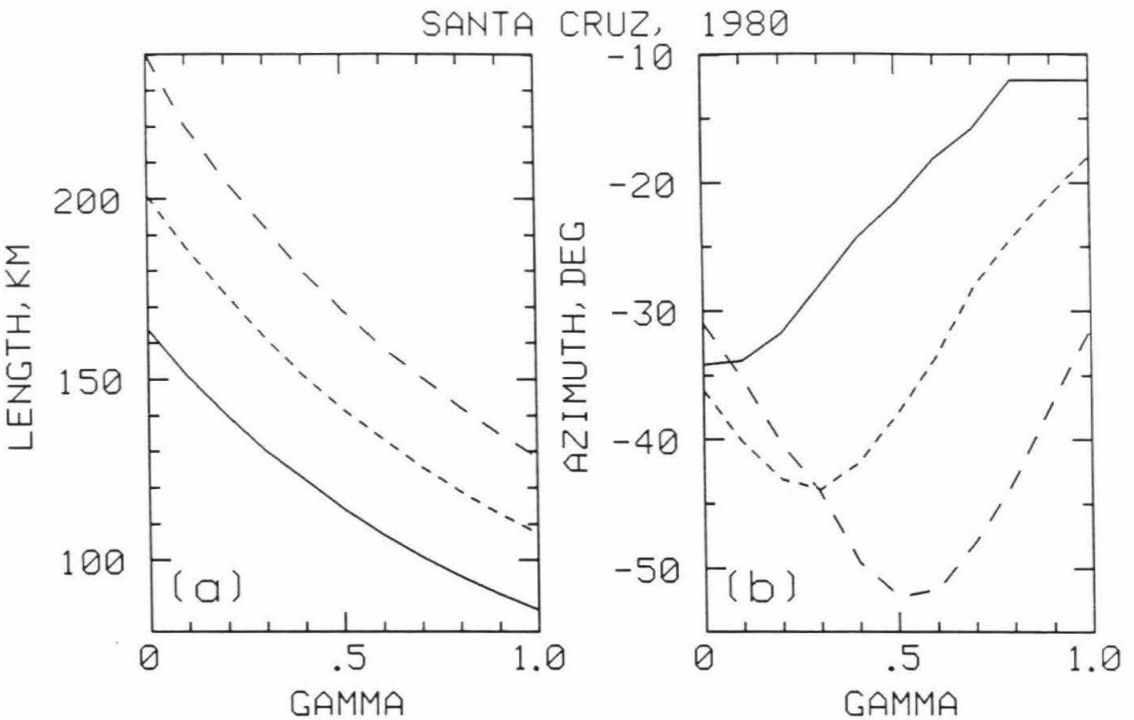

Figure 2.6 Santa Cruz earthquake. The rupture parameters as functions of the ratio γ for the rupture velocities of 2 (real line), 2.5 (dash line), and 3 (dot line) km/sec. The inversion is at the period of 256 sec. (a) The rupture length. The rupture is assumed to be unilateral toward the north. (b) The rupture azimuth. The rupture is assumed to be unilateral with a length of 120 km.

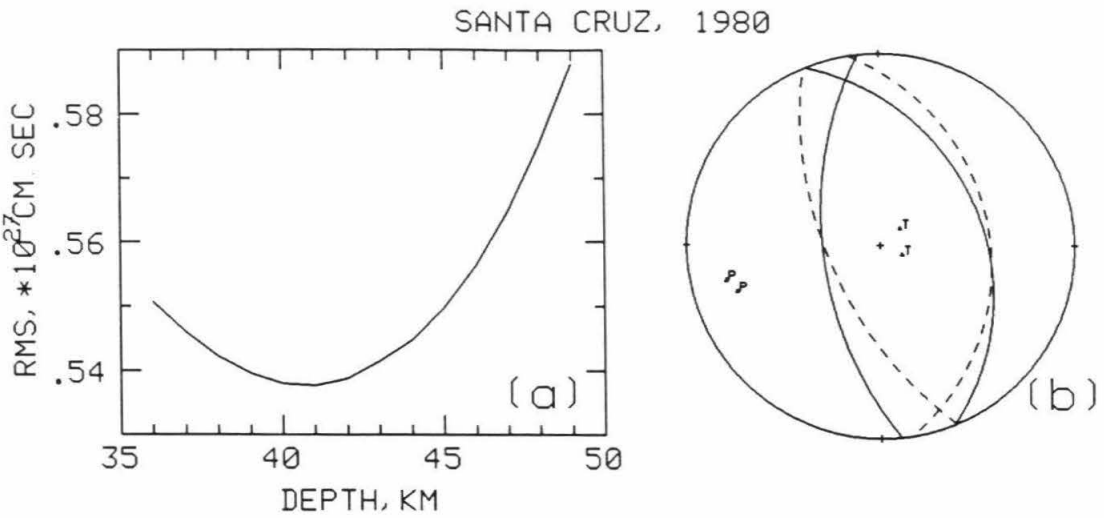

Figure 2.7 Santa Cruz earthquake. (a) Residual versus depth curves by the moment tensor inversion are given for the finite-fault model obtained. (b) The source mechanism of the major double couple listed in Table 2 (solid line) is compared to the Harvard CMTS (dash line).

length and the rupture azimuth are 114 km and $N22^{o}\ W$ respectively. These estimates are consistent with the aftershock area and the strike of the trench.

We used this rupture model in the determination of the depth of the earthquake. Although these estimates are subject to errors due to the uncertainties in V and γ, we found that using other estimates obtained for different V and γ did not significantly change the estimate of the depth. Figure 7a shows the *rms* versus centroid-depth curve for the moment-tensor inversion using (K70, 5.08M). The moment-tensor solution is listed in Table 2, which is almost a pure double couple.

The depth estimates obtained for other combinations of Q models and excitation functions are summarized in Figures 8 and 9. The results obtained for (K70, 5.08M) and (D-S, R-A) are listed in Tables 2, 3 and 4.

There is no evidence that the earthquake broke the surface. Since the minimum errors in the inversion for a centroid source does not significantly differ from that for an extended source, whether the earthquake broke the surface or not cannot be determined from the analysis of long-period surface waves.

Kanamori and Given (1982) used IDA data and found the dip angle of the earthquake to be about 33^{o} for the source depth of 33 km. Nakanishi and Kanamori (1984) used the P-wave first motion data, which permit the dip of one of the nodal planes to vary from 38^{o} to 55^{o}, to constrain the dip of one nodal plane ($\delta = 52^{o}$) and found the dip angle of another plane to be 38^{o} for the source depth at 33 km. In Figure 7b, the major double couple determined with (K70, 5.08M) is compared with the major double couple of the CMTS. Our solution is consistent with CMTS. The best double couple of CMTS has a

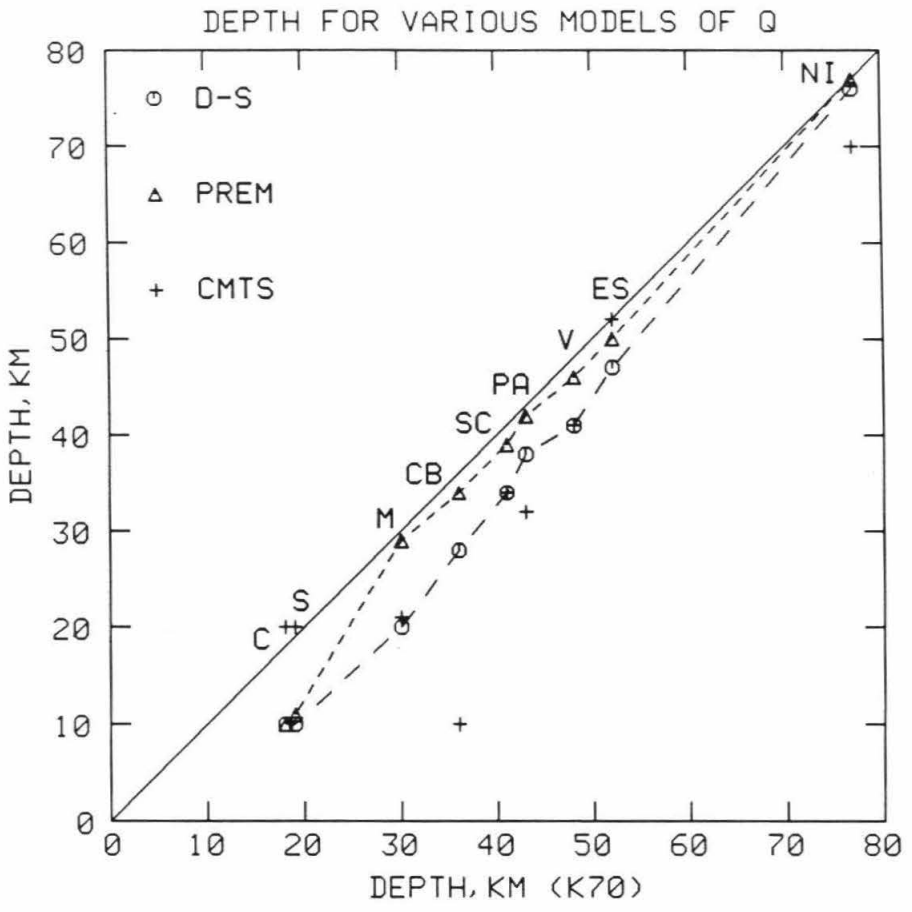

Figure 2.8 The depths obtained by the moment tensor inversion with various Q models using the excitation functions computed for 5.08M. The earthquakes are Colombia-Ecuador (C), Santa Cruz Is. (SC), Samoa (S), Playa Azul, Mexico (PA), El Salvador (ES), New Ireland (NI), Chagos Bank (CB), Valparaiso, Chile (V), and Michoacan, Mexico (M). The depths for D-S (circles) and PREM (triangles) and the CMTS (crosses) depths are plotted versus the depth for K70.

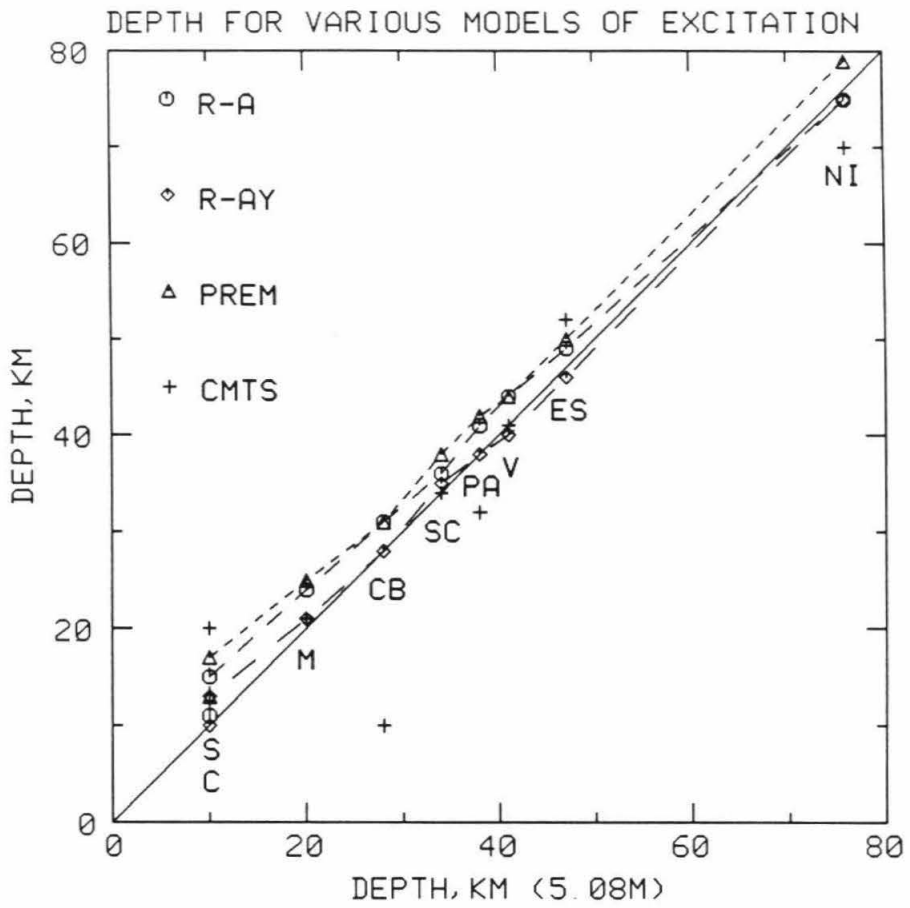

Figure 2.9 The depths obtained by the moment tensor inversion with various models of excitation functions using the D-S Q model. The excitation functions are for the models of 5.08M (solid line); PREM (triangles); R-A (circles); and R-AY (diamonds). The depths of Harvard CMTS are shown by crosses. The depths obtained are plotted versus the depth for the model 5.08M for each earthquake.

dip angle of 31^o for the nodal plane dipping to the east. Our moment-tensor solution determined with the various combinations of Q and excitation functions has a centroid depth ranging from 36 to 41 km and a dip angle of the nodal plane ranging from 30^o to 34^o. These results are consistent with the results of other studies.

We also estimated the depth using a point source model with 88 sec duration determined by Zhang and Kanamori (1987); we obtained a centroid depth of 33 km by the moment tensor inversion and by the fault inversion with (K70, 5.08M).

2.6.3 1981 Samoa Earthquake

The September 19, 1981 Samoa Islands earthquake occurred in the northernmost region of the Tonga Island arc between the arc and the trench. In this region the trench abruptly bends westward from $N20^o E$ to $N70^o W$, and shallow earthquakes often clustered. Isacks et al. (1969) found that the shallow earthquakes have steeply dipping E-W-striking fault planes and reflect primarily downward motion of the part of the Pacific plate subducting under the Tonga Islands with respect to the Pacific plate to the north of the Tonga trench (Samoa Islands). The shallow earthquakes are considered to result directly from the relative motion of the two parts of the Pacific plate.

The aftershocks of the earthquake reported from NEIC PDE report are distributed in a zone of about 110 km long extending to *SSE*. The epicenter of the main shock is close to the northern end of the aftershock area.

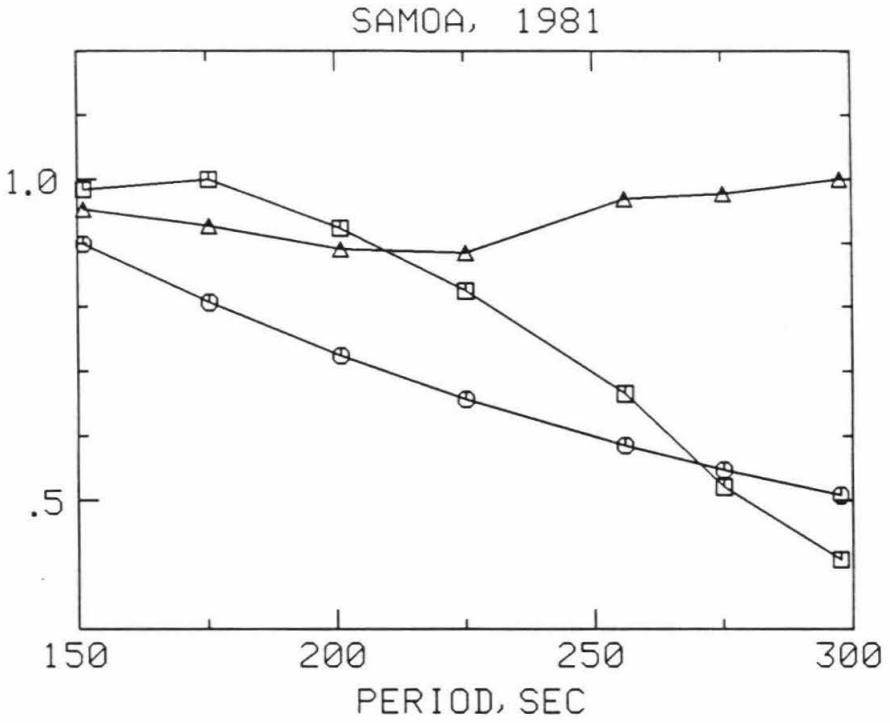

Figure 2.10 Samoa earthquake. $\overline{V}(\omega)$ (triangles), $\overline{S}(\omega)$ (circles), and $\eta(\omega)$ (squares) at various periods.

In determining the source-process time of the earthquake, the errors in the inversion at the periods of 256, 275, and 300 sec are larger than that at the periods of 150, 175, 200, and 225 sec (Zhang and Kanamori, 1987). We assumed that the rupture was in $S\,25^{o}\,E$ direction (L_1 direction) parallel to the aftershock area to estimate the rupture length of the earthquake. Results indicate that the rupture is unilateral in this direction. We estimated the rupture length using the inversion at the periods of 150, 175, 200, 225, 256, 275, and 300 sec separately. The minimum errors obtained at the periods of 256, 275, and 300 sec are larger than those obtained at other periods. This indicates that the source finiteness of the earthquake cannot be determined well from the data at these periods. We compared the observability of the source-finiteness of the earthquake at these periods.

Figure 10 shows the curves of the average of observed amplitude spectrum $\overline{V}(\omega)$, the magnitude of the source finiteness effect $\overline{S}(\omega)$, and the observability of the source-finiteness $\eta(\omega)$ versus period. In the figure the maxima of $\overline{V}(\omega)$ and $\eta(\omega)$ are normalized to 1 in the period range. The source-finiteness effect is calculated using an unilateral rupture of 110 km long along L_1 direction with a rupture velocity of 2.5 km/sec. The $\overline{V}(\omega)$ at long periods is about the same as, or slightly larger than, that at short periods. This is different from $\overline{V}(\omega)$ for the Akita-Oki, Colombia-Ecuador, Valparaiso, Michoacan, and Sumbawa earthquakes, which decreases as the period exceeds 256 sec (Zhang and Kanamori, 1987). For the Samoa earthquake, the minimum error for the inversion at short periods is smaller than that at long periods, and the magnitude of the source-finiteness effects at short period is larger than at long periods. The overall observability of the source-finiteness

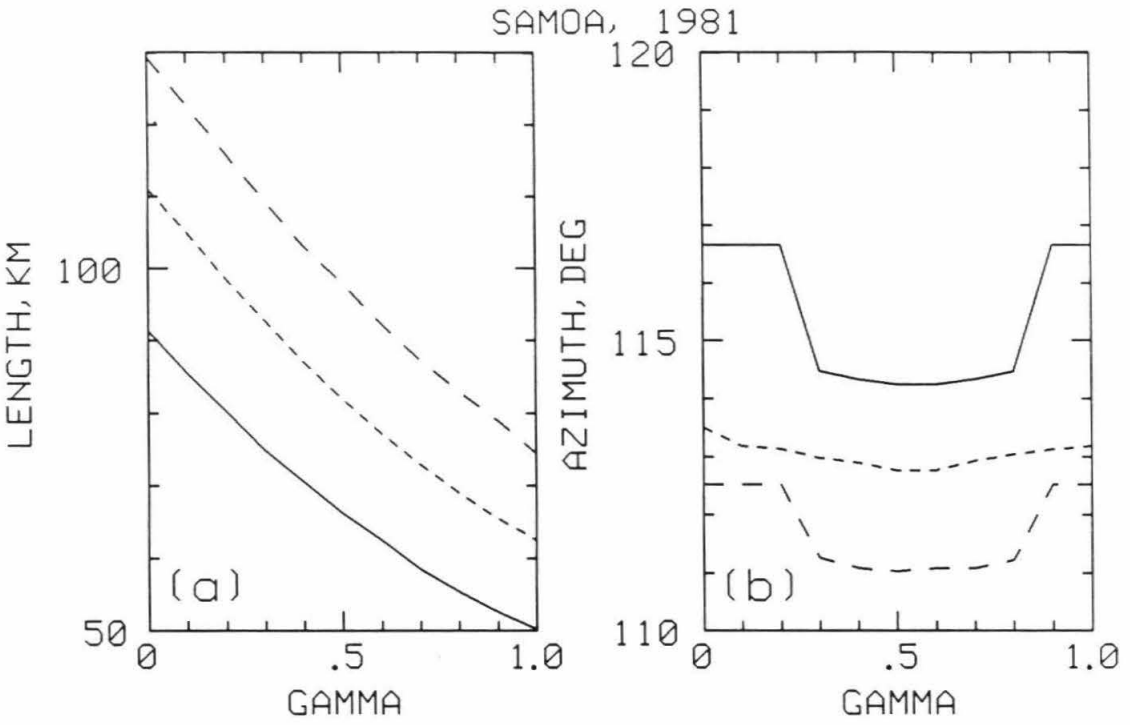

Figure 2.11 Samoa earthquake. The rupture parameters as functions of the ratio γ for the rupture velocities of 2 (real line), 2.5 (dash line), and 3 (dot line) km/sec. The inversion is at the period of 175 sec. (a) The rupture length. The rupture is assumed to be unilateral toward $S25^{o}E$. (b) The rupture azimuth. The rupture is assumed to be unilateral with a length of 110 km.

at short periods becomes larger than at long periods. In Figure 10 $\eta(\omega)$ is largest at 175 sec. Therefore, we used the data set of 175 sec period to estimate the source finiteness of the earthquake.

Figures 11a and 11b show the rupture length and rupture azimuth versus γ curves respectively for rupture velocities V = 2, 2.5, and 3 km/sec. For V = 2.5 km/sec and $\gamma = 0.1$ the estimates of the rupture length and the rupture azimuth are 107 km and 113^o respectively, which are consistent with the aftershock area.

In determining the depth, we used an unilateral rupture of 107 km long with a rupture velocity of 2.5 km/sec in the azimuth of 113^o and $\gamma = 0.1$. Figure 12a shows the *rms* error versus centroid depth curve obtained by the moment tensor inversion (with (K70, 5.08M)), which indicates a 19 km depth of the centroid. The moment tensor solution for the depth of 19 km has a scalar moment of $3.2\times10^{27} dyne.cm$ and normal-fault mechanism for the major double couple. The centroid depth estimated by the fault inversion is 17 km (Figure 12b). Figure 12c shows the *rms* error versus depth extent curve obtained by the moment tensor inversion, which indicates that the depth extent is 30 km.

Figure 12d compares the mechanism of the major double couple of the moment tensor solution for the centroid depth of 19 km with the P-wave first motion mechanism reported by NEIC. If the nodal plane dipping toward the south is the fault plane, the fault motion reflects that the southern part of the Pacific plate is sliding down with respect to the northern part on a plane steeply dipping to the south. The rupture of the earthquake, unilateral toward the east, suggests that the Pacific plate to the south of the epicenter is tearing

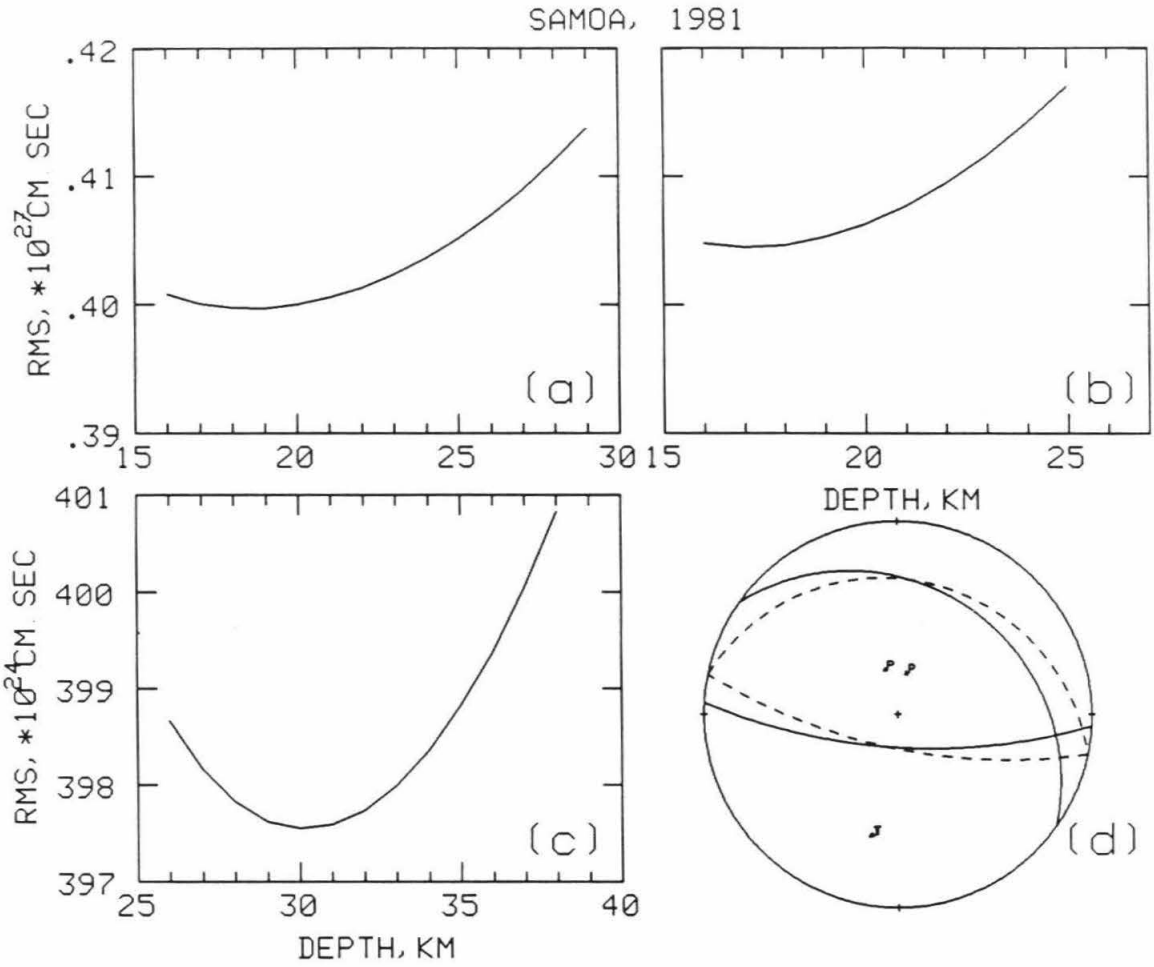

Figure 2.12 Samoa earthquake. Residual versus depth curves by the moment tensor inversion are given for the finite-fault model obtained. (a) Point source (centroid) by the moment tensor inversion; (b) Point source (centroid) by the fault inversion; (c) Distributed source by the moment tensor inversion; (d) The source mechanism of the major double couple listed in Table 2 (solid line) is compared to the Harvard CMTS (dash line).

off from the surfacial part of the Pacific plate to the north, because of the collision of the Pacific plate and the Australian plate.

We also estimated the depth using a point source model with 45 sec duration determined by Zhang and Kanamori (1987); we obtained a centroid depth of 22 km by the moment tensor inversion and of 20 km by the fault inversion with (K70, 5.08M).

The depth estimates obtained for various combinations of Q models and excitation functions are summarized in Figures 8 and 9. The results obtained for (K70, 5.08M) and (D-S, R-A) are listed in Tables 2, 3 and 4.

2.6.4 1981 Playa Azul, Mexico Earthquake

This earthquake ($M_s = 7.3$) occurred in the center of the Michoacan gap about 40 km to the south of the epicenter of the 1985 ($M_s = 8.1$) earthquake (Havskov et al., 1983; UNAM seismology group, 1986). The depth of CMTS for this earthquake is 32 km. Astiz et al. (1987) obtained a depth of 27 km from modeling of WWSSN long-period P-waves.

Aftershocks were recorded by a portable array operated in the epicentral area for 6 days starting 19 hours after the main shock. They are clustered in two groups, one on the northeast and the other on the northwest of the main shock epicenter (Havskov et al., 1983). Some aftershocks are as deep as 26 km. The aftershocks recorded by the array during the 6-day period with a coda duration more than 30 sec are distributed in an area of about 40 km long in the E-W direction parallel to the trench. Since the main shock location (determined from readings of 13 stations within distances less than 450 km

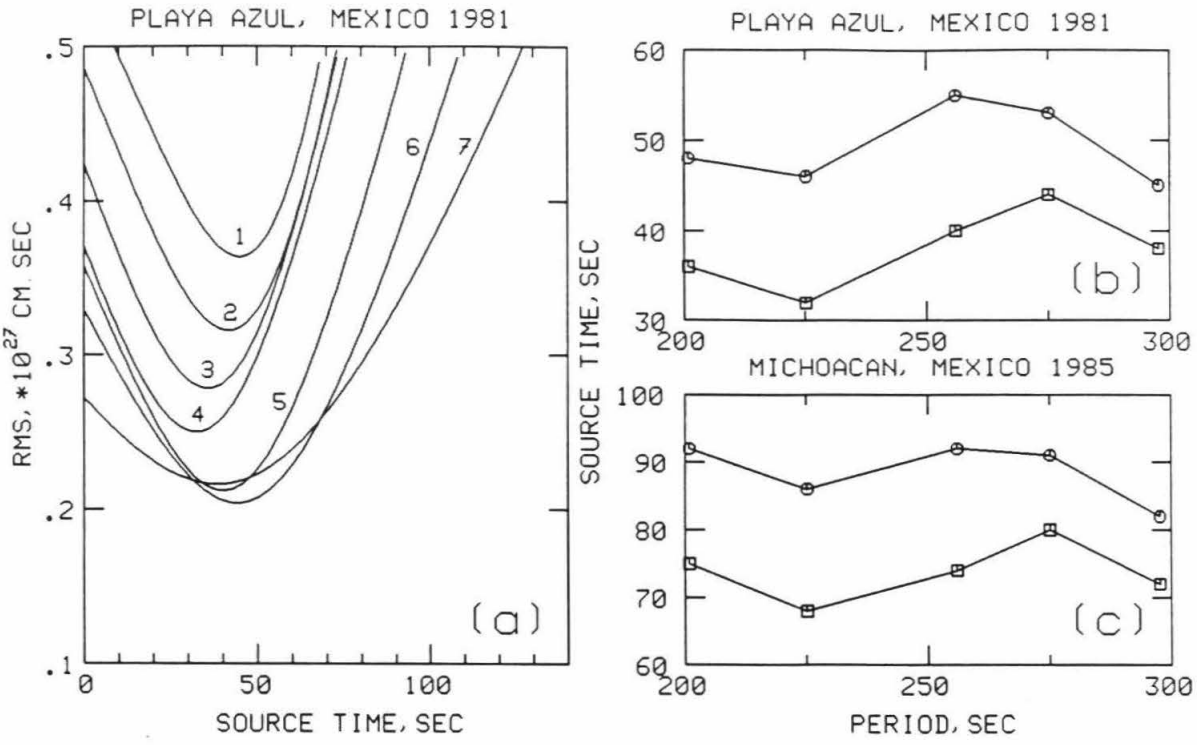

Figure 2.13 (a) Playa Azul, Mexico earthquake. The *rms* error plotted versus trial source-process time for the inversion at the periods of (1) 150, (2) 175, (3) 200, (4) 225, (5) 256, (6) 275, and (7) 300 sec respectively. The time corresponding to the minimum error on each curve is taken as the source-process time measured at that period. (b) Comparison of the estimated source-process times of the Playa Azul, Mexico earthquake measured at the periods of 200, 225, 256, 275, and 300 sec by the inversion method for two phase velocity models; phase velocity is calculated (1) from the average observed normal-mode periods compiled by Gilbert and Dziewonski (1975) (triangles), (2) from a laterally heterogeneous earth model (M84C) obtained by Woodhouse and Dziewonski (1984) (squares). (c) Comparison of the estimated source-process times of the Michoacan, Mexico earthquake for the two phase velocity models.

from the epicenter) is less reliable than that of the aftershocks, the relationship between the main shock location and the aftershock area is not clear.

We used fifty-two Rayleigh wave phases R_1 and R_2 or R_2 and R_3 recorded at IDA and GDSN stations (R_1 and R_2: SPA, SUR, GRFO, GUMO, NWAO, SNZO, TATO, CTAO, KONO, SLR; R_2 and R_3: CMO, KIP, BDF, ERM, ESK, GUA, PFO, RAR, SSB, TWO, ANMO, BOCO, MAJO, JAS, SCP; R_2 only: LON; R_3 only: NNA). We computed the spectra of these wave trains and determined the source process time of the earthquake using the linear inversion method of Zhang and Kanamori (1987). Figure 13a shows the *rms* error of the inversion for various source-process times in the range of 0 to 140 sec for periods from 150 to 300 sec. The spectral data used here are corrected for the propagation phase delay with the model M84C. We obtained a source process time of 42 sec, which is the average of the estimates at the periods of 256 and 275 sec. The source process time is at least twice as long as the rupture time inferred from the aftershock area.

We also used a homogeneous model (HOM) of phase velocities (Kanamori and Given, 1981) to correct for the phase delay and obtained the source process time. Figure 13b shows the source-process times obtained for the models M84C and HOM from inversions at periods from 200 to 300 sec. The model HOM gives estimates 10 sec or more longer than the model M84C. Note that for the 1985 Michoacan, Mexico earthquake similar results were obtained by Zhang and Kanamori (1987) (Figure 13c).

We used $\gamma = 1$ and V = 2 km/sec to estimate the rupture length and the rupture azimuth of the earthquake. If we assumed that the rupture was bilateral, the inversion gives a total rupture length of 80 km in the direction

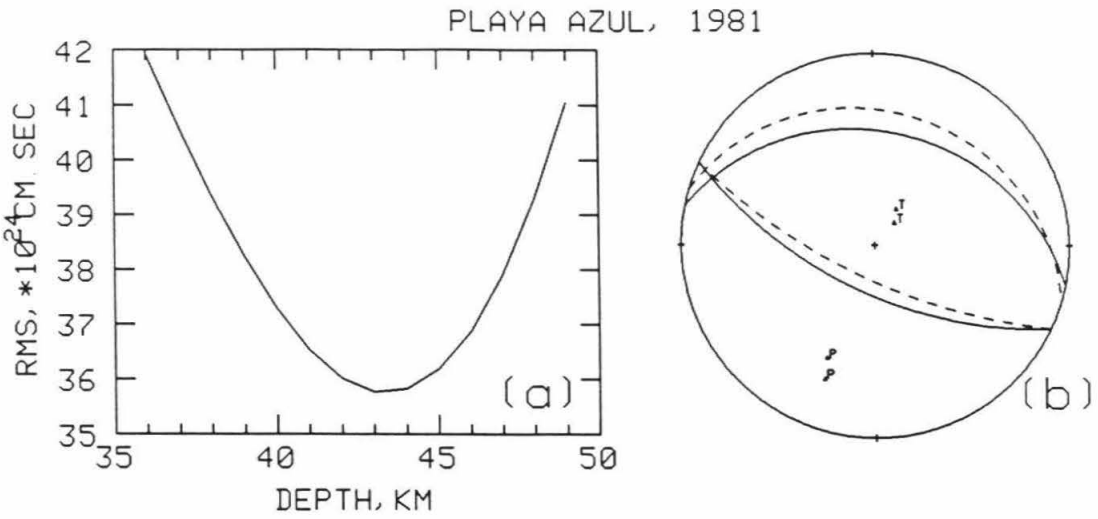

Figure 2.14 Playa Azul, Mexico earthquake. (a) Residual versus depth curves by the moment tensor inversion are given for the finite-fault model obtained. (b) The source mechanism of the major double couple listed in Table 2 (solid line) is compared to the Harvard CMTS (dash line).

$N\,86^{o}\,E$, which is consistent with the direction of the aftershock area. For an unilateral rupture the inversion gives a rupture length 40 km toward $N\,57^{o}\,E$. We used the bilateral rupture to approximate the source finiteness of the earthquake.

Since this earthquake is relatively small, the choice of this particular finiteness model is not critical. Any source finiteness model with a time constant of 40 sec yielded essentially the same result.

Using a finite-fault model and (K70, 5.08M), we obtained a centroid depth of 43 km from the moment tensor inversion (Figure 14a). The best double couple of the moment tensor solution is compared with that of CMTS in Figure 14b. The centroid depth and mechanism obtained from the moment tensor and the fault inversion are listed in Table 2 and 3 respectively.

The depth estimates obtained for other combinations of Q models and excitation functions are summarized in Figures 8 and 9. The result obtained for (D-S, R-A) is listed in Table 4.

2.6.5 1982 El Salvador Earthquake

This earthquake occurred at the coast of El Salvador between the Middle America Trench and the line of historically active volcanoes, where the Cocos plate is moving northerly relative to the Caribbean plate. The earthquake is relatively small ($M_s = 7$) compared to other earthquakes studied here. The depth of the earthquake hypocenter reported by NEIC is 82 km. The depth of the CMTS is 52 km.

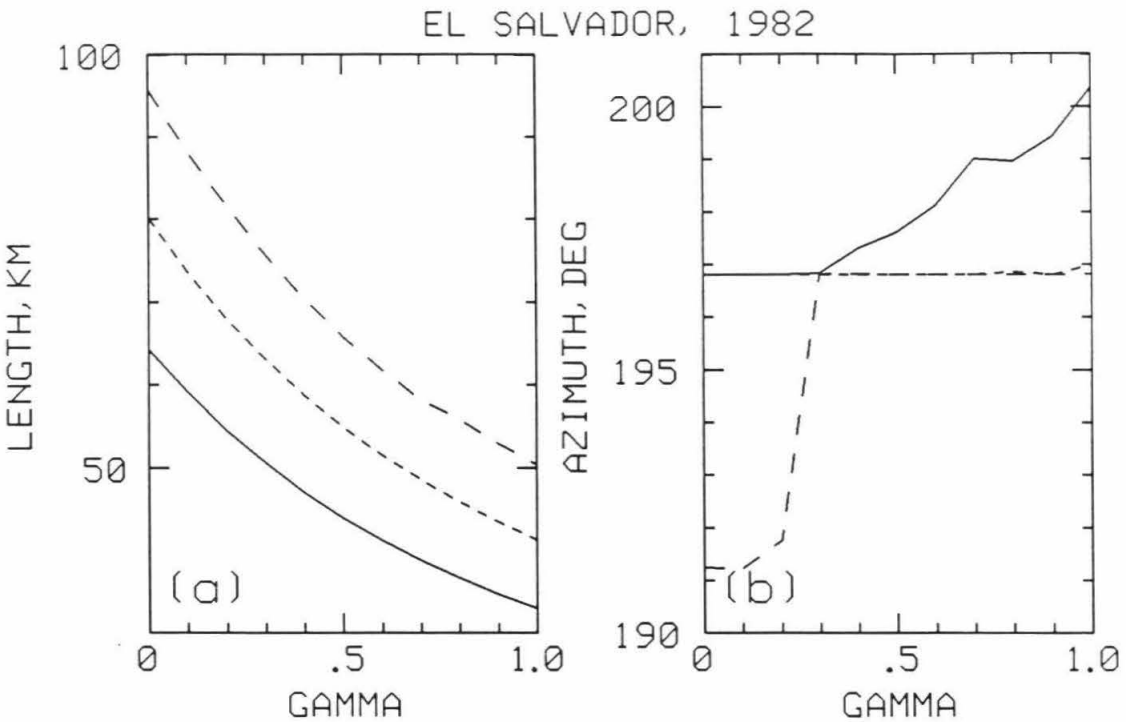

Figure 2.15 El Salvador earthquake. The rupture parameters as functions of the ratio γ for the rupture velocities of 2 (real line), 2.5 (dash line), and 3 (dot line)km/sec. The inversion is at the period of 256 sec. (a) The rupture length. The rupture is assumed to be unilateral toward $S25^{o}W$. (b) The rupture azimuth. The rupture is assumed to be unilateral with a length of 70 km.

Aftershocks reported from NEIC PDE catalog are very sparse. A few events located within a distance of about 70 km to the SSW of the epicenter of the main shock. The inversions of the Rayleigh-wave spectra do not constrain well the rupture mode of the earthquake; the minimum of the error curve, which suggests an unilateral rupture, is not well defined. Figures 15a and 15b show the rupture length and the rupture azimuth estimated for an unilateral rupture for various γ and V respectively. For $\gamma = 0.1$ and $V = 2$ km/sec the estimates of the rupture length and the rupture azimuth are 59 km and $S\,17^{o}\,W$ respectively. These estimates are consistent with the aftershock distribution.

In determining the depth, we used the source-finiteness model of an unilateral rupture of 59 km long toward the $S\,17^{o}\,W$ of the epicenter with a rupture velocity of 2 km/sec and $\gamma = 0.1$. The depths of the centroid obtained by the moment tensor inversion and the fault inversion with (K70, 5.08M) are 52 and 51 km respectively. Figure 16a shows the *rms* error versus trial centroid-depth curve for the moment tensor inversion. The moment tensor solution for the depth of 52 km, which is almost a pure double couple, is listed in Table 2. The double couple solution obtained from the fault inversion is listed in Table 3. The solution indicates that the earthquake is primarily a normal-fault event with one nodal plane steeply dipping to the NE and parallel to the trench. Figure 16b shows the comparison of the best double couples of the moment tensor solution and the CMTS. Our solution agrees well with the CMTS.

Using the model of a point source with 35 sec duration determined by Zhang and Kanamori (1987), we obtained a centroid depth of 56 km by the

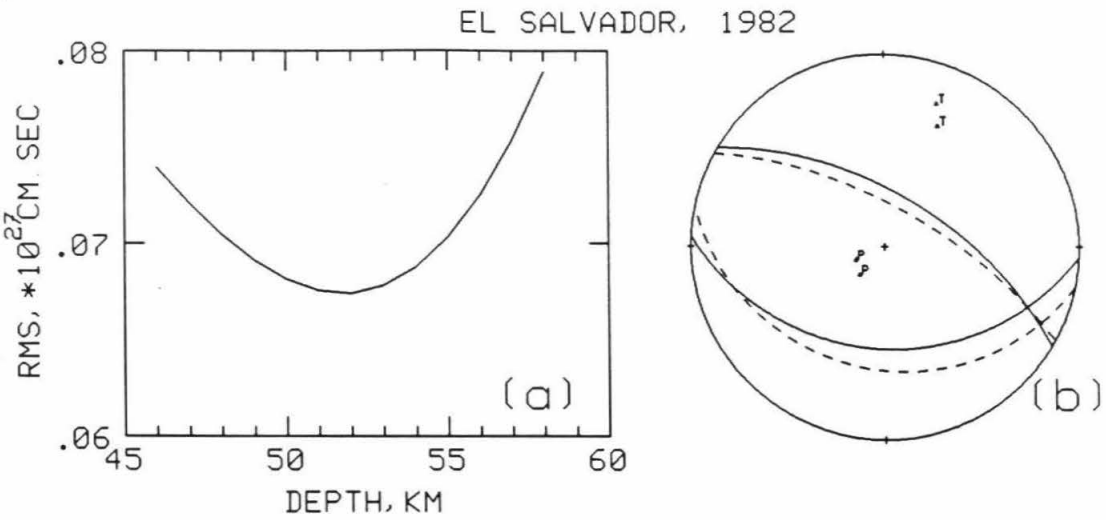

Figure 2.16 El Salvador earthquake. (a) Residual versus depth curves by the moment tensor inversion are given for the finite-fault model obtained. (b) The source mechanism of the major double couple listed in Table 2 (solid line) is compared to the Harvard CMTS (dash line).

moment tensor inversion and by the fault inversion with (K70, 5.08M).

The depth estimates obtained for other combinations of Q models and excitation functions are summarized in Figures 8 and 9. The result obtained for (D-S, R-A) is listed in Table 4.

2.6.6 1982 New Ireland Earthquake

This earthquake occurred at the northwestern portion of the Solomon arc near the junction of the Solomon and New Britain trenches. Previous studies indicate that the Solomon Sea plate subducts toward the northeast under the Solomon trench and toward the northwest under the New Britain trench (Johnson and Molnar, 1972; Lay and Kanamori, 1980). The depth of the earthquake reported by NEIC is 89 km. The CMTS has a depth of 70 km.

Aftershocks of the earthquake from NEIC PDE report are distributed in an area about 120 km long around the main shock. The inversions of the Rayleigh-wave spectra do not constrain well the rupture mode of the earthquake. Figures 17a and 17b show the rupture length (one side from the epicenter) and the rupture azimuth estimated for a bilateral rupture for various γ and V respectively. For $\gamma = 0.1$ and V = 2 km/sec, the estimate of the total rupture length is about 200 km, which is about twice as long as the aftershock area. If the aftershock area represents the extent of the faulting of the earthquake, Figure 17a indicates that the rupture of the earthquake has a large γ than usually expected. Assuming a rupture velocity of 2 km/sec and $\gamma = 1$, the estimate of the total rupture length is 120 km in the azimuth of 104^{o}. Both the rupture time and the rise time for this rupture model are 30 sec long.

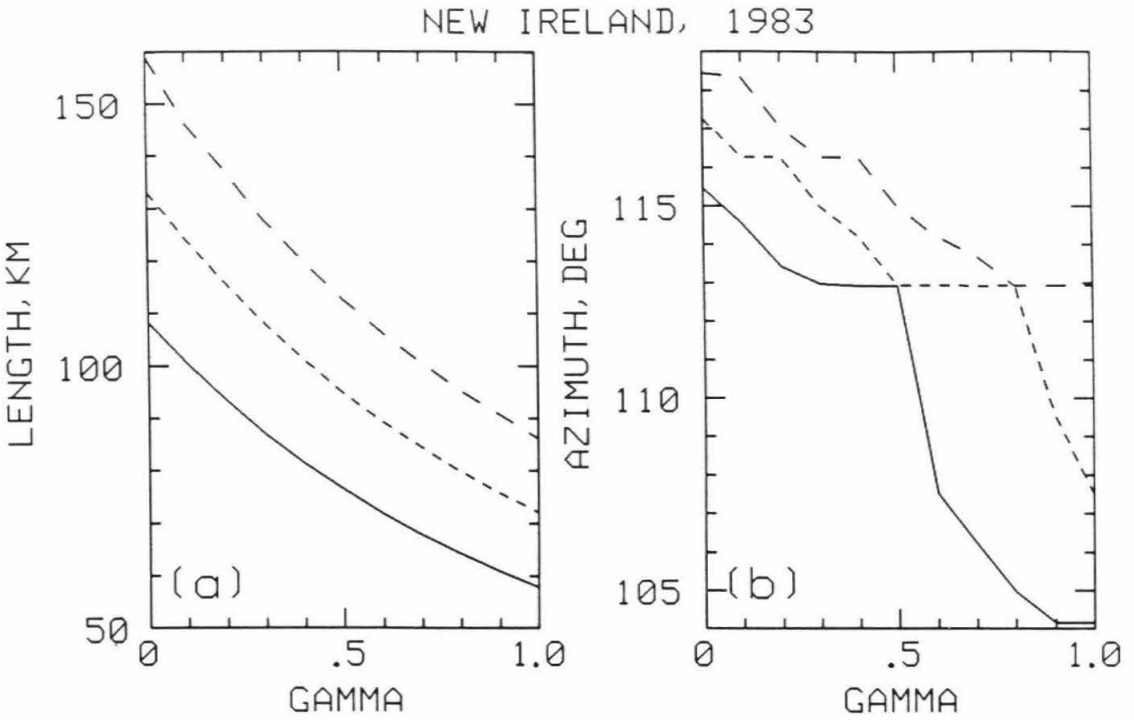

Figure 2.17 New Ireland earthquake. The rupture parameters as functions of the ratio γ for the rupture velocities of 2 (real line), 2.5 (dash line), and 3 (dot line)km/sec. The inversion is at the period of 256 sec. (a) The half rupture length, L. The rupture is assumed to be strictly bilateral ($L_1 = L_2 = L$) with L_1 toward the east. (b) The rupture azimuth. The rupture is assumed to be strictly bilateral with a half length L of 60 km.

The long rise time may represent the long duration of hinge faulting.

If we assumed that the rupture was unilateral with a rupture velocity of 2 km/sec and $\gamma = 0.1$, the estimate of the total rupture length is 100 km in the azimuth of 294^o. The rupture direction obtained here for an unilateral or a bilateral rupture is parallel to the Solomon trench. The minimum error in inversions using various combinations of rupture lengths suggests marginally that the rupture of the earthquake is perhaps bilateral.

We used the finite-fault model of a bilateral rupture with the total rupture length of 120 km and a rupture velocity of 2 km/sec toward the azimuth of 104^o and $\gamma = 1$ to estimate the depth of the earthquake. The centroid depth obtained by the moment tensor inversion and the fault inversion with (K70, 5.08M) are 77 and 78 km respectively. Figure 18a shows the *rms* error versus trial centroid-depth curve for the moment tensor inversion. The moment tensor solution for the depth of 77 km is listed in Table 2, which has a major double couple of reverse fault type with a small strike-slip component. The double couple solution obtained from the fault inversion is listed in Table 3. Figure 18b shows the comparison of the best double couples of the moment tensor solution and the CMTS. If we used the unilateral rupture to represent the source finiteness of the earthquake, the depths obtained by the moment tensor or fault inversion are about the same.

Using a point source model with 58 sec duration determined by Zhang and Kanamori (1987), we obtained the same centroid depth as that using the finite-fault model.

The depth estimates obtained for other combinations of Q models and excitation functions are summarized in Figures 8 and 9. The result obtained

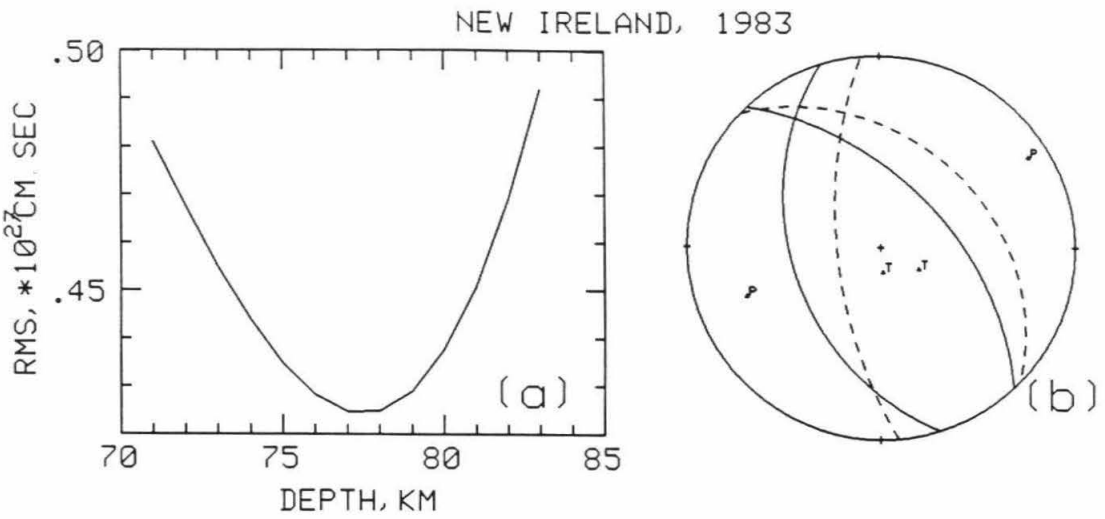

Figure 2.18 New Ireland earthquake. (a) Residual versus depth curves by the moment tensor inversion are given for the finite-fault model obtained. (b) The source mechanism of the major double couple listed in Table 2 (solid line) is compared to the Harvard CMTS (dash line).

for (D-S, R-A) is listed in Table 4.

2.6.7 1983 Chagos Bank Earthquake

This earthquake ($M_s = 7.7$) occurred at the southern end of the Chagos Bank in an young lithosphere of the Indian plate, near the Central Indian ridge and gives evidence of massive internal deformation taking place in the Indian plate (Stein and Okal, 1978; Weissel et al. 1980). Near-ridge earthquakes occur along all major mid-ocean ridge systems, but the Central Indian Ocean ridge is unusually active; normal-fault events occur primarily in the Indian Ocean (Wiens and Stein, 1984; Bergman and Solomon, 1984). The body waves of the 1983 earthquake recorded at GDSN stations suggest that the earthquake is a nearly pure normal-fault event along a fault striking roughly east-west (Wiens and Stein, 1984), a typical mechanism for events near the Chagos Bank (Stein, 1978; Bergman and Solomon, 1984). The hypocenter depth reported by NEIC is 10 km. The CMTS gives 10 km. The centroid depth of the USGS moment tensor solution reported by NEIC is 36 km.

The aftershocks within one day after the main shock reported by NEIC are distributed in an area about 110 km long extending to $N65^{o}\ W$ from the epicenter of the main event.

The inversions of the spectra for various combinations of the rupture lengths and azimuths yield a minimum for an unilateral rupture. This minimum is not significantly smaller than other local minima for different rupture modes. This indicates that the rupture mode cannot be determined well from the inversion. Figures 19a and 19b show the rupture length and the

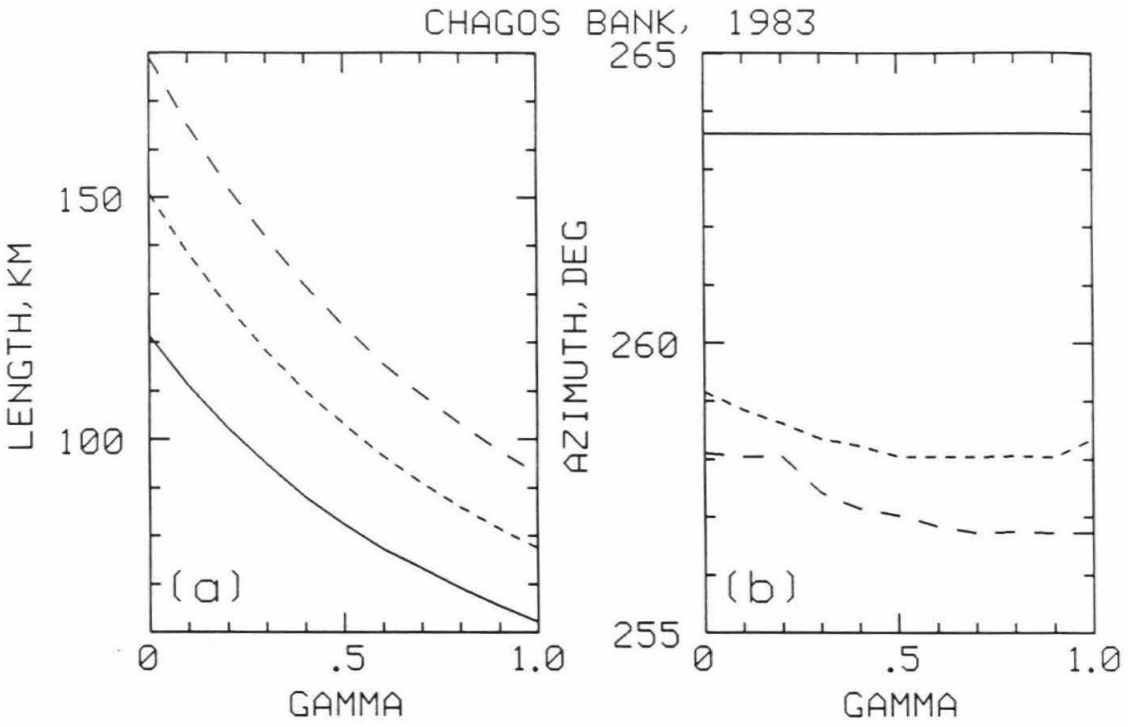

Figure 2.19 Chagos Bank earthquake. The rupture parameters as functions of the ratio γ for the rupture velocities of 2 (real line), 2.5 (dash line), and 3 (dot line)km/sec. The inversion is at the period of 256 sec. (a) The rupture length. The rupture is assumed to be unilateral toward $N65^{o}\ W$. (b) The rupture azimuth. The rupture is assumed to be unilateral with a length of 110 km.

rupture azimuth estimated for an unilateral rupture for various γ and V respectively. For a rupture velocity of 2 km/sec and $\gamma = 0.1$, the estimates of the rupture length and the rupture azimuth are 110 km and 258^o respectively.

Using the finite-fault model obtained, we determined the centroid depth. The model is an unilateral rupture of 110 km with a rupture velocity of 2 km/sec in the $S\,78^o\,W$ direction and $\gamma = 0.1$. The centroid depths obtained by the moment tensor inversion and the fault inversion with (K70, 5.08M) are both 36 km (Figure 20a). This is much larger than the depth reported by NEIC and the CMTS depth. Our estimate is consistent with the depth of the USGS moment tensor solution.

The moment tensor solution for the centroid depth of 36 km is listed in Table 2. The scalar moment is 7.7×10^{27} dyne.cm. Figure 20b compares the mechanism of the best double couple of the moment tensor solution obtained with the CMTS. These solutions are in general consistent and indicate a north-south tension in this region.

Using a point source model with 63 sec duration determined by Zhang and Kanamori (1987), we obtained a centroid depth of 34 km by the moment tensor inversion and by the fault inversion.

The depth estimates obtained for other combinations of Q models and excitation functions are summarized in Figures 8 and 9. The result obtained for (D-S, R-A) is listed in Table 4.

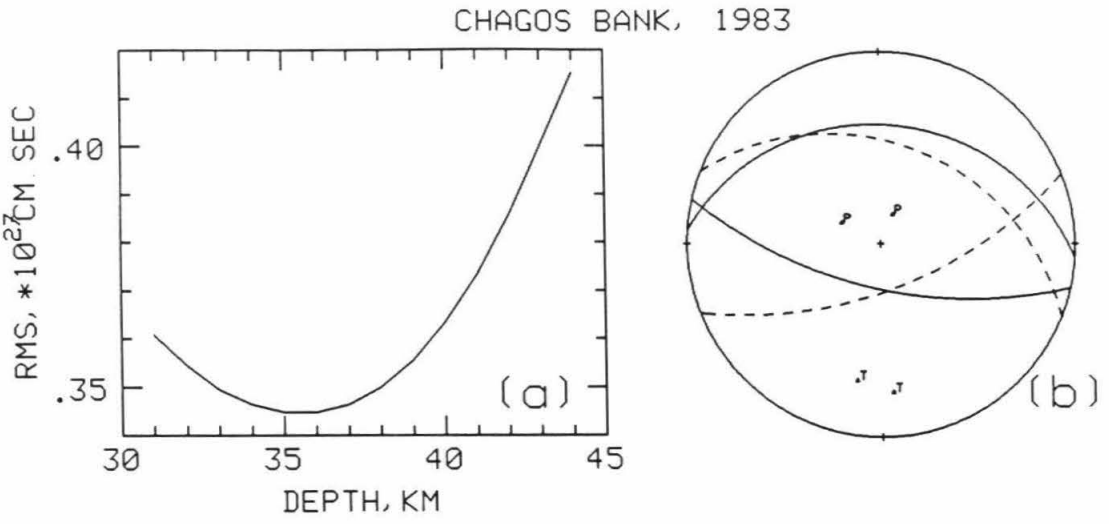

Figure 2.20 Chagos Bank earthquake. (a) Residual versus depth curves by the moment tensor inversion are given for the finite-fault model obtained. (b) The source mechanism of the major double couple listed in Table 2 (solid line) is compared to the Harvard CMTS (dash line).

2.6.8 1985 Valparaiso, Chile Earthquake

This earthquake occurred under the coast of Central Chile, where the subduction of the Nazca plate has a smaller dip angle($<30^o$) than at the Northern and Southern Chile (Barazangi and Isacks, 1976). The Harvard and USGS moment tensor solutions give 41 and 51 km for the centroid depth respectively.

In determining the depth of the earthquake, we adapted the finite-fault model obtained by Zhang and Kanamori (1987). In this model, the rupture is unilateral, 149 km long with a rupture velocity of 2.5 km/sec toward the $S\,15^o\,W$ direction and $\gamma = 0.1$. The centroid depth is estimated to be 48km by the moment tensor inversion with (K70, 5.08M) (Figure 21a). The moment tensor solution obtained for the depth is listed in Table 2. The solution is consistent with the CMTS. In Figure 21b, the two nodal planes of the major double couple of the moment tensor are compared with CMTS, which has strike=11^o, dip=26^o, and slip=110^o. The depth obtained by using the fault inversion is 44 km. The double couple mechanism obtained for the fault inversion at the depth is listed in Table 3.

The depth estimates obtained for other combinations of Q models and excitation functions are summarized in Figures 8 and 9. The result obtained for (D-S, R-A) is listed in Table 4.

Most of the recent large earthquakes in the Central Chile have the typical thrust mechanism of interplate earthquakes with depths from 20 to 70 km (Malgrange et al., 1981; Malgrange and Madariaga, 1983; Korrat and Madariaga, 1986). The 1985 earthquake may also be one of these earthquakes near or

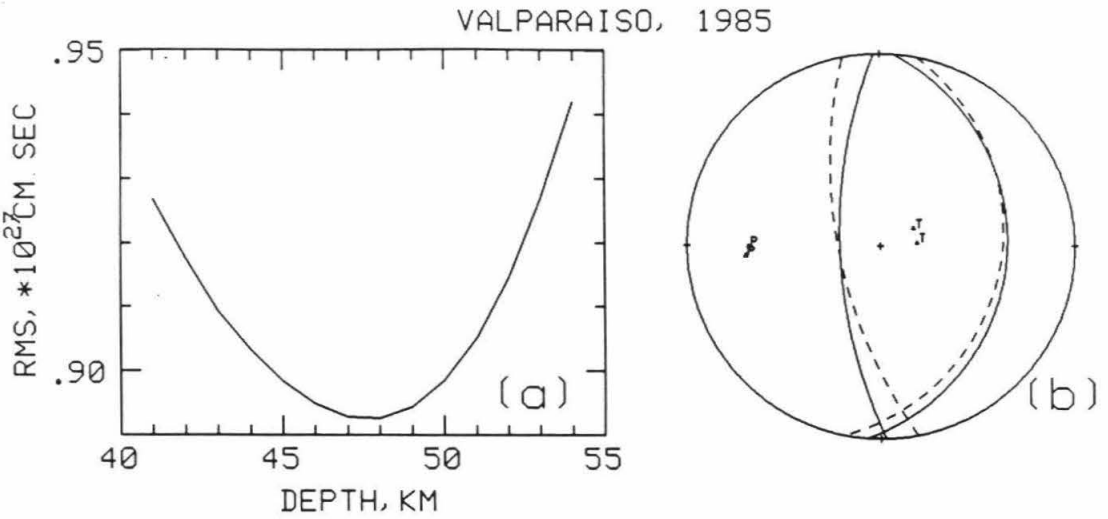

Figure 2.21 Valparaiso, Chile earthquake. (a) Residual versus depth curves by the moment tensor inversion are given for the finite-fault model obtained by Zhang and Kanamori (1987). (b) The source mechanism of the major double couple listed in Table 2 (solid line) is compared to the Harvard CMTS (dash line).

beneath the interface between the two converging plates representing the underthrusting of the Nazca plate beneath the South America plate. Analysis of the geodetic data by Barrientos and Ward (1987) on elevation changes due to deformation associated with the earthquake suggests that most of the fault slip of the earthquake occurred at a depth between 30 and 40 km. The Body-wave study of Christensen and Ruff (1986) defines a depth distribution with a lower bound of about 40 km for the earthquake.

Dewey et al. (1985) relocated teleseismically well recorded earthquakes (magnitude 4.5 or larger) that occurred from 1964 through March, 1985, in and near the aftershock zone of the 1985 earthquake. The seismicity near plate thrust-interface in this region clustered into a pair of deep and shallow thrust-zones, which are separated by a 20 km region of lower seismicity centered at a depth of about 35 km in the plane of the interface. Most of the aftershocks of the earthquake (magnitude less than 6.0) were concentrated in the shallow zone; in the deep zone there are some aftershocks of magnitude 6.0 or greater occured the first day after the main shock, but few shocks of magnitude between 4.5 and 5.9.

If body waves were radiated mostly from the upper 40 km portion of the fault plane, the centroid depth at 48 km obtained from our study suggests that rupture extended considerably below the centroid depth and was responsible for radiation of long period waves. If we assumed that the rupture extended from depths of 40 to 60 km with a fault width $W = 20/\sin 21^{o}\ km$ and a fault length $L = 149\ km$, the average displacement would be about $\overline{D} = 2.1\ m$ for a rigidity $\mu = 7\times10^{11}\ dyne.cm^{2}$. The stress drop was $\Delta\sigma\sim$ 9 bars. The seismic slip of the earthquake is much smaller than the

cumulative displacement (7.2 m), since the 1906 earthquake calculated from the Nazca-South America convergence rate of 9 cm/yr.

Using a point source model with 69 sec duration determined by Zhang and Kanamori (1987), we obtained a centroid depth of 47 km by the moment tensor inversion and of 44 km by the fault inversion with (K70, 5.08M).

2.6.9 1985 Michoacan, Mexico Earthquake

This earthquake occurred at the northwest portion of the Middle America Trench, where Cocos plate is subducting to the northeast under the North America plate. The depth of the earthquake reported from NEIC is 28 km. The centroid depth given by CMTS is 21.3 km.

In determining the depth from Rayleigh-wave data, we used the source finiteness model obtained by Zhang and Kanamori (1987), which has the rupture length of 165 km, the rupture velocity of 2.5 km/sec in the azimuth of 123^o and $\gamma = 0.1$. Figure 22a shows the residual versus centroid-depth curve for the moment tensor inversion with (K70, 5.08M). The estimate of the centroid depth is 30 km. The moment tensor solution for the centroid depth at 30 km is listed in Table 2, which has a dip angle of 30.8^o for the best double couple of the moment tensor. The results obtained by using the fault inversion are similar to those obtained from the moment tensor inversion. The centroid depth and fault mechanism obtained from fault inversion are listed in Table 3.

The tsunami generated by the earthquake has 1.4 m peak-to-trough high at Acapulco, Mexico, about 400 km away to the southeast from the epicenter,

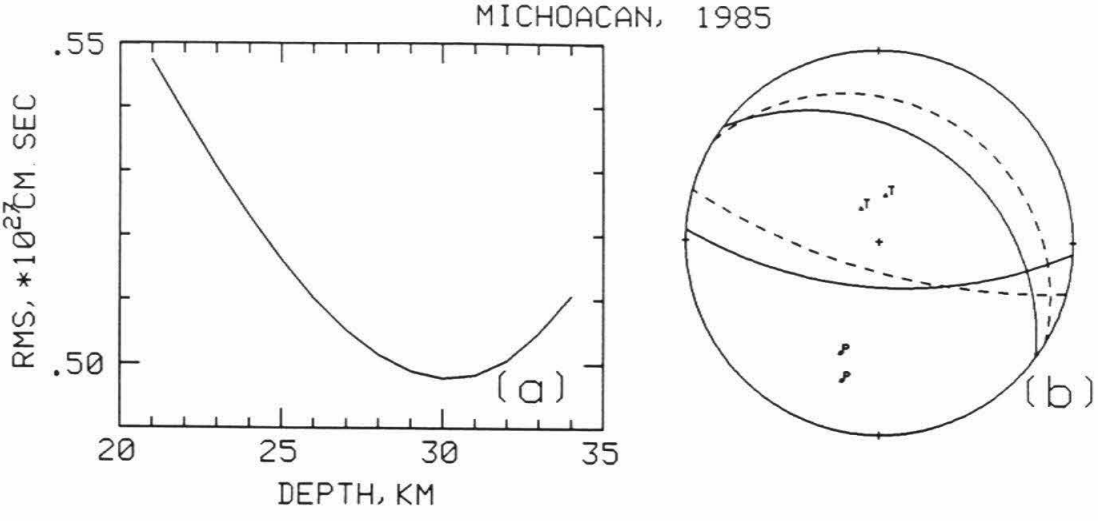

Figure 2.22 Michoacan, Mexico earthquake. (a) Residual versus depth curves by the moment tensor inversion are given for the finite-fault model obtained by Zhang and Kanamori (1987). (b) The source mechanism of the major double couple listed in Table 2 (solid line) is compared to the Harvard CMTS (dash line).

which may suggest that the fault broke the surface. We used the moment tensor inversion with excitation functions of extended source and found a depth extent of 54 km.

In Figure 22b, the two nodal planes of the major double couple of the moment tensor are compared with CMTS. We also determined the depth of the earthquake using other source finiteness models, which include the models of the source-process time and the source directivity with various rupture lengths and rupture velocities. The results remain about the same.

The depth estimates obtained for other combinations of Q models and excitation functions are summarized in Figures 8 and 9. The result obtained for (D-S, R-A) is listed in Table 4. The centroid depth obtained with (D-S, R-A) is approximately the same as that of CMTS.

The dip angle obtained from our method is greater than the dip angle of the fault plane from P-wave first motion solution reported from NEIC and CMTS. The discrepancy reflects the difficulty and uncertainty in determining the dip angle for shallow earthquakes.

Using a point source model with 77 sec duration determined by Zhang and Kanamori (1987) and (K70, 5.08M), we obtained the same centroid depth as that using the finite-fault model.

2.7 Resolution of Depth

Since the wavelength of Rayleigh waves with a period of 150-300 sec the wavelength is about 1000 km, there is in general a large uncertainty in the estimate of the depth at which the preferred minimum occurs. A t test can be

applied to estimate the uncertainty of the depth estimated from long-period surface waves.

The moment-tensor or the double-couple solution of the best fitting source minimizes the sum of the squared residual,

$$\rho^2 = \sum_{i=1}^{5K} \rho_i^2 ,$$

where

$$\rho_i = \Lambda_i - \hat{\Lambda}_i , \qquad (i = 1, \ldots, 5K) .$$

Here Λ_i and $\hat{\Lambda}_i$ are the observed and predicted components of vector Λ in (13).

The differences of the square residuals ρ_i^2 at two depths A and B $(\sum_{i=1}^{5L} \rho_{iA}^2 > \sum_{i=1}^{5L} \rho_{iB}^2)$

$$\delta_i = \rho_{iA}^2 - \rho_{iB}^2 , \qquad (i = 1, \ldots, 5K)$$

can be considered samples of a random variable following a normal distribution with mean μ and standard deviation σ. In order to assess the statistical significance of the differences, we test the null hypothesis $\mu = 0$. We define the statistic

$$t = \frac{\overline{\delta}}{s \,/\, \sqrt{5K}} ,$$

where $\overline{\delta}$ and s are the mean and the square root of the variance of δ_i $(i = 1, \ldots, 5K)$. If t exceeds a threshold value t_α determined by the student's t distribution for a given significance level α, then the alternate hypothesis $\mu > 0$ is accepted, which indicates that the solution at depth B is

Table 2.5 : Depth (km) (centroid) determined in this study compared with CMTS

Event	Location	Depth	Depth range †	CMTS
1	Colombia-Ecuador	11	9 - 24	20
2	Santa Cruz Is.	36	18 - 46	34
3	Samoa	15	9 - 26	20
4	Playa Azul, Mexico	41	28 - 49	32
5	El Salvador	49	41 - 55	52
6	New Ireland	75	72 - 79	70
7	Chagos Bank	31	16 - 41	10 fixed
8	Valparaiso, Chile	44	15 - 54	41
9	Michoacan, Mexico	24	12 - 34	21

† The depth range is for 90% confidence.

better than at depth A at the given significance level.

For each earthquake, we computed the t statistic for the best fitting depth and nearby depths. We determine the depths at which t exceeds the threshold value t_α for a 90% confidence using a one-sided student's t test with 5K-1 degree of freedom. In the inversion, we used the group velocities and Q of D-S and the excitation function of R-A. Table 5 lists the 90% confidence interval for the depth of each earthquake.

For the New Ireland earthquake, the CMTS depth is slightly shallower than the depth range given in Table 5, 72 to 79 km. For the Chagos Bank earthquake, the CMTS depth is fixed at 10 km, which is shallower than the depth range obtained here, 16 to 41 km. For other earthquakes, the CMTS depths are within the depth range given in Table 5.

2.8 Discussion

The accuracy of the depth determination depends critically on how accurately we can correct the observed spectra for the source finiteness effect and propagation effects on both phase and amplitude. Also the choice of the excitation functions is important.

For the correction of source finiteness effect, the method developed by Zhang and Kanamori (1987) is effectively used for very large earthquakes. For the smaller events, the details of the source finiteness effect cannot be determined. However, since its effect on the depth determination is small, the uncertainty in the source finiteness model is not a serious problem for these smaller events. We feel that we can correct for the source finiteness effect

with sufficient accuracy for reliable depth determination.

The propagation effects on the phase can be estimated with good accuracy using recently developed laterally heterogeneous earth models such as M84C at periods longer than 150 sec. At periods shorter than 150 sec, presently available models are not adequate.

The propagation effects on the amplitude can be estimated using global average Q models. As Figure 8 shows, the difference in the depth estimate determined for different Q models is small. However, the difference is systematic for different models, and is significant for shallow events. Since the model presented by Dziewonski and Steim (1982) is considered a good global average, we prefer the results obtained using this model.

The effect of different earth models used for the computation of excitation functions is very small. Any reasonable earth model can be used for the purpose of depth determination. However, since most earthquakes studied in this paper occurred in subduction zones, the average ocean model of Regan and Anderson (1984) may be a reasonable choice. We summarize the results obtained with the combination of D-S Q model and R-A earth model in Tables 4 and 5 as our preferred solutions.

2.9 Conclusions

We determined the depths and source mechanisms of nine large earthquakes from long-period (150 to 300 sec) Rayleigh waves recorded at IDA and GDSN stations. We inverted the data set of complex source spectra for a moment tensor (linear) or a double couple (nonlinear). By solving a least-

squares problem, we obtained the centroid depth or the extent of the distributed source of each earthquake.

The depths and source mechanisms of large shallow earthquakes determined from long-period Rayleigh waves depend on the models of source finiteness, wave propagation, and the excitation. We tested various models of the source finiteness, Q, the group velocity, and the excitation. We conclude that the depth estimates obtained using the Q model of Dziewonski and Steim(1982) and the excitation functions computed for the average ocean model of Regan and Anderson(1984) are most reasonable. Dziewonski and Steim's(1982) Q model represents a good global average of Q determined over a period range of the Rayleigh waves used in this study. Since most of the earthquakes studied here occurred in subduction zones Regan and Anderson's(1984) average ocean model is considered most appropriate.

Our depth estimates are in general consistent with the Harvard CMT solutions. The centroid depths and their 90 % confidence intervals (numbers in the parentheses) determined by the Student's t test are: Colombia-Ecuador earthquake (12 December 1979), d = 11 km, (9, 24) km; Santa Cruz Is. earthquake (17 July 1980), d = 36 km, (18, 46) km; Samoa earthquake (1 September 1981), d = 15 km, (9, 26) km; Playa Azul, Mexico earthquake (25 October 1981), d = 41 km, (28, 49) km; El Salvador earthquake (19 June 1982), d = 49 km, (41, 55) km; New Ireland earthquake (18 March 1983), d = 75 km, (72, 79) km; Chagos Bank earthquake (30 November 1983), d = 31 km, (16, 41) km; Valparaiso, Chile earthquake (3 March 1985), d = 44 km, (15, 54) km; Michoacan, Mexico earthquake (19 September 1985), d = 24 km, (12, 34) km.

2.10 References

Aki, K., 1960a. The use of Love waves for the study of earthquake mechanism. *J. Geophys. Res.*, 65: 323-331.

Aki, K., 1960b. Study of earthquake mechanism by a method of phase equalization applied to Rayleigh and Love waves. *J. Geophys. Res.*, 65: 729-740.

Anderson, D.L. and Given, J.W., 1982. Absorption band Q model for the Earth. *J. Geophys. Res.*, 87: 3893-3904.

Anderson, D.L. and Hart, R.S., 1978a. Attenuation models of the earth. *Phys. Earth and Planet. Int.*, 16: 289-306.

Anderson, D.L. and Hart, R.S., 1978b. Q of the earth. *J. Geophys. Res.*, 83: 5869-5882.

Astiz, L., Kanamori, H. and Eissler, H.K., 1987. Source characteristics of earthquakes in the Michoacan seismic gap in Mexico. *Bull. Seis. Soc. Am.*, 77: 1326-1346.

Backus, G.E. and Mulcahy, M., 1976. Moment tensors and other phenomenological descriptions of seismic sources, I, Continuous displacements. *Geophys. J. R. astr. Soc.*, 46: 341-361.

Barazangi, M. and Isacks, B.L., 1976. Spatial distribution of earthquakes and subduction of the Nazca plate beneath South America. *Geology*, 4: 686-672.

Barrientos, S.E. and Ward, S.N., 1987. Slip distribution of the 1985 Central Chile earthquake from geodetic observations (abstract). *Seism. Res. Lett.*, 58: 8.

Ben-Menahem, A., 1961. Radiation of seismic surface waves from finite moving sources. *Bull. Seism. Soc. Am.*, 51: 401-435.

Ben-Menahem, A., Smith, S.W. and Teng, T.L., 1965. A procedure for source studies from spectra of long-period seismic body waves. *Bull. Seism. Soc. Am.*, 55: 203-235.

Bergman, E.A. and Solomon, S.C., 1984. Source mechanisms of earthquakes near mid-ocean ridges from body waveform inversion: Implications for the early evolution of oceanic lithosphere. *J. Geophys. Res.*, 89: 11415-11441.

Chael, E. and Anderson, D.L., 1982. Global Q estimates from antipodal Rayleigh waves. *J. Geophys. Res.*, 87: 2840-2850.

Chapple, W.M. and Forsyth, D.M., 1979. Earthquakes and bending of plates at trenches. *J. Geophys. Res.*, 84: 6729-6749.

Chase, C.G., 1971. Tectonic history of the Fiju plateau. *Bull. Seis. Soc. Am.*, 82: 3087.

Christensen, D.H. and Ruff, L.J., 1983. Outer-rise earthquakes and seismic coupling. *Geophys. Res. Lett.*, 10: 697-700.

Christenson, D.H. and Ruff, L.J., 1986. Rupture process of the March 3, 1985 Chilean earthquake. *Geophys. Res. Lett.*, 13: 721-724.

Dewey, J.W., Choy, G.L. and Nishenko, S.P., 1985. Asperities and paired thrust zones in the focal region of the Chilean earthquake of March 3, 1985 (abstract). *EOS Trans. AGU*, 66: 950.

Dziewonski, A.M. and Anderson, D.L., 1981. Preliminary reference Earth model. *Phys. Earth and Planet. Int.*, 25: 297-356.

Dziewonski, A.M. and Steim, J.M., 1982. Dispersion and attenuation of mantle waves through waveform inversion. *Geophys. J. R. astr. Soc.*, 70: 503-527.

Dziewonski, A.M. and Woodhouse, J.H., 1983. An experiment in systematic study of global seismicity: Centroid-moment tensor solutions for 201 moderate and large earthquakes of 1981. *J. Geophys. Res.*, 88: 3247-3271.

Dziewonski, A.M., Chou, T.-A. and Woodhouse, J.H., 1981. Determination of earthquake source parameters from waveform data for studies of global and regional seismicity. *J. Geophys, Res.*, 86: 2825-2852.

Fukao, Y. and Kobayashi, M., 1983. Phase and group velocities and Q of mantle Love and Rayleigh waves of the first two modes and their azimuthal dependences for the 1963 Kurile Islands Earthquake. *Phys. Earth Planet. Inter.*, 32: 4-35.

Giardini, D., Dziewonski, A.M. and Woodhouse, J.H., 1985. Centroid-moment tensor solutions for 113 large earthquakes in 1977-1980. *Phys. Earth Planet. Inter.*, 40: 259-272.

Gilbert, F. and Dziewonski, A.M., 1975. An application of normal mode theory to the retrieval of structure parameters and source mechanisms from seismic spectra. *Phil. Trans. R. Soc. Lond, A.*, 278: 187-269.

Havskov, J., Singh, S.K., Nava, E., Dominguez, T. and Rodriguez, M., 1983. Playa Azul, Michoacan, Mexico, earthquakes of 25 October, 1981 (M_S=7.3). *Bull. Seis. Soc. Am.*, 73: 449-458.

Herd, D.G., Youd, T.L., Meyer, H., Arango, J.L., Person, C.W.J. and Mendoza, C., 1981. The great Tumaco, Colombia earthquake of 12 December 1979. *Science*, 211: 441-445.

Isacks, B.L., Sykes, L.R. and Oliver, J., 1969. Focal mechanism of deep and shallow earthquakes in the Tonga-Kermadec region and the tectonics of island arcs. *Geol. Soc. Am. Bull.*, 80: 1443-1470.

Johnson, T. and Molnar, P., 1972. Focal mechanism and plate tectonics of the southwest Pacific. *J. Geophys. Res.*, 77: 5000-5032.

Kanamori, H., 1970. Velocity and Q of mantle waves. *Phys. Earth and Planet. Int.*, 2: 259-275.

Kanamori, H. and Given, J.W., 1981. Use of long-period surface waves for rapid determination of earthquake-source parameters. *Phys. Earth Planet. Inter.*, 27: 8-31.

Kanamori, H. and Given, J.W., 1982. Use of long-period surface waves for rapid determination of earthquake-source parameters, 2. Preliminary determination of source mechanisms of large earthquakes ($M_s \geq 6.5$) in 1980. *Phys. Earth Planet. Inter.*, 30: 260-268.

Kanamori, H. and Stewart, G.S., 1976. Mode of the strain release along the Gibbs fracture zone, Mid-Atlantic ridge. *Phys. Earth Planet. Inter.*, 11: 312-332.

Korrat, I. and Madariaga, R., 1986. Rupture of the Valparaiso (Chile) gap from 1971 to 1985. in *Earthquake Source Mechanics*, pp. 247-258, edited by S. Das, J. Boatwright, and C. H. Scholz, American Geophys. Union, Washington, D.C..

Lay, T. and Kanamori, H., 1980. Earthquake Doublets in the Solomon Islands. *Phys. Earth and Planet. Int.*, 21: 283-304.

Le Pichon, X., 1968. Sea-floor spreading and continental drift. *J. Geophys. Res.*, 73: 3661-3697.

Malgrange, M. and Madariaga, R., 1983. Complex distribution of large thrust and normal fault earthquakes in the Chilean subduction zone. *Geophys. J. Res. astr. Soc.*, 73: 489-506.

Malgrange, M., Deschamps, A. and Madariaga, R., 1981. Thrust and extensional faulting under the Chilean coast, 1965, 1971 Aconcagua earthquakes. *Geophys. J. R. astr. Soc.*, 66: 313-331.

Mendoza, C. and Dewey, J.W., 1984. Seismicity associated with the great Colombia-Ecuador earthquakes of 1942, 1958, and 1979: Implications for barrier models of earthquake rupture. *Bull. Seism. Soc. Am.*, 74: 577-593.

Mills, J.M., 1978. Great-circle Rayleigh wave attenuation and group velocity, Part IV: Regionalization and pure-path models for shear velocity and attenuation. *Phys. Earth and Planet. Int.*, 17: 323-352.

Mills, J.M. and Hales, A.L., 1977. Great-circle Rayleigh wave attenuation and group velocity, Part I: Observations for periods between 150 and 600 seconds for seven great-circle paths. *Phys. Earth and Planet. Int.*, 14: 109-119.

Mills, J.M. and Hales, A.L., 1978. Great-circle Rayleigh wave attenuation and group velocity, Part II: Observations for periods between 50 and 200 seconds for nine great-circle paths and global averages for periods of 50 to 600 seconds. *Phys. Earth and Planet. Int.*, 17: 209-231.

Molnar, P. and Sykes, L.R., 1971. Plate tectonics in the Hispaniola area: Discussion. *Geol. Soc. Amer. Bull.*, 82: 1123.

Nakanishi, I., 1979. Phase velocity and Q of mantle Rayleigh waves. *Geophys. J. R. Astr. Soc.*, 58: 35-59.

Nakanishi, I. and Anderson, D.L., 1983. Measurements of mantle wave velocities and inversion for lateral heterogeneity and anisotropy - I. Analysis of great

circle phase velocities. *J. Geophys. Res.*, 88: 10267-10283.

Nakanishi, I. and Anderson, D.L., 1984. Measurements of mantle wave velocities and inversion for lateral heterogeneity and anisotropy - II. Analysis by the single-station method. *Geophys. J. R. astr. Soc.*, 78: 573-617.

Nakanishi, I. and Kanamori, H., 1984. Source mechanisms of twenty-six large, shallow earthquakes ($M_s \geq 6.5$) during 1980 from P-wave first motion and long-period Rayleigh wave data. *Bull. Seism. Am.*, 74: 805-818.

Press, F., 1970. Earth models consistent with geophysical data. *Phys. Earth and Planet. Int.*, 3: 3-22.

Regan, J. and Anderson, D.L., 1984. Anisotropic models of the upper mantle. *Phys. Earth Planet. Int.*, 35: 227-263.

Romanowicz, B.A. and Guillemant, P., 1984. An experiment in the retrieval of depth and source mechanism of large earthquakes using very long-period Rayleigh wave data. *Bull. Seism. Soc. Am.*, 74: 417-437.

Romanowicz, B.A. and Monfret, T., 1986. Source process times and depth of large earthquakes by moment tensor inversion of mantle wave data and the effect of lateral heterogeneity. *Ann. Geophy.*, 4: B, 3, 271-283.

Silver, P.G. and Jordan, T.H., 1983. Total moment spectra of fourteen large earthquakes. *J. Geophys. Res.*, 88: 3273-3293.

Stauder, W., 1968. Tensional character of earthquake foci beneath the Aleutian trench with relation to sea-floor spreading. *J. Geophys. Res.*, 73: 7693-7701.

Stein, S. and Okal, E.A., 1978. Seismicity and tectonics of the Ninetyeast Ridge area: Evidence for internal deformation of the Indian Plate. *J. Geophys.*

Res., 83: 2233-2246.

Tajima, F. and Kanamori, H., 1985. Global Survey of aftershock area expansion patterns. *Phys. Earth and Planet. Int.*, 40: 77-134.

Tajima, F., Ruff, L.J., Kanamori, H. and Zhang, J., 1987. The source rupture and subduction in the Santa Cruz Islands region. in preparation.

Tanimoto, T., 1985. The Backus-Gilbert approach to the three-dimensional structure in the upper mantle - I. Lateral variation of surface wave phase velocity with its error and resolution. *Geophys. J. R. astr. Soc.*, 82: 105-123.

Tanimoto, T., 1986. The Backus-Gilbert approach to the three-dimensional structure in the upper mantle - II. SH and SV velocity. *Geophys. J. R. astr. Soc.*, 84: 49-69.

UNAM seismology group, 1986. The September 19, 1985 Michoacan earthquake: Aftershock distribution and history of rupture. *Geophys. Res. Lett.*, 13: 573-576.

Weissel, J.K., Anderson, R.N. and Geller, C.A., 1980. Deformation of the Indo-Australian plate. *Nature*, 287: 284-291.

Wiens, D.A. and Stein, S., 1983. Age dependence of oceanic intraplate seismicity and implications for lithospheric evolution. *J. Geophys. Res.*, 88: 6455-6468.

Wiens, D.A. and Stein, S., 1984. Intraplate seismicity and stresses in young oceanic lithosphere. *J. Geophys. Res.*, 89: 11442-11464.

Woodhouse, J.H. and Dziewonski, A.M., 1984. Mapping the upper mantle: Three-dimensional modeling of Earth structure by inversion of seismic waveforms. *J. Geophys. Res.*, 89: 5953-5986.

Zhang, J. and Kanamori, H., 1987. Source finiteness of large earthquakes measured from long-period Rayleigh waves. *Phys. Earth and Planet. Int.*, in press.

Chapter 3

Depths of the 1977 Sumbawa and 1983 Akita-Oki Earthquakes Determined from Long-Period Rayleigh Waves

3.1 Introduction

Most large and great earthquakes occur at subduction zones. Most of them are thrust earthquakes occurring on the subduction-zone thrust boundary such as the 1960 Chilean earthquake and the 1964 Alaskan earthquake. Another class of earthquakes consists of large normal-fault earthquakes which occur near the trench axis. The notable examples include the 1933 Sanriku, Japan earthquake and the 1977 Sumbawa, Indonesia earthquake.

The vertical extent of faulting of large thrust events provides key information on the nature of interplate coupling at subduction zones. Many recent studies (e.g. Uyeda and Kanamori, 1979; Ruff and Kanamori, 1980; Peterson and Seno, 1984) suggest that interplate interaction is a key element that determines tectonic features at plate boundaries. Also, estimation of seismic slip rate at subduction plate boundaries is essential for assessment of long-term seismic potential (e.g. Kanamori, 1977; Sykes and Quittmeyer, 1981). In order to accurately estimate seismic slip rate from seismic moment, I need to have accurate estimates of the fault length and width. Direct determination of the vertical extent of faulting provides this key information on the fault width.

The study of the state of the stress in the subducting plate is important for a better understanding of the dynamics of subduction and of distribution of earthquake generating stress near subduction plate boundaries (Ruff and Kanamori, 1980; Christensen and Ruff, 1983; Ward, 1983).

Normal-fault earthquakes near the trench axis are usually considered to be due to bending of an oceanic plate as it begins to subduct at the trench (e.g. Stauder, 1968; Hanks, 1971; Chapple and Forsyth, 1979). Another possibility is that these events are caused by extensional stress due to the negative buoyancy of the subducting slab, as well as by the bending stress, and break through almost the entire thickness of the lithosphere (Kanamori, 1971). Accurate determination of the vertical extent of faulting of these earthquakes is the key to resolution of this problem.

The vertical extent of faulting of large earthquakes is usually inferred from the extent of the aftershock activity. This method, however, is indirect and vague. The lack of aftershocks at a large depth does not necessarily mean that no seismic slip occurs there. Because of the increased temperature at large depths, the fault zone there may not be capable of generating aftershocks, even if it can slip coseismically when driven by slip at shallow depths.

The vertical extent of faulting could be estimated from geodetic data, but for these large earthquakes along subduction zones, geodetic coverage is seldom complete enough to determine the depth of faulting. Modeling of seismic body waves often provides a good estimate of the hypocentral depth (e.g. Sipkin, 1982). For these large earthquakes, however, body waves are often off-scale or, even if they are on-scale, too complex to model. Furthermore, the

hypocentral depth does not necessarily represent the overall vertical extent of faulting. It thus appears that the use of long-period seismic waves is the only means to directly determine the depth of faulting.

Several methods using surface waves to determine the earthquake depth have been developed (e.g. Harkrider, 1970; Tsai and Aki, 1971; Mendiguren, 1977; Romanowicz and Guillemant, 1984; Romanowicz and Monfret, 1986; Zhang and Kanamori, 1987b). Recently several methods have been developed to determine the earthquake source mechanism from surface-wave and free-oscillation data (e.g. Dziewonski, et al. 1981; Kanamori and Given, 1981; Dziewonski and Woodhouse, 1983; Silver and Jordan, 1982; 1983). In these methods, the source is usually assumed to be a point source, or approximated by a centroid. While these methods are useful to determine the gross source parameters, more analysis is warranted to resolve fine structures of the individual source. In this study, I determined the depths of the May 26, 1983 Akita-Oki, Japan earthquake ($02^h\,59^m\,59.6^s\,UT$, $40.462^o\,N$, $139.102^o\,E$, 24 km, $M_s = 7.7$), and the August 19, 1977 Sumbawa, Indonesia earthquake ($06^h\,08^m\,55.2^s\,UT$, $11.085^o\,S$, $118.464^o\,E$, 33 km, $M_s = 7.9$).

The Sumbawa earthquake is one of the largest normal-fault earthquakes, and its depth extent has an important bearing on the state of stress in the oceanic plate at subduction zones. The Akita-Oki earthquake has been studied thoroughly by many investigators using seismic, geodetic and tsunami data, and its depth extent is determined well. Thus I hope that comparison of these two events will provide an important constraint on the vertical extent of the Sumbawa earthquake.

For each earthquake, I first inverted the spectra of long-period Rayleigh waves of fundamental modes (150 to 300 sec) to determine the depth and the mechanism using the method presented in Chapter 2 of this thesis. Second, I directly compared the observed seismograms of fundamental-mode and overtone Rayleigh-waves with synthetic seismograms computed for various depths with a given source mechanism to estimate the depth. These two methods yielded consistent results on the vertical extent of the earthquakes, which are 30 km for the Akita-Oki earthquake and 50 to 80 km for Sumbawa earthquake.

3.2 Inversion of Fundamental-Mode Rayleigh Waves

In the following, I invert the complex spectra of fundamental-mode Rayleigh waves of periods from 150 to 300 sec for a moment tensor or a double couple to determine the depths and source mechanisms of the Akita-Oki and Sumbawa earthquakes. We use digital seismograms recorded at IDA (International Deployment of Accelerographs: Agnew et al. 1976) and GDSN (Global Digital Seismograph Network: Engdahl et al. 1982) stations. The GDSN seismograms were low-pass filtered with a cut-off period of 30 sec and decimated to a sample per 10 sec. The vertical component seismograms of Rayleigh waves were windowed, tapered, and Fourier-transformed to obtain the displacement spectra.

We used seven periods, 150, 175, 200, 225, 250, 275, and 300 sec for the inversion. The data with periods shorter than 150 sec were not included because they were strongly affected by the lateral heterogeneity of the earth

and the effects cannot be removed properly using the presently available earth models. At periods longer than 300 sec, the signal becomes small and the excitation of surface waves becomes insensitive to the depth of the source due to the very large wavelength.

We used the same data sets as those used in Chapter 1 for both earthquakes. The source spectra are obtained from the spectra of observed seismograms corrected for the effects of source finiteness and propagation. The estimates of the depth of large earthquakes obtained from the inversion of the source spectra depend on the models of source finiteness, propagation, and excitation (Chapter 2).

3.2.1 Correction for Source Finiteness

In the correction for the effects of source finiteness the finiteness is often represented by a source process time. In this simplest correction, the source is represented by a point source with finite duration that represents the overall duration of rupture and the source dislocation time, and the correction is independent of the azimuth. We call this a constant source-finiteness model (CSF). If the geometry and the length of the rupture are known, the finiteness factor can be calculated as a function of the azimuth. We call this a variable source-finiteness model (VSF).

The source finiteness of large earthquakes is usually inferred from the aftershock area. Hypocenter determination for aftershocks of the Akita-Oki earthquake recorded by microearthquake networks in the Tohoku district suggests that the rupture of the main shock is about 120 km long toward the

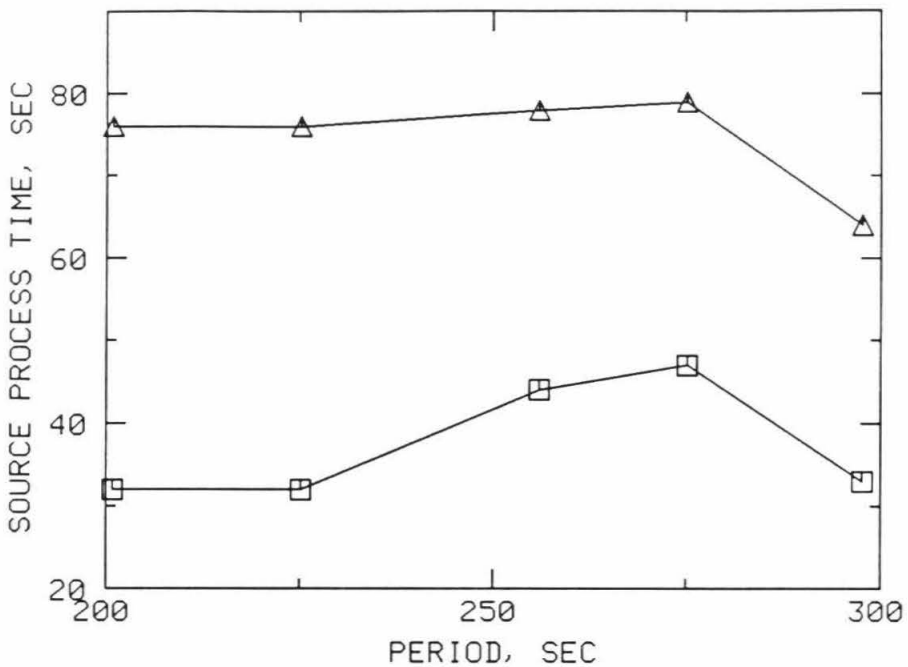

Figure 3.1 Source-process time of the 1983 Akita-Oki earthquake (squares) and the 1977 Sumbawa earthquake (triangles) determined at the periods of 200, 225, 256, 275, and 300 sec from the inversion method. Source-process times are obtained using the phase velocities of a laterally heterogeneous earth model (M84C) obtained by Woodhouse and Dziewonski (1984).

north from the epicenter of the main shock (Umino et al. 1985; Sato et al. 1986). For the Sumbawa earthquake, the aftershock area extends about 200 km in the $N60^{o}E$ direction with the main shock at the middle of the area (Fitch et al. 1981; Spence, 1986).

The first model of the source finiteness, CSF, is a point source with finite duration, represented by the source-process time. In Chapter 1 I determined the source-process times of the Akita-Oki and Sumbawa earthquakes from long-period Rayleigh waves using two methods, a linear inversion method and Furumoto's method (Furumoto, 1979; Furumoto and Nakanishi, 1983). The results obtained by these methods are consistent. Figure 1 shows that the source process times of these earthquakes measured at various periods from 180 to 300 sec by the linear inversion method. In this method, first, individual measurements were made at each period. Then the average of the measurements at periods of 256 and 275 sec is taken as our estimate of the source-process time, which is 46 sec for the Akita-Oki earthquake and 79 sec for the Sumbawa earthquake respectively.

For the Akita-Oki earthquake, the estimate of the source-process time is consistent with the overall rupture time if the rupture velocity is about 2.5 km/sec and the rupture length is about the same as that of the aftershock area.

The source-process time of the Akita-Oki earthquake has been measured by Satake (1985) using Furumoto's method and Dziewonski et al. (1983) using the centroid-moment-tensor (CMT) technique. Our result is consistent with theirs. However, there is a significant difference between the estimates of the source-process time of the Sumbawa earthquake obtained from different

methods, which range from a few sec to 79 sec (Silver and Jordan, 1983; Furumoto and Nakanishi, 1983; Giardini et al. 1985; Silver et al. 1986; Zhang and Kanamori, 1987a). The cause of this large discrepancy is not known.

The second model of the source finiteness, VSF, is a finite fault model, which consists of the length and direction of the rupture and the dislocation time. Using the source-finiteness function introduced by Ben-Menahem (1961), In Chapter 1 I determined the rupture extent and direction of the two earthquakes by the inversion of the spectra of long-period Rayleigh waves. For a rupture velocity of 2.5 km/sec, the estimated rupture was unilateral and 100 km long and along the strike $N26^{o}\ W$ for the Akita-Oki earthquake, and bilateral and in the direction $N60^{o}\ E$ for the Sumbawa earthquake. These azimuthally dependent source finiteness models, VSF, are consistent with the aftershock area of these earthquakes. In these models, a ratio of the rise time to the rupture time of 0.1 is assumed for the Akita-Oki earthquake and 0.6 for the Sumbawa earthquake, which correspond to a rise time of about 4 and 30 sec respectively. For the Sumbawa earthquake, if the average rupture velocity is between 2 and 3 km/sec and the rupture is bilateral with the fault length comparable to that of the aftershock area, the 79 sec source-process time suggests that the earthquake has a considerably larger rupture extent in the down-dip direction than that of the Akita-Oki earthquake (Chapter 1).

We used the two models of the source finiteness, CSF and VSF, for the Akita-Oki earthquake and for the Sumbawa earthquake described above to correct for the source finiteness in the determination of the depths and mechanisms of these earthquakes.

3.2.2 Correction for Propagation

In correcting for the attenuation effects I used the average group velocities obtained by Nakanishi and Anderson (1983) and Q values given by Dziewonski and Steim (1982). For the propagation phase shifts, I used the two phase-velocity models. The first is a laterally homogeneous one (denoted by HOM) that consists of the phase velocity data compiled by Gilbert and Dziewonski (1975). The second is a laterally heterogeneous one (denoted by HVD) calculated for the model M84C obtained by Woodhouse and Dziewonski (1984).

3.2.3 Inversion Results

We determine the depths and source mechanisms from long-period fundamental-mode Rayleigh waves using the method presented in Chapter 2 of this thesis, which is essentially similar to the method proposed by Romanowicz and Guillemant (1984) and Romanowicz and Monfret (1986). We formulate the inversion of surface waves for a moment-tensor source (linear) or a double couple source (nonlinear) as (equation (11) in Chapter 1 and equation (13) in Chapter 2)

$$B\ D = V\ , \tag{15}$$

and

$$\Gamma\ M = \Lambda\ . \tag{16}$$

In (15) vector V consists of real and imaginary parts of the observed Rayleigh-wave spectra after corrections have been made for the propagation effects and

the source finiteness effects, the elements of matrix B consists of trigonometric functions of the station azimuth. In the determination of the depth and source mechanism, (15) is solved first for the vector D at several frequencies: $\omega_1, \omega_2, \cdots, \omega_K$. In (16), Λ is a vector which consists of the components of D obtained by solving (15), Γ is a matrix of excitation functions. The elements of the vector M are linear combination of the moment tensor components for the moment tensor inversion, and trigonometrical functions of fault-orientation parameters for the fault inversion. The moment tensor or double couple is obtained by solving (16).

The inversion of (16) is performed to obtain $\mathrm{M} = \hat{M}$ for a fixed point source depth, and the root-mean-square residual, $rms = \sqrt{(\Gamma \hat{M} - \Lambda, \Gamma \hat{M} - \Lambda) / 5K}$, is calculated. We invert (16) for a moment tensor or a double couple at various depths and obtain the best depth that minimizes the rms. This procedure is essentially similar to those used by Romanowicz and Guillemant (1984). In the inversion of (16), I use the excitation functions computed for an average ocean model of Regan and Anderson (1984).

A similar inversion can be performed for a source extending from the surface to a depth using excitation functions calculated for an extended source (Kanamori and Given, 1981). In the average ocean model of Regan and Anderson (1984), the ocean bottom, which is at about 5 km in depth, is the upper limit of the extended source.

For the Akita-Oki earthquake, I inverted about 26 Rayleigh wave phases (R_2 and R_3) obtained from the IDA and GDSN network stations. Using the laterally heterogeneous model M84C and the source-finiteness model VSF, I

inverted the data for various depths. Figure 2 shows the *rms* (with its minimum subtracted) as the function of depth. We found that a point source depth of 18 km minimizes the residual. We used a student's t test described in Chapter 2 to estimate the uncertainty of the depth obtained from this method. The 90% confidence limit constrains the centroid depth between 8 and 34 km. For the extended source model, I obtained approximately 29 km for the vertical extent of the faulting.

The moment tensor solution obtained for a point source at the depth of 18 km is essentially a pure double couple; the scalar moment of the minor double couple of the moment tensor is less than 2 percent of that of the major double couple of the moment tensor. The source parameters of the best fit point-source model are: 1st nodal plane; strike = 24^o, dip = 21^o, slip angle = 124^o; 2nd nodal plane; strike = 168^o, dip = 73^o, slip angle = 78^o; seismic moment = 8.1×10^{27} dyne.cm ($M_W = 7.9$). This solution is in accord with the nodal plane solution of the first-motion data obtained by Ishikawa et al. (1984) and the solutions by inversion of long-period surface waves and modeling of tsunami waveforms obtained by Satake (1985) and Kanamori and Astiz (1985).

Figure 3 compares the amplitude and phase spectra of observed seismograms with those computed for the best fit model. At the period of 300 sec, the fit is satisfactory for both the amplitude and phase. At 225 sec, however, the amplitude data show a considerable scatter. At 150 sec, both the amplitude and phase data show a large scatter suggesting that the laterally heterogeneous model here is poorer at this period than at longer periods. Since the data from relatively short periods (100 to 150) are important for the depth

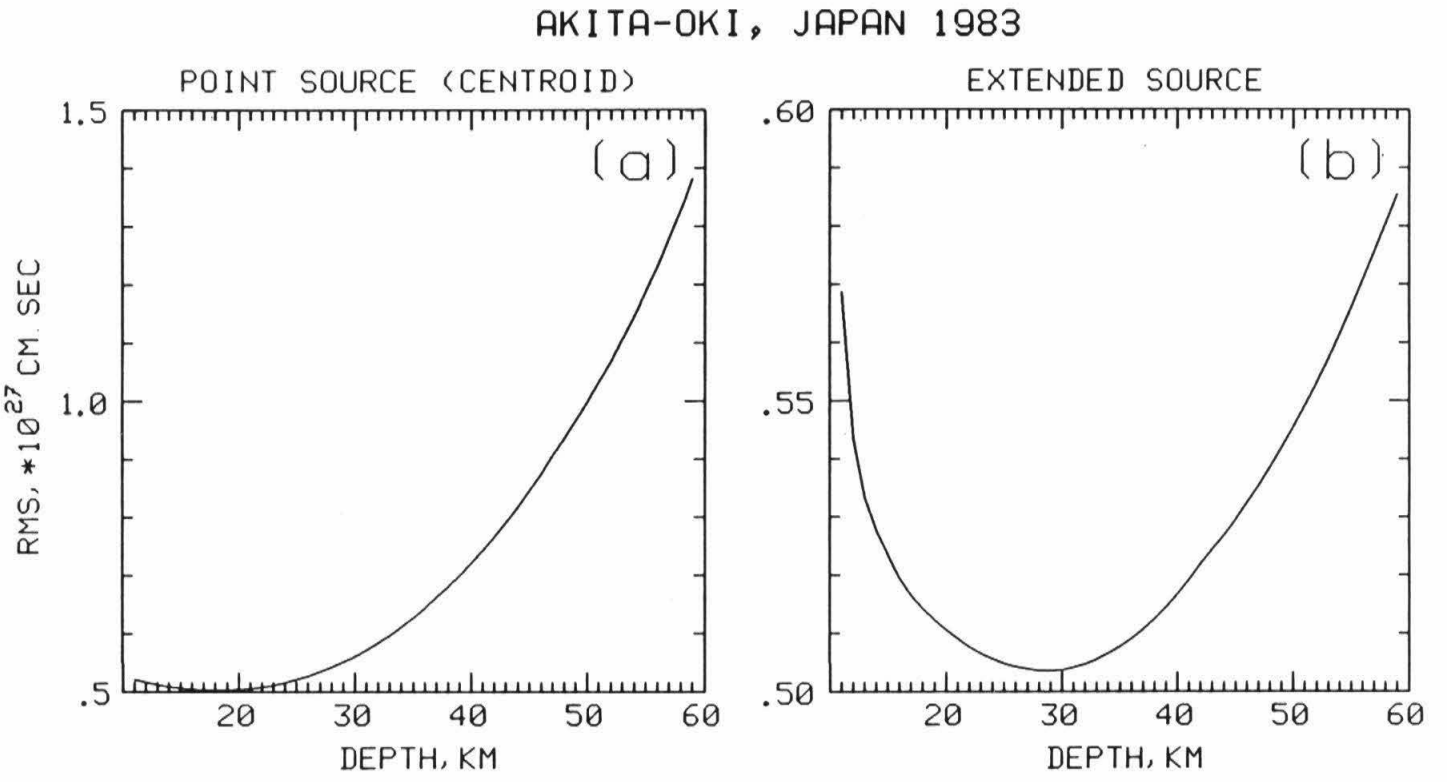

Figure 3.2 26 May 1983 Akita-Oki, Japan earthquake. The root-mean-square residual versus depth curves are given for the finite-fault model. (a) point source (centroid) by the moment tensor inversion; (b) distributed source by the moment tensor inversion.

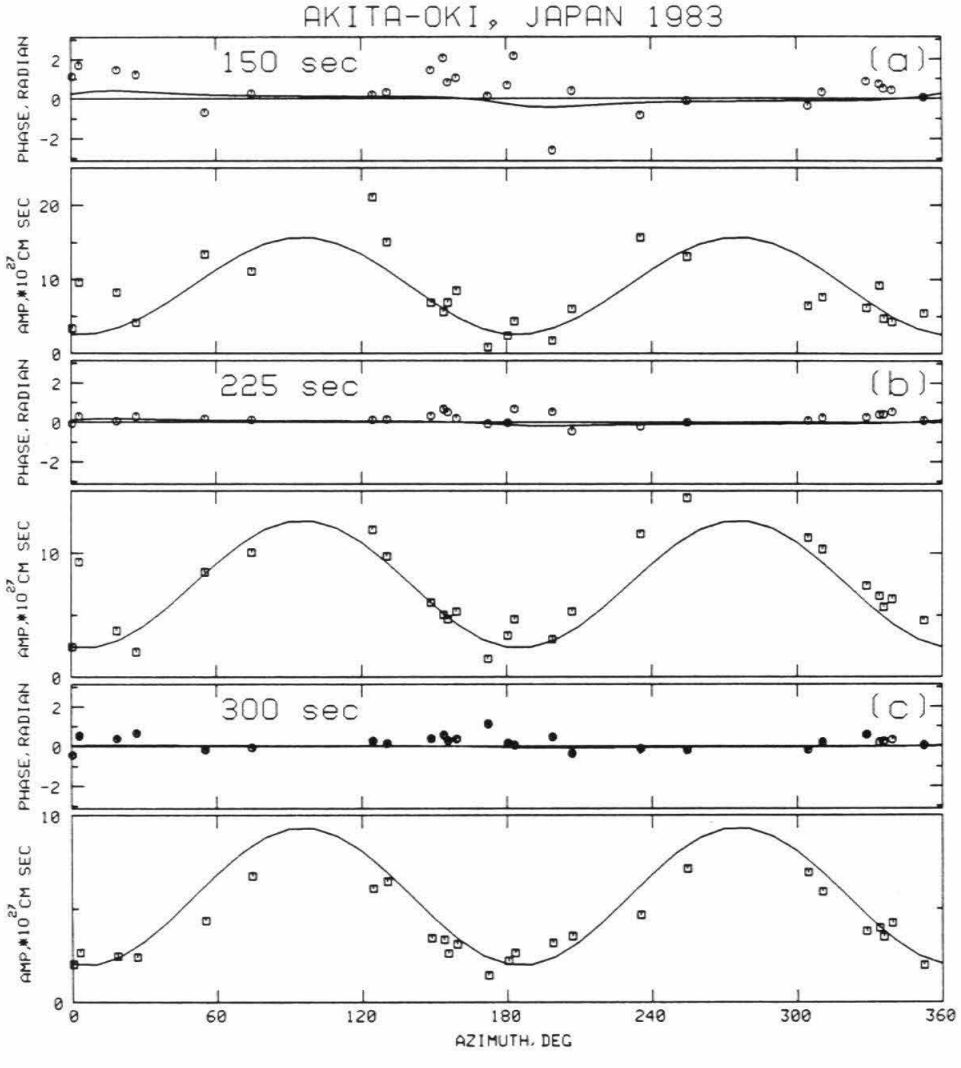

Figure 3.3 Comparison of the observed amplitude and phase with the predicted values from results by the moment tensor inversion for the Akita-Oki earthquake.

determination, a better earth model which would allow the use of these short period waves for the inversion is desirable.

For the Sumbawa earthquake, I used about 20 Rayleigh wave phases recorded at IDA and GDSN stations. Since many IDA stations were off-scale for a few hours after the origin time, I had to use later phases such as R_4 and R_5 in the inversion. We used the model VSF in correcting for the source-finiteness. Figure 4 shows the *rms* (with its minimum subtracted) as the function of depth. For the point source model, a depth of 48 km is obtained. For the extended-source model, I obtained 96 km depth. In general, the best point-source depth is about 1/2 of the vertical extent of the fault. Hence, in the following, I interpret the point-source depth to be half the vertical extent of the faulting.

The ratio of the minimum *rms* obtained for the Sumbawa earthquake to that for the Akita-Oki earthquake is about twice larger than the ratio of the scalar moments of these earthquakes. This suggests that the noise in the data set for the Sumbawa earthquake is much larger than that for the Akita-Oki earthquake. Because of this large noise, the uncertainty in the depth of this earthquake is larger than that for other earthquakes studied in Chapter 2. The 80% and 90% confidence limits for the centroid depth of the Sumbawa earthquake are 21 to 58 km and 11 to 62 km respectively. Despite this large uncertainty, however, we can conclude that the centroid depth of the Sumbawa earthquake is significantly larger than that of the Akita-Oki earthquake.

For the point source at 48 km depth, the source parameters are: 1st nodal plane; strike $= 289^o$, dip $= 65^o$, slip angle $= 300^o$; 2nd nodal plane; strike $= 55^o$, dip $= 38^o$, slip angle $= 223^o$; seismic moment $= 7.2 \times 10^{28}$ dyne.cm

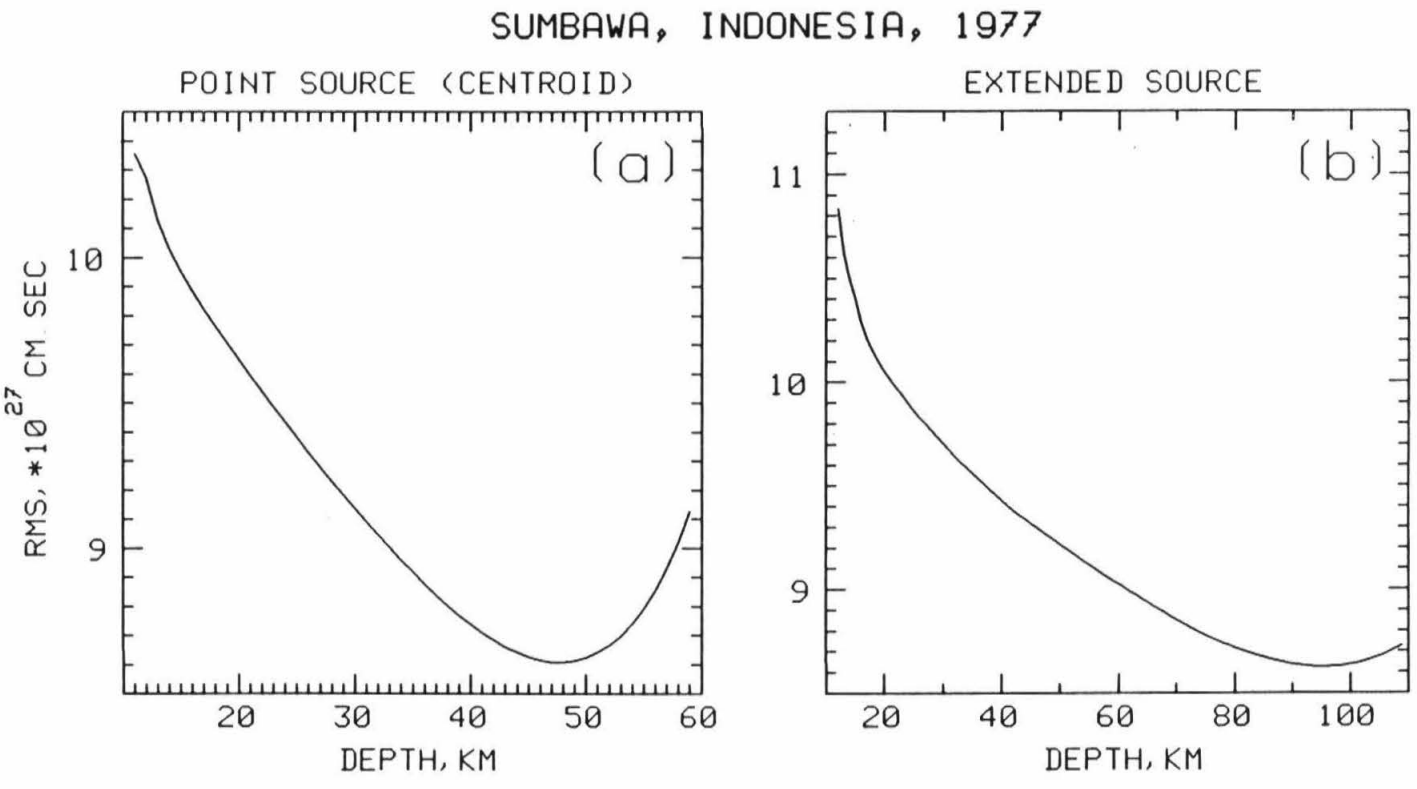

Figure 3.4 19 August 1977 Sumbawa, Indonesia earthquake. The root-mean-square residual versus depth curves are given for the finite-fault model. The result is shown for a point source (a) and an extended source (b).

($M_W = 8.5$).

On the basis of these preliminary results, I examined effects of the lateral heterogeneity, source finiteness, and excitation function, which may introduce biases in the depth determination. We first compare the *rms* of the inversion using various combinations of the phase-velocity models, HOM and HVD, and source-finiteness models, CSF and VSF.

Figure 5 shows the variation of the *rms* for various combination of the structure of the phase velocity and the source finiteness models. The results are shown for periods of 175 sec, 256 sec, and a combination of the 7 periods. The variance reduction given by F value (the ratio of the variance before and after each step) is shown. For both earthquakes, the critical value in a F test for the 95% confidence is about 1.7 for the inversion at a single period and less than 1.5 for the inversion at a combination of the 7 periods respectively. Figure 5 indicates that the variance reduction by introduction of the laterally heterogeneous model was significant at the 95% confidence level for the inversion. Tanimoto and Kanamori (1986) made a similar comparison for many large events. These examples demonstrate that the use of a laterally heterogeneous model is crucial for a better depth determination.

The introduction of the azimuthally dependent source finiteness effect did not significantly reduce the variance. Since the ruptures of these earthquakes are more likely unidirectional than multi-directional as suggested by the spectra of the long-period Rayleigh waves and aftershock areas of these earthquakes, the model VSF is certainly superior to the model CSF to approximate the source finiteness of these earthquakes.

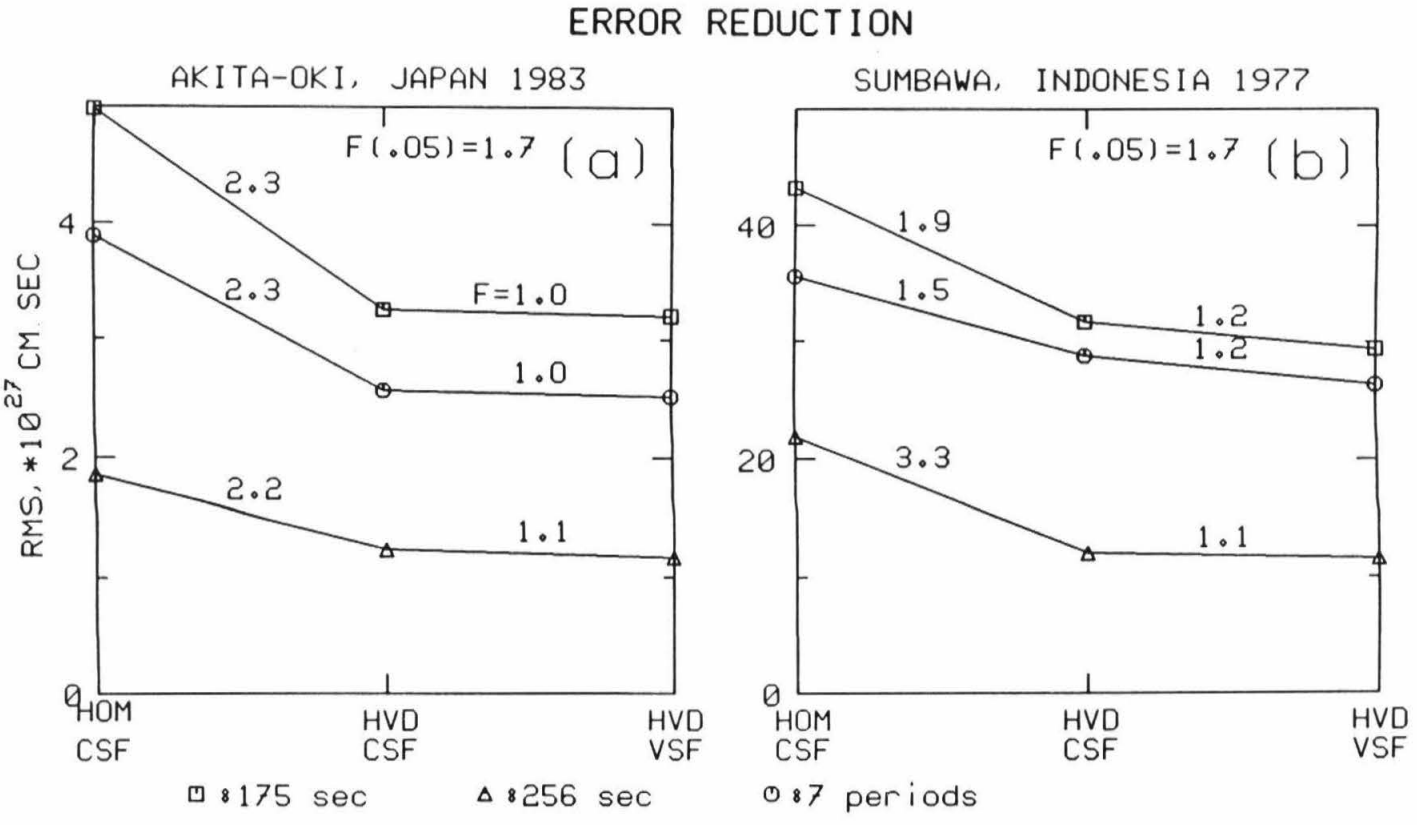

Figure 3.5 The root-mean-square residual of the inversion for various combination of the earth models and the source finiteness.

3.3 Overtone Amplitude

Although these results obtained from fundamental-mode surface waves were encouraging, it is desirable to obtain an independent estimate of the depth from other data. To this end, I used surface-wave overtone amplitude data. In general, the amplitude ratio of overtone to fundamental-mode surface waves increases as the depth increases. For both the Akita-Oki and Sumbawa earthquakes, Rayleigh-wave overtone were recorded clearly.

Here I directly compare the observed surface-wave trains with synthetic seismograms to determine the source depth. We used the vertical component of the GDSN and IDA data, because the vertical component is not contaminated by Love waves and has a better signal-to-noise ratio. The seismograms used contain the fundamental R_2 and its higher order overtones and were selected to avoid the interferences from other phases.

Figure 6 shows the seismograms observed at several GDSN stations for the Akita-Oki earthquake. The traces are about 90 minutes long and the R_2 phases are aligned vertically. Synthetic seismograms were computed for each station by summing up 3355 normal modes with periods greater than 45 sec of the earth model 1066A (Gilbert and Dziewonski, 1975). The synthetic seismograms were computed for sources at depths of 15, 20, 40, and 50 km respectively, using the fault mechanism obtained by Kanamori and Astiz (1984) and a 46 sec source-process time. Since the effect of lateral heterogeneities of the structure is large at periods shorter than 100 sec, the observed and synthetic seismograms are filtered with a Gaussian band-pass filter with a passband from 80 to 1500 sec.

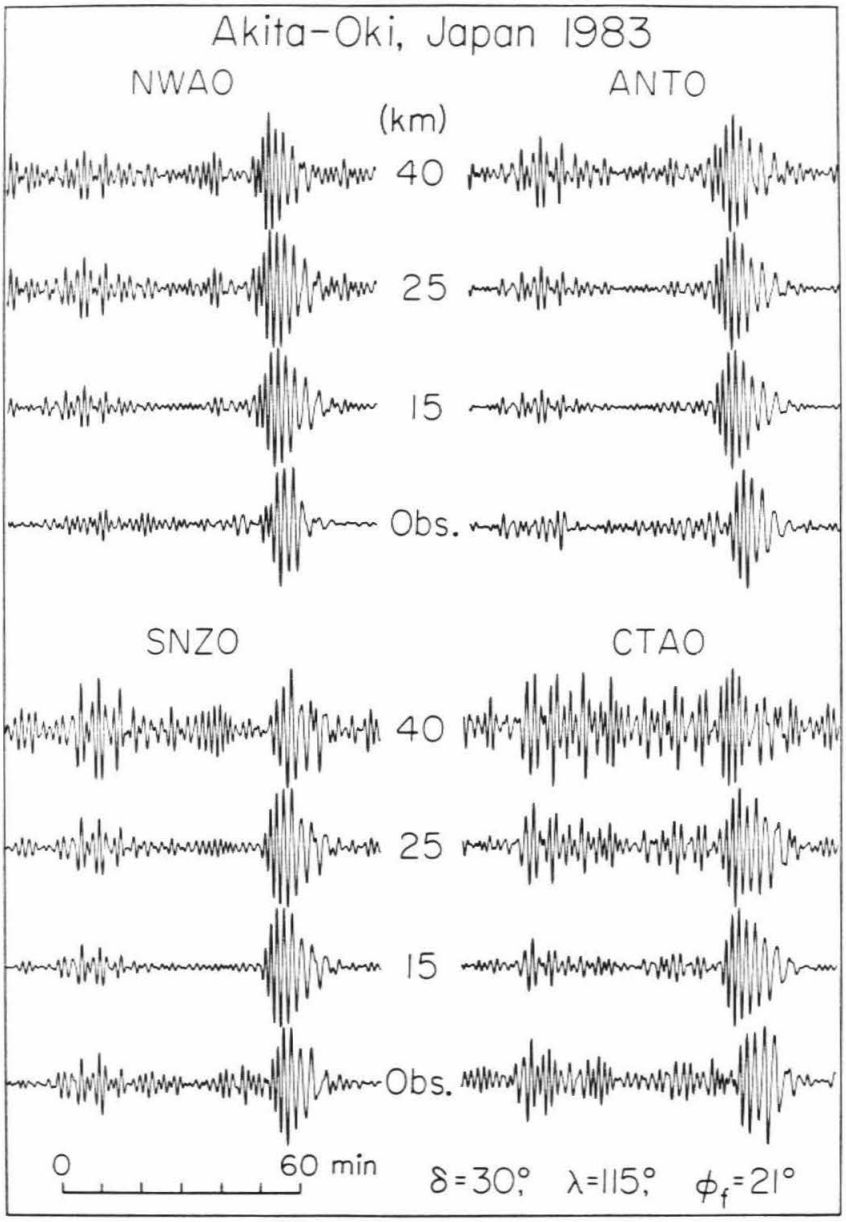

Figure 3.6 Comparison of the observed Rayleigh waves for the Akita-Oki earthquake (fundamental-mode and overtones of R_2) with synthetic seismograms computed for three depths, 15, 25, and 40 km. The stations used are NWAO, ANTO, SNZO, and CTAO.

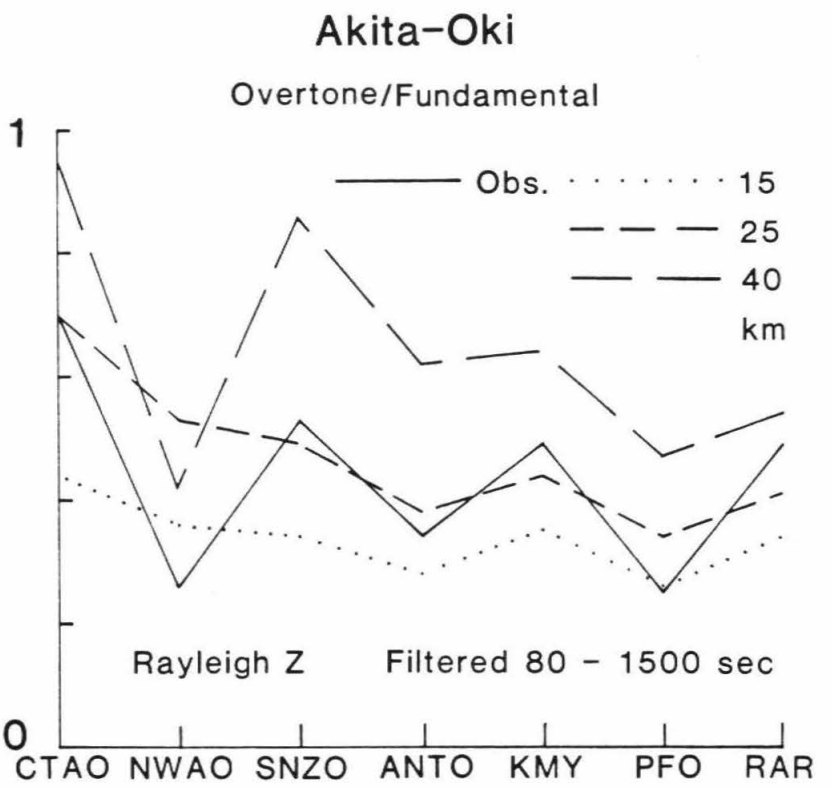

Figure 3.7 The amplitude ratios of overtones to fundamental-mode Rayleigh waves for the observed and synthetic seismograms at the GDSN stations of CTAO, NWAO, SNZO, ANTO, and IDA stations of KMY, PFO, and RAR.

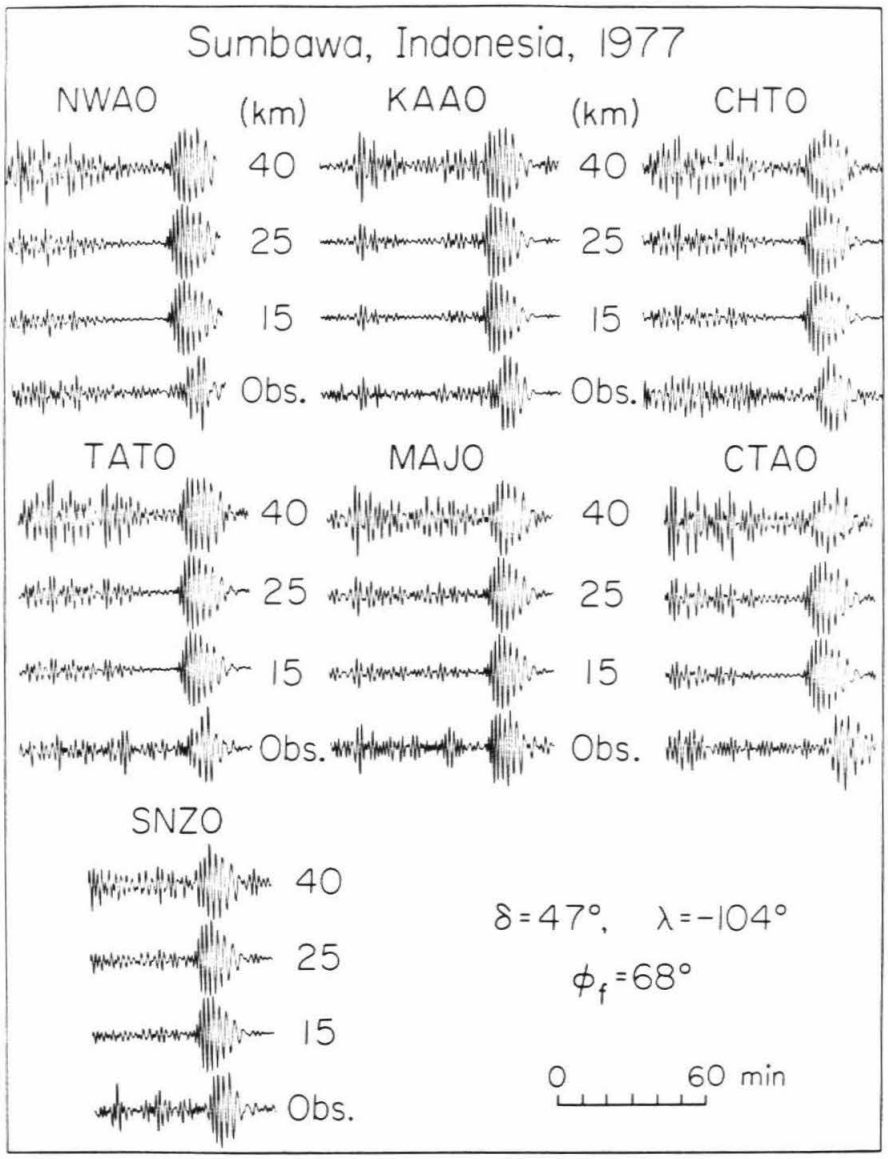

Figure 3.8 Comparison of the observed Rayleigh waves for the Sumbawa earthquake (fundamental-mode and overtones of R_2) with synthetic seismograms computed for three depths, 15, 25, and 40 km. The stations used are NWAO, KAAO, CHTO, TATO, MAJO, SNZO, and CTAO.

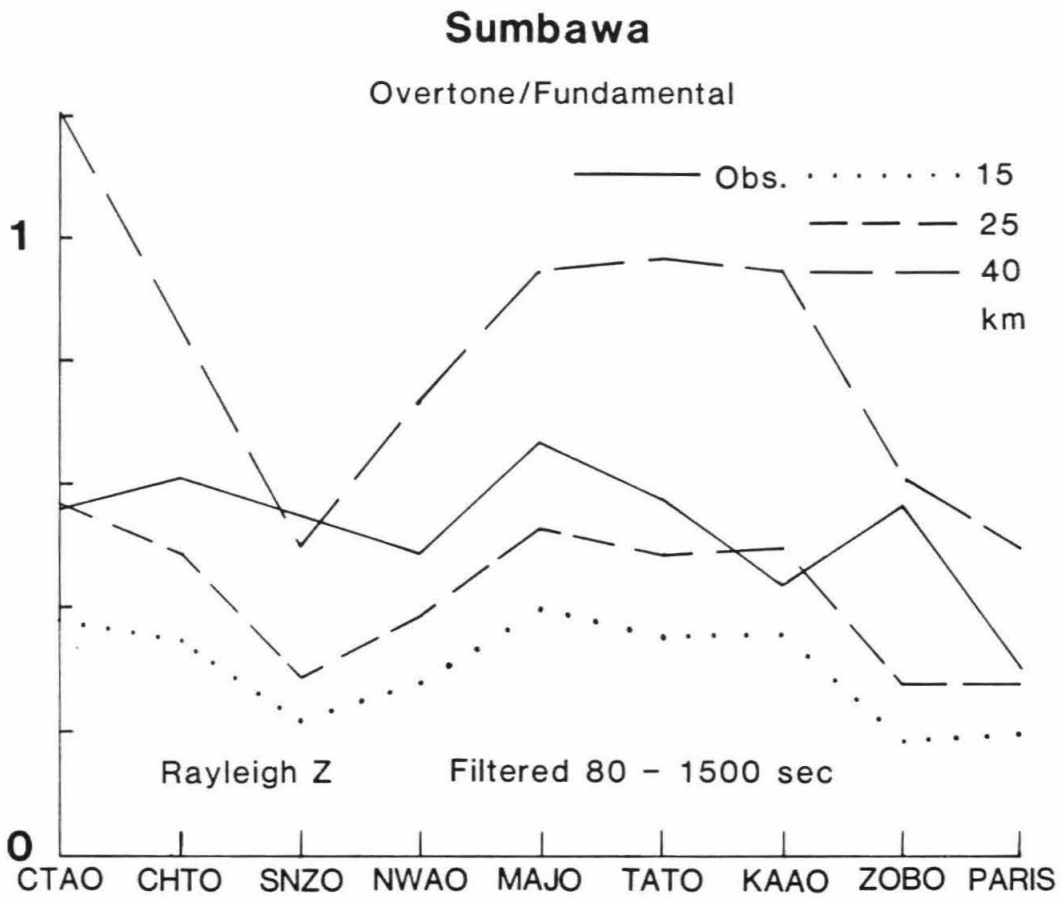

Figure 3.9 The amplitude ratios of overtones to fundamental-mode Rayleigh waves for the observed and synthetic seismograms at the GDSN stations of CTAO, CHTO, SNZO, NWAO, MAJO, TATO, KAAO, ZOBO and a French station at Paris.

Figure 6 compares the observed and synthetic seismograms for four GDSN stations. The amplitude ratio of the overtone to fundamental-mode surface waves on the observed seismogram is comparable to that of the synthetics for the depths of 15 or 25 km. Figure 7 compares the amplitude ratio for the observed seismogram with those for the synthetics for four GDSN and three IDA stations. The observed ratios indicate depths ranging from 10 to 30 km with the average of 17.5 km.

For the Sumbawa earthquake, I computed the synthetic with the P-wave first motion solution ($\delta = 47^o, \lambda = -104^o, \phi_f = 68^o$) and a source process time of 79 sec. Figure 8 shows the results. The observed ratios indicate depths ranging from 20 to 40 km, with the average of 35 km (Figure 9) using the seismograms recorded at 8 GDSN stations and by a ultra-long period seismograph operated in Paris by The Institute for the Physics of the Earth of the University of Paris. These depth estimates are slightly different from those obtained earlier by the inversion of fundamental-mode surface waves, but they agree within the errors involved in both methods.

3.4 Discussion

The Akita-Oki earthquake has been studied thoroughly by many investigators using seismic, geodetic and tsunami data, and the vertical extent of faulting is determined well. Figure 10 shows some of the results. Tada (1984) estimated the vertical extent of faulting to be 35 km. An analysis of the tsunami data by Aida (1984) indicates that the fault motion extended to a depth of 30 km. The aftershocks have been located accurately using the

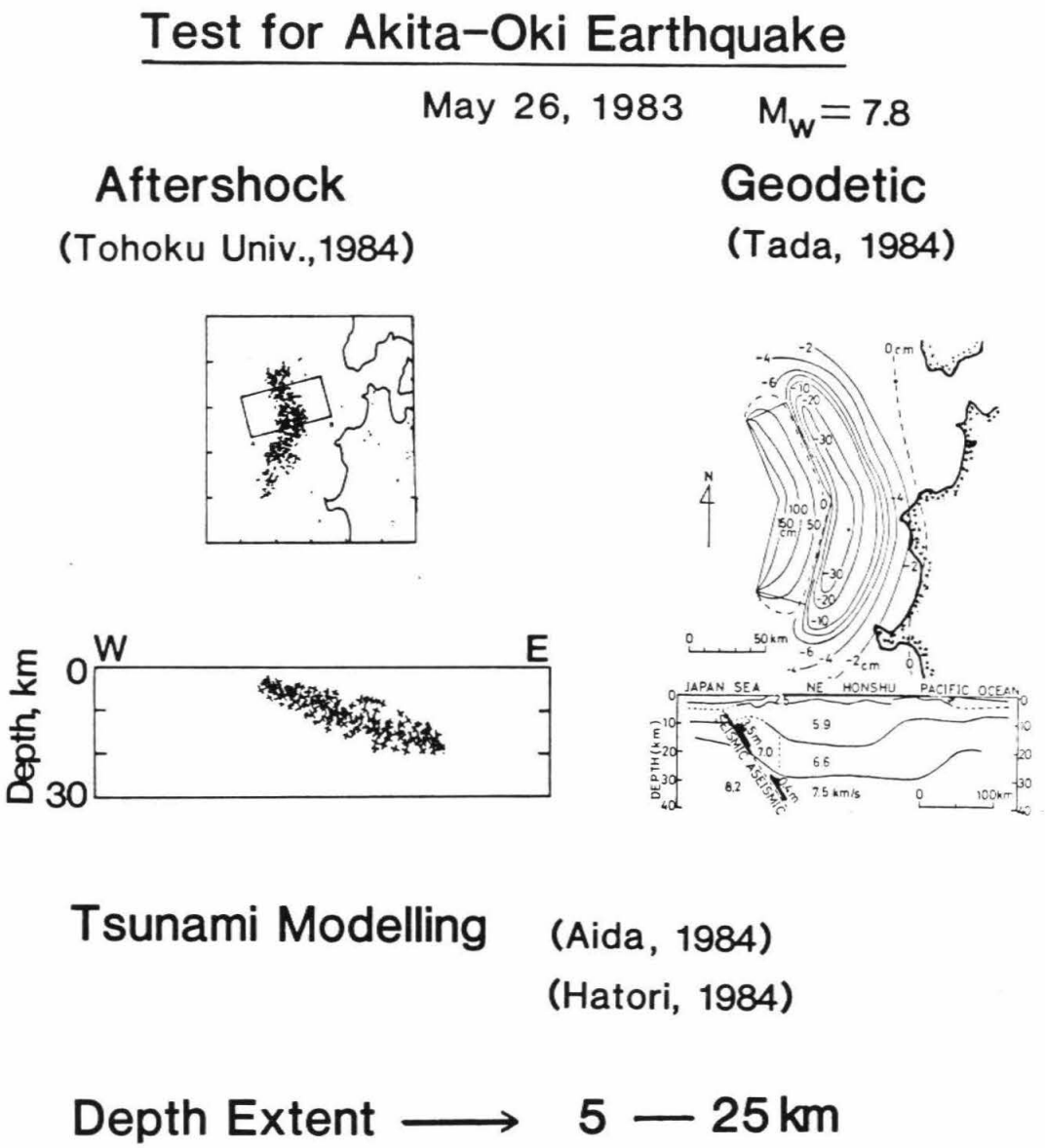

Figure 3.10 Depth of the 1983 Akita-Oki earthquake estimated from various data.

seismic networks as well as ocean-bottom seismographs of the Tohoku University and of Hirosaki University (Umino et al., 1985; Sato et al., 1986). As shown in the figure, the aftershock activity extends to a depth of 20 km.

These results suggest that the vertical extent of faulting of the Akita-Oki earthquake is approximately 30 km or less. The results of our surface-wave analysis suggest that it is 30 $\pm$ 5 km, which agrees reasonably well with that obtained from the other data.

The fault plane mapped by the aftershock distribution changes its strike halfway along the length of the aftershock area, striking in $N15^{o} - 20^{o} E$ in the southern part and $N10^{o} - 15^{o} W$ in the northern part, and dips in an easterly direction with an angle of about 20^{o} for both parts of the fault (Sato et al., 1986). The fault parameters obtained here from the inversion of long-period Rayleigh waves with a point source (centroid) at the depth of 18 km are consistent with those inferred from aftershock distributions.

Combining the centroid depth of 48 $\pm$ 10 km estimated from the fundamental-mode Rayleigh waves, and 35 km estimated from the overtones, I estimate that the centroid depth of the 1977 Sumbawa earthquake ranges from 30 to 40 km. If the fault plane extends to the surface, the above estimate indicates a vertical extent of faulting of 60 to 80 km. If the fault plane extends to a depth of 10 km, the vertical extent is 50 to 70 km. The uncertainties caused by many factors such as the unknown dislocation distribution of slip on the fault plane and the complex structure near the source area precludes a very accurate determination of the vertical extent. Nevertheless, the comparison of this earthquake with the Akita-Oki earthquake suggests that the faulting of the Sumbawa earthquake extends over a significantly larger depth

range than the Akita-Oki earthquake, and involved a substantial part of the oceanic plate. Although the absolute value is somewhat uncertain, the depth relative to that of the Akita-Oki earthquake is more reliable.

When only long-period waves are used, the *rms* value does not vary much as a function of depth. In contrast, the effect of the lateral heterogeneity and the source finiteness has a significant effect on *rms*. It is therefore important to use a good earth model (laterally heterogeneous) and a source finiteness model in the inversion. Only after the corrections for the lateral heterogeneity and the source finiteness have been made accurately, can the depth determination be made with a good accuracy.

We also used the CSF model to determine the depths of these earthquakes, the result remains about the same as that for the VSF model. Since the fault length of these events is relatively short, the azimuthally dependent part of the source finiteness effect is small and the azimuthally independent source delay is sufficient for the present purpose. For earthquakes with a larger fault length, however, azimuthally dependent finiteness corrections become increasingly important.

3.5 Conclusions

We determined the vertical extent of faulting of the 1983 Akita-Oki, Japan and the 1977 Sumbawa, Indonesia earthquakes using long-period surface waves. We used two independent data sets. First data set consists of the spectra of Rayleigh waves of periods from 150 to 300 sec. Second data set consists of the amplitude ratio of overtones to fundamental-mode Rayleigh

waves. Using the first data set, I used the moment tensor inversion to find the source depth. We used the laterally heterogeneous earth model obtained by Woodhouse and Dziewonski (1984) and a detailed model of source finiteness. These models significantly improved the moment tensor inversion. Using the second data set, I compared the amplitude ratio of observed seismograms with that of the synthetic seismograms computed for various depths. The estimates of vertical extent of faulting is 30 km for the Akita-Oki earthquake and 50 to 80 km for the Sumbawa earthquake. A combination of these two methods provided a more reliable estimate of the vertical faulting of these earthquakes.

3.6 References

Agnew, D., Berger, J., Buland, R., Farrell, W. and Gilbert, F., 1976. International deployment of accelerograms: a network for very long period seismology. *EOS Trans. AGU*, 57: 180-188.

Aida, I., 1984. A source model of the tsunami accompanying the 1983 Nihonkai-Chubu earthquake. *Bull. Earthq. Res. Inst. Univ. Tokyo*, 59: 93-104 (in Japanese).

Anderson, D.L. and Given, J.W., 1982. Absorption band Q model for the Earth. *J. Geophys. Res.*, 87: 3893-3904.

Ben-Menahem, A., 1961. Radiation of seismic surface waves from finite moving sources. *Bull. Seism. Soc. Am.*, 51: 401-435.

Chapple, W.M. and Forsyth, D.M., 1979. Earthquakes and bending of plates at trenches. *J. Geophys. Res.*, 84: 6729-6749.

Christensen, D. and Ruff, L.J., 1983. Outer-rise earthquakes and seismic coupling. *Geophys. Res. Lett.*, 10: 697-700.

Dziewonski, A.M., Chou, T.-A. and Woodhouse, J.H., 1981. Determination of earthquake source parameters from waveform data for studies of global and regional seismicity. *J. Geophys. Res.*, 86: 2825-2852.

Dziewonski, A.M. and Anderson, D.L., 1981. Preliminary reference Earth model. *Phys. Earth and Planet. Int.*, 25: 297-356.

Dziewonski, A.M. and Steim, J.M., 1982. Dispersion and attenuation of mantle waves through waveform inversion. *Geophys. J. R. astr. Soc.*, 70: 503-527.

Dziewonski, A.M. and Woodhouse, J.H., 1983. An experiment in systematic study of global seismicity: Centroid-moment tensor solutions for 201 moderate and large earthquakes of 1981. *J. Geophys. Res.*, 88: 3247-3271.

Dziewonski, A.M., Franzen, J.E. and Woodhouse, J.H., 1983. Centroid-moment tensor solutions for April-June 1983. *Phys. Earth and Planet. Int.*, 33: 243-249.

Engdahl, E.R., Peterson, J. and Orsini, N.A., 1982. Global digital networks - current status and future directions. *Bull. Seism. Soc. Am.*, 72: S242-S259.

Fitch, T.J., North, R.G. and Shields, M.W., 1981. Focal depths and moment tensor representations of shallow earthquakes associated with the great Sumba earthquake. *J. Geophys. Res.*, 86: 9357-9374.

Furumoto, M., 1979. Initial phase analysis of R waves from great earthquakes. *J. Geophys. Res.*, 84: 6867-6874.

Furumoto, M. and Nakanishi, I., 1983. Source times and scaling relations of large earthquakes. *J. Geophys. Res.*, 88: 2191-2198.

Giardini, D., Dziewonski, A.M. and Woodhouse, J.H., 1985. Centroid-moment tensor solutions for 113 large earthquakes in 1977-1980. *Phys. Earth Planet. Inter.*, 40: 259-272.

Gilbert, F. and Dziewonski, A.M., 1975. An application of normal mode theory to the retrieval of structure parameters and source mechanisms from seismic spectra. *Phil. Trans. R. Soc. Lond. A.*, 278: 187-269.

Hanks, T.C., 1971. The Kuril trench-Hokkaido rise system: large shallow earthquakes and simple models of deformation. *Geophys. J. R. astr. Soc.*, 23: 123-189.

Harkrider, D.G., 1970. Surface waves in multilayered media - II. Higher mode spectra and spectral ratios from point sources in plane-layered earth models. *Bull. Seism. Soc. Am.*, 60: 1937-1987.

Kanamori, H., 1971. Great earthquakes at island arcs and the lithosphere. *Tectonophysics*, 12: 187-198.

Kanamori, H., 1977. Seismic and aseismic slip along subduction zones and their tectonic implications. in *Island Arcs, Deep Sea Trenches, and Back-Arc Basins*, edited by M. Talwani and W. C. Pitman III, p. 163-174, American Geophysical Union, Washington, D. C.

Kanamori, H. and Astiz, L., 1985. The 1983 Akita-Oki earthquake ($M_w = 7.8$) and its implications for systematics of subduction earthquakes. *Earthq. Predict. Res.*, 3: 305-317.

Kanamori, H. and Given, J.W., 1981. Use of long-period surface waves for rapid determination of earthquake-source parameters. *Phys. Earth Planet. Inter.*, 27: 8-31.

Mendiguren, J.A., 1977. Inversion of surface wave data in source mechanism studies. *J. Geophys. Res.*, 82: 889-894.

Nakanishi, I. and Anderson, D.L., 1983. Measurements of mantle wave velocities and inversion for lateral heterogeneity and anisotropy - I. Analysis of great circle phase velocities. *J. Geophys. Res.*, 88: 10267-10283.

Peterson, E.T. and Seno, T., 1984. Factors affecting seismic moment release rates in subduction zones. *J. Geophys. Res.*, 89: 10233-10248.

Regan, J. and Anderson, D.L., 1984. Anisotropic models of the upper mantle. *Phys. Earth Planet. Int.*, 35: 227-263.

Romanowicz, B.A. and Guillemant, P., 1984. An experiment in the retrieval of depth and source mechanism of large earthquakes using very long-period Rayleigh wave data. *Bull. Seism. Soc. Am.*, 74: 417-437.

Ruff, L. and Kanamori, H., 1980, Seismicity and the subduction process; *Phys. Earth Planet. Int.*, 23: 240-252.

Satake, K., 1985. The mechanism of the 1983 Japan Sea earthquake as inferred from long-period surface waves and tsunamis. *Phys. Earth Planet. Inter.*, 37: 249-260.

Sato, T., Kosuga, M., Tanaka, K. and Sato, H., 1986. Aftershock distribution of the 1983 Nihonkai-Chubu (Japan sea) earthquake determined from relocated hypocenters. *J. Phys. Earth*, 34: 203-223.

Silver, P.G. and Jordan, T.H., 1982. Optimal estimation of scalar seismic moment. *Geophys. J. R. astr. Soc.*, 70: 755-787.

Silver, P.G. and Jordan, T.H., 1983. Total moment spectra of fourteen large earthquakes. *J. Geophys. Res.*, 88: 3273-3293.

Silver, P.G., Riedesel, M.A., Jordan, T.H. and Sheehan, A.F., 1986. Low frequency properties of the Sumbawa earthquake of 1977. *EOS Trans. AGU*, 67: 309.

Sipkin, S.A., 1982. Estimation of source parameters by the inversion of waveform data: synthetic waveforms. *Phys. Earth and Planet. Int.*, 30: 242-259.

Sipkin, S.A., 1986. Estimation of source parameters by the inversion of waveform data: global seismicity, 1981-1983. *Bull. Seism. Soc. Amer.*, 76: 1515-1541.

Spence, W., 1986. The 1977 Sumba earthquake series: Evidence for slab pull force acting at a subduction zone. *J. Geophys. Res.*, 91: 7225-7239.

Sykes, L.R. and Quittmeyer, R.C., 1981. Repeat times of great earthquakes along simple plate boundaries. in *Earthquake Prediction: An international Review, Maurice Ewing Ser.*, vol. 4, edited by D. W. Simpson and P. G. Richards, pp. 217-247, AGU, Washington, D. C.

Tada, T., 1984. Nihonkai-Chubu earthquake and crustal deformation. *The Earth Monthly*, 6: 18-21.

Tanimoto, T. and Kanamori, H., 1986. Linear programming approach to moment tensor inversion of earthquake sources and some tests on the three-dimensional structure of the upper mantle. *Geophys. J. R. astr. Soc.*, 84: 413-430.

Tsai, Y.B. and Aki, K., 1971. Amplitude spectra of surface waves from small earthquakes and underground nuclear explosions. *J. Geophys. Res.*, 76: 3440-3452.

Umino, N., Hasegawa, A., Obara, K., Matsuzawa, T., Shimizu, H., Takagi, A., Tanaka, K. and Kosuga, M., 1985. Hypocenter distribution of forshocks and aftershocks of the 1983 Japan sea earthquake. *Zisin*, 38: 399-410 (in Japanese).

Uyeda, S. and Kanamori, H., 1979, Back-arc opening and the mode of subduction. *J. Geophys. Res.*, 80: 1053-1064.

Ward, S.N., 1983. Body wave inversion: moment tensors and depths of oceanic intraplate bending earthquakes. *J. Geophys. Res.*, 88: 9315-9330.

Woodhouse, J.H. and Dziewonski, A.M., 1984. Mapping the upper mantle: Three-dimensional modeling of Earth structure by inversion of seismic waveforms. *J. Geophys. Res.*, 89: 5953-5986.

Zhang, J. and Kanamori, H., 1987a. Source finiteness of large earthquakes measured from long-period Rayleigh waves. *Phys. Earth and Planet. Int.*, in press.

Zhang, J. and Kanamori, H., 1987b. Depth of large earthquakes determined from long-period Rayleigh waves. submitted to *J. Geophys. Res.*

Appendix A

Inversion of Long-Period Rayleigh and Love Waves

For Love waves, equations of the inversion for the moment tensor or the double couple are described as follows, which are similar to those for Rayleigh waves.

A.1 Moment Tensor Inversion of Love Waves

For the transverse component of Love waves, the real (α) and imaginary (β) parts of the source spectrum (1) of a deviatoric moment tensor are

$$\alpha = -\frac{1}{2}P_L^{(1)}(\omega, h)(M_{yy} - M_{xx})\sin 2\phi - P_L^{(1)}(\omega, h)M_{xy}\cos 2\phi , \quad \text{(A1a)}$$

$$\beta = -Q_L^{(1)}(\omega, h)M_{xz}\sin\phi + Q_L^{(1)}(\omega, h)M_{yz}\cos\phi , \quad \text{(A1b)}$$

where ω is the angular frequency, $P_L^{(1)}$ and $Q_L^{(1)}$ are the excitation functions given by Kanamori and Stewart (1976), which depend on the elastic properties in the source region and the source depth (h).

For the moment tensor inversion, the first step solves the following system

$$B\ D = V , \quad \text{(A2)}$$

where

$$B = \begin{bmatrix} \frac{1}{2}\sin 2\phi_1 & -\cos 2\phi_1 & 0 & 0 \\ 0 & 0 & -\sin\phi_1 & \cos\phi_1 \\ \frac{1}{2}\sin 2\phi_2 & -\cos 2\phi_2 & 0 & 0 \\ 0 & 0 & -\sin\phi_2 & \cos\phi_2 \\ \cdot & \cdot & \cdot & \cdot \\ \cdot & \cdot & \cdot & \cdot \\ \cdot & \cdot & \cdot & \cdot \\ \frac{1}{2}\sin 2\phi_N & -\cos 2\phi_N & 0 & 0 \\ 0 & 0 & -\sin\phi_N & \cos\phi_N \end{bmatrix},$$

and

$$D = \Big[P_L^{(1)}(\omega, h)(M_{xx} - M_{yy}),\ P_L^{(1)}(\omega, h)M_{xy},\ Q_L^{(1)}(\omega, h)M_{xz},\ Q_L^{(1)}(\omega, h)M_{yz}\Big]^T,$$

and

$$V = \Big[\alpha(\omega, h, \phi_1),\ \beta(\omega, h, \phi_1),\ \cdots,\ \alpha(\omega, h, \phi_N),\ \beta(\omega, h, \phi_N)\Big]^T,$$

where N is the number of records obtained from stations with azimuths $\phi_1, \cdots, \phi_N$ from the source, and α and β are defined in (A1). B is an $2N \times 4$ real matrix, and V is a real vector with dimension 2N. The system (A2) is solved for $D(\omega)$ using the data vector $V(\omega)$ at several frequencies: $\omega_1, \omega_2, \ldots, \omega_K$.

The second step solves the following system

$$\Gamma M = \Lambda \tag{A3}$$

for the moment tensor from the vectors $D(\omega_i)$, $(i = 1, \ldots, K)$ for given

excitation functions, where

$$\Gamma = \left[\Gamma_1 , \Gamma_2 , \cdots , \Gamma_K \right]^T ,$$

$$\Gamma_i = diag \left[P_L^{(1)}(\omega_i , h), P_L^{(1)}(\omega_i , h), \right.$$

$$\left. Q_L^{(1)}(\omega_i , h), Q_L^{(1)}(\omega_i , h) \right], \qquad (i = 1, \ldots, K) ,$$

$$M = \left[(M_{xx} - M_{yy}), M_{xy} , M_{xz} , M_{yz} \right]^T ,$$

and

$$\Lambda = \left[D^T(\omega_1), D^T(\omega_2), \ldots, D^T(\omega_K)\right]^T .$$

A.2 Double Couple Inversion of Love Waves

For a double-couple source, (A1) is replaced by

$$\alpha = P_L^{(1)}(\omega, h) M_o \; p_L , \tag{A4a}$$

$$\beta = Q_L^{(1)}(\omega, h) M_o \; q_L , \tag{A4b}$$

respectively, where M_o is the scalar seismic moment, p_L and q_L are determined from the fault parameters, dip angle δ, slip angle λ, and strike ϕ_f defined by Ben-Menahem et al. (1965) (also see Kanamori and Stewart, 1976).

For the fault inversion, the system (A2) is solved in the first step for $D(\omega)$ at various frequencies. Here the matrix B remains unchanged, while the vector $D(\omega)$ is replaced by

$$D = \left[- P_L^{(1)}(\omega, h)m_2, P_L^{(1)}(\omega, h)m_1, Q_L^{(1)}(\omega, h)m_5, Q_L^{(1)}(\omega, h)m_4 \right]^T ,$$

where m_i (i=1,...,5) are defined in the text.

In the second step, a system in the form of (A3) is solved for M_o, δ, λ, and ϕ_f using the vector Γ. Here Γ_i ($i=1, \ldots, K$) remain the same as in (A3); while the vector M in the system is replaced by $M = (-m_2, m_1, m_5, m_4)$, where m_i (i=1,...,5) are nonlinear functions of δ, λ, and ϕ_f.

A.3 Moment Tensor and Double Couple Inversion of both Rayleigh and Love Waves

If both Rayleigh waves and Love waves are used, equations for the first step and the second step are similar to (4), (A2), and (13), (A3) respectively. For the moment tensor inversion, the first step solves the following system

$$B\ D = V\ , \tag{A5}$$

where

$$B = \left[B_1^T\ , B_2^T\ , \ldots, B_N^T\right]^T\ ,$$

$$B_i = \left[B_{iR}^T\ , B_{iL}^T\right]^T\ , \qquad (i = 1, \ldots, N)\ ,$$

$$B_{iR} = \begin{bmatrix} -\sin 2\phi_i & \frac{1}{2}\cos 2\phi_i & -\frac{1}{2} & 0 & 0 & 0\ 0\ 0\ 0 \\ 0 & 0 & 0 & \sin\phi_i & \cos\phi_i & 0\ 0\ 0\ 0 \end{bmatrix}, \quad (i = 1, \ldots, N)\ ,$$

$$B_{iL} = \begin{bmatrix} 0\ 0\ 0\ 0\ 0 & \frac{1}{2}\sin 2\phi_i & -\cos 2\phi_i & 0 & 0 \\ 0\ 0\ 0\ 0\ 0 & 0 & 0 & -\sin\phi_i & \cos\phi_i \end{bmatrix}, \quad (i = 1, \ldots, N)\ ,$$

and

$$D = \left[P_R^{(1)}(\omega, h)M_{xy}\ , P_R^{(1)}(\omega, h)(M_{yy} - M_{xx})\ , S_R^{(1)}(\omega, h)(M_{yy} + M_{xx})\right.,$$

$$Q_R^{(1)}(\omega, h)M_{yz}\,,\ Q_R^{(1)}(\omega, h)M_{xz}\,,\ P_L^{(1)}(\omega, h)(M_{xx} - M_{yy}),$$

$$P_L^{(1)}(\omega, h)M_{xy}\,,\ Q_L^{(1)}(\omega, h)M_{xz}\,,\ Q_L^{(1)}(\omega, h)M_{yz}\Big]^T\ ,$$

and

$$V = \Big[\alpha_R(\omega, h, \phi_1),\ \beta_R(\omega, h, \phi_1),\ \alpha_L(\omega, h, \phi_1),\ \beta_L(\omega, h, \phi_1),\ \cdots\ ,$$

$$\alpha_R(\omega, h, \phi_N),\ \beta_R(\omega, h, \phi_N),\ \alpha_L(\omega, h, \phi_N),\ \beta_L(\omega, h, \phi_N)\Big]^T\ .$$

If only Rayleigh waves (or Love waves) are used at a station with the azimuth ϕ_i, then only $\alpha_R(\omega, h, \phi_i)$ and $\beta_R(\omega, h, \phi_i)$ (or $\alpha_L(\omega, h, \phi_i)$ and $\beta_L(\omega, h, \phi_i)$) are included in the data vector V, and B_{iR} (or B_{iL}) is used for B_i. The system (A5) is solved for $D(\omega)$ at several frequencies: $\omega_1, \omega_2, \ldots, \omega_K$.

The second step solves the following system

$$\Gamma M = \Lambda\ , \tag{A6}$$

where

$$M = \Big[M_{xy}\,,\ (M_{yy} - M_{xx}),\ (M_{yy} + M_{xx}),\ M_{yz}\,,\ M_{xz}\Big]^T\ ,$$

$$\Lambda = \Big[D^T(\omega_1),\ D^T(\omega_2),\ \ldots,\ D^T(\omega_K)\Big]^T\ .$$

and

$$\Gamma = \Big[\Gamma_{1R}\ ,\ \Gamma_{1L}{}^T\ ,\ \Gamma_{2R}\ ,\ \Gamma_{2L}{}^T\ ,\ \cdots\ ,\ \Gamma_{KR}\ ,\ \Gamma_{KL}{}^T\Big]^T\ ,$$

$$\Gamma_{iR} = diag\Big[P_R^{(1)}(\omega_i, h),\ P_R^{(1)}(\omega_i, h),\ S_R^{(1)}(\omega_i, h),$$

$$Q_R^{(1)}(\omega_i, h),\ Q_R^{(1)}(\omega_i, h)\Big],\qquad (i = 1, \ldots, K)\ ,$$

$$\Gamma_{iL} = (\Gamma_{iL}{}^{jl})\ ,\qquad (i = 1, \ldots, K\ ;\ j = 1, \ldots, 4\ ;\ l = 1, \ldots, 5)\ .$$

Here the only nonzero components of $\Gamma_{iL}{}^{jl}$ are $\Gamma_{iL}{}^{21} = -\Gamma_{iL}{}^{12} = P_L^{(1)}(\omega_i, h)$ and $\Gamma_{iL}{}^{35} = \Gamma_{iL}{}^{44} = Q_L^{(1)}(\omega_i, h)$.

For the fault inversion, the first step inversion solves the same system as (A5). In the second step, the equation (A6) is solved for the scalar moment and fault parameters, with the moment tensor components replaced by the nonlinear functions m_i (i=1, ...5) defined in the text.

Appendix B

Seismograms of the Vertical Component of Rayleigh Waves

The vertical component seismograms of eleven large earthquakes studied in Chapter 1 recorded at IDA and GDSN stations are shown by a series of figures in this appendix. Each seismogram shown here is about 80 min long and the R_2 phases are aligned vertically. These seismograms are filtered with a Gaussian band-pass filter with a passband from 80 to 1500 sec. The azimuth and distance from the epicenter of each earthquake to the station are shown for each seismogram. Seismograms recorded at stations close to the source or the antipode have overlapped R_2 and R_3 wave trains and are not included.

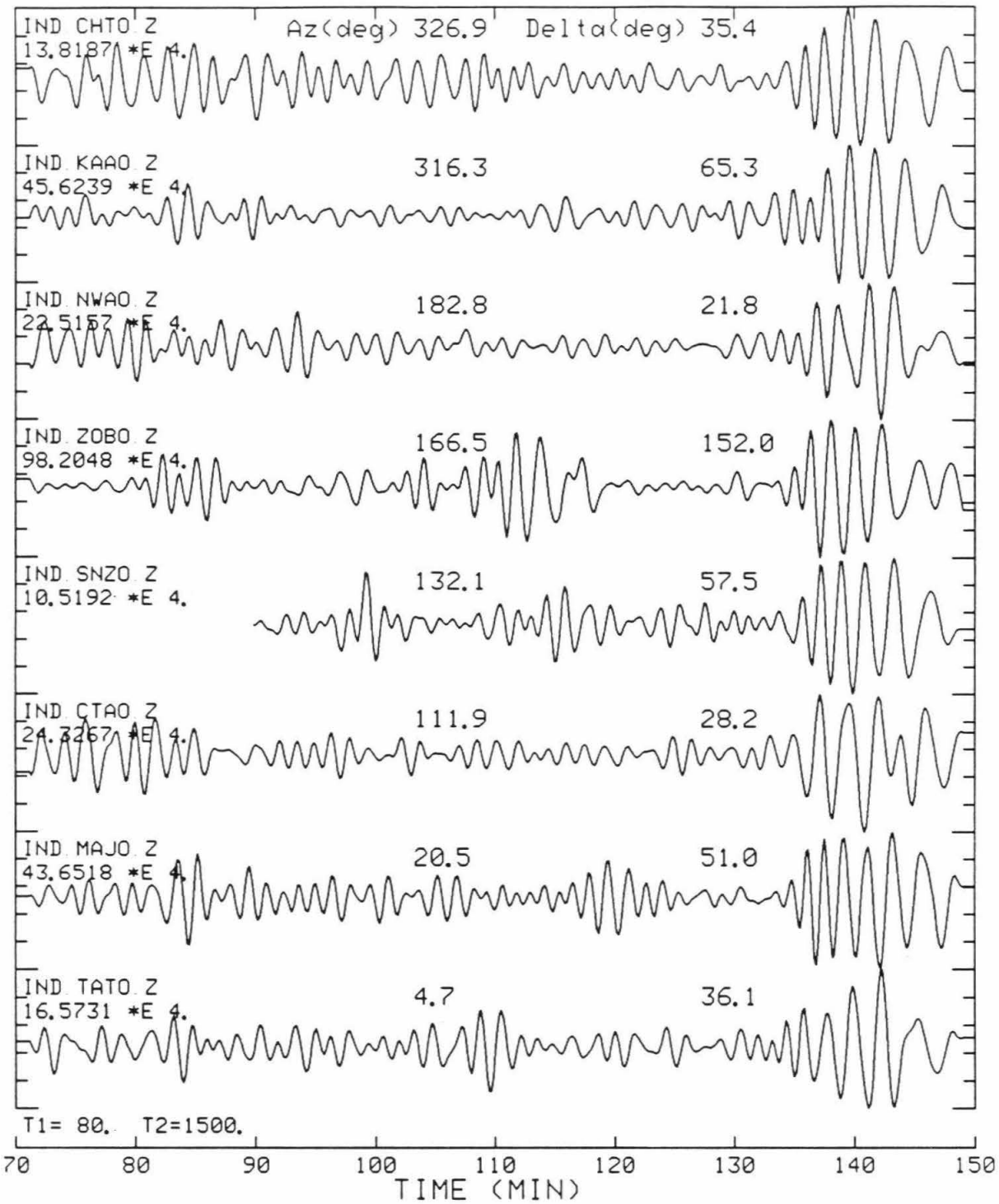
IND CHTO Z
13.8187 *E 4.
Az(deg) 326.9 Delta(deg) 35.4
IND KAAO Z
45.6239 *E 4.
316.3
65.3
IND NWAO Z
22.5157 *E 4.
182.8
21.8
IND ZOBO Z
98.2048 *E 4.
166.5
152.0
IND SNZO Z
10.5192 *E 4.
132.1
57.5
IND CTAO Z
24.3267 *E 4.
111.9
28.2
IND MAJO Z
43.6518 *E 4.
20.5
51.0
IND TATO Z
16.5731 *E 4.
4.7
36.1
T1= 80. T2=1500.
70
80
90
100
110
120
130
140
150
TIME (MIN)

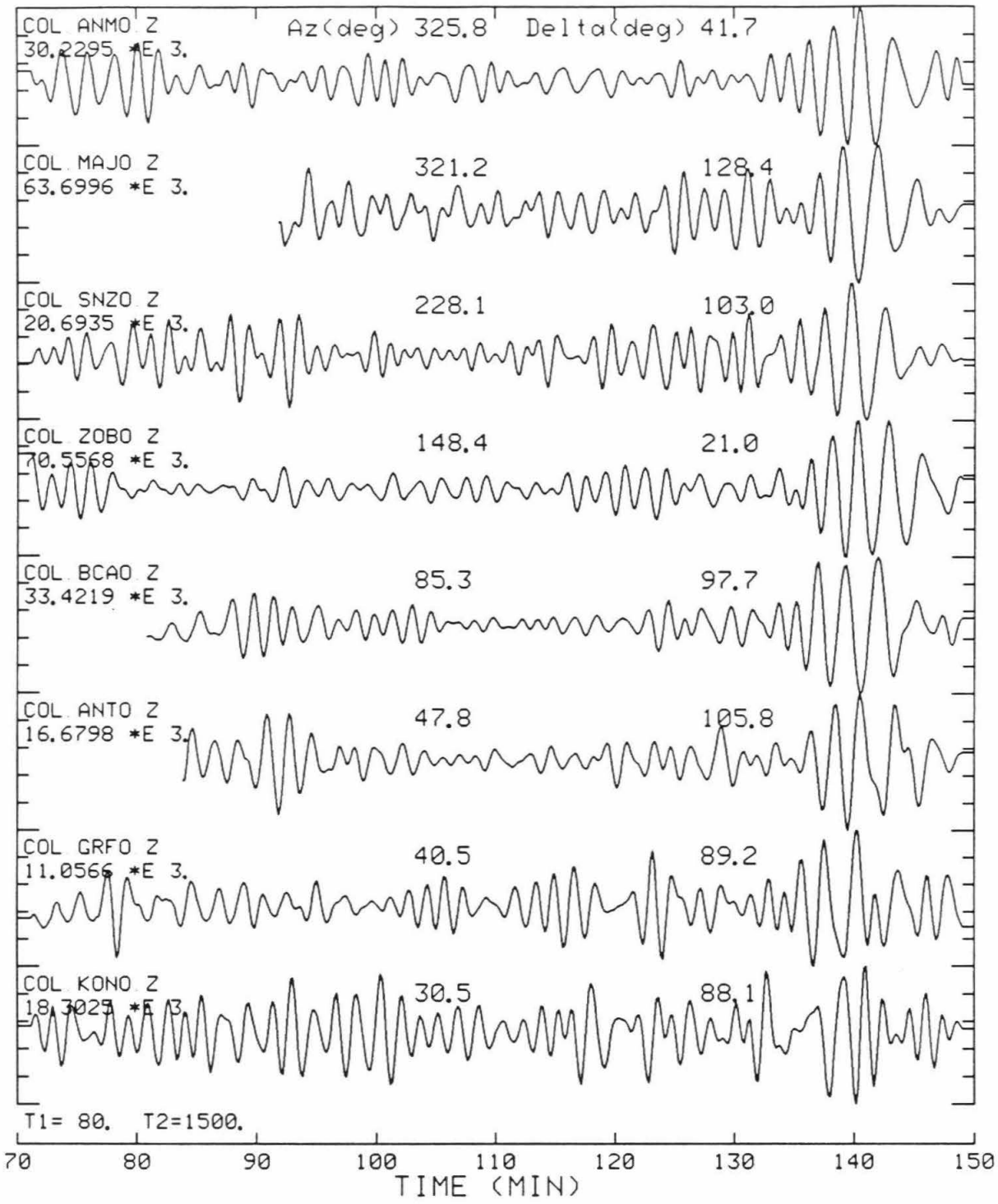
COL ANMO Z
30.2295 *E 3.
Az(deg) 325.8 Delta(deg) 41.7
COL MAJO Z
63.6996 *E 3.
321.2
128.4
COL SNZO Z
20.6935 *E 3.
228.1
103.0
COL ZOBO Z
70.5568 *E 3.
148.4
21.0
COL BCAO Z
33.4219 *E 3.
85.3
97.7
COL ANTO Z
16.6798 *E 3.
47.8
105.8
COL GRFO Z
11.0566 *E 3.
40.5
89.2
COL KONO Z
18.3025 *E 3.
30.5
88.1
T1= 80. T2=1500.
70
80
90
100
110
120
130
140
150
TIME (MIN)

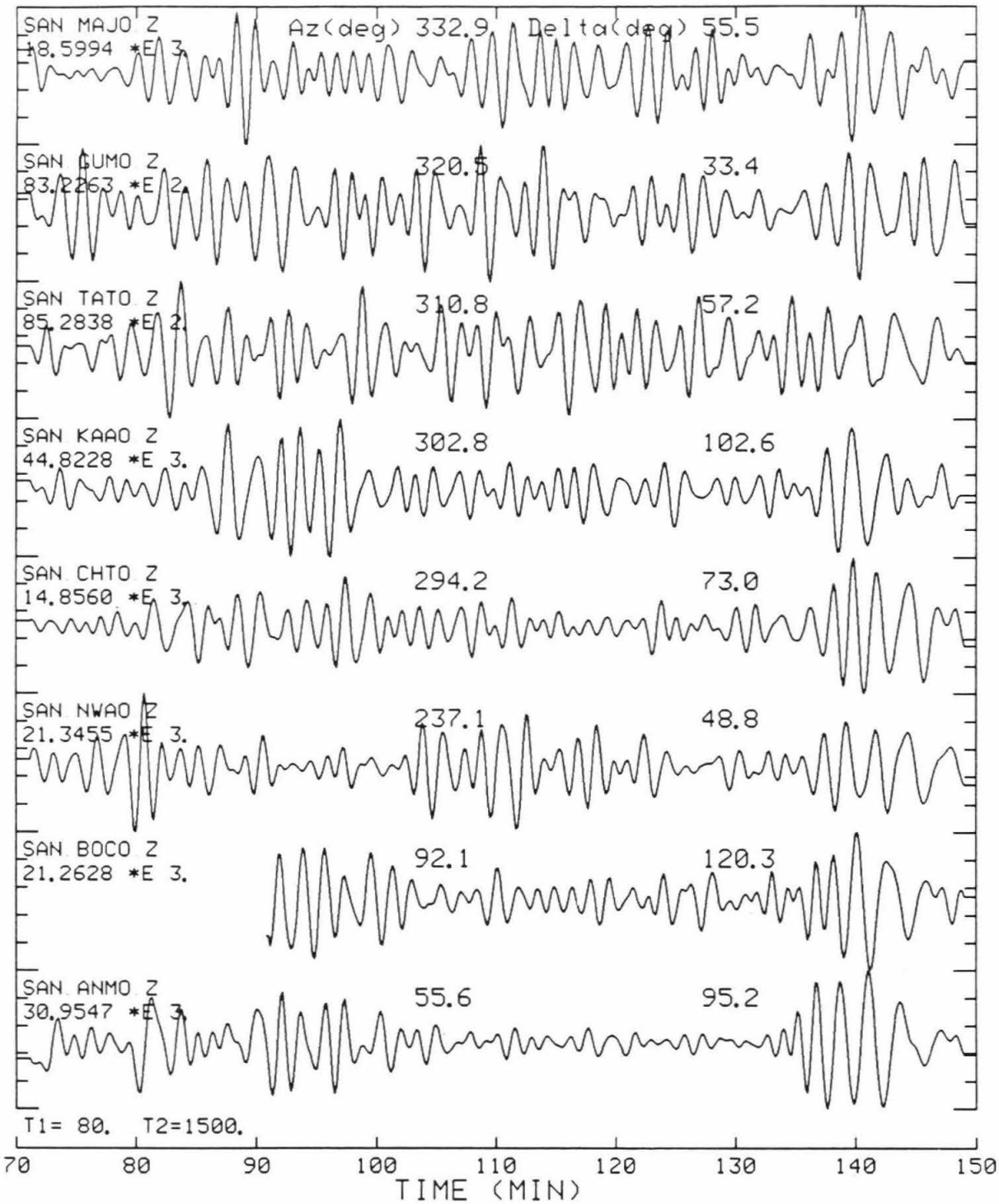
SAN MAJO Z
18.5994 *E 3.
Az(deg) 332.9 Delta(deg) 55.5
SAN SUMO Z
83.2263 *E 2.
320.5
33.4
SAN TATO Z
85.2838 *E 2.
310.8
57.2
SAN KAAO Z
44.8228 *E 3.
302.8
102.6
SAN CHTO Z
14.8560 *E 3.
294.2
73.0
SAN NWAO Z
21.3455 *E 3.
237.1
48.8
SAN BOCO Z
21.2628 *E 3.
92.1
120.3
SAN ANMO Z
30.9547 *E 3.
55.6
95.2
T1= 80. T2=1500.
70
80
90
100
110
120
130
140
150
TIME (MIN)

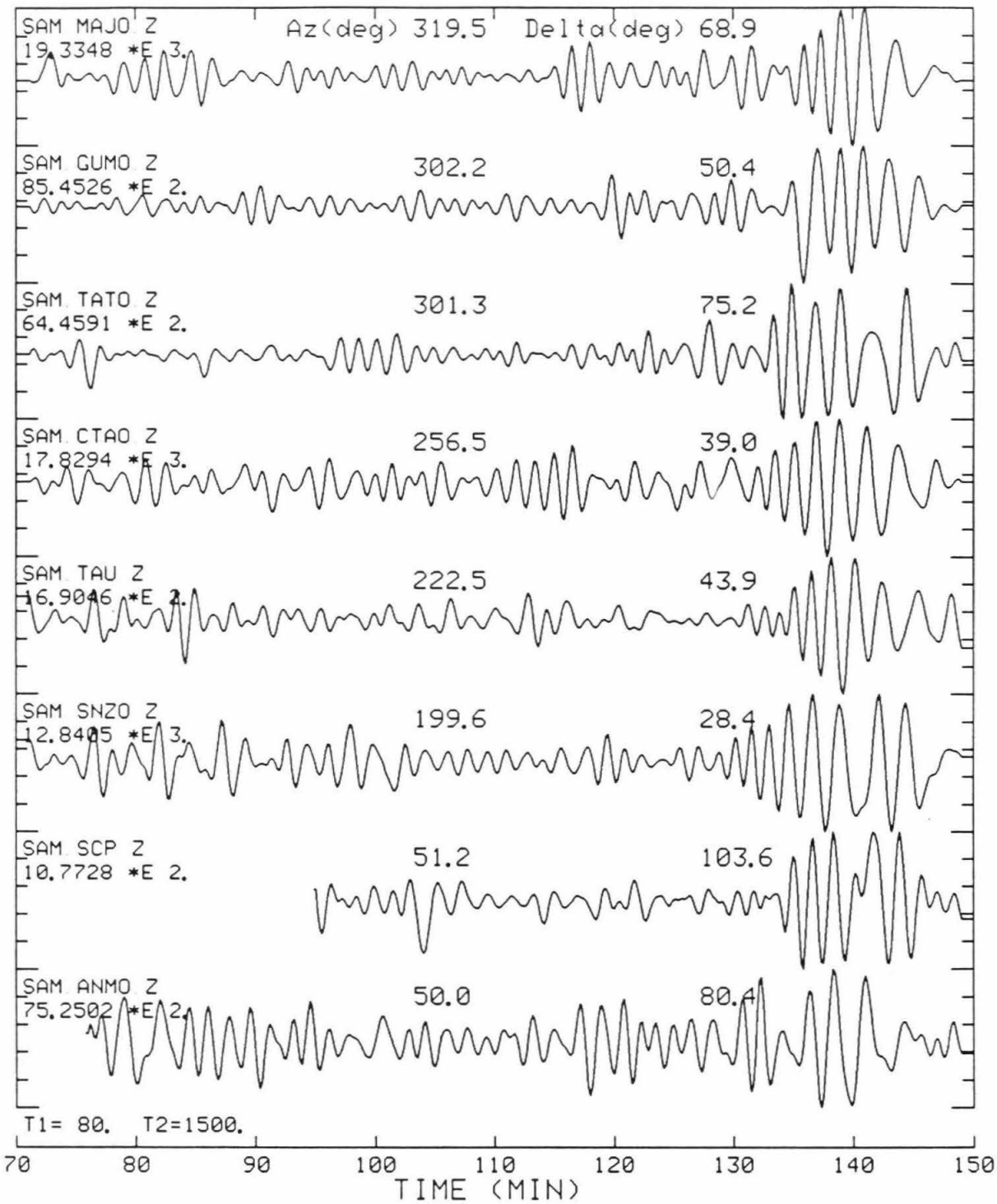
SAM MAJO Z
19.3348 *E 3.
Az(deg) 319.5 Delta(deg) 68.9
SAM GUMO Z
85.4526 *E 2.
302.2
50.4
SAM TATO Z
64.4591 *E 2.
301.3
75.2
SAM CTAO Z
17.8294 *E 3.
256.5
39.0
SAM TAU Z
16.9046 *E 2.
222.5
43.9
SAM SNZO Z
12.8405 *E 3.
199.6
28.4
SAM SCP Z
10.7728 *E 2.
51.2
103.6
SAM ANMO Z
75.2502 *E 2.
50.0
80.4
T1= 80. T2=1500.
70
80
90
100
110
120
130
140
150
TIME (MIN)

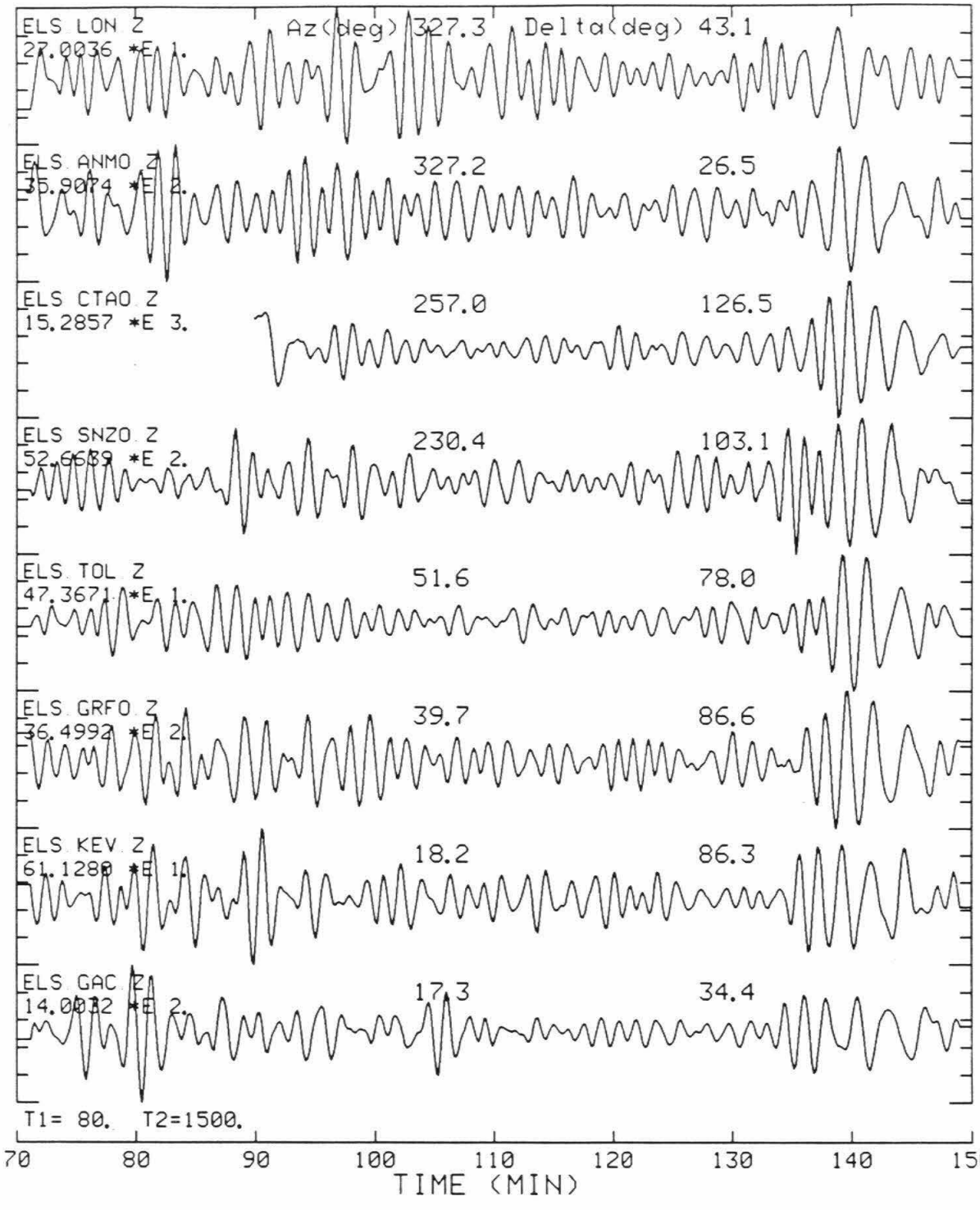
ELS LON Z
27.0036 *E 1.
Az(deg) 327.3 Delta(deg) 43.1
ELS ANMO Z
35.9074 *E 2.
327.2
26.5
ELS CTAO Z
15.2857 *E 3.
257.0
126.5
ELS SNZO Z
52.6689 *E 2.
230.4
103.1
ELS TOL Z
47.3671 *E 1.
51.6
78.0
ELS GRFO Z
36.4992 *E 2.
39.7
86.6
ELS KEV Z
61.1280 *E 1.
18.2
86.3
ELS GAC Z
14.0032 *E 2.
17.3
34.4
T1= 80. T2=1500.
70
80
90
100
110
120
130
140
150
TIME (MIN)

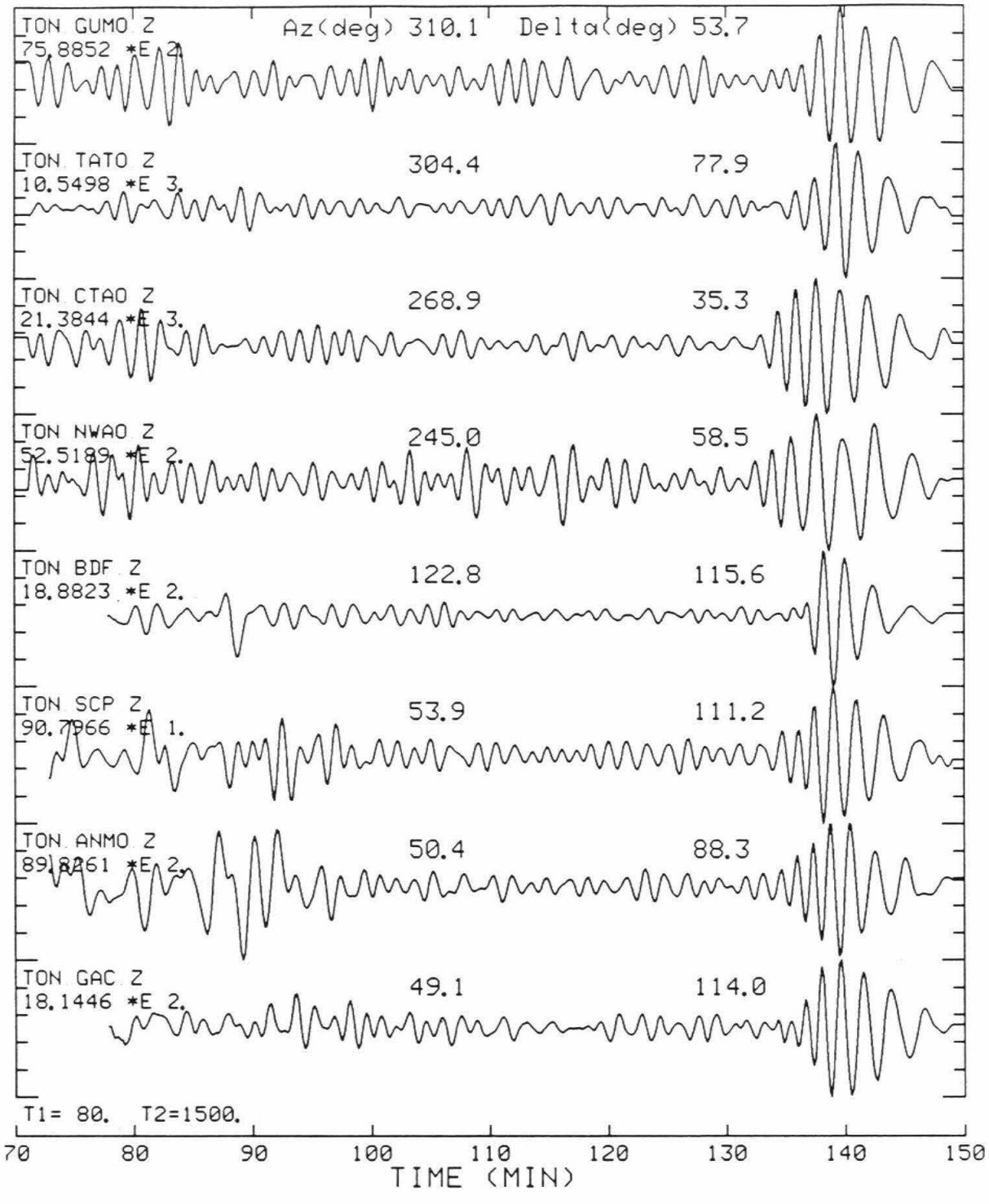
TON GUMO Z
75.8852 *E 2.
Az(deg) 310.1
Delta(deg) 53.7
TON TATO Z
10.5498 *E 3.
304.4
77.9
TON CTAO Z
21.3844 *E 3.
268.9
35.3
TON NWAO Z
52.5189 *E 2.
245.0
58.5
TON BDF Z
18.8823 *E 2.
122.8
115.6
TON SCP Z
90.7966 *E 1.
53.9
111.2
TON ANMO Z
89.8261 *E 2.
50.4
88.3
TON GAC Z
18.1446 *E 2.
49.1
114.0
T1= 80. T2=1500.
70
80
90
100
110
120
130
140
150
TIME (MIN)

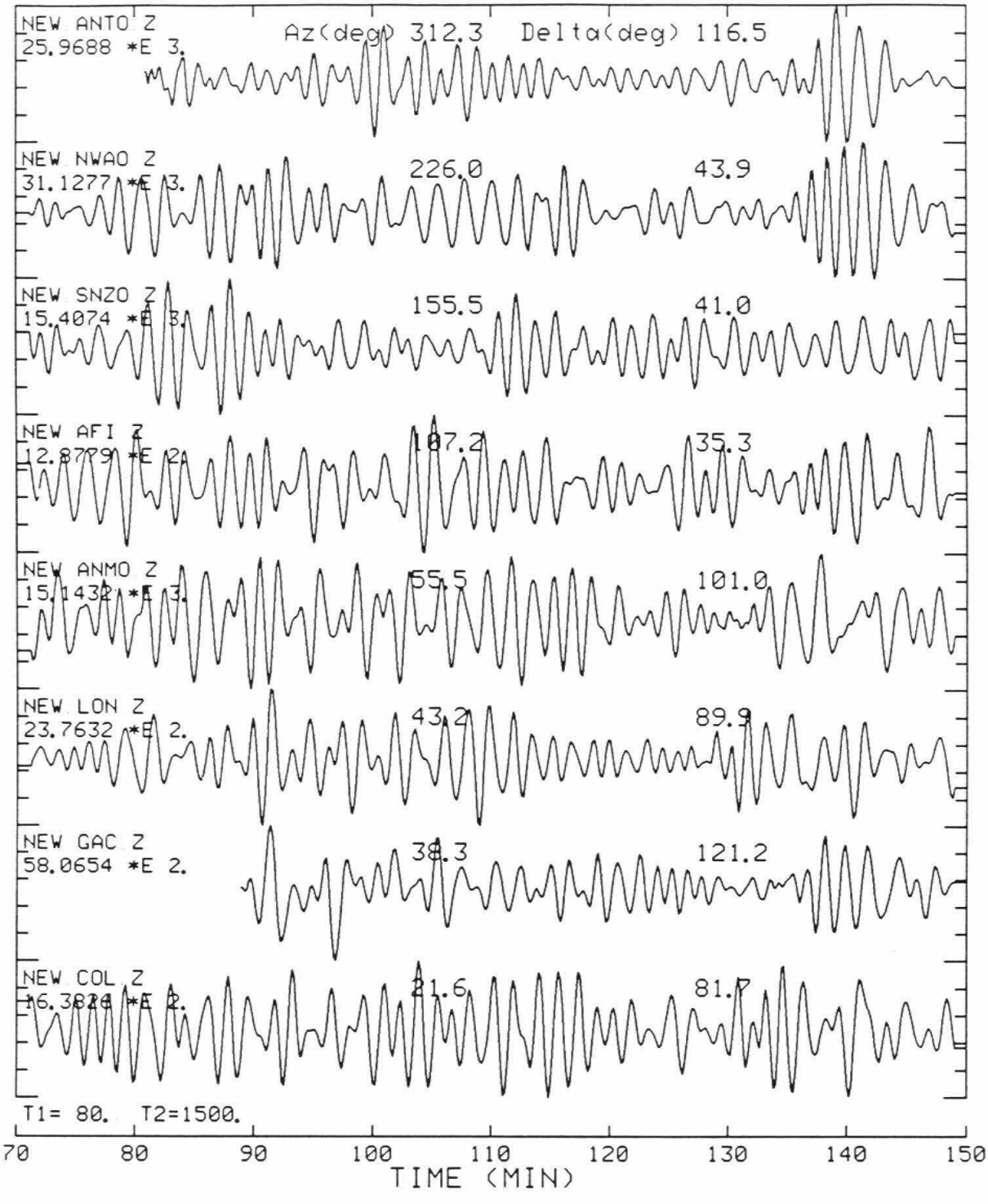
NEW ANTO Z
25.9688 *E 3.
Az(deg) 312.3 Delta(deg) 116.5
NEW NWAO Z
31.1277 *E 3.
226.0
43.9
NEW SNZO Z
15.4074 *E 3.
155.5
41.0
NEW AFI Z
12.8779 *E 2.
107.2
35.3
NEW ANMO Z
15.1432 *E 3.
55.5
101.0
NEW LON Z
23.7632 *E 2.
43.2
89.9
NEW GAC Z
58.0654 *E 2.
38.3
121.2
NEW COL Z
16.3826 *E 2.
21.6
81.7
T1= 80. T2=1500.
70
80
90
100
110
120
130
140
150
TIME (MIN)

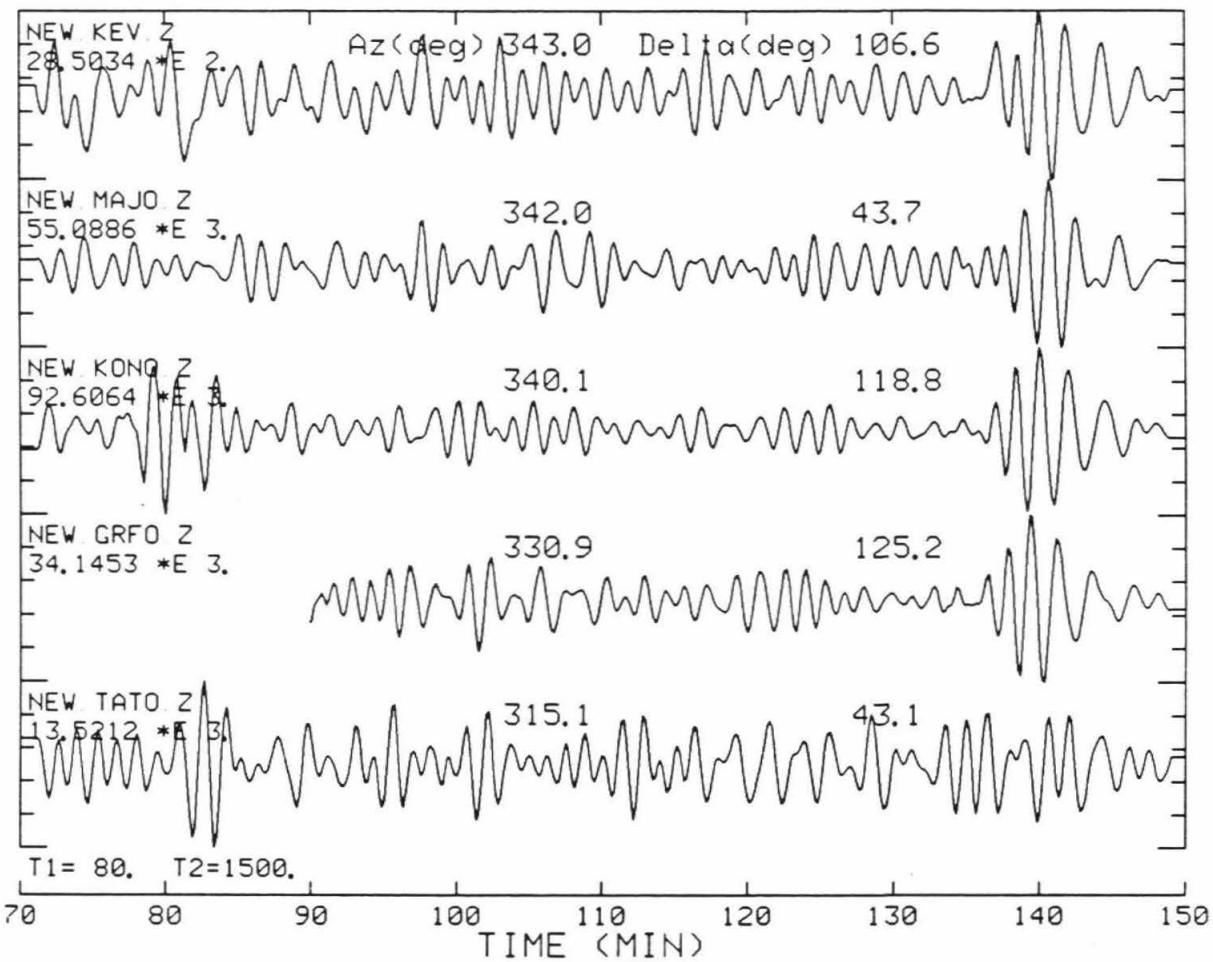
NEW KEV Z
28.5034 *E 2.
Az(deg) 343.0 Delta(deg) 106.6
NEW MAJO Z
55.0886 *E 3.
342.0
43.7
NEW KONO Z
92.6064 *E 3.
340.1
118.8
NEW GRFO Z
34.1453 *E 3.
330.9
125.2
NEW TATO Z
13.5212 *E 3.
315.1
43.1
T1= 80. T2=1500.
70
80
90
100
110
120
130
140
150
TIME (MIN)

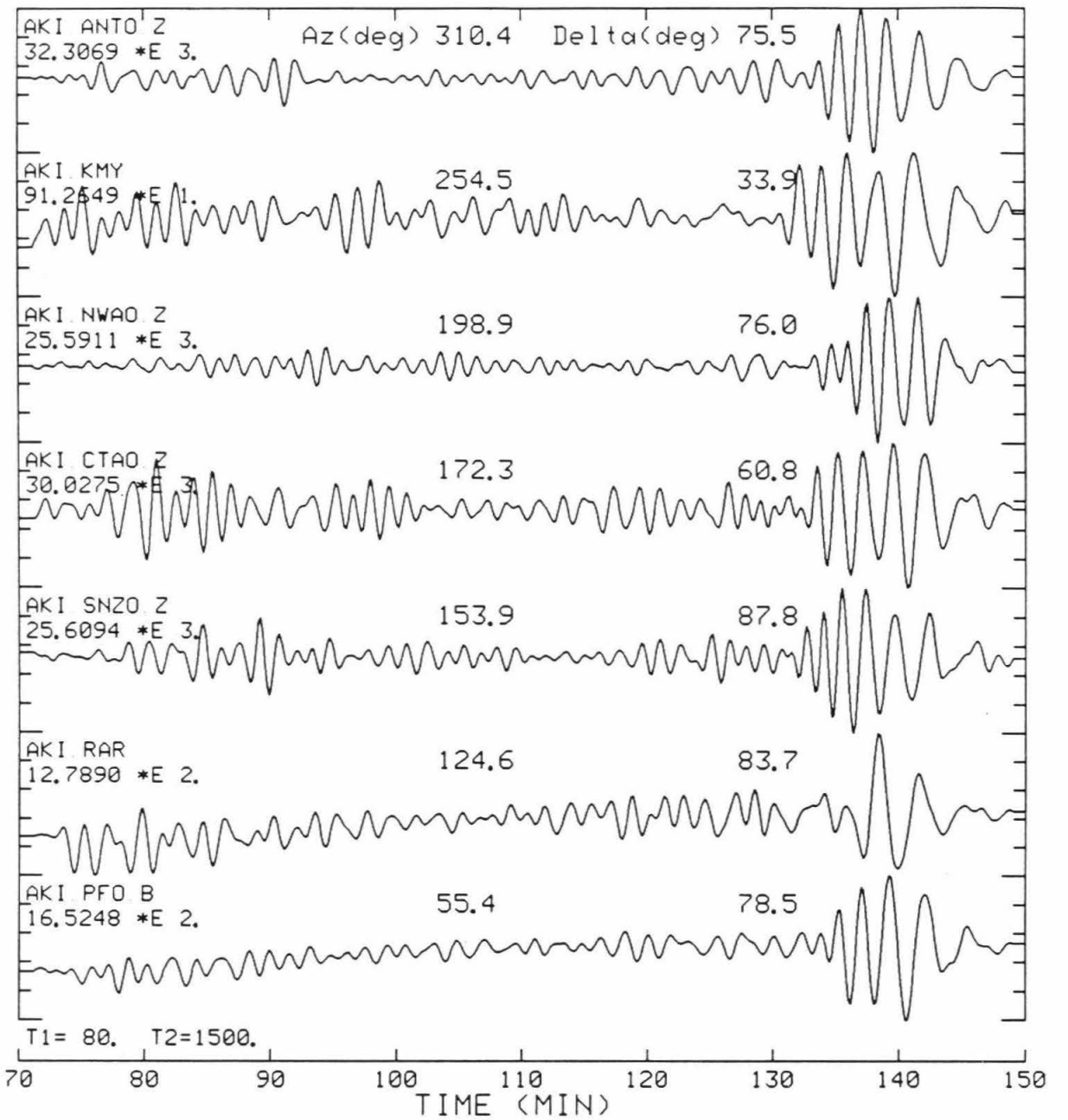
AKI ANTO Z
32.3069 *E 3.
Az(deg) 310.4 Delta(deg) 75.5
AKI KMY
91.2549 *E 1.
254.5
33.9
AKI NWAO Z
25.5911 *E 3.
198.9
76.0
AKI CTAO Z
30.0275 *E 3.
172.3
60.8
AKI SNZO Z
25.6094 *E 3.
153.9
87.8
AKI RAR
12.7890 *E 2.
124.6
83.7
AKI PFO B
16.5248 *E 2.
55.4
78.5
T1= 80. T2=1500.
70
80
90
100
110
120
130
140
150
TIME (MIN)

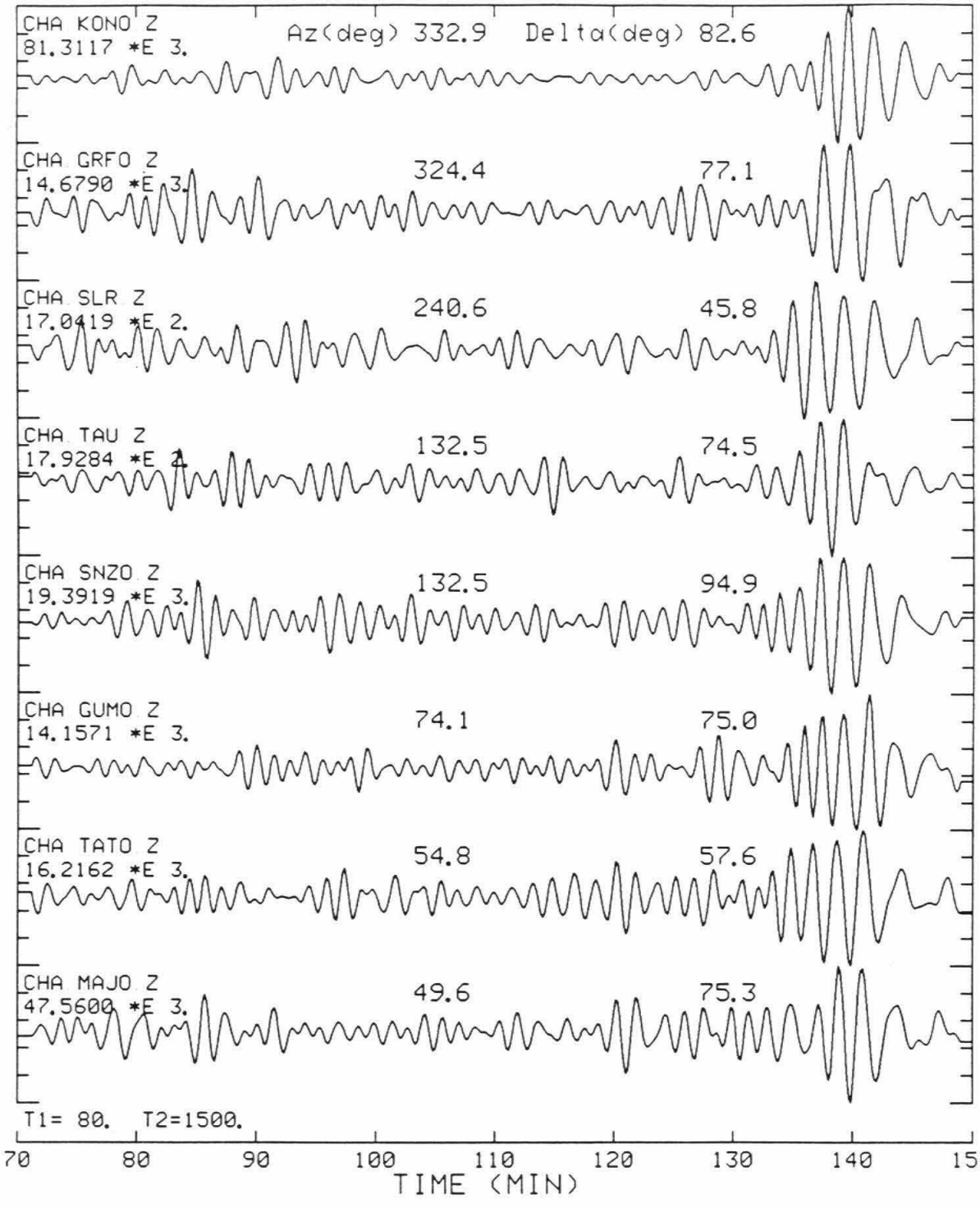
CHA KONO Z
81.3117 *E 3.
Az(deg) 332.9 Delta(deg) 82.6
CHA GRFO Z
14.6790 *E 3.
324.4
77.1
CHA SLR Z
17.0419 *E 2.
240.6
45.8
CHA TAU Z
17.9284 *E 2.
132.5
74.5
CHA SNZO Z
19.3919 *E 3.
132.5
94.9
CHA GUMO Z
14.1571 *E 3.
74.1
75.0
CHA TATO Z
16.2162 *E 3.
54.8
57.6
CHA MAJO Z
47.5600 *E 3.
49.6
75.3
T1= 80. T2=1500.
70
80
90
100
110
120
130
140
150
TIME (MIN)

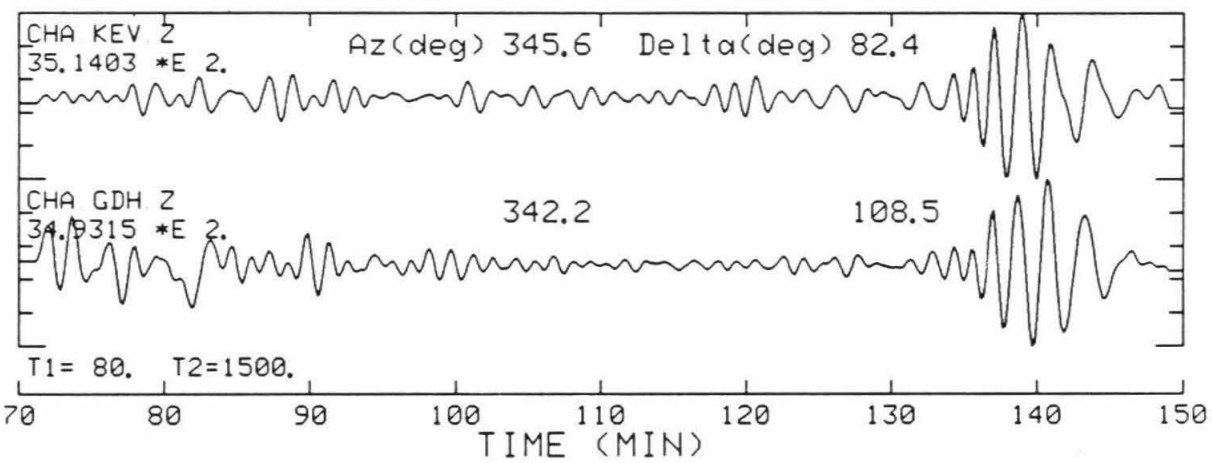
CHA KEV Z
35.1403 *E 2.
Az(deg) 345.6 Delta(deg) 82.4
CHA GDH Z
34.9315 *E 2.
342.2
108.5
T1= 80. T2=1500.
70
80
90
100
110
120
130
140
150
TIME (MIN)

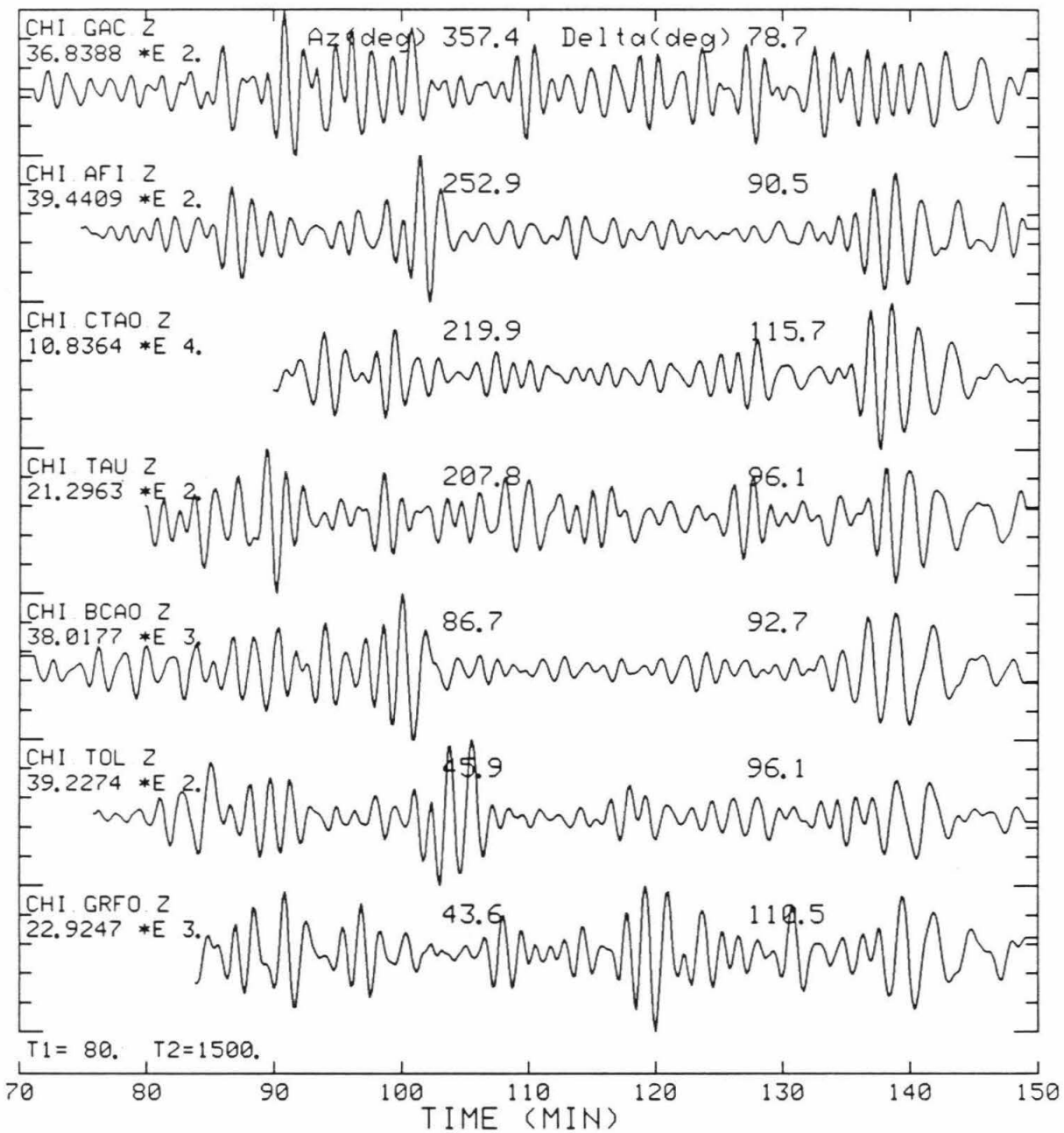
CHI GAC Z
36.8388 *E 2.
Az(deg) 357.4 Delta(deg) 78.7
CHI AFI Z
39.4409 *E 2.
252.9
90.5
CHI CTAO Z
10.8364 *E 4.
219.9
115.7
CHI TAU Z
21.2963 *E 2.
207.8
96.1
CHI BCAO Z
38.0177 *E 3.
86.7
92.7
CHI TOL Z
39.2274 *E 2.
45.9
96.1
CHI GRFO Z
22.9247 *E 3.
43.6
110.5
T1= 80. T2=1500.
70
80
90
100
110
120
130
140
150
TIME (MIN)

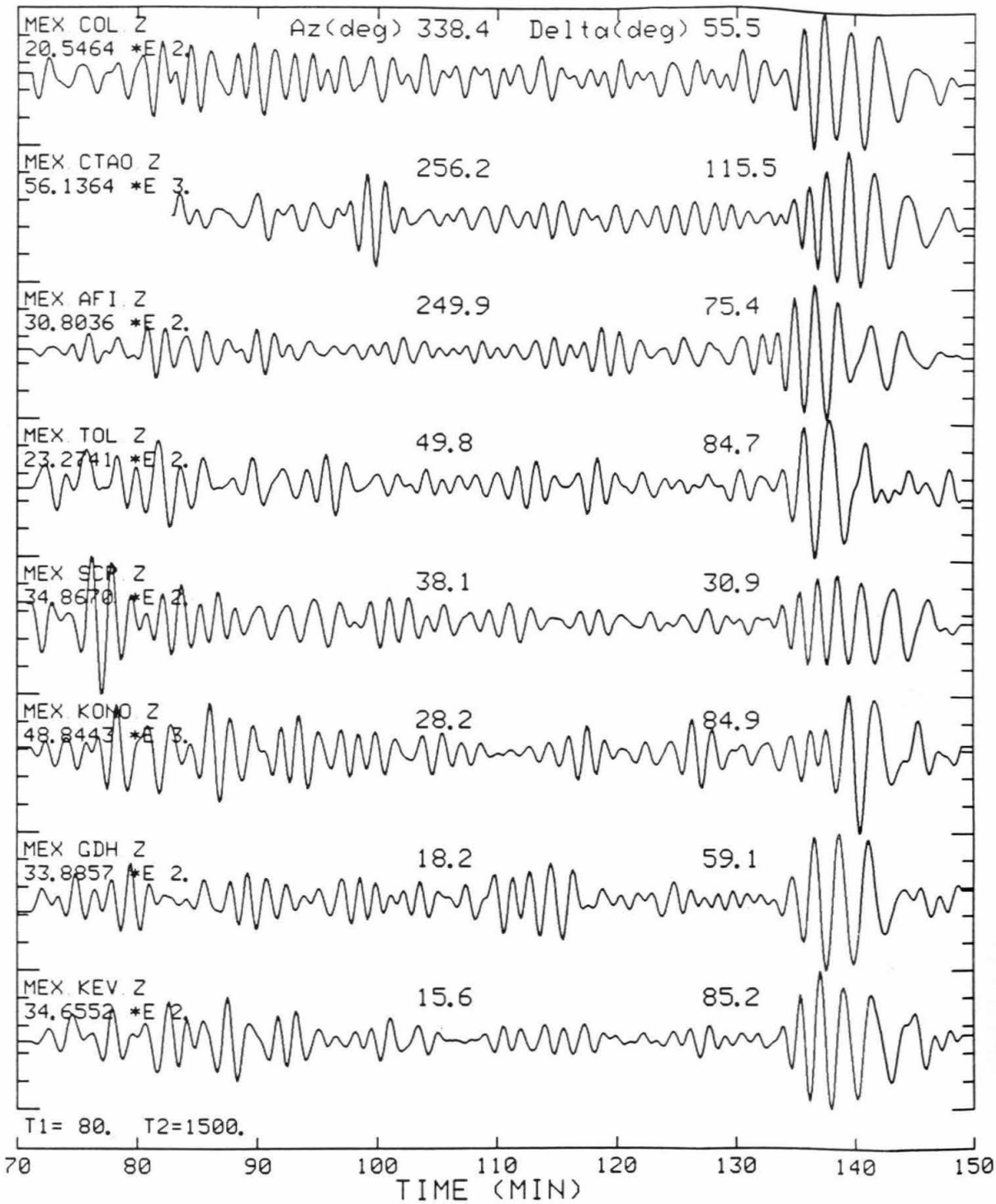
MEX COL Z
20.5464 *E 2.
Az(deg) 338.4 Delta(deg) 55.5
MEX CTAO Z
56.1364 *E 3.
256.2
115.5
MEX AFI Z
30.8036 *E 2.
249.9
75.4
MEX TOL Z
23.2741 *E 2.
49.8
84.7
MEX SCP Z
34.8670 *E 2.
38.1
30.9
MEX KONO Z
48.8443 *E 3.
28.2
84.9
MEX GDH Z
33.8857 *E 2.
18.2
59.1
MEX KEV Z
34.6552 *E 2.
15.6
85.2
T1= 80. T2=1500.
70
80
90
100
110
120
130
140
150
TIME (MIN)